DISSERTATION

submitted

to the

Combined Faculty for Natural Sciences and Mathematics

of

HEIDELBERG UNIVERSITY, GERMANY

for the degree of

Doctor of Natural Science

Put forward by

M. Sc. Mathematics, M. Sc. Computational Engineering

Ruth Malin Kopitzsch, née Schemschat

born in

Lebrade OT Rixdorf, Schleswig-Holstein, Germany

Oral examination:

Analysis of Human Push Recovery Motion Based on Optimization

Advisors: Prof. Dr. Katja Mombaur

Prof. Dr. Martin Giese

Zusammenfassung

Auf große Störungen während des Laufens zu reagieren, ist sowohl für Menschen als auch für humanoide Roboter essentiell, um nicht hinzufallen. Jeden Tag verletzen sich Millionen von Menschen in Folge von Stürzen. Dies ist nicht nur für die Betroffenen, sondern auch für die Gesellschaft ein großes Problem, da es die Gesundheitssysteme jährlich Milliarden Euro kostet. In dieser Arbeit wird eine Kombination aus Optimierung, Mensch-Modellen und aufgezeichneten gestörten Laufbewegungen verwendet, um besser zu verstehen, wie Menschen Störungen während des Laufens wahrnehmen.

Das Ziel dieser Arbeit ist, Grundprinzipien zu bestimmen, die den menschlichen Bewegungen zur Sturzvermeidung zu Grunde liegen. Der Mensch wird durch starre Segmente, die mit Gelenken miteinander verbunden sind, modelliert. Dies resultiert in einem unteraktuierten Mehrkörpersystem. Das Modell des Menschen wird in ein mehrphasiges Optimalsteuerungsproblem einbezogen, um die menschlichen Bewegungen zur Sturzvermeidung rekonstruieren und generieren zu können. Die Dynamik des Menschen wird dabei über den gesamten Zeitraum berücksichtigt. Auf Grund der starken Nichtlinearität wird das Optimierungsproblem mit einer auf Mehrfachschießen basierenden Methode gelöst.

Mit Hilfe der Kombination von Optimierung und Modellierung werden dynamisch konsistente Bewegungen für das Modell generiert, welche sehr nah an den experimentell erzeugten Daten sind. Die Gelenkwinkel und die Momente in den Gelenken des Menschmodells, welches durch die Ableitungen der Momente in den Gelenken gesteuert wird, werden für gestörte und ungestörte Bewegungen von zwei Probanden verglichen. Die Ergebnisse unterstützen die Annahme, dass umso stärker die Störung ist und umso höher die Störung am Rücken angebracht wird, desto höher sind die Momente, die für die Auffangbewegungen nötig sind. Wir zeigen außerdem, dass optimal gewählte Feder-Dämpfer-Elemente in den Gelenken die aktiven Momente in den Gelenken deutlich verringern. Außerdem untersuchen wir Zustände, die am meisten durch eine Störung betroffen sind und einen Hinweis auf eine Störung geben können. Die Reaktionszeiten von Beginn der Störung bis zu einer erkennbaren Änderung der Modellzustände werden untersucht.

Um ein besseres Verständnis menschlicher Sturzvermeidungsbewegungen zu erlangen, verfolgen wir außerdem die Methode der Bewegungserzeugung. Eine Steuerungsmethode wird in Form einer bestimmten Zielfunktion formuliert. Mit einer Periodizitätsformulierung in Kombination mit der Minimierung des Aufwandes konnten menschenähnliche Bewegungen erzeugt werden. Auf der Grundlage dieser Methode wird der Einfluss der Störungsstärke analysiert. Für ein Set unterschiedlicher Zielfuntionen werden gestörte Laufbewegungen generiert und mit Referenzdaten verglichen. Diese Untersuchungen zielen darauf ab, eine Zielfunktion als gewichtete Linearkombination der verschiedenen Kriterien in ein Inverses Optimalsteuerungsproblem zu integrieren und optimale Zielfunktionen zu generieren, welche zu menschenähnlichen Bewegungen führen. Diese Zielfunktion können dann auch verwendet werden, um Auffangbewegungen für z.B. humanoide Roboter oder Exoskelette zu berechnen.

Die Kombination aus Modellierung, Optimierung und Referenzdaten wird außerdem an zwei kombinierten Mensch-Exoskelett-Modellen angewendet, was zur Verbesserung dieser Unterstützungstechnologien führt. Die Verwendung ermöglicht uns die Gelenke in den Momenten zu berechnen, die ein Exoskelett für die Auffangbewegungen benötigt. Da die berechneten Momente relativ hoch sind, formulieren wir ein kombiniertes Mensch-Exoskelett-Modell mit passiven Feder-Dämpfer-Elementen, welche parallel zu den aktiven Momenten in den Gelenken wirken. Diese Formulierung führt zu einer deutlichen Verringerung der benötigten aktiven Momente in den Gelenken für die Auffangbewegungen. Eine solche Verringerung kann Energieeinsparungen oder das Abfangen stärkerer Störungen bei gleichem Kraftaufwand durch das Exoskelett ermöglichen.

Abstract

The ability to cope with large perturbations is essential to avoid falling for humans as well as for humanoid robots. Every day millions of people are affected by injuries due to falling. This is a huge problem not only for the individuum but also for the society as it costs the health care systems billions of euros. Also in the field of humanoid robots fall avoidance is very important as it protects robots against breakage.

In this thesis, the problem of fall avoidance is addressed using a combination of optimization, human-modeling and recorded push recovery motions. The aim is to identify the principles that lead to human-like push recovery motions. The human is modeled by rigid segments combined by joints leading to an underactuated multi-body representation. These models are included in multiple-stage optimal control problems to reconstruct and sythesize human push recovery motions considering the dynamics of a human over the whole time horizon. Due to the high nonlinearity, the optimization problem is solved based on a direct multiple shooting method.

To analyze the human push recovery motions, dynamically-consistent motions for the model that closely track experimental data are produced. The joint angles and joint torques for the human model controlled by joint torque derivatives are compared for perturbed and unperturbed motions from two subjects. The results verify the assumption that the heavier the perturbation is and the higher it is applied at the upper body, the larger are the resulting joint torques. We show that including optimally chosen spring-damper elements in the joints can reduce the active joint torques significantly. We further exploit our motion reconstruction approach to determine the states that are most affected during a perturbation. Relevant parameters such as the orientation and position of the head and body, joint angles and torques of the perturbed motions are analyzed for deviations to the unperturbed motions at the point in time when the push occurs. Identifying the point in time when the model states of the perturbed motions differ from the unperturbed motions, the reaction times are determined.

To better understand human push recovery motions, we also investigate in a motion sythesis approach. This approach enables a control hypothesis, in the form of a specific objective function, to be formed. The minimization of effort combined with a periodicity formulation results in human-like motions and the influence of the push strength is analyzed. Formulating the objective function as a weighted linear combination of possible optimality criteria provides the possibility to analyze different optimality criteria and their resulting motion. The difficulty is, that for a given motion, it is not known, which criteria lead to that specific motion. In this thesis, the results for different basal objective functions are analyzed. These studies prepare to determine the optimal weights of the criteria by including the presented motion generation formulation in an inverse optimal control problem. Having analyzed general weights that lead to a good approximation of the human recovery motions, the resulting objective function can be used to generate push recovery motions also for humanoid robots or assistive devices such as exoskeletons.

To show another application in the improvement of technical assistive devices, we include two combined human exoskeleton models of different weights in our calculations. This allows us to analyze the joint torques for these models including the exoskeletons and compare the results to a human model. As the resulting joint torques are quite large, we also formulate combined human exoskeleton models with passive spring-damper elements that act in parallel to the active torques. This compliant formulation leads to a significant reduction of the active joint torque needed for the recovery motion. The reduction of the active joint torques allows the reduction of energy needed for the recovery motion or can enable the recovery from stronger perturbations.

Acknowledgements

This thesis was conducted at the *Optimization in Robotics and Biomechanics* (ORB) group of the *Institute of Computer Engineering* (ZITI) and member of the *Interdisciplinary Center for Scientific Computing* (IWR) at the Faculty of Mathematics and Computer Science at Heidelberg University in Mathematics. It was financially supported by the *Heidelberg Graduate School Mathematical and Computational Methods for the Sciences* (HGS Mathcomp) and the *Graduate Academy Heidelberg University*.

First of all, I would like to express my appreciation to my first supervisor *Prof. Dr. Katja Mombaur*, who went with me through many fruitful discussions about my thesis especially in the last years of my thesis. She also made it possible that I could visit the conferences and workshops I went to during the first years of the thesis, which provided the opportunity to network with international people.

I would like to offer my special thanks to my other supervisors *Dr. Debora Clever*, who supported my work with a huge amount of energy - textually and mentally - in the first years, and to *Prof. Dr. Martin Giese*, who did not only help with his neurological input but also allowed my experiments in his lab at CIN in Tübingen. I am particularly grateful for the assistance given by *Dr. Enrico Chiovetto* during the experiments and the transformation of data was. He also influenced my work with his inspiring ideas about my motion analysis. Assistance provided by my probands and all other people involved during the experiments is also appreciated.

My thanks are extended to the research group *Simulation and Optimization* (of IWR, Heidelberg University) of *Prof. Dr. Dr. h.c. mult. Hans Georg Bock* for giving me the possibility to work with their software package MUSCOD-II, which has been used to achieve the results of this thesis. I also want to thank *Martin Felis* for providing the rigid multi-body dynamics library `RBDL` used for the models in this work, the *KIT* for the Master Motion Map `MMM` used for the conversion of the recorded experimental data and *Felix Aller* for a converter used to convert these data to our model.

I would like to thank my colleagues at ORB for the inspiring working environment, especially *Henning* for the discussions and support in the first years, *Benjamin* not only for setting up experimental environment and constructing the pushing device, but also the help in all other technical questions, to *Alex* for the support with IMUs and his IOC experience, Sascha for the computer support. Special thanks to *Marina* and *Davide*, my first office mates who welcomed and integrated me in the group and all other office mates, making my work more joyful and giving productive input to my thesis. The advice given by *Yue* has been a great help keeping organized and focused. Thanks to *Matt* for all the discussions about pushing and balance motions as well as for the general thesis writing advice, which pushed me to finish. My thanks are extended to *Anton*, *Tobi*, *Kevin*, *Marina*, *Debora* and *Matt* for proofreading parts of my thesis.

Great thanks go to my parents, who always supported me to go my own way and never showed any doubt to believe in my abilities. I also have to thank my brother and his family who cheered me up with their pleasant way of life and all my friends who made me smile whenever I got frustrated not seeing the end of the work. The same holds for the family, friends, and colleagues of my husband, who always found motivating words for me struggling to finish. Finally, I want to thank my husband *Anton* who went through all the bad moods with patience, cared for our children and provided help as good as he could. Last but not least I thank my children *Katinka* and *Kosimo* for their distractions - making my life enjoyable even in the stressful time of the thesis - and for inspiring me, making a race with my simulations to learn how to balance.

To my family

Our greatest glory is not in never falling, but in rising every time we fall.

- A tumbler toy -

Contents

Introduction

The real world is full of obstacles, uneven floors, and unpredictable pushes from fellow humans. When observing toddlers as they learn how to move, the challenge of balancing and recovering from perturbation becomes clear immediately. Learning how to walk, young children fall very often, but they suffer very seldom from serious injury. Growing older, falling becomes less frequent, but if they fall their injuries are more serious and their recovery is slower [116]. For the elderly, the frequency of falling increases again and often the injuries even cause death [97, 184]. Falling is a huge problem not only for the individuals but also a cost factor for society [2, 157].

One way to remain independent is to rely on technical devices such as prostheses or exoskeletons [22]. The problem of enabling these assistive devices to react to perturbations and prevent humans from falling is a future leading field of research which is closely linked to robotics. Also for robots, especially humanoids, it is still a huge challenge to recover even from small perturbation [63].

This thesis aims to provide a better understanding of human push recovery motions to enhance fall avoidance abilities. Identifying rules on how humans manage to recover from perturbation can also be applied to the development and improvement of exoskeletons and also humanoid robots. Many researchers investigated in the analysis of perturbation during standing based on experimental records [5, 11, 55, 69, 83, 193] or to balance small disturbances due to body sway [64, 189]. The investigations on heavily perturbed walking motions that require recovery motions as regarded in this work are often based on experimental measurements [42, 61, 114] or video analysis [154].

In this work, the focus lies on the analysis of human push recovery motions based on recordings from experiments and full-body human models combined with optimization algorithms. The perturbations are applied during straight walking on even ground. We regard pushes from the back which vary in push strength and the height of the point at the spine where the push is applied (push point) as well as in the timing of the push during the gait cycle. To analyze these complex motions, we use model-based nonlinear optimal control methods. The analysis is mainly motivated by the following questions:

- How does a human sense a perturbation?
- How do the motions of perturbed and unperturbed walking compare?
- How does a human recover from perturbation?
- How can compliant actuators support the human push recovery motion?
- What capabilities would an exoskeleton have to have to enhance human push recovery abilities?

Scope of this Thesis

This thesis is dedicated to analyze push recovery motions during human walking. Human walking is a complex and well-coordinated interaction between body segments. To this end, rigid multi-body dynamics models and optimal control strategies are combined with reference data for motion capture experiments. In the following, an overview of the investigated approaches is given.

For our analysis we set-up rigid multi-body dynamics models that can cope with strong perturbations during walking motions. The models are implemented in the rigid multi-body dynamics library `RBDL` [40]. To keep the effort manageable, we only regard two-dimensional models. As we concentrate our investigations on perturbations from the back in walking direction (sagittal plane) during straight walking on even ground, a two-dimensional model is sufficient to represent the regarded motions well. We record human push recovery motions during walking using a Vicon camera system and the applied push force and push direction using a force sensor from OptoForce in the motion capture lap from CIN in Tübingen. Modeling the perturbation as an external force allows the analysis of heavily perturbed motions. To be able to include the recorded motion capture data in our calculations, we convert them to the model using the master motor map (MMM) from KIT [176].

To address the first two questions of comparing perturbed and unperturbed motions and analyzing how a human senses a perturbation, we follow a motion reconstruction approach. To this end, the dynamics of the model are included as constraints in a multiple-stage optimal control problem. An objective function is formulated that minimizes the distance from model states to joint angles from reference data in a least-squares sense. The resulting highly non-linear multiple-phase optimal control problem is solved using the direct multiple-shooting method implemented in MUSCOD-II [12]. From the reconstructed model motion, data can be established, that are not or not easily measurable by experiments, e.g. the internal joint torques, angular momentum, ground reaction forces, etc. These variables are compared for the different perturbations and motions without perturbation.

The next question to be answered is how humans recover from strong perturbations during walking. To this end, a motion synthesis approach is formulated. A first guess of an objective function is given that already results in human-like recovery motions during walking. However, the objective function for the gait synthesis formulation is not known beforehand. One way of identifying a human-like cost function is to formulate the cost function as a weighted linear combination of optimality criteria. To determine the weights of the objective function which results in a motion as close as possible to reference data, the optimal control problem in the motion synthesis formulation can be included as an inner problem in an inverse optimal control problem. Then in the outer problem, the difference between the model data to the reference data is minimized by using an objective function similar to the one of the reconstruction formulation. To prepare for the inverse optimal control method, we investigate in step synthesis with a set of basal objective functions and analyze the resulting motions on similarity to reference data.

We use the reconstruction formulation to investigate the question of how a compliant formulation can support push recovery motions from perturbations during straight human walking motions on even ground. We do not investigate in muscle controls as in the human but we analyze how optimally chosen spring-damper systems in the joints influence the active joint torques. Assistive devices such as exoskeletons typically lack these compliant properties that a human has.

To analyze what capabilities would exoskeletons have to have to enhance human balance recovery, we include combined human-exoskeleton models in our motion reconstruction formulation. First, we concentrate on the analysis of joint torques the exoskeleton has to provide. In a second study, we analyze how to choose the optimal parameters for compliant actuators in exoskeletons.

Contributions of the Thesis

This thesis has several contributions each relating to the dynamics and control of balance recovery during walking. The main contributions of this thesis can be classified to the following fields:

Database of Push Recovery Motions during Walking

The first contribution is an experimental measurement and analysis of the movements and forces during balance recovery. The motions cover normal human steps, perturbed human steps and the steps after the perturbation. The walking motions are perturbed by pushes from the back. Pushes of different strengths are applied at three different heights at the spine. The motion is recorded using a motion capture camera system from Vicon. The perturbation is recorded using a force sensor from OptoForce. The data include recordings of two subjects. Analyzing this data, we found that all motions including a perturbation are faster than the motions without perturbation. We have made the data collected during the experiments publicly available in the Koroibot Database[1] so that others can build on this work.

Human Multi-Body Dynamics Model for Push Recovery Motions during Walking

The high complexity of the human body makes it difficult to analyze human motions. The human body has many degrees of freedom that allow relative motions of all segments of the body, and the system is highly redundant for performing many motion tasks. It is modeled as a dynamic multi-body system with rigid segments, which is driven by internal joint torques at all internal degrees of freedom, resulting overall in an underactuated system. The perturbation is modeled as an applied force that is a continuous function of time. This novel formulation allows for the analysis of heavily perturbed motions. Formulating a walking motion with or without a push for such a system results in a hybrid dynamics problem, i.e. it contains multiple continuous motion phases with different equations of motions as well as instantaneous phases describing discontinuities, e.g. in the velocities at the impact of a foot on the ground.

Optimization-Based Synthesis of Perturbed Human Walking Motions

The motion synthesis studies are based on the general assumption that human motions, as many processes in nature, are always optimal or close to optimal in some sense [8]. We, therefore, approach the problem of generating push recovery motions utilizing mathematical optimization, or, more specifically, optimal control. As a human model, we use the two dimensional rigid multi-body model for push recovery motions described by differential equations of motions including the perturbation as an external force. The dynamics of the physical model are considered as underlying constraints of a multiple-stage optimal control problem. As a first assumption, we formulate an objective function, minimizing the effort while beeing as periodic as possible. For the first time, a heavily perturbed walking motion is generated using the presented full-body human model. It can be shown that motions with stronger perturbations are less periodic. Furthermore, the joint torque of the right ankle increases the stronger the perturbation.

Investigating in the perturbed motions generated by basal objective functions with forces from reference data, it can be shown, that the minimization of the derivative of the right ankle torque and the minimization of the end-time lead to motions less similar to the reference motion than the minimization of other joint torque derivatives. Our investigations indicate that a general objective function (e.g. calculated by including the investigated optimal control problem in an inverse optimal control formulation) to generate unperturbed human gait differs from the objective function to generate the recovery step from perturbations during walking.

---

[1] `https://koroibot-motion-database.humanoids.kit.edu/`

Optimization-Based Reconstruction of Perturbed Human Walking Motions

Motion reconstruction approaches are formulated that enables to analyze variables and parameters of heavily perturbed and unperturbed walking motions from the database in humans.

- **General Analysis of Human Push Recovery Walking Motions**
  We also use a combination of optimization and modeling to analyze which states are most affected during the perturbed human walking motions from our database. To gain these physical quantities, we use the same human model as for the motion generation studies. Other than for the motion generation approach a least-squares optimal control problem (OCP) is formulated to fit this model to the recorded perturbed human walking motions from the database introduced above. The results show, the kinetic energy is larger, the higher the push point is located at the spine and that the higher the perturbation is located at the spine and the stronger the perturbation, the larger are the joint torques needed to recover from the perturbation.

- **Analysis of Indicators to Sense a Perturbation**
  We further exploit the motion reconstruction approach to identify principles that are most relevant to sense a perturbation. The results of this work indicate that torques in the stance shoulder and the orientation of the head are the most important physical quantities in order to both sense and reject a perturbation. Another important factor is the position of the head towards the body. The results suggest that the chest is not an optimal position to place a balance sensor because not all perturbations can be sensed at this point. The mean reaction time of all considered motions is only a bit longer than the reaction time to simple tasks with only one sensory system stimulated. This result indicates that the human brain is very fast in processing information about perturbation and making a decision on how to react.

- **Analysis of Influence of Compliance in Human Push Recovery Motions**
  To analyze the influence of compliant actuators, the human model is reformulated with active and passive control elements. In this novel compliant formulation, spring-damper elements act in parallel to the active joint torques. Optimally chosen parameters for these compliant actuators result in a significant reduction of the active joint torques needed during the recovery motions.

Design Optimization of Exoskeletons to Support Human Push Recovery Motions

We follow a novel integrated design approach, where whole-body optimal control is used to simultaneously simulate a person and the exoskeleton worn by the person.

- **Analysis of Joint Torques an Exoskeleton Has to Provide**
  In the first study, it is determined how large the total joint torques during the recovery motions have to be for humans only and humans with different exoskeletons, and how they change with different push locations and push magnitudes. This work follows the optimization-based reconstruction approach in which a combined model of a person and an exoskeleton is fitted to data of perturbed and unperturbed walking on level ground. It serves to determine the required joint torques as well as torque-angle relationships and structural loads for different combinations of body and exoskeleton masses. The joint torques increase not only for heavier exoskeletons but also for increasing strength of perturbation. Since the resulting torques an exoskeleton has to provide to recover from perturbations are quite high, a second study is investigated how the active joint torques can be supported by appropriately chosen parallel passive spring-damper elements.

- **Analysis of the Influence of Compliant Acutators**
  In a second study, we include parameterized spring-damper elements in parallel to all active torques in the exoskeleton joints. The spring-damper constants that lead to the best possible support of the active torques are determined by the optimization process. The results of this novel approach show a significant reduction in active joint torques due to the passive elements. This leads on the one hand to the possibility of higher total joint torques to allow more extensive push recovery motions, and on the other hand, it reduces the active torques and removes joint torque peaks which results in saving energy and might lead to more lightweight exoskeletons.

Thesis Overview

This thesis is organized into ten chapters, the first four focus on the experimental and mathematical background required to address the five research questions. In Chapter 1 an introduction to push recovery motions is given. After the presentation summary on human push recovery motions and the methods, an introduction to senses is given. The sensory systems most relevant for the detection of perturbation during human walking motions are described briefly. An overview of the reaction times for the sensory systems is given. The theory of sensory reweighting, which allows the influence of multiple sensors in an action, is characterized. Finally, postural reflexes relevant in the scope of push recovery motions are presented very briefly.

The following Chapter 2 deals with the recording of reference data using a motion capture system as well as the experimental setup including the equipment. The conversion of the recorded data to the reference data for a human rigid multi-body model is described. Two data sets of perturbed and unperturbed motions used for our simulations are presented. The main characteristics of the motions are analyzed.

In Chapter 3 the physical human model used for our simulations is introduced. After a short overview of rigid multi-body dynamics modeling, a description of the modeling of human gait as a hybrid dynamics problem consisting of multiple stages is given. Various possibilities of how to implement the perturbation are presented.

Chapter 4 covers the theory of optimal control problems for human gait analysis and their solutions. The modeling of human gait including perturbation results in a large-scale multiple stage optimal control problem. To solve this problem, a direct multiple shooting method is used, including a condensed sequential quadratic program algorithm.

In Chapters 5-8 the results of perturbed human walking motion analysis using the methods from the previous chapters are presented. Chapter 5 deals with the reconstruction of the reference data from experiments to the human model. The joint angles, joint torques and other model parameters that can be derived from the model are compared for perturbed and unperturbed motions from the two datasets. In Chapter 6 principles that are used to sense a perturbation during human walking motions and the reaction times to the perturbations are identified. In the following Chapter 7 a method to generate human push recovery motions with a fixed initial position and objective function is presented and the resulting motions are analyzed. We also investigate which basal objective function leads to the most human-like motion to prepare for inclusion in inverse optimal control. Furthermore, the influence of compliance to the internal joint torques during push recovery motions is analyzed using a human model with compliant joints in Chapter 8.

The analysis of lower-limb human-exoskeleton models is presented in Chapter 9. First, a torque analysis for two different exoskeletons (differing mainly in weight) is given. In a second study, the influence of compliant actuators in the lower-limb exoskeleton is analyzed.

In Chapter 10 the results are summarized and possible extensions, as well as applications of the presented work, are presented.

Chapter 1

Perturbation of Human Motion

Unperturbed human motion barely exists in real life. In daily life, a human being has to adapt his motion to the environment every second. The challenge in keeping the body in balance becomes clear if we observe toddlers when they learn how to control their motions. To balance only small perturbations is a demanding task. Strong perturbations usually result in falls. Growing up, we learn to pay attention to the ground, we walk on and learn how to prepare for the uneven pavement to avoid falling. And even for unforeseen perturbations, we learn how to capture. Usually, the push recovery process is subconscious, it is based on reflexes triggered by senses.

In this chapter, first, an overview to push recovery motions and methods is given. Then postural control based on senses is described briefly. The main sensory systems relevant for the detection of push perturbations relevant in the scope of this thesis are presented and the theory of sensory reweighting to rate the relevant sensory systems is introduced. Finally, a brief outline of some postural reflexes relevant for our investigations is given.

1.1 Push Recovery During Posture and Walking Motion

In this work, the focus lies on the analysis of strongly perturbed walking motions. During walking, humans have to adapt to many kinds of perturbations. It can be, that the ground is uneven, that there are obstacles humans have to avoid or that the human is pushed. We investigate perturbed straight walking on even ground. To be even more precise, one step during which a push from the back is applied to a human is considered. To capture from a perturbation during gait the following recovery motions are expected. On one hand, the goal of the recovery motion can be to come back to the previous motion, which means, in this case, to remain walking. On the other hand, the goal can be not to fall and for example, end in a stable static posture.

Searching for the analysis of push recovery motions, often pushes from standing position are analyzed. In some studies the step length of the capture motion is taken into account [11, 69, 193]. Intensive studies are done on postural control of humans in [64]. In [65] the same author investigates in the analysis of neural control of balance to prevent falls. The influence of senses to posture and push recovery control is described in detail in the next Section 1.3. Most of the studies are based on experimental measurements. In [83] they provided a recovery strategy selection based on the detection of the beginning, direction, and intensity of pushes from the standing position with and without taking a step. An interesting question is if the step length varies for perturbed steps compared to the unperturbed motion.

Some researchers investigate in the analysis of the effect of perturbations during walking motions. Lee et al. present in [102] the results of their studies on push recovery stability of biped locomotion. The results of their studies including experimental data of 30 healthy probands and a simulated biped show that the stride length, the walking speed as well as the crouching ankle influence the capability of recovering from a push. The reaction on perturbation during walking motion based on experimental measurements is investigated in [42, 61, 114]. Many age-related studies on the frequency and severity of falls have been made e.g. in [70, 97, 116, 163, 184]. In [3] a full-body human model that can handle pushes from any direction during walking motions is presented. Oliveira suggests in [130] a modular organization of muscular activation during recovery of balance during gait.

Gaining a fundamental understanding of the mechanisms of push recovery is important in the field of humanoid robotics because it prevents from falling and breakage of a robot [106]. Robots cannot react to perturbations without being given explicit strategies on how to detect, classify and compensate disturbances. Most of the approaches to push recovery in robotics are based on mimicking human behavior, building the bridge between biomechanics and robotics. To this end often robots are equipped with sensors similar to the human senses [65]. Humans mainly use three senses to control their posture: vision, the vestibular system and the somatosensory system (proprioception), described in detail in the next Section 1.3. To gain information for a robot, as the somatosensory system provides in a human (mainly joint positions as well as muscle activity) [190], force sensors can be installed, furthermore, the motion itself such as joint angles or acceleration of body parts has to be captured. The vestibular system of the inner ears is typically imitated using one or more gyroscopes and accelerometers to measure the postural angular velocity (semi-circular canals) and linear acceleration (otoliths organs) [174]. The easiest way to imitate vision is to install a camera. Still, the information the camera provides has to be processed to gain useful data such as the optic flow [90]. Often the information of more than one system is combined following the method of sensory reweighting [90, 108, 174], described in detail in Section 1.3.3.

1.2 Push Recovery Methods

Push recovery and push sensing have been a very active field of research in recent years, in particular in the robotics and biomechanics community. Most of the push recovery methods in the literature are motivated by human behavior. A common approach to gain a better understanding of human motion is the analysis of joint torques. The determination of joint torques is essential for the analysis of human walking and push recovery motions. Vaughan even talks of joint torque as the 'Holy Grail' of human gait analysis in [181]. He provides a summary of data collected over five years, concluding the advantages and disadvantages of the joint torque approach. The problem in analyzing human motions is that in a human body many more muscle activators are controlled than independent equations defining the system. To overcome this problem all muscle, bone and ligament forces are summarized to a single resulting joint force and torque. The joint torques can then be estimated using an inverse dynamics approach as presented in this work. In [118] and [161] the joint torques during human-running motions are analyzed based on this approach. Wit and Czaplicki determine the joint muscle torques during walking motions using a mathematical modeling method based on artificial neural networks in [192]. In other studies, the joint muscle torque is measured by sensor systems [72]. In [178], Tu and Lee use a two-link manipulator approach to calculate the joint torque during walking on various grounds. Accelerometers are installed on human limbs to measure joint angles. Based on dynamics equations, joint torques and energies are estimated. As their approach is very sensitive to the parameters used such as link length and weight, which are hard to measure, their contribution is rather the comparison between different grounds.

Since for the implementation of a method on a robot, the focus often is on short computation times, many studies are performed on simplified models of walking. A common model is the linear inverted pendulum (LIP) which is a very simplified representation of human and robot walking. Kajita presents a 3D formulation of the LIP in [80]. The use of a LIP model to analyze when and where to take a step during human walking is widely spread [134, 171, 173, 174]. In [53] it is used for the prediction when a robot is going to fall. Some researchers extend the LIP formulation for their use [148]. A LIP based formulation of human motion is good if a fast computation is needed, but for specific motion analysis, it is not very accurate. Therefore in this work, we investigate in a full-body model of a human for our analysis. Nevertheless, it is important to mention the LIP model as most of the control strategies are based on these kinds of simplified models.

Many of the control strategies for push recovery motions in robots are based on or can be categorized in a hierarchy of capture strategies suggested in [171, 190] The strategies are categorized into three levels:

1. Movement of the ankles to apply torque to the ground (ankle strategy) [89, 143],
2. Movement of hips and arms to apply horizontal ground forces (hip strategy) [64],
3. Movement of hips and knees to take a step or squat (foot placement) [107].

The idea of these strategies is, that for weak perturbation only a small reaction is needed to recover from the perturbation, and the reaction motion increases the stronger the perturbation, see also Figure 1.1. These strategies were applied successfully to robots [4, 126, 165, 194]. The ankle strategy can be described by a torque applied at the ankle joints opposite to the direction of the perturbation and is applied for weak perturbation. Increasing the perturbation this will not be enough to capture from the perturbation and a fall is inevitable. To avoid falling, hip strategies are liable. The hip rotates along the direction of the perturbation to minimize the influence of the perturbation and moves back again to the original pose. Many researchers investigated the decision between the hip and ankle strategy. Park found in [135] that the hip share increases and ankle decreases nearly linearly with the magnitude of the perturbation. Jalgha investigated in [75] on the decision of ankle versus hip strategy based on the initial inclination angle and angular relation velocity after the push in the sagittal plane. Vlutters et al. performed anteroposterior perturbation during human walking experiments with subjects wearing an orthosis that minimizes the support area of the feet. This makes the results comparable to a footless LIP model. To prohibit recovery by use of the ankle strategy, the ankle was physically blocked. They investigated in push recovery motions to decide between stepping and hip strategy [182]. Further increasing the perturbation, again, this will not countervail against a fall and step has to be taken. This sounds very simple, but the question remains, where to take the step.

Many control algorithms are based on the concept of the zero moment point (ZMP) [35, 79, 98, 105, 120]. The ZMP is the point where the foot can be placed on the ground such that the inertial and gravity forces are zero [183]. The idea of a ZMP based method is to maintain the ZMP within the support polygon of the feet and ground.

A commonly used method of push recovery stepping based on the ZMP is the theory of the capture point [24, 35, 93, 148, 153]. The capture point denotes the point where a system has to step in order to come to a complete stop which enables for example robots to calculate when and where to step after a push [148]. In [153] capture points for a three dimensional (3D) humanoid model with 12 degrees of freedom (DoF) were computed by learning the offsets to the capture points predicted by a LIP model. In [88] and [98] the capture point method was implemented to stabilize bipedal walking motions. In [120] the ZMP method was implemented for walking on uneven terrain.

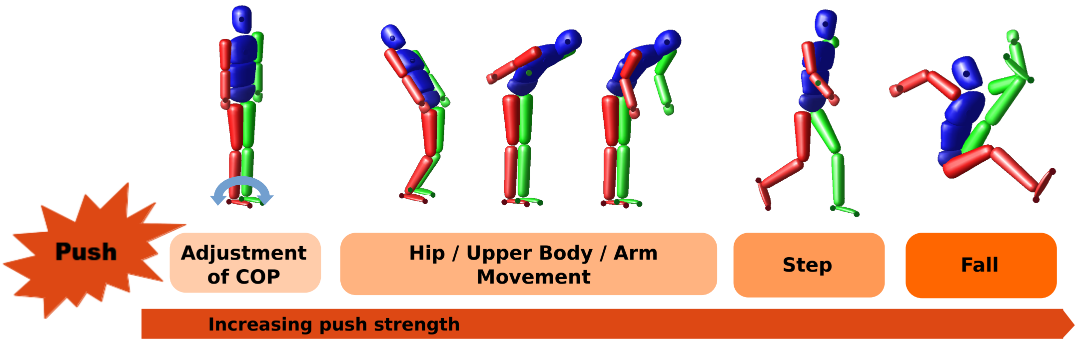

Figure 1.1: Increase of reaction motion the stronger the perturbation.

Note, that Kineologists differentiate between ideal (minimal joint angles and torques from experiments) and normal (calculated least amount of muscular support and minimal stress of joints) posture [139]. This indicates the observation that humans take a step before the magnitude of perturbation reaches the ankle and hip thresholds from theory calculations defined by the ankle and hip strategies [128].

In a robot, the perturbation can also be compensated by finding the best material for robot joints that has the right compliance to compensate for external perturbation [21]. In most studies only balance during standing is investigated [169, 172, 187]. The role of compliance in human and humanoid locomotion has been studied intensively in [71].

Another theory is based on the centroidal angular momentum [166, 195]. It is used, when stepping is not possible or the contact surface is limited. Herr investigated in [60] in the analysis of the angular momentum during human walking motions.

A field of application closely connected to robotics is the field of prostheses and exoskeletons. Since it is still a challenge to perform unperturbed motions for most exoskeletons, studies about the push recovery behavior of exoskeletons during walking motions are rare. In [77] a motion control algorithm for exoskeletons is presented, that allows the exoskeleton to take one step in the frontal plane to capture from two cases of perturbation: 1) The exoskeleton is pushed, meaning the interaction with another moving object. 2) The exoskeleton is standing on a platform that rapidly changes speed. Both scenarios include only pushes from standing. In [76] optimization-based controllers for push recovery motions of an exoskeleton are compared.

1.3 Sensing

Analyzing human motion, it is important to take into account the human senses. In this part, it is described how human movement is based on sensory information. A general description of the senses in the human body and how these senses are used to provide balance in posture and during motion is presented.

1.3.1 General Introduction to Senses

What comes first to our mind thinking about senses, are the five senses defined by the Greek philosopher Aristotle: vision (eyes), hearing (ears), touch (skin), taste (mouth/tongue), smell (nose). In the view of the ancient Greeks, the pain had no specific sensory modality. Instead, it was related to the soul. Greek philosophers had a hard time thinking about knowledge. They came up with the theory that knowledge is connected to the senses.

Nowadays, it is known that - regardless of the specific sense we look at - the receptor cell transforms sensory information to neuronal activity. One type of stimulus energy is transformed into electrical signals. These are encoded as trains of action potentials. The information is transferred by afferent nerves of the peripheral neural system (PNS) to the central neural system (CNS) consisting of the spinal cord and brain. Some information is directly processed by the spinal cord, some are processed further to the brain by neuronal activity. In the brain, the thalamus processes the signal to the according sensory cortex, see Figure 1.2. The brain analyses the stimulus of the neurons, turns the sensory information into knowledge, compares it to existing knowledge and provides reaction control which is sent back by the efferent nerves of the PNS to the periphery of the body (muscles, organs, etc.). In Section 1.3.4 the times needed for this process are described for the different systems. The detailed analysis of brain processing is very complex - brains do not only change due to the different abilities of different individuals but also because the brain adapts to repetitive actions - it learns. Imagining, for example, a tight robe walker who is trained to remain balanced in situations others would fall. This indicates that not only the five senses mentioned above exist.

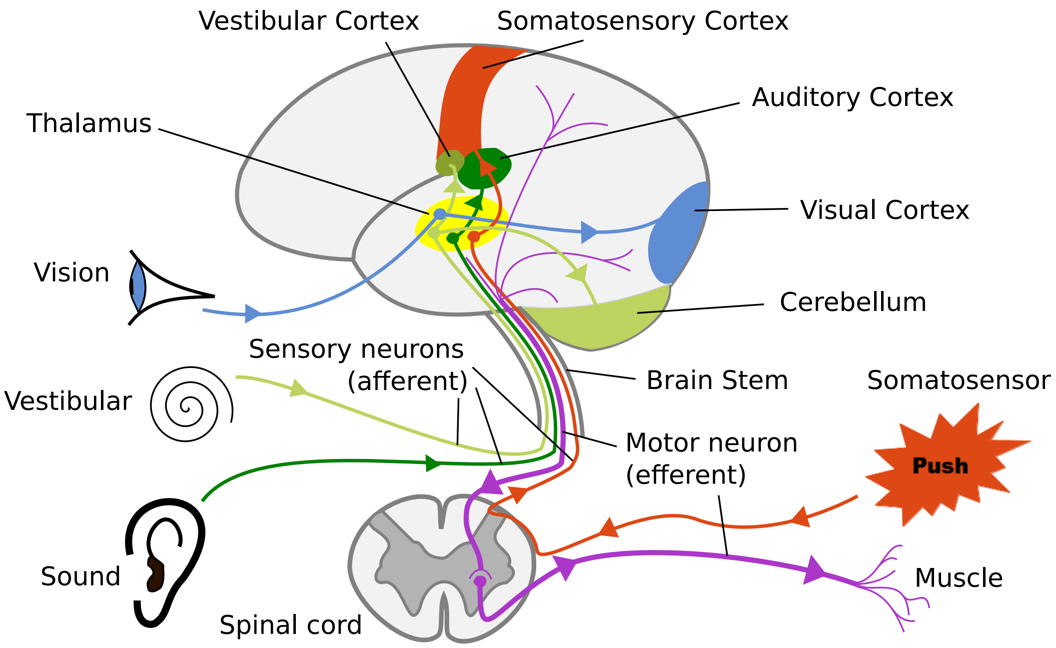

Figure 1.2: Signal flow from sensory stimuli to cortex.

Recent research has also shown that we have a lot more than the five senses from ancient Greek philosophy [81]. The vestibular senses of balance which define the position of the body in a gravitational field and give information about head movement are fundamental for controlling human motion. Besides from these senses, the somatosensory modalities is a very important field of sense. The somatosensory system consists of receptors in the whole body. To this field, recent researchers count the ability to feel touch, vibration, itch, temperature, pain, and pressure as well as proprioceptive abilities, including the sensors in the muscles (muscle spindles), the sensors in the tendons (Golgi-tendon receptors) and the sensors in the joints (mechanoreceptors). Proprioception is very important to control posture and movement like locomotion. It describes the ability to examine posture and movement of the own body by determining the body segment configuration. This means that even if we cannot see it, we know the location of our hand. Furthermore, the somatosensory system gives information about the quality of the support surface and the forces that the body exerts against the surface. In the next part, the function of these senses and their influence in the control of posture and movement are described briefly.

1.3.2 Sensory Systems for Postural Control and Perturbed Motion

Many researchers focused on how human control posture [5, 11, 55, 64, 69, 83, 189, 193]. Most of them investigated in understanding the quiet stance. The understanding of quiet stance is the basis to investigate movement and perturbed motions. In [66] the influence of the somatosensory, the vestibular and the visual system to postural orientation and equilibrium is considered. Postural orientation is the relative positioning of body segments concerning each other and the environment. Postural equilibrium is the state in which all forces acting on the body are balanced.

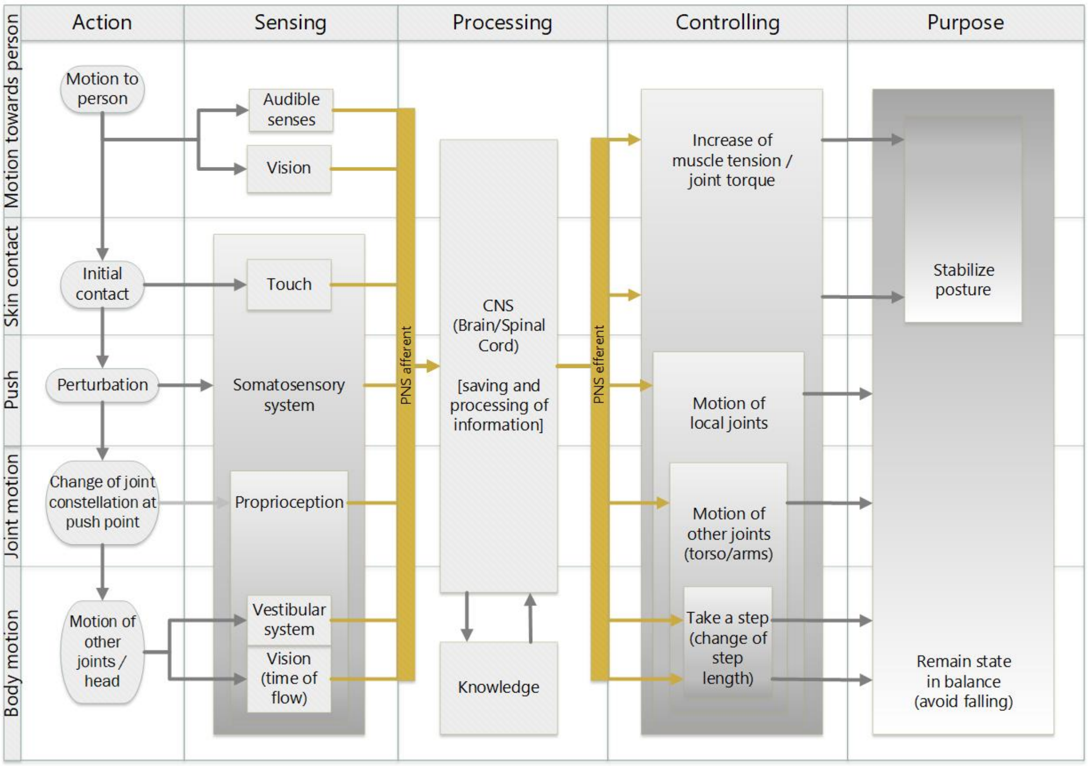

Figure 1.3: Reaction to a perturbation during human motion.

When humans are perturbed in posture or during movement, the postural equilibrium of the balance system is disturbed. Several sensory systems provide feedback to the central nervous system (CNS) about the orientation and position of the body, see Figure 1.3, second column. The multiple sensory inputs are integrated and resolved by the postural control system (PNS), Figure 1.3 third column. They are compared to an internal model of the body and the resulting error to the desired position is calculated. To maintain the required postural variables, corrective motor controls are calculated and send to the muscles. The muscles are activated, which results in a change of joint torques for weak perturbation to stabilize the posture [139]. For a stronger perturbation, the recovery motion aims to remain the state in balance. For a weak perturbation only local joints are involved in the recovery movement, for stronger perturbation also other joints are involved. For an even stronger perturbation, the recovery motion ends in taking a step from a standing position or changing the step length e.g. during walking, Figure 1.3 fourth and fifth column. Due to the fact that in some situations some sensors cannot help to figure out the orientation or position of the body, dynamic weighting of sensory inputs is necessary (also called sensory reweighting further described in Section 1.3.3). This is possible because using all senses redundant information is sent. Therefore balance can be maintained even if the information of one or more sensory inputs is missing. For example in well-lit and clear environment vision dominates posture control [122], while in darkness, blurry scenes and on moving objects or in rotating rooms, the input of vision is noisy. In this case, the other systems such as somatosensory and vestibular systems get more weight and overtake the role of vision [65]. Also during aging, the use of senses for posture control is shifted from vision to vestibular and somatosensory system: while visual information is heavily weighted in infancy and early childhood, the elderly rather use somatosensory and vestibular input. Ozdemir investigated in [131] in the importance of vision for postural control performing experiments with blindfolded and sighted subjects. It is no surprise that the sighted subjects had better performance than the blindfolded. In the following, the influence of the somatosensory, the vestibular and the audible system as well as of vision on postural control and push recovery are described briefly.

Somatosensory System

Regarding external perturbations such as pushes, the sense of touch plays a central role as the initial contact is recognized. To avoid an unstable posture the muscle tension is increased, leading to an increase of joint torques. As mentioned above, the sense of touch is part of the somatosensory system. It is maybe the largest sensory system as it consists of receptors in the whole body. It is not only responsible for the detection of contact with surfaces but includes also the ability of proprioception, meaning to know the constellation of the body parts towards each other, which is particularly important to remain balanced in case of perturbation. The somatosensory system informs the nervous system about the quality of the surface (slipperiness etc.) as well as the forces the body exerts against those surfaces. Mainly, it consists of mechanoreceptors in the skin, detecting for example perturbation of stance, muscle spindles, Golgi tendon organs, and joint receptors [66]. They are particularly sensitive to stretch of the skin [33] and, therefore, able to fire as soon as a change in shearing forces occurs. In case of a perturbation during posture or movement, this is fundamental because not only the push itself from the initial contact until the release can be sensed but also the change of forces between the feet and the ground. The rate of firing provides information about the velocity of the perturbation [54, 170]. Many pieces of research are done to analyze the influence of the somatosensory information from the feet [30, 113], e.g. in the weighting between the ankle of hip strategies described in Section 1.2. Muscle spindles are small parts of the muscles, connecting extrafusal muscle fibers. They detect changes in the length of the muscle. Processing this information to the brain, the position of body parts, for example, the position of the trunk and the degree of body tilt, can be determined. The influence of muscle receptors to postural control is investigated in e.g. [113, 99, 155]. Golgi tendon organs and joint receptors determine the force of load on limbs induced by perturbation and joint receptors give information about angular displacement, meaning body sway [31]. This information is particularly important for the control of balance and to detect perturbation of the posture or motion [111, 67]. In [20, 142, 175] the influence of the proprioceptive information from the neck is investigated. In combination with vestibular information, the neck position towards the body provides head stability, body tone, and postural stability.

Vestibular System

A much smaller sensory system, which is also essential for controlling balance, is located in the inner ear: the vestibular system. It consists mainly of two parts: the otoliths and the semicircular canals. Otoliths are a calcium carbonate structure, also called the vestibular labyrinth of vertebrates. They are sensitive to angular and linear acceleration of the head, as they are stimulated when the head tilts with respect to gravity. However, studies underwater have shown that they are not the only organ being responsible for balance or vertical sense as the results from keeping balance, meaning knowing the orientation of the body, underwater were a lot worse than on land [125]. Perception of the upright is mainly determined by gravity, not by the direction of balance [133]. Semicircular canals are three tiny fluid-filled tubes in the inner ear that help to keep balance. If the head moves, the fluid moves tiny hair in the canal which can be measured. It is also called angular accelerometer and can be understood as a level sensor: If the sensor is tilted, the fluid inside reaches its edge and a feeling of falling is induced [174]. The semicircular canals are more sensitive to higher frequencies than the otoliths and detect therefore rapid postural sways, such as rapid hip flexion or extension, but no tiny perturbation during quiet stance [140, 162, 123].

Audible System

The person being pushed might be able to hear a noise the moment he or she is pushed or before. The audible system consists mainly of the outer, the middle and the inner ear. In case of a noise, the sound waves are collected by the outer ear. The special shape of the outer ear helps the brain to locate the noise. After entering the auditory canal, the sensory information reaches the tympanic membrane entering the middle ear. Here, it is converted into sound vibrations of higher pressure, which then enter the inner ear. The sound waves are transformed into electric neural signals and processed to the brain. If the noise is already known, the brain can recognize it and the person knows what might happen next and the muscle tension increases to stabilize the posture.

Vision

Also vision plays a great role in controlling balance. The sensing system vision is linked to the eyes. As the auditory system, the visual system gives information about objects that are not in contact with the body. Distances to objects close and far away from the body can be measured. The motion of objects and the body itself is recognized. Many studies have been made to analyze the influence of vision to control quiet stance. The main outcomes are: To remain stable is much harder with eyes closed than with open eyes. To blindfold subjects leads to an increase of 30% sway in a quiet feet-apart stance [66]. Vision stabilizes sway at frequencies lower than 0.1 Hz. Objects must be closer than 2.5 m to the subject to stabilize a quiet stance [138]. Healthy adults do not sway beyond their limits from visual induced sway [28, 104]. The movement of the visual surround has a stronger influence if also the support surface is in motion. The visual system dominates in the case of low frequencies of body sway and in the case of conflict between vision and other sensory inputs [101, 100]. Vision has a great impact when learning a difficult balancing task [168] and also on feed-forward control for avoiding obstacles and adapting to changing environmental conditions. The sense of vision could influence predicting the perturbation if the perturbation is in the field of sight of the perturbed person. Then, as a reaction, muscle tension is increased to stabilize the posture.

1.3.3 Sensory Reweighting

As already indicated describing the influence of the different sensory systems to postural control, the influence of the sensor is task-dependent. The selection and reweighting of sensory information adaptively are one of the most critical factors for postural control [129]. Sensory reweighting is a common approach. It is based on the idea that not only one sense or sensory system is capable to control or analyze a certain motion. The sensory contributions are adjusted to balance control. Healthy human balance control using active feedback mechanisms. Note, that also here the weighting is dependent on the specific task as well as on the individuum. As an example, one may imagine a dancer performing twist motions, who trained to suppress information from the vestibular system, relying more on the vision to avoid dizziness. In [10] corrective torque is generated based on a combination of movement and orientation cues from the visual, the vestibular and the proprioceptive systems. The contributions of each system changes depending on the perturbation applied. Other examples on sensory reweighting are given in [14, 15, 56, 78, 87, 108, 109, 112, 115, 136, 141, 179]. For our work sensory reweighting is a very interesting approach as we can include the different sensory systems into our optimal control problem in a weighted way. To determine the weights, the approach of inverse optimal control can be used, see Section 7.3.

1.3.4 Reaction Times

The reaction time describes the time needed from a sensory stimulus until a reaction motion is performed. It mainly consists of a) the time needed to convert the sensory input to neural signals, b) the time needed to be processed to the thalamus, c) the time to be processed in the brain, d) the time the response needs until it reaches the muscle and e) the time until the muscle contracts and a joint moves. It is still ongoing research, how much time is needed for all of these processes. Note, that the time of the described processing steps is strongly dependent on the task and also the sensory system involved. Moreover, sometimes the signals are not processed in the brain but directly processed in the CNS which sends the signal to the muscle.

Many researchers investigated the dependency of the reaction time of the different sensory systems and tasks. Above the signal flow of a stimulus is described. Figure 1.4 shows the large differences in the processing times from stimulus to reaction for simple and choice tasks of healthy subjects found in the literature. The reaction time of simple tasks (e.g. react as quickly as possible to a signal) is faster than of more complex tasks (e.g. tasks that include choices) [58, 17]. This is also stated in the Hick's Law [149] shown in Figure 1.5. Comparing simple and choice reaction times, researchers tried to distinguish perceptual from cognitive processes. The cerebral cortex has to be activated for at least 100 ms for cognitive processes, everything of shorter durance keeps unconscious [156]. As already mentioned, the human also shifts the input of the different sensory systems depending on the task and input from the systems [57]. The time delays from stimulus to reaction are not only dependent on the task but also on the specific sensory system involved.

In the literature, different reaction times can be found. Some researchers investigate in the overall reaction time, the subjects need to react on a stimulus [17]. Other researchers are interested in the time the signal needs to reach the brain (audible: $8-10$ ms, visual: $20-40$ ms) [86] or the time until the detection of the signal [177] or the time to reach a specific region of the brain in order to better understand the processes in the human brain. In general, multi-sensory input leads to faster response times than uni-sensory input [58].

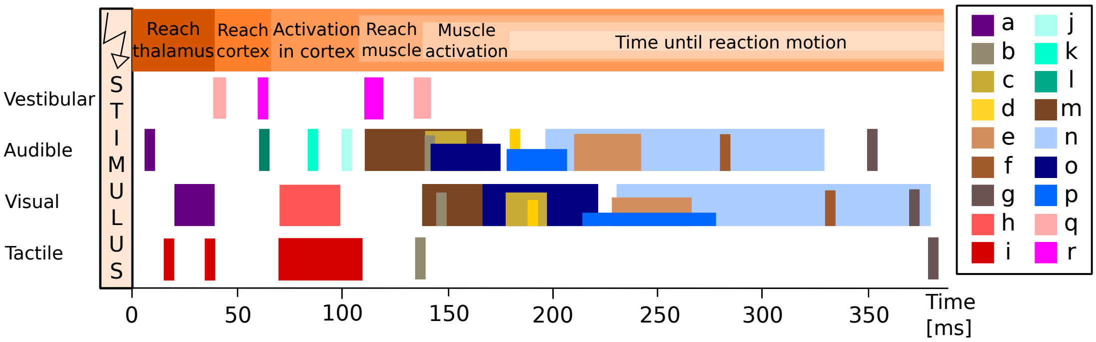

Figure 1.4: Schematic time flow of the reaction time to simple and choice tasks of the different sensory systems using different measurement methods. a)-n) simple reaction times a) signal reaching brain [86] b) catch ruler [82] c) stimuli detection [177] d) reaction by pressing button [84] e) reaction time [74] f) reaction by pressing button [167] g) reaction move to button and press button [17] h)-i) activation time in brain i) [47, 73] j)-l) [132] j) reaction time until mucsle activation in sprint starts k) reaction time in sprint starts l) reaction time m) reaction time of male basketball players [49] n)-p) choice reaction times n) choice reaction time of male basketball players [49] o) choice reaction time healthy people (visual: red light, auditory: click) [137] p) choice reaction time healthy people (visual: green light, auditory: tone) [137] q)reaction time until muscle activation in the arm [13] r) reaction time until muscle activation in the leg [13].

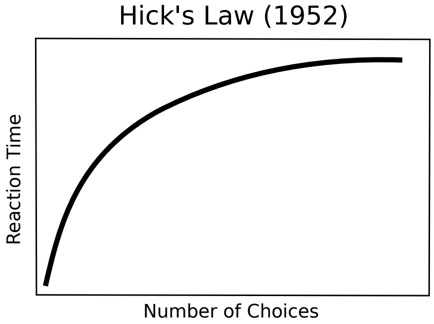

Figure 1.5: The relation between reaction time and number of choices.

In [17] the reaction time to visual, auditory and tactile stimuli for simple and choice tasks is compared for different individuums of different ages, gender and education levels. The results show that the simple reaction (pressing a button without choice included) to auditory stimuli (350 ms) is faster than to visual stimuli (370 ms) and to tactile stimuli (380 ms). Other researchers investigated the influence of athletic people, normal healthy people and people suffering from diabetic. The results for the healthy group indicate different reaction times of about 180 ms for the auditory system and 190 ms for the vision [84]. In [167] the experiments result in mean reaction times on simple tasks (only pressing the button without finger placement) of 284 ms for the auditory system and 331 ms for the vison. This indicates the strong dependency of these studies on the individuals and the specific task. In both studies, a button needed to be pressed to show a reaction to the stimuli. In the first study [17], the subjects had to move their finger from an initial position to the button, whereas in the latter study [84], the finger was directly placed on the button. Other experiments are done without a specific measurement device using only a ruler, that needs to be caught to show a reaction on sound, visual stimuli or touch [82]. Here, the resulting reaction times are 148 ms for the visual stimulation, 141 ms for the audible stimulation and 139 ms for the tactile stimulation. Nevertheless, most researchers found the audible signals to be faster than the visual signals [74, 84, 86, 132, 167, 177].

Many researchers studied visual perception. Often they approach the problem of understanding vision by studying how long viewers need to see e.g. a word, to be able to correctly process the information. To read a word $50-60$ ms are needed [151]. To interpret a scene, more time, 150 ms is needed [152]. In contrast to these results from 2008, recent research shows that 13 ms is sufficient to analyze a scene [145]. This result suggests, that a perturbation needs to be long enough and strong enough to enforce a visual effect that can be sensed. This timing is independent of the processing time of $70-100$ ms, meaning the time, that is needed from the time light hits the retina until the signal reaches the brain to process the visual information. The mean visual reaction time found in literature from seeing a stimulating action to performing a motion with e.g. the finger is about $150-200$ ms [9, 188]. Note, that these values are strongly dependent on the specific task and also the individuum: in general, e.g. elderly people perform slower visual reaction times (460 ms) than younger probands (370 ms). Growing older, usually also the audible system becomes worse.

Comparing young subjects to elderly people, the audible reaction time decreases from 370 ms for 11-year-old subjects until the age of 30 (330 ms) and then increases again (500 ms at the age of 60) [17]. Moreover, as already noted, the time delay is not only age-related but also task-dependent. The mentioned times refer the task to simply react on a noise. The time delay to analyze the pitch of a noise is about 1121 ± 308 ms and to locate a noise 1069 ± 204 ms [6] Furthermore, the reaction time varies due to habits. Often researchers investigate the influence of training on the reaction time. Shortest auditory reaction times can be found for sprint starts [132]. For athletes, the reaction motion can be observed at 85 ms after the audible stimulus. In the leg muscles, a change can be observed already 60 ms after the stimulus. This indicates a latency time of 15 ms for the muscles which is included in the reaction time for every sensory system.

Independent on the sensory system a stimulus comes from, a healthy nerve transmits information with a velocity of 120 m/sec. Because the auditory system and the eyes are located quite near to the brain, the processing time from these sensory systems to the brain might be shorter than for the somatosensory system. Assuming, a touch at the back in 80 cm distance from the brain, it would take 6 ms for the signal to reach the brain. It is still ongoing research on how much time passes from sensory input until the reaction motion is performed, as perception is strongly dependent on the specific task and also the individuum.

Often the sensory processing is presented as a hierarchical scheme. In [144] Pleger and Villringer give a precise overview of the research of perception to decision making of the somatosensory system. In [73, 68, 47] they investigated in the time, a certain region of the brain is activated. The times vary from $14.4-22.4$ms (depending on region) in [73]. The time delay from stimulation at the hand to the measured peaks in the brain is 20 ms (contralateral primary somatosensory cortex (SI) hand area), 85 ms (secondary somatosensory cortices (SII) in both hemispheres) and $70-110$ms (contralateral parietal cortex) [47].

The vestibular system is especially interesting in the scope of sensing a perturbation because it is capable of balancing. First muscle activations as a reaction to a vestibular stimulus occur $50-70$ms after the stimulus and a second peak in the opposite direction $100-120$ms after the stimulus application [13, 26, 25, 43, 44, 46, 124].

1.4 Postural Reflexes

Postural reflexes help the human to remain or reconstitute a muscle tension necessary for a specific posture of the body force position and movement [27]. They ensure that the body remains upright and aligned and allow for subconscious control of posture, balance, and coordination in active motions and static positions. Local postural reflexes are triggered by gravitational force stimuli leading to an increase of muscle tension in a body segment. Segmental postural reflexes define those body segment motions caused by the motion of another body segment. Generalized postural reflexes describe those reflexes that modify a certain position depending on the position of the head. Other than the primitive reflexes, which develop in the womb and are fully present at birth, the postural reflexes take up to three and a half years to be fully developed [52]. In the literature, many kinds of categorizing reflexes can be found. One way is the categorization by the control center: reflexes triggered by the spinal cord are called segmental reflexes, those triggered by the medulla are called tonic reflexes and those by the midbrain and cerebral cortex are called righting reflexes. Another categorization is in righting reflexes and equilibrium reactions. Righting are those reflexes reacting on a misalignment of the head. A common example of a righting reflex is a falling cat landing on its legs. If a cat drops with its legs turned to the sky, the visual and vestibular system trigger a motion of the head, such that the head turns. As a result of the tonic neck reflex, the body follows. Righting reflexes are reaction reflexes that restore posture when the posture is disturbed. If the equilibrium of the body is under threat, the reflex is counted as an equilibrium reaction. In the following two basic postural reflexes relevant for this thesis are listed briefly [1]:

- **Neck Reflexes**
  The tonic neck reflexes are triggered by mechanoreceptors. They describe variations in the muscle tension between the trunk and the limbs triggered by the position of the head towards the body.
- **Labyrinth Reflexes**
  The tonic labyrinth reflexes are triggered by otoliths in the labyrinth of the human ear. They describe the reaction on a variation of the motion/direction of the body and the position/posture of the head towards the ground.

Chapter 2

Human Push Recovery Motion Capturing

In this chapter, an overview of the capturing of human push recovery motions is given. First, criteria for the selection of perturbation and the selected motions are presented, then the setup of experiments and recording of motion capture data as well as the generation of reference data is described. In the last part the datasets used for the analysis of human push recovery motions in this thesis are presented in detail.

2.1 Selection of Motion

At the beginning of this study, useful motions had to be chosen. These motions had to fulfill several criteria:

- The motion has to be recordable.
- The recorded motion should be analyzable in a multi-body simulation.
- The perturbation has to be measurable.
- The reaction on the perturbation has to be measurable.
- Perturbation from standing and during walking motions should be possible.

Experiments were done to find possible motions and perturbation meeting these requirements. In experiments using a seesaw, the subjects were not perturbed visually. The subjects were standing on one end of the seesaw and weights were put immediately on the other side. As a reaction, the subjects jumped in their place, but there was no relevant recovery motion. Also balancing on or walking over the seesaw did not lead to satisfying results. We also took into account tearing perturbations. The advantage of this kind of perturbation is, that the strength of the tearing can be measured and give a rate of perturbation. The disadvantage is that the subject knows were the perturbation will be applied if not many force sensors attached to different places at the subject are installed. Therefore, in this work, pushing motions are considered. To be more precise, we studied push recovery motions from pushes applied from to back at the spine of the subjects during standing and walking. Our investigations in perturbations during standing show huge differences in the recovery motions if the subject was blindfolded or not. Applied pushes at the back during standing lead very often to recovery steps for seeing subjects - even if the subjects are asked to try not to take a step. To blindfold the same subjects, the subjects remain standing and rather move the arms and the upper body and the hips and knees to capture from the perturbation. In this thesis, push recovery motions during walking, including perturbations from the back at different heights at the spine of different strengths and different timings, are analyzed. We only work in the sagittal plane.

2.2 Experiments

To gain reference data of humans being pushed from the back during walking motions, experiments are set up, see Figure 2.1. The data are recorded in the motion capture lab at CIN in Tübingen. In this section, the experimental procedure, as well as the recording instruments are presented in detail.

2.2.1 Experimental Procedure

Two subjects are recorded during walking on level ground. The pushes were applied at three locations at the spine differing in height as follows

- Middle between the left and right posterior superior iliac spine (Pelvis Segment, pelvis),
- 1st Lumbar Vertebrae (Middle Trunk, belly),
- 2nd Thoracic Vertebrae (Upper Trunk, chest).

These push locations are visualized in Figure 2.2. They are also called push points in this thesis. The pushes also vary in strength: soft, middle and hard and in timing during the steps (gait phase). Experimental protocols are set up in advance which define, the height at the back as well as the force and the timing of the perturbation for each trial. The subject was not informed beforehand what kind of perturbation would be applied. The influence of learning is neglected, meaning, we do not consider if the trial is at the start or the end of the recording session. In total one set of recordings consists of 27 motions, such that all possible combinations of push location, timing and strength occur once. Note, that not all of these motions are compatible with our investigations because most of the perturbations hold for longer than one step but in our calculations, we only investigate in motions of one step. The order of the different possibilities is chosen randomly, but each possible height, force, and timing was occurring equally often.

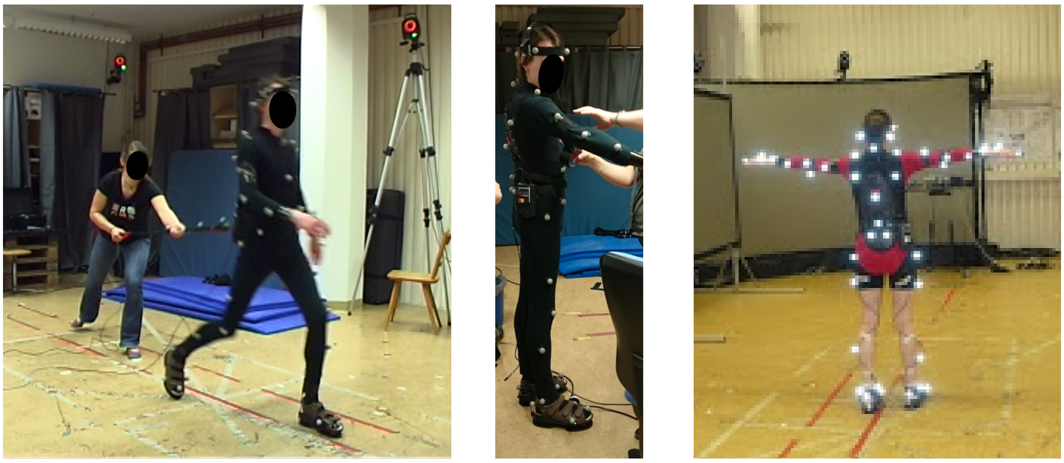

Figure 2.1: Setup of the experiments: Subject being pushed recorded by vicon camera system (left). Subject equipped with markers for motion capturing (middle). Subject in T-pose (right).

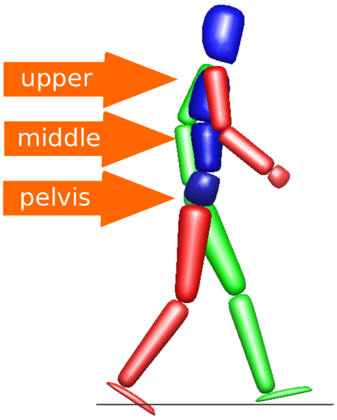

Figure 2.2: Placement of pushes from the back.

The subjects are pushed from the back to avoid visual prediction of the perturbation. To avoid audible prediction of the perturbation, the pushing person is wearing socks, but no shoes. In the experiments considered for the calculations in this work, the subjects are not blindfolded. They can see where to step. During the experiments, the subjects are wearing a protector to secure from pain and injury. The influence of the tissue of the protector is neglected in our simulation. Additionally, the subjects are wearing XSENS shoes [36], which measure the ground reaction forces and the accelerations of the two feet using two MTxs and two force load cells per shoe, see Figure 2.3. Also, the influence of these shoes on the walking motion is neglected for the simulation. All of the data can be found in the Koroibot Database[1].

For the collection of the experimental data different systems are used: A system of Vicon cameras is installed to record motions. A detailed description of a Vicon system is given below in Section 2.2.2. Also, a video camera is installed to record the motion visually for reference reasons. The force of the push is measured using an OptoForce 3D force sensor attached to a stick, see Section 2.2.3. To be able to synchronize the output data of the OptoForce sensor and the Vicon system, the stick is dropped down vertically to the ground. In the visualization of the Vicon data, this point in time can be seen and readout. In the OptoForce data, this point in time can be determined by the first significant increase in the force. In the same setup, also pushes during standing are recorded and experiments in which the subjects are told not to take a step or to step in a defined area, but these were not included in our calculations.

Figure 2.3: XSENS Shoe with force plates to measure ground reaction forces.

---

[1] `https://koroibot-motion-database.humanoids.kit.edu/`

2.2.2 Vicon

A Vicon (Oxfor, UK) motion capture system[2] made of ten infrared cameras is used to record whole-body motion kinematics, see Figure 2.4. The system tracks the spatial positions of 42 reflective markers with a high spatial resolution (error below 1.5 mm). The markers are attached with double-sided adhesive tape to tight clothing worn by the participants, see Figure 2.1. Markers are placed on the locations specified by the Koroibot Marker Set[3]. The positions of these points according to a coordinate system is saved as data files. The motion is recorded with a rate of 100 Hz.

Figure 2.4: Example of a Vicon camera.

2.2.3 OptoForce Sensor

The force of the perturbation is measured with the 3D force sensor $OMD-50SA-1800N$ from OptoForce . It is a three-axis force sensor that measures slippage and shear forces using infrared light and different kinds of optical grade elastomers to detect the smallest deformation in the shape of the outer surface, see Figure 2.5. Deforming surfaces are physically separated from the sensing element. It has a robust design and sensitive silicone surface. It is water, acid and heat resistant. For our experiments, we attached the sensor to a stick to be able to push the subjects properly, see Figure 2.6. As the motion, also the push force is recorded with a rate of 100 Hz.

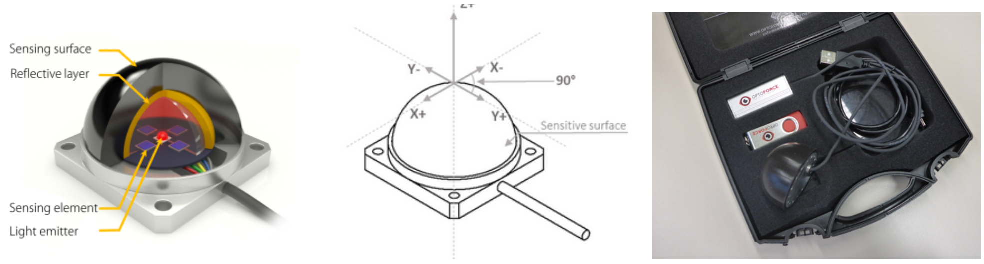

Figure 2.5: Function of the OptoForce sensor (left), Axis of the OptoForce sensor (middle) and the unmounted sensor (right).

Figure 2.6: Picture of the OptoForce push stick with markers.

---

[2] `http://www.vicon.com/`

[3] `https://koroibot-motion-database.humanoids.kit.edu/marker_set/`

2.3 Generation of Reference Data from Experimental Data

For our approach of the analysis of human push recovery motions reference data is needed. The experimental setup to record this data is described in the previous Section 2.2. An overview of the generation of the motion capture data from these recordings is shown in Figure 2.7. Left, a subject with attached markers, a part of the system of Vicon cameras in the background and the pushing person with the push stick can be seen. The motion kinetic and kinematic analyzer Mokka[4] can be used to visualize the recorded data. The timing of the step phases and perturbations is determined using this visualization. The Master Motion Map (MMM[5], [176]), KIT is used to map the three-dimensional position data of the markers to a kinematic model to calculate the joint angles. This data is converted to the planar human model based on `HeiMan` described in detail in Section3 which can be visualized with `MeshUp` [39]. For the force data, no conversion has to be done. The data can directly be read out from the output data file from the OptoForce sensor taking into account the synchronization. From these two datasets (motion and force dataset) single steps are cut based on the data from the analysis of the motions using Mokka. We regard normal walking motions without perturbation, walking motions with perturbations and one step after the perturbation to analyze the reaction on the perturbation. The data used for our simulation are described in detail in the next Section 2.4.

Note, that in our case, we convert the data to a two-dimensional model. Therefore, it is important to ensure that the motion that is to be analyzed is mostly in the sagittal plane. To this end, the subjects were asked to walk in a straight line and the pushes of different strengths were applied from the back.

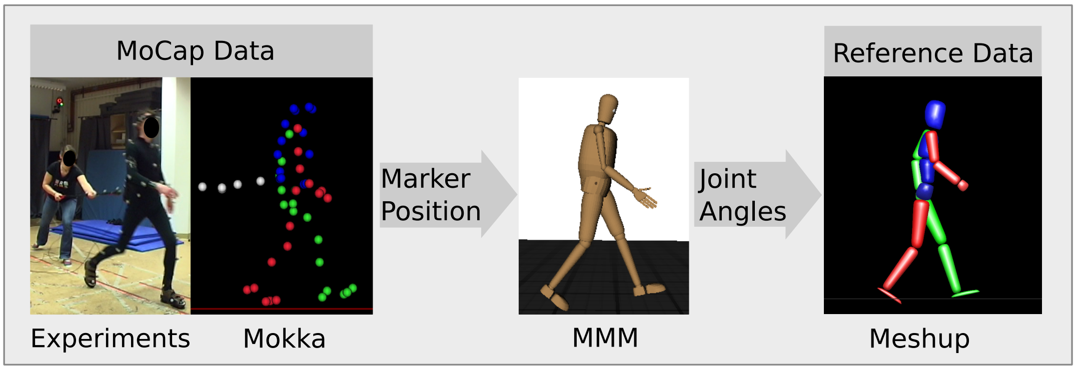

Figure 2.7: Overview of the conversion of the human motion to the joint angles used in the model: Person and push device with markers for the motion capture procedure with Vicon, Visualization of the marker positions with Mokka, Joint angles of the kinematic MMM model, Motion of planar dynamical human model visualized with MeshUp.

---

[4] `https://biomechanical-toolkit.github.io/mokka/`
[5] `https://mmm.humanoids.kit.edu/`

2.4 Data Sets

In this work, the reference data are determined as described above from motion capture data recorded at CIN in Tübingen. They are divided into two different datasets from two different subjects for the calculations. The second dataset consists of many more unperturbed motions than the first one to have one dataset with a representable number of unperturbed motions. This enables us to compare the perturbed motions to the unperturbed ones. Straight walking motions with and without perturbations are considered. The walking motions are perturbed by pushes from the back, which is the negative x-direction in our model. The pushes are applied at three different locations at the spine: at the pelvis, the middle and the upper trunk, see Figure 2.2. These perturbations in the motions also vary in push strength and timing. For all motions, we consider one single step of a gait cycle, starting with the left leg as swing leg and the right leg as stance leg. If the motions were recorded with the right leg as swing leg and the left leg as stance leg, we regard the mirrored motion. We model one single step. In Table 2.1 the main properties of the two subjects are listed. For a detailed description of the segment lengths needed for the conversion from experimental data to reference data, see Table A1 in the Appendix.

Dataset A consists of nine motions: Four motions are pure walking motions without perturbation, referred to as *NoPushA1* and *NoPushA4*. The other motions show reactions to different types of perturbations. For one motion a push at the pelvis is applied, referred to as *PelvisA*. For two motions a push at the middle trunk is applied, referred to as *MiddleA1* and *MiddleA2* and for two motions a push at the upper trunk is applied, referred to as *UpperA1* and *UpperA2*. Dataset B consists of 35 motions: The unperturbed motions are referred to as *NoPushB1* to *NoPushB23*, the perturbed motions at the pelvis with *PelvisB1* and *PelvisB2*, etc. Of all kinds of perturbation locations, two motions exist in dataset B. Figure 2.8 shows the trajectories of the forces for the motions of dataset A (left) and dataset B (right). In the next Section 2.5 the properties such as push forces, timing and step lengths of perturbecd and unperturbed motions from both datasets are analyzed.

Table 2.1: General subject data.

	Height [m]	**Weight** [kg]	**Age** [a]	**Gender**
Dataset A	1.77	57	26	male
Dataset B	1.60	49	25	female

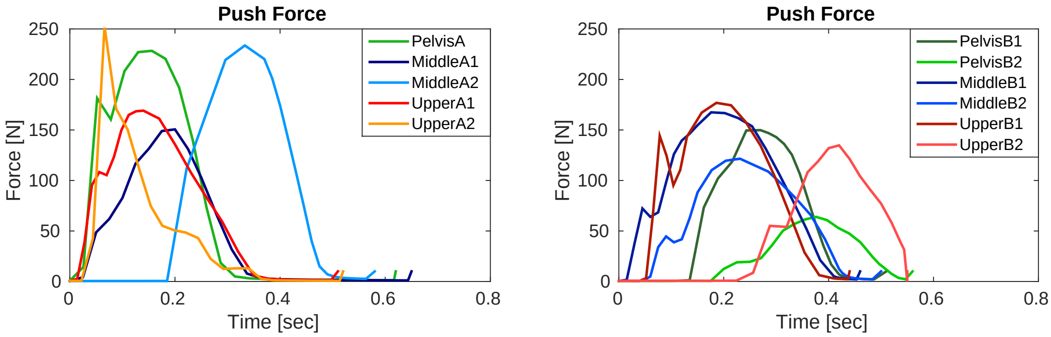

Figure 2.8: Strengths and profiles of the applied push forces, at different height of the spine for dataset A (left) and dataset B (right).

2.5 Push and Motion Data Analysis

First, the strengths, as well as the timing of the perturbations, are presented. Then the steplengths of the perturbed motions are compared to the ones of the steps before the perturbations to analyze the influence of the perturbation on the steplength.

2.5.1 Push Force

The normalized forces applied to the subjects as perturbations are shown in Figure 2.8 Figure 2.9 shows the maximal push forces as well as the integral of push force over time. The maximal push forces for most motions in dataset B are weaker than those in dataset A: For dataset A the maximal push force varies between about 140 N and 250 N, see also Table A3 in the Appendix. The maximal push force in dataset B varies between about 65 N and nearly 180 N, see also Table A5 in the Appendix. For most of the motions with stronger maximal push force also the force integral is larger. This is not the case for the UpperA2 motion with the peak shaped push, see Figure 2.8. This Figure shows the time-dependent amplitude The PelvisA and MiddleA2 motions are of a similar push shape, but different timing. The MiddleA1 and the UpperA1 are of a similar shape and timing but differ in push location. In dataset B the PelvisB2 and UpperB2 motions are different from the other motions as the push occurs later than in the other motions. The push in the other motions ends at a similar time at 0.4 sec. For an analysis of the push timing considering the push phases see Figure 2.10 in the next section. The push in the PelvisB2 motion is much smaller than in the other motions. The pushes of the MiddleB1 and UpperB1 motion is similar.

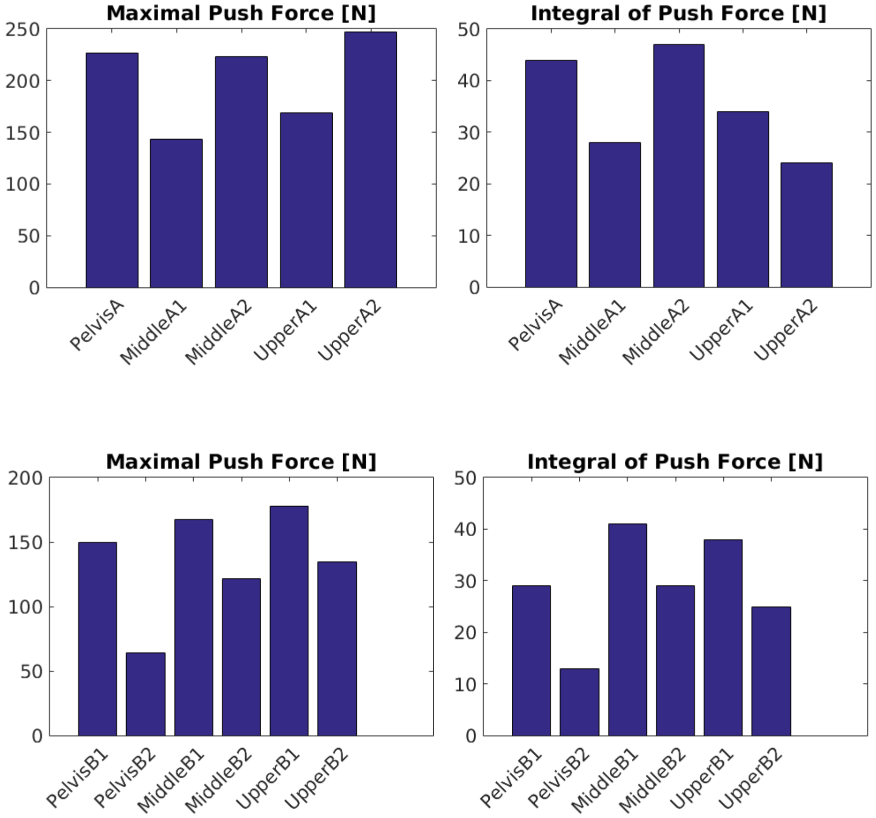

Figure 2.9: Maximal push forces and integrals over time of push force of the two datasets (upper row: dataset A, lower row: dataset B).

2.5.2 Step and Push Timing

In this section, the timing of the perturbed and unperturbed steps from dataset A and B are analyzed. Figure 2.10 shows the phase times and the durance of the push for the motions of the two datasets. The following rules can be observed.

The human gait is divided into four phases, respectively, see Section 3.3. The timing for all pushes in dataset A is similar: The pushes start in phase one and end in phase two, meaning the perturbation is applied during the swinging phase of the left leg: after the liftoff of the left hallux and before the touchdown of the left heel. Only the timing of the perturbation in motion *MiddleA2* differs a lot from the other motions in this dataset. This is not the case for dataset B: Here, also all perturbations start in phase 1 (starting during the swinging phase of the left leg: after the liftoff of the left hallux and before the touchdown of the left heel) but the ending varies between phase three and four. In Table A2 and A4 in the Appendix a more detailed overview of the timing of the steps and perturbations is given. The average duration of a normal step in dataset A is 0.73 seconds (0.63 seconds in dataset B). The maximum duration of the normal steps in dataset A is 0.79 seconds (0.71 seconds in dataset B) and the minimum 0.69 (0.58 seconds in dataset B) which is longer than the duration of all motions considered including a push for both datasets.

For dataset A the steps are faster the higher the push point is located, but it does not hold for all motions of dataset B. In dataset B the stronger pushes result in faster steps. Comparing the perturbed with the unperturbed motions, all unperturbed steps take longer than the perturbed steps.

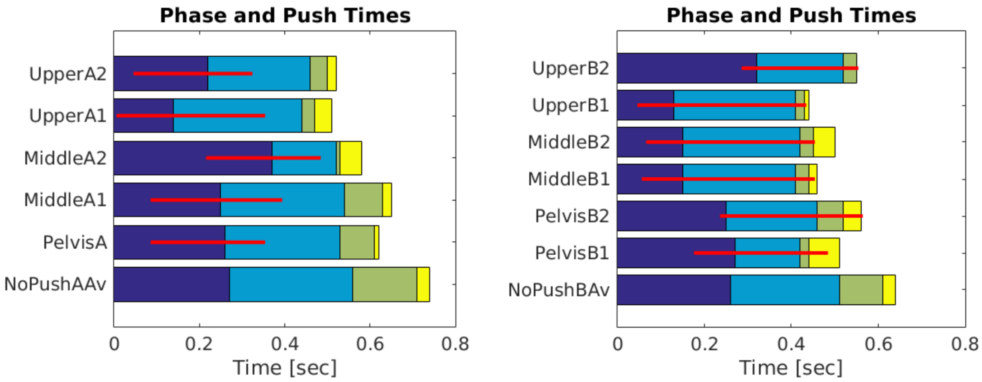

Figure 2.10: Phase (blue to yellow bars) and push durance (red line) for the two datasets (left: dataset A, right: dataset B).

2.5.3 Step Lengths

Figure 2.11 shows the step lengths of the perturbed step and the unperturbed steps before the perturbed steps for datasets A and B. While the step lengths for the unperturbed motions do not differ a lot from the unperturbed step before the regarded steps, the step lengths for most of the perturbed steps is larger than the step length of the previous unperturbed step. But from the analyzed data no rule can be concluded about an increase of the steplength for a stronger push or a higher located push point. Nevertheless, there is only one motion in which the step length of the perturbed step is smaller than the one for the previous unperturbed step. A detailed list of the step lengths before and after the perturbed step is given in Table A3 and A5 in the Appendix. The maximal step length in dataset A is 0.847 m, die minimal steplength is 0.405 m, the average of the steplengths of the unperturbed motions is 0.62 m. In dataset B the variation of the maximal and minimal step lengths is smaller: the maximal step length is 0.79 m, die minimal steplength is 0.5 m, the average of the steplengths of the unperturbed motions is 0.6 m.

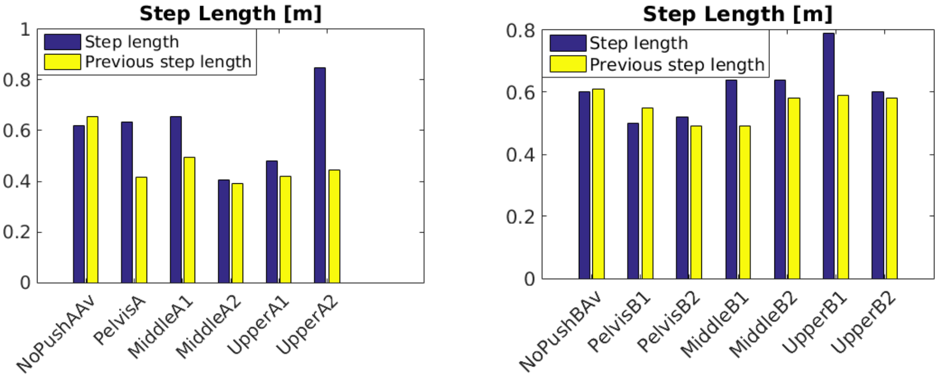

Figure 2.11: Step lengths and previous step lengths for the two datstasets (left: dataset A, right: dataset B).

Chapter 3

Modeling of Perturbed Human Walking

In this chapter, first, the human model used for our simulation is introduced. Its simulation with rigid multi-body dynamics is described in Section 3.2. In the following section, the modeling of normal and unperturbed human gait described by different phases is characterized. Finally, we present the different methods of how to simulate the perturbation.

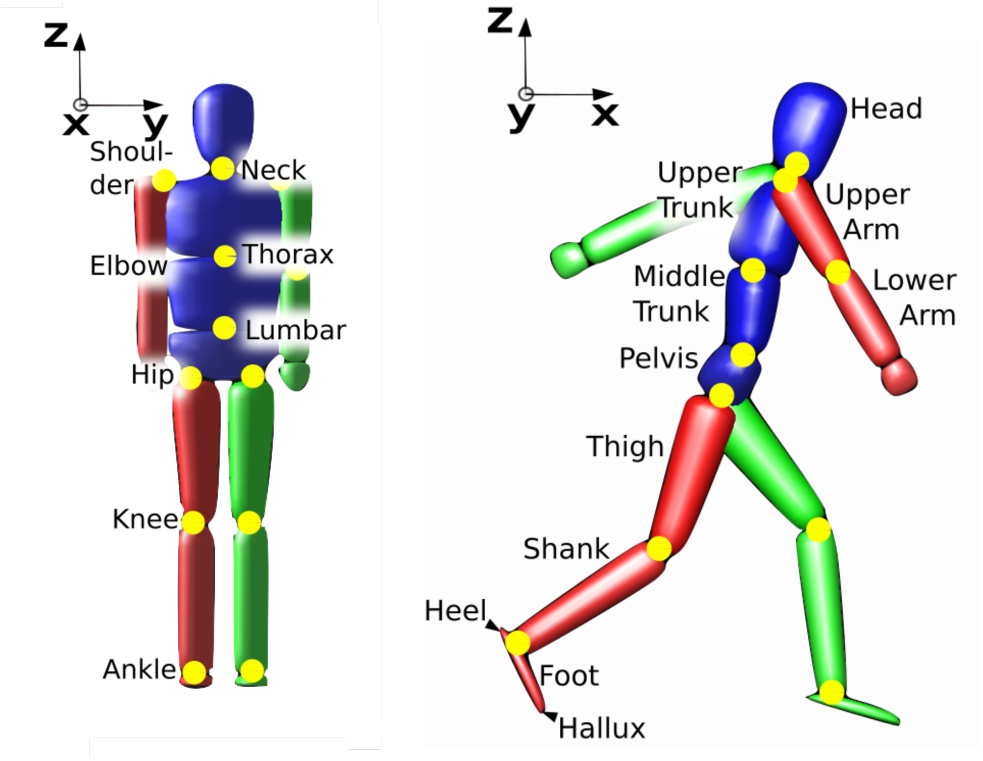

Figure 3.1: The sagittal human model with definition of body segments.

3.1 Human Model

In this section the multi-body human model which is able to represent the dynamics of human push recovery motions is described. It is a multi-body system in the sagittal plane that consists of 14 segments (head, two upper arms, two lower arms, upper trunk, middle trunk, pelvis, two thighs, two shanks and two feet) connected by 13 joints (neck, two shoulders, two elbows, thorax, lumbar, two hips, two knees, two ankles) that enable rotations around the y-axis. The locations of the joints are shown in Figure 3.1. In Table 3.1 the segment masses, the center of masses and the gyrations are listed. To allow for movements of the whole body in space, the pelvis is modeled as a floating base that enables translations in the z- and x-directions and rotations around the y-axis. In total, the model has 16 degrees of freedom.

The model used in this work is implemented in the rigid body dynamics library `RBDL` [40]. It is based on the `HeiMan` model [41], a highly parametrized rigid multi-body model for humans. The human body is approximated by a system of rigid bodies connected by rotational joints. The dynamics of the model can be described by the differential equation of motion described in the following Section 3.2.

In our model, there are two sources of external forces acting on the model. One is the ground reaction force which is described by constraint forces. In our model, the contact of the feet with the ground during a step is represented by two contact points per foot: one in each heel and one in each hallux. In total there are four contact points for the ground contact. In Section 3.3 a more detailed description of the modeling of human gait is given. The other source is the perturbation of the motion simulated as an external force acting on the model. For the simulation for the perturbations, a fifth contact point is added to the model at three different locations at the spine depending on where the perturbation is applied in the reference data.

Table 3.1: Parameters of the human model. The masses and segment lengths are given relative as a percentage of the total body mass and height. The center of mass is given relative to the respective segment length.

Segment	**CoM Human**			**Gyration Human**			**Length**	**Mass**
	C_x	C_y	C_z	g_x	g_y	g_z	l	m
Lower Trunk	0.	0.	0.6115	0.615	0.551	0.587	0.0837	0.1117
Middle Trunk	0.	0.	0.4502	0.482	0.383	0.468	0.1238	0.1633
Upper Trunk	0.	0.	0.2999	0.716	0.454	0.659	0.098	0.1596
Thigh	0.	0.	-0.3918	0.3148	0.3148	0.1425	0.2425	0.1416
Shank	0.	0.	-0.4392	0.2508	0.2458	0.102	0.2529	0.0433
Foot	0.1576	0.	-0.6168	0.124	0.245	0.257	0.0200	0.0137
Upper Arm	0.	0.	-0.7461	0.3684	0.3477	0.2042	0.1618	0.0271
Lower Arm	0.	0.	-0.4107	0.2478	0.238	0.1087	0.1545	0.0162
Hand	0.	0.	-0.7900	0.628	0.513	0.401	0.0495	0.0061
Head	0.	0.	0.5002	0.303	0.315	0.261	0.1395	0.0694

3.2 Rigid Multi-Body Dynamics

The dynamics of a human body can be approximated by a system of rigid bodies connected by rotational joints. The model used in this work is implemented in the rigid body dynamics library `RBDL`, [40]. The dynamical behavior of the model can be described by the following differential equation of motion

$$\boldsymbol{M}(\boldsymbol{q})\ddot{\boldsymbol{q}} + \boldsymbol{C}(\boldsymbol{q},\dot{\boldsymbol{q}}) = \boldsymbol{\tau}. \tag{3.1}$$

Pelvis position and orientation and the joint angles are defined by the vector $\boldsymbol{q} = (q^{(1)},\ldots,q^{(n_q)})$, $q^{(i)} : \mathbb{R} \to \mathbb{R}$, $i = 1,\ldots,n_q$, with n_q being the number of degrees of freedom. Analogously $\dot{\boldsymbol{q}}$ defines the corresponding velocities and $\ddot{\boldsymbol{q}}$ the accelerations. The joint torques are described by the vector $\boldsymbol{\tau} = (0,0,0,\tilde{\boldsymbol{\tau}}^T)^T \in \mathbb{R}^{n_q}$, where the first three entries correspond to the free floating body. Note, that in the context of optimal control the control vector is defined by the $n_q - 3$ elements of the torque vector which correspond to the actuated joints $\tilde{\boldsymbol{\tau}}$, see also Chapter 4. The inertia term is described by the symmetric and positive definite matrix $\boldsymbol{M}$ depending also on the joint angles. The vector of functions $\boldsymbol{C}(\boldsymbol{q},\dot{\boldsymbol{q}})$ describes the amount of forces that has to be applied to enforce the acceleration $\ddot{\boldsymbol{q}}$ to be zero. This term can include the Coriolis and gravity as well as centrifugal and friction forces. Considering contacts, e.g. of the feet with the ground, additional constraint equations

$$\boldsymbol{g}(\boldsymbol{q}) = 0 \tag{3.2}$$

have to be fulfilled. The impacts with the ground are simulated as perfect inelastic collisions. Equation (3.1) changes to

$$\boldsymbol{M}(\boldsymbol{q})\ddot{\boldsymbol{q}} + \boldsymbol{C}(\boldsymbol{q},\dot{\boldsymbol{q}}) = \boldsymbol{\tau} + \boldsymbol{G}(\boldsymbol{q})^T\boldsymbol{\lambda}, \tag{3.3}$$

where $\boldsymbol{\lambda} \in \mathbb{R}^m$ are the constraint forces corresponding to the constraints $\boldsymbol{g}(\boldsymbol{q})$ (m = number of constraint equations) and $\boldsymbol{G}(\boldsymbol{q}) := \frac{\partial}{\partial \boldsymbol{q}}\boldsymbol{g}(\boldsymbol{q})$ is the Jacobi Matrix of the constraints.

Note, that in the case of additional external perturbations also the Jacobian of the push point G_{push} is calculated. Combined with the applied force $\boldsymbol{f}_{\text{push}}$ it is included into the model by adding it to the torques in the joints

$$\boldsymbol{\tau} \longmapsto \boldsymbol{\tau} + \boldsymbol{G}^T_{\text{push}}\boldsymbol{f}_{\text{push}}. \tag{3.4}$$

In Section 3.4 a detailed description how to model the perturbation is given.

By differentiation of (3.2), equation (3.3) can be formulated as a linear system with the unknowns $\ddot{\boldsymbol{q}}$ and $\boldsymbol{\lambda} \in \mathbb{R}^m$:

$$\begin{pmatrix} \boldsymbol{M} & \boldsymbol{G}^T \\ \boldsymbol{G} & \boldsymbol{0} \end{pmatrix} \begin{pmatrix} \ddot{\boldsymbol{q}} \\ -\boldsymbol{\lambda} \end{pmatrix} = \begin{pmatrix} -\boldsymbol{C} + \boldsymbol{\tau} \\ -\dot{\boldsymbol{G}}\dot{\boldsymbol{q}} \end{pmatrix}. \tag{3.5}$$

It has to be ensured that the constraints $\boldsymbol{g}(\boldsymbol{q}) = 0$ are satisfied at the beginning. After that, they are fulfilled on the acceleration level.

Based on these equations, human gait can be modeled as a multi-phase problem. The equations of motion for each phase can be formulated by an index 1 system with invariants of the following form:

$$\begin{gathered} \dot{\boldsymbol{q}} = \boldsymbol{v}, \quad \dot{\boldsymbol{v}} = \boldsymbol{a}, \\ \begin{pmatrix} \boldsymbol{M}(\boldsymbol{q}) & \boldsymbol{G}(\boldsymbol{q})^T \\ \boldsymbol{G}(\boldsymbol{q}) & \boldsymbol{0} \end{pmatrix} \begin{pmatrix} \boldsymbol{a} \\ \boldsymbol{\lambda} \end{pmatrix} = \begin{pmatrix} -\boldsymbol{C}(\boldsymbol{q},\boldsymbol{v}) + \boldsymbol{\tau} \\ -\dot{\boldsymbol{G}}\dot{\boldsymbol{q}} \end{pmatrix}, \\ \boldsymbol{g}_q = \boldsymbol{g}(\boldsymbol{q}(t)) = \boldsymbol{0}, \quad \boldsymbol{g}_v = \boldsymbol{G}(\boldsymbol{q}(t))\boldsymbol{v}(t) = \boldsymbol{0}. \end{gathered} \tag{3.6}$$

3.3 Modeling of Human Gait

The constraints and the right-hand sides of the differential equation describing the dynamics of the model are changing during a gait cycle. Usually, six phases are distinguished defined by the change of the contacts of the heel and the hallux of the left and the right foot, respectively. These changes are described in detail in this section.

Impacts of the feet with the ground result in discontinuities of the velocities $\boldsymbol{v}$ defined by the following linear system

$$\begin{pmatrix} \boldsymbol{M}(\boldsymbol{q}) & \boldsymbol{G}(\boldsymbol{q})^T \\ \boldsymbol{G}(\boldsymbol{q}) & \boldsymbol{0} \end{pmatrix} \begin{pmatrix} \boldsymbol{v}_+ \\ \boldsymbol{\Lambda} \end{pmatrix} = \begin{pmatrix} \boldsymbol{M}(\boldsymbol{q},\boldsymbol{p})\boldsymbol{v}_- \\ \boldsymbol{0} \end{pmatrix}, \tag{3.7}$$

where $\boldsymbol{v}_+$ defines the velocities immediately before the impulse $\boldsymbol{\Lambda}$ and $\boldsymbol{v}_-$ the ones immediately after this impulse.

As mentioned, the equations of motion change according to the contacts of the model with the environment and itself. During human walking the contact points of the feet with the ground change during the gait cycle as shown in Table 3.2 and Figure 3.2. In all studies of this work, a single step of a human is modeled. This step is described by the change of the contacts of the feet resulting in the following four phases: Two model phases that describe single support, where only one foot is in contact with the ground, and two phases that describe double support, where parts of both feet are in contact with the ground. These phases are distinguished by the change of only heel, only toe or flat foot contacts with the ground as described in Table 3.2. Two additional transition phases are implemented to allow for discontinuities in time whin the left heel and the left hallux touch the ground. Note, that in the analysis of phase lengths, these two phases are not taken into account because their time is zero. Therefore in the analysis of the phases, only four phases are analyzed. To model the changes of the feet contact points, switching functions between the phases are implemented. The body segments and the joints at the right side of the body are referred to as stance body segments and stance joints and the ones on the left side as swing body segments and swing joints. A whole human step during normal walking motions including the contact points is shown in Figure 3.2. Also, the different phases of the gait cycle described before are marked. For normal walking, we assume the motion to be periodic. In this case, we define periodicity conditions in the optimal control problem, see Section 4. The perturbation is modeled as a continuous function over time acting at a specific point of the body as described in detail in the next section.

Table 3.2: Contact points during the phases of a normal step of a human.

Contact	**Phase 1**	**Phase 2**	**Phase 3**	**Phase 4**
Right hallux	yes	yes	yes	yes
Right heel	yes	no	no	no
Left hallux	start	no	no	yes
Left heel	no	no	yes	yes
	Single Support		Double Support	

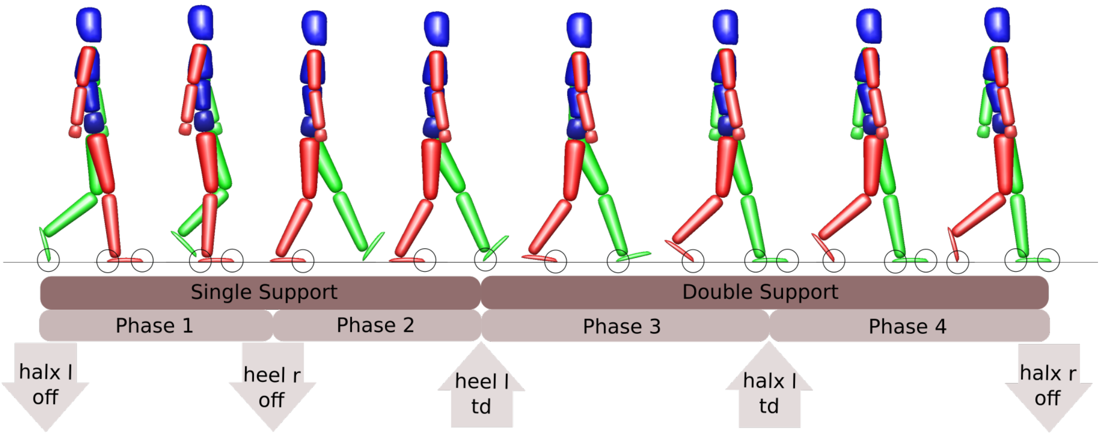

Figure 3.2: Visualization of the different phases of a step of a human during normal walking. The circles mark the active contact points.

3.4 Modeling of Perturbation

The phases of the regarded perturbed human walking motions are basically the same as for the unperturbed walking described in the previous section, see Figure 3.3. The motion consists of six phases in total. Two of these phases are transition phases where the impacts of the left heel and hallux are applied. There also exist recovery motions in which the human starts to jump which ends up in a flying phase for the model. These kinds of recovery motions are not considered in this work.

On top of the described phases that are similar to normal walking, we need to model the perturbation. In our case, the perturbation is a push applied from the back at a defined height at the spine of a human. As described in Sections 2.2 and 2.3 we measure the force and the direction of the push using a force sensor. This allows us to describe the force of the perturbation as a function of time and allows us to include the reference data from the experiments. In the following the different possibilities of how to model this push are discussed.

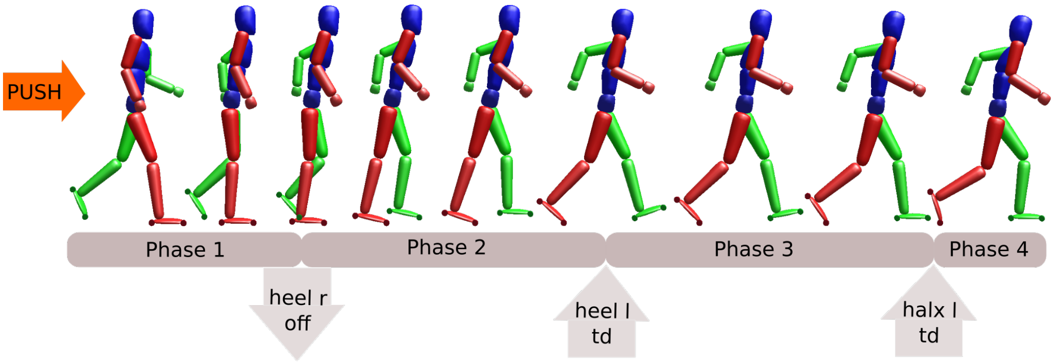

Figure 3.3: Phases of human walking motion with push force modeled as impact in orange.

3.4.1 Impact

First, we present a simple but not very realistic approach of modeling the push force as an extra transition phase at the time when the push is applied. This has the advantage that discontinuities in the velocities are allowed at the time when the push is applied. Figure 3.4 shows an example of how the phases could look like. But the push phase could also be in another phase if the push is at another point in time during the step. This is one of the disadvantages of this approach: The phase in which the push is applied has to be known in advance as the order of the phases has to be fixed in advance. Furthermore, this approach is not very realistic as in reality the push is never instantaneous. It always lasts over a period of time. This observation leads to the approach presented in the next section.

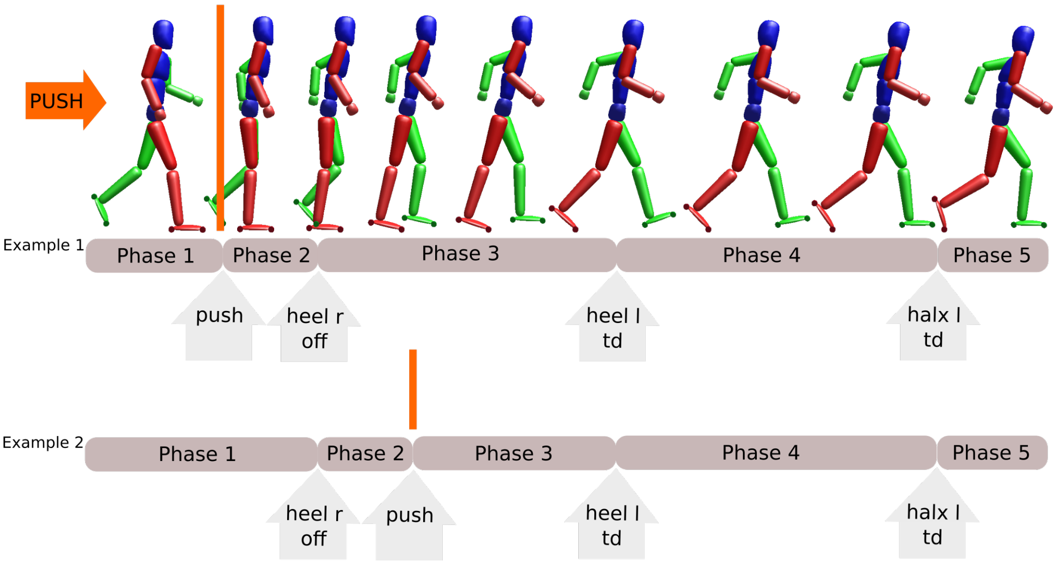

Figure 3.4: Phases of human walking motion with push force modeled as impact in orange.

3.4.2 Continuous

In this section the implementation of an additional external force acting on the model as a continuous function is presented, meaning the external perturbation is implemented as a continuous function of time over the whole motion, see Figure 3.5. This allows for different strength, durance, and shapes of the perturbation. At the moment only punctual perturbations applied at a specific point of the body are modeled. To this end, the Jacobian of the push point $\boldsymbol{G}_{\text{push}}$ is calculated. Combined with the applied force $\boldsymbol{f}_{\text{push}}$ (strength and direction of the perturbation) it is included into the model by adding it to the torques in the joints as follows.

$$\boldsymbol{\tau} = \begin{pmatrix} 0 \\ 0 \\ 0 \\ \tilde{\boldsymbol{\tau}} \end{pmatrix} + {\boldsymbol{G}_{\text{push}}}^T \boldsymbol{f}_{\text{push}}. \tag{3.8}$$

Note, that this can also generate nonzero values in the first three entries of $\boldsymbol{\tau}$.

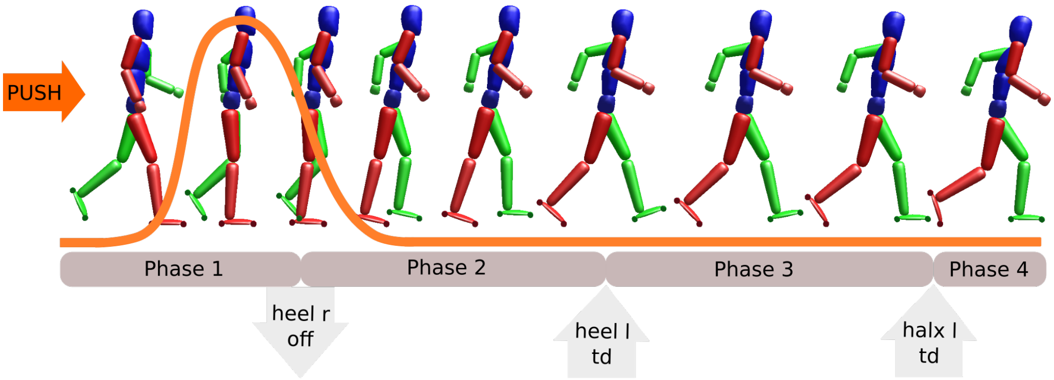

Figure 3.5: Phases of human walking motion with push force modeled continuously in orange.

3.4.3 Combination

A combination of the two possibilities introduced in the previous sections is to model the push force first as an impact in a transition stage and then as a continuous function, see Figure 3.6. This approach has the advantage that it allows for jumps in the velocities at the start of the perturbation and at the same time the push can be simulated as a function of time over the period it is applied which is much more realistic than to model it only as impact. But also in this approach, the phase during which phase the push takes place has to be defined in advance.

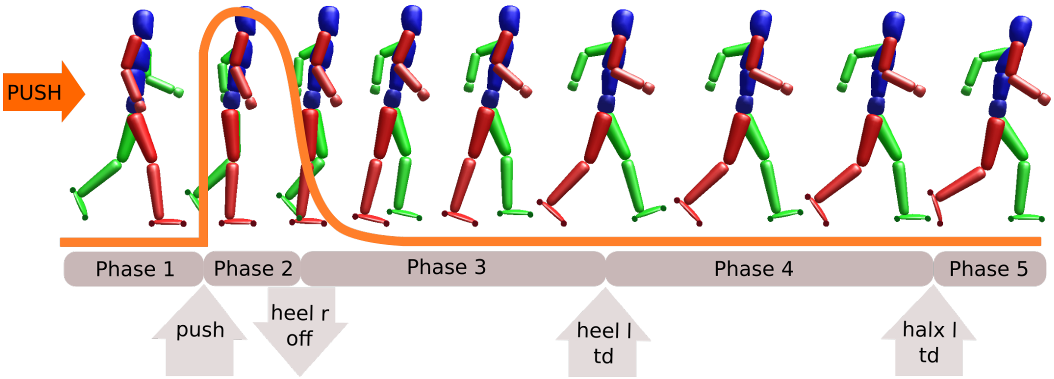

Figure 3.6: Phases of human walking motion with push force modeled as impact at the start and then as continuous function in orange.

3.4.4 Discussion of Push Simulation Possibilities

As already described in the previous sections the different possibilities on how to implement the push in our model come with various advantages and disadvantages. While some of the approaches are more realistic, some are not very precise. In Table 3.3 these advantages and disadvantages are listed. The first approach of the implementation as a transition stage comes with the two big disadvantages that the push can only be simulated as an instantaneous perturbation and that the phase in which the push occurs has to be known beforehand. The second approach comes with the advantage that these two points are neglected. But this continuous approach does not allow for discontinuities in the states at the point in time when the push occurs. This can be realized in the first approach. Therefore the idea to combine both approaches and to simulate the push force at the start as a transition stage and then as a continuous function appears obvious. This combined approach allows for discontinuities in the states at the start of the push (advantage of the first approach) and the push can be simulated continuously (advantage of the second approach). Nevertheless, we decided against the combined method but for the approach with only a continuous function because for this approach, the phase in which the push takes place does not need to be defined beforehand. This is no problem for a motion reconstruction as in Chapter 5 ff. but for a motion synthesis approach presented in Chapter 7 it is not known in which phase the perturbation will take place.

Table 3.3: Discussion of push simulation possibilities.

Instantaneous push as impact (transition stage)	**Continuous perturbation** as function over time	**Combination** impact at start, then continuous
Allows for discontinuities in states	Does not allow for discontinuities in states	Allows for discontinuities in states
Not realistic: instantaneous	Push can last over a period of time	Push can last over period of time
Phase of push has to be known beforehand	Phase of push does not need to be defined in advance	Phase of push start has to be known beforehand

Chapter 4

Optimization Methods for the Analysis of Human Push Recovery During Walking

In the first part of this section, an optimal control problem (OCP) for human gait is presented. In the second part, the solution methods used in this work are described. The description of the theory and methods are based on [12, 29, 48, 50, 62, 85, 103, 127, 150].

4.1 Optimal Control Problem Formulation for Gait Analysis

The OCP for human gait analysis is characterized by an objective function which is minimized fulfilling differential equation constraints and usually other constraints, such as (in-)equality constraints

$$\min_{\boldsymbol{x}(t),\boldsymbol{u}(t),\boldsymbol{p},\boldsymbol{s}} \quad \Phi[\boldsymbol{x},\boldsymbol{u},\boldsymbol{p},\boldsymbol{s}] \tag{4.1a}$$

$$\text{s.t.} \quad \dot{\boldsymbol{x}}(\mathrm{t}) = \boldsymbol{f}_{\mathrm{i}}(\mathrm{t},\boldsymbol{x}(\mathrm{t}),\boldsymbol{u}(\mathrm{t})), \text{ for } \mathrm{t} \in \mathcal{I}_{\mathrm{i}}, \tag{4.1b}$$

$$\boldsymbol{x}(s_i^+) = \boldsymbol{x}(s_i^-) + c_i(s_i^-,\boldsymbol{x}(s_i^-)), \tag{4.1c}$$

$$\boldsymbol{g}_i(t,\boldsymbol{x}(t),\boldsymbol{u}(t)) \geq \boldsymbol{0}, \text{ for } t \in \mathcal{I}_i, \tag{4.1d}$$

$$\boldsymbol{r}_{eq}(\boldsymbol{x}(s_0),\ldots,\boldsymbol{x}(s_{n_{ph}}),\boldsymbol{p}) = \boldsymbol{0}, \tag{4.1e}$$

$$\boldsymbol{r}_{ineq}(\boldsymbol{x}(s_0),\ldots,\boldsymbol{x}(s_{n_{ph}}),\boldsymbol{p}) \geq \boldsymbol{0}, \tag{4.1f}$$

$$i = 1,\ldots,n_{ph}-1, \;\; s_0 = 0, \;\; s_{n_{ph}} = T.$$

For the analysis of human gait including recovery motions, we introduce a multi-phase optimal control problem, where the time horizon $\mathcal{I} = [s_0,s_f] = [0,T]$ is divided in n_{ph} subintervals $\mathcal{I}_i = [s_i,s_{i+1}]$, $i = 0,1,\ldots,n_{ph}-1$, $s_{n_{ph}} = s_f$, where n_{ph} denotes the number of stages of the model, see Section 3.3, also called phases in the scope of the optimal control formulation. The end-time meaning the time needed for the motion (in our case one step of the gait cycle) is described by $s_{n_{ph}} = s_f = T$. Note, that the switching times $\boldsymbol{s} = (s_0,\ldots,s_f)$ are free for the motion synthesis approach and fixed for the motion reconstruction approach.

In the OCP (4.1a)-(4.1f) $\boldsymbol{x}(t) = (x_1(t),\ldots,x_{n_x}(t))^t : \mathcal{I} \to \mathbb{R}^{n_x}$ represents the differential states defined by

$$\boldsymbol{x}(t) := \begin{pmatrix} \boldsymbol{q}(t) \\ \dot{\boldsymbol{q}}(t) \end{pmatrix} \in \mathbb{R}^{2n_{Dof}}, \tag{4.2}$$

where $\boldsymbol{q}$ defines the generalized position variables, meaning mainly the angles of the joints, and $\dot{\boldsymbol{q}}$ defines the generalized velocity variables, n_{Dof} stands for the number of degrees of freedom of the model. The controls are represented by $\boldsymbol{u}(t) = (u_1(t),\ldots,u_{l_u}(t))^t : \mathcal{I} \to \mathbb{R}^{n_u}$, where n_u describes the number of actuated joints and $\boldsymbol{u}$ describes the inner joint torques. Note that here a general case is described. We will see that for other problem formulations and models the states and control variables can vary. For example, we often take the derivatives of the joint torques as controls and take the joint torques as additional states. The finite-dimensional vector of parameters is defined by $\boldsymbol{p} \in \mathbb{R}^{n_p}$, where n_p describes the number of parameters that are minimized or maximized during the optimization such as step lengths or slack variables defining the periodicity gap, see Section 7.

In the general case, the objective function is described by

$$\Phi[\boldsymbol{x},\boldsymbol{u},\boldsymbol{p},\boldsymbol{s}] = \sum_{i=0}^{n_{ph}} \phi_{M_i}(t_i,\boldsymbol{x}(t_i),\boldsymbol{p},\boldsymbol{s}) + \int_{s_i}^{s_{i+1}} \phi_{L_i}(t,\boldsymbol{x}(t),\boldsymbol{u}(t),\boldsymbol{p},\boldsymbol{s})dt. \tag{4.3}$$

It can be divided in Mayer terms (Φ_M) and Lagrange terms (integral). This formulation is also called Bolza functional. In the case of the motion reconstruction approach, see Section 5, an objective function is formulated that enables to determine the control that leads to joint angles which are as close as possible to the joint angles from reference data. This ends up in a least-squares formulation

$$\Phi[\boldsymbol{x},\boldsymbol{u},\boldsymbol{p},\boldsymbol{s}] = \frac{1}{n_{\tilde{x}} n_{\tilde{t}}} \sum_{k}^{n_{\tilde{x}}-1} \sigma_k \sum_{l=0}^{n_{\tilde{t}}-1} (M(x_k(t_l)) - \tilde{x}_{k,l})^2, \tag{4.4}$$

where $(\tilde{x}_{k,l})_{k=0,\ldots,n_x-1,l=0,\ldots,n_{\tilde{t}}-1}$ denotes the postprocessed reference data which consist of $n_{\tilde{x}}$ motion trajectories defined at the discrete time points $t_l, l = 0,\ldots,n_{\tilde{t}} - 1$. To project the state variables $\boldsymbol{x}$ to its position part $\boldsymbol{q}$ the transfer function M is defined. To allow for a component-wise scaling of the deviations of the $n_{\tilde{x}}$ reference trajectories, scaling factors $\omega_k, k = 0,\ldots,n_{\tilde{x}}$ are introduced. A more detailed description of the different possibilities to define objective functions for the motion synthesis approach is given in Section 7.

The dynamics of the model defined by a differential equation, see Section 3.2,

$$\ddot{\boldsymbol{q}} = (\boldsymbol{M}(\boldsymbol{q}))^{-1}(\tau - \boldsymbol{C}(\boldsymbol{q},\dot{\boldsymbol{q}}) + \boldsymbol{G}(\boldsymbol{q})^T \lambda) =: \boldsymbol{f}(t,\boldsymbol{q},\dot{\boldsymbol{q}},\boldsymbol{u}) \tag{4.5}$$

is included in the constraints of the optimal control problem (4.1b). Using the formulation of the states as above (4.2), we get

$$\boldsymbol{x}(t) := \begin{pmatrix} \boldsymbol{x}_1(t) \\ \boldsymbol{x}_2(t) \end{pmatrix} = \begin{pmatrix} \boldsymbol{q} \\ \dot{\boldsymbol{q}} \end{pmatrix} \qquad \Rightarrow \qquad \frac{\mathrm{d}}{\mathrm{d}t}\boldsymbol{x}(t) = \begin{pmatrix} \dot{\boldsymbol{q}} \\ \ddot{\boldsymbol{q}} \end{pmatrix} = \begin{pmatrix} \boldsymbol{x}_2 \\ \tilde{f}(t,\tilde{\boldsymbol{x}}_1(t),\tilde{\boldsymbol{x}}_2(t),\boldsymbol{u}(t)) \end{pmatrix} \tag{4.6}$$

which can be included in the optimal control system as $\dot{\boldsymbol{x}}(t) = \boldsymbol{f}(t,\boldsymbol{x}(t),\boldsymbol{u}(t),\boldsymbol{p})$. On each time interval (representing a phase) $\mathcal{I}_j$, where $\boldsymbol{f}_i : \mathbb{R}^{n_x} \times \mathbb{R}^{n_u} \times \mathbb{R}^{n_p} \to \mathbb{R}^{n_x}$. The constraints vary for each phase to simulate the changes of contacts.

Equation (4.1c) describes the conditions for the phase transition: The discontinuities of the states $\boldsymbol{x}(t)$ at the switching times $\boldsymbol{s}$ are described as transitions from the right-side limit s_i^- of the time interval $\mathcal{I}_i$ of phase i to the left-side limit s_i^+ of the time interval $\mathcal{I}_{i+1}$ of phase $i+1$ using the phase transitions functions $\boldsymbol{c}_i : \mathbb{R}^{n_x} \times \mathbb{R}^{n_p} \to \mathbb{R}^{n_x}$.

The path constraints are defined in (4.1d) with $\boldsymbol{g}_i : \mathbb{R}^{n_x} \times \mathbb{R}^{n_u} \times \mathbb{R}^{n_p} \to \mathbb{R}^{n_g}$, where n_g defines the number of path constraints. These constraints include the upper and lower bounds for the states $\boldsymbol{x}$, the controls $\boldsymbol{u}$, the parameters $\boldsymbol{p}$ and the stage times $\boldsymbol{s}$. The bounds are chosen based on the reference data. For the optimization, it is important not to choose these variables too loose to avoid the possibility of redundant solutions. For the motion reconstruction problem, they are defined by taking the maximal and minimal values from the reference data with a small variation. For the motion synthesis approach, this variation is a bit bigger to allow for more motions.

The last two equations (4.1e) and (4.1f) define the (in-)equality interior point constraints that contain kinematic constraints and ground reaction force constraints, e.g. for the collisions with the ground during walking.

4.2 Numerical Solution of Optimal Control Problems

In this section, we present how to solve an OCP of the form (4.1a) - (4.1f). For notation reasons we regard an OCP of the form

$$\min_{\boldsymbol{x},\boldsymbol{u}} \Phi[\boldsymbol{x},\boldsymbol{u}] = \int_{t_a}^{t_b} \phi(t,\boldsymbol{x}(t),\boldsymbol{u}(t))dt \tag{4.7a}$$

$$\text{s.t.} \quad \dot{\boldsymbol{x}}(t) = f(t,\boldsymbol{x}(t),\boldsymbol{u}(t)),\ t \in [t_a,t_b], \tag{4.7b}$$

$$r_a(\boldsymbol{x}(t_a)) + r_b(\boldsymbol{x}(t_b)) = 0, \tag{4.7c}$$

$$g(t,\boldsymbol{u}(t)) \geq 0,\ t \in [t_a,t_b]. \tag{4.7d}$$

Note, that (4.1a) - (4.1f) can be reformulated to (4.7a) - (4.7d). Figure 4.1 shows an overview of the optimization flow for an OCP.

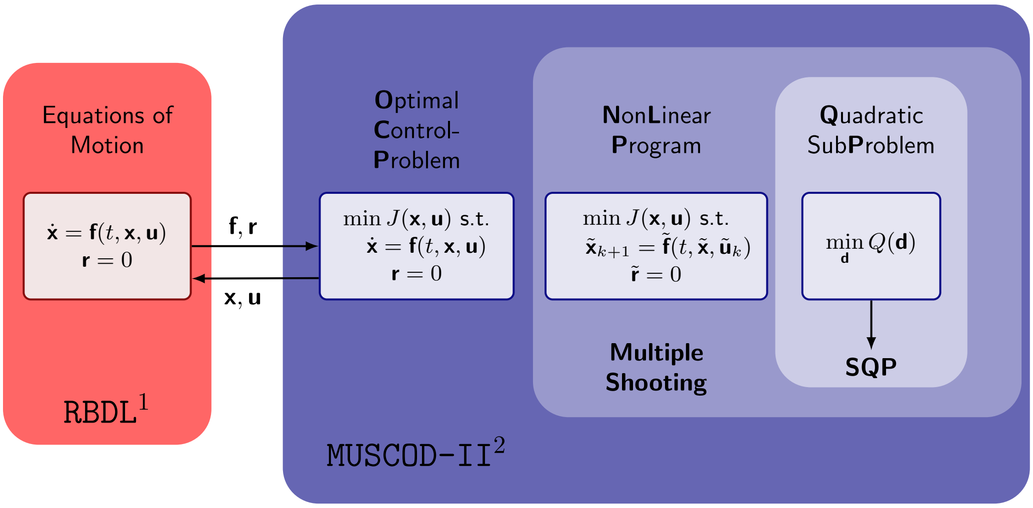

[1] Rigid-body dynamics library by M. Felis, ORB, IWR, University of Heidelberg
[2] by H. G. Bock, D. B. Leineweber, et al., SimOPT, IWR, University of Heidelberg

Figure 4.1: Overview of the optimization flow using the multiple shooting algorithm MUSCOD and the rigid body dynamics library RBDL.

In the software package `MUSCOD-II` of the Interdisciplinary Center for Scientific Computing, Heidelberg University, [12, 103] a direct multiple shooting approach for the discretization coupled with an efficient sequential quadratic programming (SQP) method for the optimization is implemented. For the solution of the equations of motion, the rigid multi-body dynamics library `RBDL` [40] is used, see Section 3. In the following, the direct multiple shooting algorithm, as well as the SQP method, are described in detail.

4.2.1 Direct Multiple Shooting

For the solution of OCPs of the form (4.7a)-(4.7d), two main different ways are explored: the indirect and the direct approach, see [12, 29, 150]. The indirect methods are based on the maximum principle leading to a boundary value problem with jumping and switching conditions. This means that the system of differential equations that satisfies endpoint and interior-point conditions has to be solved, which are hard to solve even for quite simple cases.

For the direct approaches, the infinite-dimensional OCP is reformulated to a large constrained finite-dimensional OCP by a control discretization coupled with a simultaneous parameterization of the state differential equations which can be solved by a recursive quadratic programming algorithm. In this work, a direct approach is used, more precisely a direct multiple shooting approach which is presented in this section.

Discretization of Controls

To discretize the controls $\boldsymbol{u}(t)$, the whole time interval $\mathcal{I} = [t_a,t_b]$ is divided into smaller Intervals $\mathcal{I}_j = [t_j,t_{j+1}]$, $j = 0,1,\ldots,n_s-1$, where n_s denotes the number of nodes of the Interval $\mathcal{I}$, leading to the following grid:

$$\Delta := (t_j)_{j=1}^{n_s}, \qquad 0 = t_a = t_0 < t_1 < t_2 < \cdots < t_{n_s-1} < t_{n_s} = t_b. \tag{4.8}$$

On each of these intervals

$$\mathcal{I}_j = [t_j;t_{j+1}],\ j = 0,1,\ldots,n_s-1, \tag{4.9}$$

we can define a finite discretization of the controls of our optimal control problem. The control vector is approximated by a finite set of parameters using given basis functions $\boldsymbol{\varphi}_j$ and parameters $\boldsymbol{\varrho}_j$

$$\boldsymbol{u}(t) := \boldsymbol{\varphi}_j(t,\boldsymbol{\varrho_j}),\ \boldsymbol{\varrho_j} \in \mathbb{R}^{n_{u_j}},\ t \in \mathcal{I}_j = [t_j,t_{j+1}],\ j = 0,1,\ldots,n_s-1. \tag{4.10}$$

Each set of basis functions $\boldsymbol{\varphi}_j$ is only defined on one interval $\mathcal{I}_j$. These basis functions can be defined as a vector of polynomials resulting in a piecewise polynomial representation of the control $\boldsymbol{u}$. The most simple definition of basis function is the piecewise constant definition

$$\boldsymbol{\varphi}_j(t,\boldsymbol{\varrho}_j) = \boldsymbol{\varphi}_j = \boldsymbol{\varrho}_j. \tag{4.11}$$

Also linear approximations are possible defined by interpolation between $\boldsymbol{\varrho}_j^1$ and $\boldsymbol{\varrho}_j^2$ on $\mathcal{I}_j$:

$$\boldsymbol{\varphi}_j(t,\boldsymbol{\varrho}_j) = v_j^1 + \frac{t-t_j}{t_{j+1}-t_j}(\boldsymbol{\varrho}_j^2 - \boldsymbol{\varrho}_j^1),\ \boldsymbol{\varrho}_j = \begin{pmatrix} \boldsymbol{\varrho}_j^1 \\ \boldsymbol{\varrho}_j^2 \end{pmatrix} \in \mathbb{R}^{2n_{u_j}}. \tag{4.12}$$

This approximation is discontinuous at the switching points t_j. For the numerical calculation, this is not a problem as t_j is known. For a continuous formulation, one needs to include the continuity conditions

$$\boldsymbol{\varphi}_j(t_{j+1},\boldsymbol{\varrho}_j) - \boldsymbol{\varphi}_{j+1}(t_{j+1},\boldsymbol{\varrho}_{j+1}) = 0. \tag{4.13}$$

Note, that also a spline interpolation of higher order is possible, but makes the optimal control problem more complex. To this end, in this thesis only constant and linear controls are used.

Parametrization of States

Using the discretization of the controls from the previous section, we could now apply a single shooting, collocation or multiple shooting method. The intuitive approach of single shooting is very costly as it requires the repeated integration of the (IVP) over the whole interval $\mathcal{I}$ and often it does not converge due to poor initial data. But even for a good initial approximation, the errors by the discretization and the roundoff as well as the instability of the ODEs grow large and lead to unsatisfying results. Therefore, in this work, we rely on a direct multiple shooting approach. For the formulation here, we assume the same grid for the states as for the controls described above. Note, that also a different grid for the states than for the controls is possible.

If we assume $\boldsymbol{x}(t;\boldsymbol{s}_j,\boldsymbol{\varrho}_j)$ to be a solution of the initial value problem (IVP)

$$\dot{\boldsymbol{x}} = \boldsymbol{f}(t,\boldsymbol{x},\boldsymbol{\varphi}(t,\boldsymbol{\varrho}_j)),\ \boldsymbol{x}(t_j) = \boldsymbol{s}_j,\ t \in \mathcal{I}_j, \tag{4.14}$$

we have to determine $\boldsymbol{s}_j$ and $\boldsymbol{\varrho}_j$ such that the function $\boldsymbol{x}$ pieced together by the solutions of the IVP (4.14)

$$\boldsymbol{x}(t) := \boldsymbol{x}(t;\boldsymbol{s}_j,\boldsymbol{\varrho}_j) \ \text{ for } \ t \in [t_j,t_{j+1}[,\ j = 0,1,\dots,n_s-1, \tag{4.15}$$

$$\boldsymbol{x}(t_{n_x}) = \boldsymbol{s}_{n_s} \tag{4.16}$$

is continuous.

The idea of the direct multiple shooting method is to simultaneously compute the solution values $\boldsymbol{s}_j = \boldsymbol{x}(t_j)$, $j = 0,1,\dots,n_s$ at all grid points and not just $s_0 = x(t_a)$. Then $\boldsymbol{x}$ represents also a solution of $\dot{\boldsymbol{x}} = \boldsymbol{f}(t,\boldsymbol{x},\boldsymbol{u})$ on $\mathcal{I}$. To be a solution of the IVP, $\boldsymbol{x}$ also needs to fulfill the boundary constraints $r_a + r_b = 0$. To include all equations in one function, we define the vector

$$\boldsymbol{y} := (\boldsymbol{s}_0,\boldsymbol{\varrho}_0,\dots,\boldsymbol{s}_{n_s-1},\boldsymbol{\varrho}_{n_s-1},\boldsymbol{s}_{n_s}) \in \mathbb{R}^{\hat{n}}, \tag{4.17}$$

$$\hat{n} = n_x(n_s-1) + \sum_{j=0}^{n_s-1} n_{u_j} \tag{4.18}$$

resulting in $\hat{m} = n_x n_s + n_r$ conditions

$$\boldsymbol{h}(\boldsymbol{y}) := \begin{pmatrix} \boldsymbol{x}(t_1;\boldsymbol{s}_0,\boldsymbol{\varrho}_0) - \boldsymbol{s}_1 \\ \boldsymbol{x}(t_2;\boldsymbol{s}_1,\boldsymbol{\varrho}_1) - \boldsymbol{s}_2 \\ \vdots \\ \boldsymbol{x}(t_{n_i};\boldsymbol{s}_{n_i-1},\boldsymbol{\varrho}_{n_i-1}) - \boldsymbol{s}_{n_i} \\ \boldsymbol{r}_a(\boldsymbol{s}_0) + \boldsymbol{r}_b(\boldsymbol{s}_{n_s}) \end{pmatrix} = 0. \tag{4.19}$$

Note, that $\boldsymbol{h}(\boldsymbol{y})$ no longer requires integration over the whole interval $\mathcal{I}$ but only on the subintervals $[t_j,t_{j+1}[$. Next, we formulate the whole optimal control problem in the discretized form.

Discretized Formulation of Optimal Control Problem

Using the grid (4.8), the discretization of the controls (4.10) and parametrization of the states (4.16) described in the previous sections, we can formulate our OCP (4.7a)-(4.7d) as general nonlinear programming (NLP) problem defined on the interval $\mathcal{I} = [t_j, t_{j+1}[$ as follows

$$\min_{\boldsymbol{y}} \Phi[\boldsymbol{y}] = \sum_{j=0}^{n_s-1} \int_{t_j}^{t_{j+1}} \phi(t, \boldsymbol{x}(t; \boldsymbol{s}_j, \boldsymbol{\varrho}_j), \boldsymbol{\varphi}(t, \boldsymbol{\varrho}_j)) \mathrm{d}t =: \sum_{j=0}^{n_s-1} \phi_j(\boldsymbol{s}_j, \boldsymbol{\varrho}_j), \tag{4.20a}$$

$$\text{s.t.} \quad \boldsymbol{h}_j(\boldsymbol{s}_{j+1}, \boldsymbol{s}_j, \boldsymbol{\varrho}_j) = \boldsymbol{x}(t_{j+1} \boldsymbol{s}_j, \boldsymbol{\varrho}_j) - \boldsymbol{s}_{j+1} = 0, \; j = 0, 1, \dots, n_s - 1, \tag{4.20b}$$

$$\boldsymbol{h}_{n_s}(\boldsymbol{s}_a, \boldsymbol{s}_{n_s}) = \boldsymbol{r}_a(\boldsymbol{s}_0) + \boldsymbol{r}_b(\boldsymbol{s}_{n_s}) = 0, \tag{4.20c}$$

$$\boldsymbol{g}_j(\boldsymbol{\varrho}_j) \geq 0, \; j = 0, 1, \dots, n_s - 1, \tag{4.20d}$$

where $\boldsymbol{y}$ is the parametrization vector defined in (4.18) and $\boldsymbol{x}(t; \boldsymbol{s}_j, \boldsymbol{\varrho}_j)$ solves the IVP (4.14). The first constraint (4.20b) is also called matching condition. If continuity at the grid points is desired, the additional equality constraints (4.13) has to be added. By defining the additional variable

$$z(t) := \int_{t_j}^{t} \phi(t, \boldsymbol{x}(t; \boldsymbol{s}_j, \boldsymbol{\varrho}_j), \boldsymbol{\varphi}(t, \boldsymbol{\varrho}_j)) \mathrm{d}t, t \in \mathcal{I}_j \tag{4.21}$$

the values of the performance index can be calculated at the same time as $\boldsymbol{x}(t_{j+1}; \boldsymbol{s}_j, \boldsymbol{\varrho}_j)$ by solving the IVP

$$\begin{pmatrix} \dot{z}(t) \\ \dot{\boldsymbol{x}}(t) \end{pmatrix} = \begin{pmatrix} \phi(t, \boldsymbol{x}(t; \boldsymbol{s}_j, \boldsymbol{\varrho}_j), \boldsymbol{\varphi}(t, \boldsymbol{\varrho}_j)) \\ \boldsymbol{f}(t, \boldsymbol{x}, \boldsymbol{\varphi}(t, \boldsymbol{\varrho}_j)) \end{pmatrix}, \begin{pmatrix} z(t_j \\ \boldsymbol{x}(t_j \end{pmatrix} = \begin{pmatrix} \boldsymbol{0} \\ \boldsymbol{s}_j \end{pmatrix}, t \in \mathcal{I}_j. \tag{4.22}$$

It follows

$$\boldsymbol{F}_j(\boldsymbol{s}_j, \boldsymbol{\varrho}_j) \equiv z(t_{j+1}; \boldsymbol{s}_j, \boldsymbol{\varrho}_j), \; j = 0, 1, \dots, n_s - 1. \tag{4.23}$$

4.2.2 Sequential Quadratic Programming Method

In this section, a short overview on a sequential quadratic programming (SQP) method for the solution of nonlinear programming (NLP) problems with constraints of the form

$$\min_{\boldsymbol{y} \in \mathbb{R}^n} \Phi(\boldsymbol{y}) \qquad \text{s.t.} \qquad \begin{cases} \boldsymbol{h}(\boldsymbol{y}) = \boldsymbol{0} \\ \boldsymbol{g}(\boldsymbol{y}) \geq \boldsymbol{0} \end{cases} \tag{4.24}$$

is given, for more details see [48, 50, 127]. As described in the previous chapter, each OCP of the form (4.1a)-(4.1f) can be reformulated to such an NLP (4.24) where all functions are explicitly or implicitly defined as functions of the multiple shooting variables. We will use the same notation as in the previous sections. The main idea of the SQP algorithm is to replace a difficult problem with an easier one. Instead of trying to solve the whole problem at once, a sequence of subproblems is defined that is more simple to solve. The main structure of the SQP algorithm is the same as for the Lagrange-Newton algorithm which is used to solve problems with only equality constraints. The formulation of the subproblems is based on optimality conditions such as Karush Kuhn Tucker (KKT) conditions. This motivates the definition of the quadratic subproblem (SQP-subproblem)

$$\min_{\boldsymbol{\sigma}_y} \nabla\Phi(\boldsymbol{y}^k)^T \boldsymbol{\sigma}_y + \frac{1}{2} \boldsymbol{\sigma}_y^T \boldsymbol{H}_k \boldsymbol{\sigma}_y \tag{4.25a}$$

$$\text{s.t.} \; \boldsymbol{h}_j(\boldsymbol{y}^k) + \nabla \boldsymbol{h}(\boldsymbol{y}^k)^T \boldsymbol{\sigma}_y = \boldsymbol{0}, \; j = 1, \dots, n_e \tag{4.25b}$$

$$\boldsymbol{g}_j(\boldsymbol{y}^k) + \nabla \boldsymbol{g}(\boldsymbol{y}^k)^T \boldsymbol{\sigma}_y \geq \boldsymbol{0}, \; j = 1, \dots, n_i \tag{4.25c}$$

for the NLP (4.24).

Now the SQP algorithm is defined as follows

Algorithm 4.2.3. (SQP algorithm)

1. Choose a starting point $(\boldsymbol{y}^0,\boldsymbol{\lambda}^0,\boldsymbol{\mu}^0)$.
2. If $(\boldsymbol{y}^k,\boldsymbol{\lambda}^k,\boldsymbol{\mu}^k)$fulfills the KKT conditions: STOP with stationary point $\boldsymbol{y}^k$.
3. Calculate for $\boldsymbol{H}_k = \nabla^2_{\boldsymbol{y}\boldsymbol{y}}L(\boldsymbol{y}^k,\boldsymbol{\lambda}^k,\boldsymbol{\mu}^k)$ the solution of the SQP-subproblem (4.25a)-(4.25c) that lies closest to 0 with the according Lagrange multipliers $\boldsymbol{\lambda}^{k+1}$ and $\boldsymbol{\mu}^{k+1}$ and set $\boldsymbol{y}^{k+1} = \boldsymbol{y}^k + \boldsymbol{\sigma}^k$ and $k \to k+1$. Return to step 2.

Under certain conditions, Q-superlinear and even Q-quadratic convergence can be shown. For the globalization of the SQP algorithm, $\boldsymbol{H}_k$ is defined as randomly chosen positive definite matrix.

Algorithm 4.2.4. (Global SQP algorithm for NLP)
Choose $\alpha \in (0,\frac{1}{2})$ for the Armijo rule. Pick $\rho > 0$ large enough, a start point $(\boldsymbol{y}^0,\boldsymbol{\lambda}^0,\boldsymbol{\mu}^0) \in \mathbb{R}^n \times \mathbb{R}^{n_e} \times \mathbb{R}^{n_i}$ and a symmetric matrix $\boldsymbol{H}_0 \in \mathbb{R}^{n,n}$. For $k = 0,1,\dots$:

1. If $(\boldsymbol{y}^k,\boldsymbol{\lambda}^k,\boldsymbol{\mu}^k)$fulfills the KKT conditions: STOP with stationary point $\boldsymbol{y}^k$.
2. Calculate the solution $\boldsymbol{\sigma}^k$ of the SQP-subproblem (4.25a)-(4.25c) that lies closest to 0 with the according Lagrange multipliers $\boldsymbol{\lambda}^{k+1}$ and $\boldsymbol{\mu}^{k+1}$. If ${\boldsymbol{\sigma}^k}^T\boldsymbol{H}^k\boldsymbol{\sigma}^k \le 0$ modify H^k and return to step 2.
3. Determine the largest $\boldsymbol{\sigma}_k \in \{1,2^{-1},2^{-2},\dots\}$ that fulfills
$$P_{l,\rho}(\boldsymbol{y}^k) - P_{l,\rho}(\boldsymbol{y}^k + \boldsymbol{\alpha}^k\boldsymbol{\sigma}^k) \ge -\gamma\boldsymbol{\sigma}^k(P_{l,\rho})'(\boldsymbol{y}^k,\boldsymbol{\sigma}^k). \tag{4.26}$$
4. Set $\boldsymbol{y}^{k+1} = \boldsymbol{y}^k + \boldsymbol{\alpha}^k\boldsymbol{\sigma}^k$ and define a new symmetric matrix $\boldsymbol{H}^{k+1}$.

For the calculation of the Hessian matrix $\boldsymbol{H}^k = \nabla^2_{\boldsymbol{y}\boldsymbol{y}}L(\boldsymbol{y}^k,\boldsymbol{\lambda}^k,\boldsymbol{\mu}^k)$ the second derivatives of the functions $\Phi,\boldsymbol{h}$ and $\boldsymbol{g}$ are needed. It is suggested to use quasi-Newton updates that fulfill the Quasi-Newton equation.

$$\boldsymbol{H}^{k+1}\boldsymbol{d}^k = \kappa^k \text{ with } \boldsymbol{d}^k := \boldsymbol{y}^{k+1} - \boldsymbol{y}^k,\ \kappa^k := \nabla_y L(\boldsymbol{y}^{k+1},\boldsymbol{\lambda}^k,\boldsymbol{\mu}^k) - \nabla_x L(\boldsymbol{y}^k,\boldsymbol{\lambda}^k,\boldsymbol{\mu}^k). \tag{4.27}$$

A commonly used Quasi-Newton update is the following Broyden-Fletcher-Goldfarb-Shanno (BFGS) update

$$\boldsymbol{H}^{k+1} = \boldsymbol{H}^{k+1}_{BFGS} := \boldsymbol{H}^k + \frac{\kappa^k {\kappa^k}^T}{{\kappa^k}^T\boldsymbol{d}^k} - \frac{\boldsymbol{H}^k\boldsymbol{d}^k(\boldsymbol{H}^k\boldsymbol{d}^k)^T}{{\boldsymbol{d}^k}^T\boldsymbol{H}^k\boldsymbol{d}^k} =: \Phi^{BFGS}(\boldsymbol{H}^k,\boldsymbol{d}^k,\kappa^k). \tag{4.28}$$

Powell suggests to use the damped version

$$\boldsymbol{H}^{k+1} = \boldsymbol{H}^{k+1}_{BFGS} =: \Phi^{BFGS}(\boldsymbol{H}^k,\boldsymbol{d}^k,\kappa^k_{mod}), \tag{4.29}$$

where

$$\kappa^k_{mod} = \theta^k\kappa^k + (1-\theta^k)\boldsymbol{H}^k\boldsymbol{d}^k \tag{4.30}$$

$$\text{with } \theta^k = \begin{cases} 1 & \text{if } {\boldsymbol{d}^k}^T\kappa^k \ge \eta {\boldsymbol{d}^k}^T\boldsymbol{H}^k\boldsymbol{d}^k, \\ \frac{(1-\eta){\boldsymbol{d}^k}^T\boldsymbol{H}^k\boldsymbol{d}^k}{{\boldsymbol{d}^k}^T\boldsymbol{H}^k\boldsymbol{d}^k - {\boldsymbol{d}^k}^T\kappa^k} & \text{else .} \end{cases} \tag{4.31}$$

Then ${\boldsymbol{d}^k}^T\kappa^k_{mod} > 0$ holds and therefore $\boldsymbol{H}^{k+1}$ is positive definite. With this modification of the BFGS update, Q-superlinear convergence of the global SQP algorithm can be shown, see [146].

4.2.5 Condensing Algorithm

Note, that the quadratic subproblem (4.25a)-(4.25c) is much larger for a multiple shooting than for a single shooting algorithms. However, by the exploration of its sparse block structure, the solution effort for the multiple shooting problem can be reduced to the same order as for the problem resulting from single shooting using the following condensing algorithm.

Using the explicit form of the linearized matching conditions

$$\boldsymbol{\sigma}_s^{j+1} = \frac{\delta \boldsymbol{x}(t_{j+1}, \boldsymbol{s}_j, \boldsymbol{\varrho}_j)}{\delta \boldsymbol{s}_j} \boldsymbol{\sigma}_s^j + \frac{\delta \boldsymbol{s}(t_{j+1}, \boldsymbol{s}_j, \boldsymbol{\varrho}_j)}{\delta \boldsymbol{\varrho}_j} \boldsymbol{\sigma}_\varrho^j + h_j(\boldsymbol{s}_{j+1}, \boldsymbol{s}_j, \boldsymbol{\varrho}_j) \tag{4.32}$$

permits a recursive equivalence transformation of the quadratic subproblem (4.25a)-(4.25c) to the condensed problem, eliminating $\boldsymbol{\sigma}_s^1, \ldots, \boldsymbol{\sigma}_s^{n_s}$, dropping the iteration index k,

$$\min_{\boldsymbol{\sigma}_s^0, \boldsymbol{\sigma}_\varrho} \; b^T \begin{pmatrix} \boldsymbol{\sigma}_s^0 \\ \boldsymbol{\sigma}_\varrho \end{pmatrix} + \frac{1}{2} \begin{pmatrix} \boldsymbol{\sigma}_s^0 \\ \boldsymbol{\sigma}_\varrho \end{pmatrix}^T B \begin{pmatrix} \boldsymbol{\sigma}_s^0 \\ \boldsymbol{\sigma}_\varrho \end{pmatrix} \tag{4.33a}$$

$$\text{s.t. } \boldsymbol{c} + \boldsymbol{C}_s \boldsymbol{\sigma}_s^0 + \boldsymbol{C}_\varrho \boldsymbol{\sigma}_\varrho = 0, \tag{4.33b}$$

$$\boldsymbol{d} + \boldsymbol{D}_s \boldsymbol{\sigma}_s^0 + D_\varrho \boldsymbol{\sigma}_\varrho \geq 0, \tag{4.33c}$$

where $\boldsymbol{b}, \boldsymbol{B}, \boldsymbol{C}_s, \boldsymbol{C}_\varrho, \boldsymbol{D}_s, \boldsymbol{D}_\varrho, \boldsymbol{c}, \boldsymbol{d}$ can be computed in a backward recursion. The much smaller and dense problem (4.33a)-(4.33c) can be solved by a standard QP-solver, e.g. QPOPT [51]. The remaining increments $s_j, j = 1 \ldots n_s$, and the Lagrange multipliers of the matching conditions, needed for the calculation of the Hessian update, can be computed by two recursions. Let $(\Delta s_0, \Delta \varrho)$ denote the solution of the condensed problem (4.33a)-(4.33c), and (μ_1, μ_2) the Lagrange multipliers corresponding to the constraints (4.33b) and (4.33c). With the linear matching condition (4.32) the KKT-Point (σ_y, λ) is completed by Δs_j in a forward recursion for $j = 1 \ldots m$ and $\lambda_{1,j} = -\frac{\delta Q}{\delta \Delta s_{j+1}} + \frac{\delta r(s_0, s_m)}{\delta s_m}$, where $\lambda_{1,m}$ are the multipliers of the condensed problem associated with the boundary conditions.

Chapter 5

Reconstruction of Human Push Recovery Motion During Walking

In this chapter perturbed human walking motions from reference data are reconstructed and analyzed. We assume that the joint torques are larger, the higher the perturbation is located at the spine of the subject and the stronger the perturbation. For this analysis the dynamics of the human described in Section 3.1 is included in the optimal control problem presented in Chapter 4 with joint torque derivatives as control. The model is fitted to reference data by defining an objective function, that minimizes the distance from the model variables to reference data. Figure 5.1 shows the motion for the model (colored) and the the reference data (white). This approach is presented in [158] using joint torques as controls.

First, the optimal control problem is specified. Then the numerical results including an intensive analysis of the joint angles and torques as well as other parameters such as ground reaction forces, the position of the center of mass as well as the potential and kinetic energies are presented. The motions from both data sets from Sections 2.4 are included in the studies.

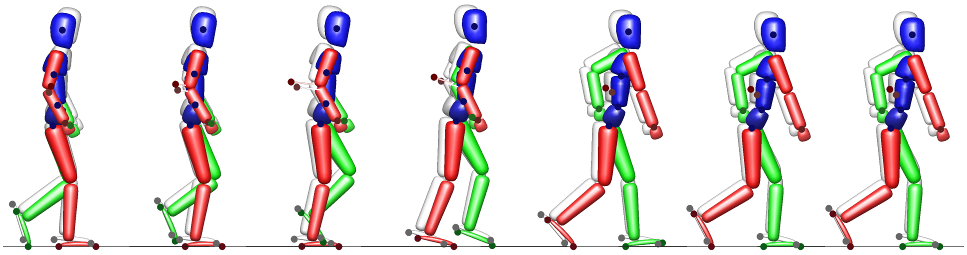

Figure 5.1: Image series of the reconstructed motion (colored in the front) and the reference data (white in the back) for a motion perturbed at the middle trunk. The line at the back of the model indicates the perturbation strength. The longer the line, the stronger the perturbation.

5.1 Optimal Control Problem Formulation

To compute the internal joint torques for perturbed human walking motions, an OCP of the form (4.1a-f) consisting of 45 state variables (joint angles, joint angle velocities and active joint torques) and 13 control variables (active joint torque derivatives) is set up.

An objective function for equation (4.1a), that minimizes the distance between the joint angles from the reference data and the joint angles from the model, in the following least-squares formulation is used:

$$\phi[\boldsymbol{x},\boldsymbol{u},\boldsymbol{p},\boldsymbol{s}] = \frac{1}{n_{\tilde{x}} n_{\tilde{t}}} \sum_{k=0}^{n_{\tilde{x}}} \sigma_k \sum_{l=0}^{n_{\tilde{t}}-1} (M(x_k(t_l)) - \tilde{x}_{k,l})^2, \tag{5.1}$$

where M defines a function that projects the states vector to the form of the reference data. In detail, we gain an OCP with $x : \mathcal{I} \to \mathbb{R}^{n_x}$ representing the differential states defined by

$$\boldsymbol{x}(t) := (\boldsymbol{q}(t), \dot{\boldsymbol{q}}(t), \tilde{\boldsymbol{\tau}}_{\boldsymbol{a}})^T, \tag{5.2}$$

where q defines the 16 generalized position variables, meaning mainly the angles of the joints of the human model and the position and orientation of the pelvis, see Section 3.1, $\dot{q}$ the according generalized velocity variables and $\tilde{\tau}_a$ the actuated internal joint torques. The controls are represented by $u : \mathcal{I} \to \mathbb{R}^{n_u}$, where n_u describes the number of actuated joints and

$$\boldsymbol{u}(t) := \dot{\tilde{\boldsymbol{\tau}}}_{\boldsymbol{a}}(t) \tag{5.3}$$

describes the derivatives of the actuated internal joint torques. Here the controls are discretized linearly on the time intervals, see Section 4.2.1. The transition times $t_1, \ldots, t_{n_{ph}}$ are fixed to values suitable to the reference data. In this motion reconstruction formulation, we do not have any parameters for the optimization.

5.2 Numerical Results

The optimal control problem from Section 5.1 is solved for motions from dataset A and B, described in detail in Section 2.4. Dataset A includes four unperturbed steps and five perturbed steps, dataset B includes 23 unperturbed steps and six perturbed steps. In some plots and tables, only the first two unperturbed steps from dataset A are considered. For dataset B the average of the unperturbed motions is calculated. In this chapter, the joint torques, joint angles, angular momentum, ground reaction forces and the center of mass positions for the perturbed motions are compared to the unperturbed motions. Before analyzing the resulting joint torques and other parameters calculated by derivatives of joint torques as controls for dataset A and B, it is proofed that the results meet the reference data well.

5.2.1 Error Analysis

In Table 5.1 the root mean squared errors of the resulting motions from the two data sets are shown. We calculate the root-mean squared (RMS) error for translational and rotational DoF separately

$$err = \sqrt{\frac{1}{n_q m}\left[\sum_{k\in C}\sum_{j=0}^{m}(q_k(t_j)-\tilde{q}_k(t_j))^2\right]}, \tag{5.4}$$

where m is the total number of multiple shooting nodes of the optimal control problem and C is the set of indexes belonging to the translational or rotational DoF. The mean errors of all motions from the datasets are 0.033 m and 0.0711 rad for dataset A and 0.0352 m and 0.045 rad for data set B. Therefore the solutions with linear joint torques derivatives as controls represent the reference data as good as the solution with constant joint torques as controls for dataset A and also for dataset B the resulting motions suit the reference data very well. Figure 5.2 and 5.3 show the differences of the joint angles from reference data (dotted lines) and the solution calculated with the derivatives of joint torques as controls (solid lines) for dataset A and B. As for all figures in this chapter, the perturbed motions are defined by colors: green for pushes at the pelvis, blue for pushes at the middle trunk and red for pushes at the upper trunk. The unperturbed motions of dataset A are indicated by gray lines (again dotted for the reference data, solid for the solution). The average of the unperturbed motions from dataset B is indicated by a thick black line. For this dataset, only the solution is plotted. The solution represents the reference data well in nearly all joints. Only the pelvis-z position, as well as the ankle joints of the solution, differ obviously from the reference data. This is due to the case that for the solution, it is demanded to stand on the ground while for the reference data, the feet sometimes fly and sometimes they stick in the ground.

Table 5.1: The rotational and translational RMS errors of the reconstructed motions to reference data for dataset A (upper rows) and B (lower rows).

	NoPushA1	**NoPushA2**	**PelvisA**	**MiddleA1**	**MiddleA2**	**UpperA1**	**UpperA2**	**mean**
Trans	0.0362	0.0305	0.0303	0.0335	0.0213	0.0345	0.0448	0.0330
Rot	0.0604	0.0649	0.0642	0.0641	0.0801	0.0765	0.0771	0.0711
	NoPushB	**PelvisB1**	**PelvisB2**	**MiddleB1**	**MiddleB2**	**UpperB1**	**UpperB2**	
Trans	0.0362	0.0319	0.0332	0.0362	0.0357	0.0299	0.0445	0.0352
Rot	0.0604	0.0416	0.0430	0.0445	0.0415	0.0529	0.0463	0.0450

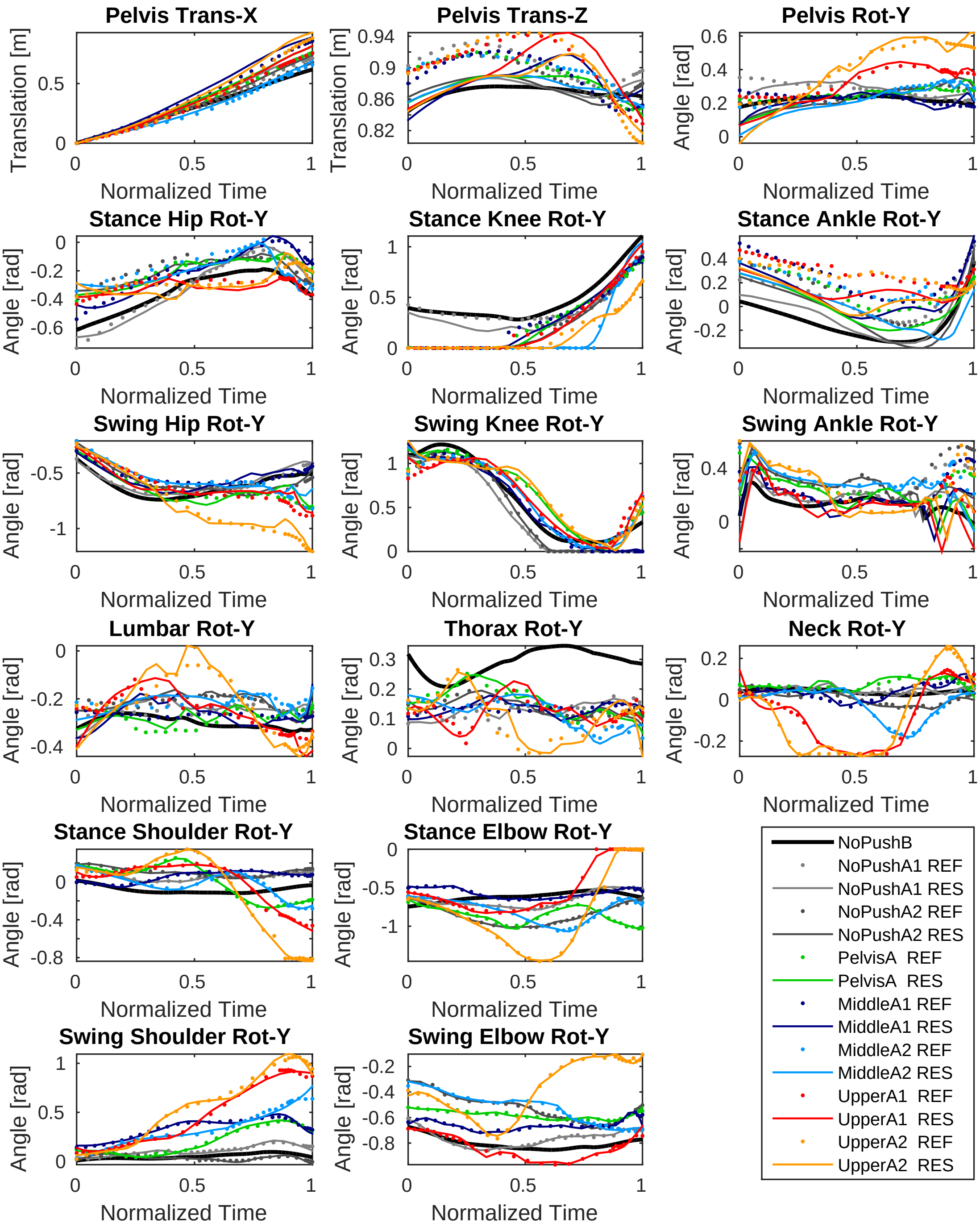

Figure 5.2: The translation and rotation of the pelvis and the joint angles of the reference data (dotted lines) and the model (solid lines) for seven analyzed motions from dataset A. The thick black line indicates the average of the unperturbed motions from dataset B.

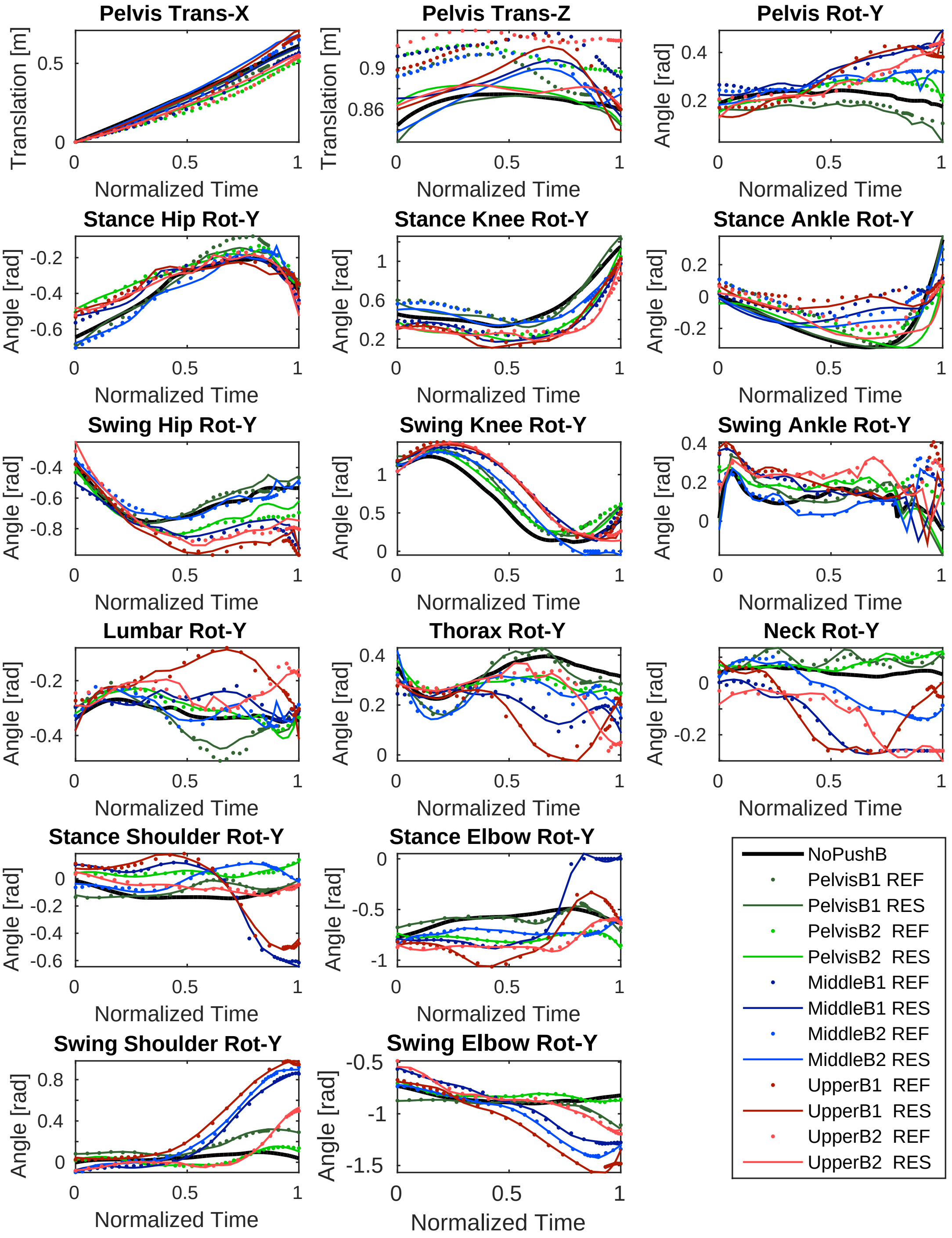

Figure 5.3: Translation of the pelvis and joint angles of the reference data (dotted lines) and the model (solid lines) for the analyzed motions from dataset B. The thick black line indicates the average of the unperturbed motions from dataset B.

5.2.2 Joint Torques and Joint Angles

First, the differences in the mean joint torques between the two datasets are compared. In Figure 5.4 the mean joint torques for the motions from both datasets are shown. The average of the unperturbed motions is nearly the same for both datasets which makes it reasonable to include data from both datasets in our analysis. The perturbed motions are ordered by strength of the perturbation (weakest perturbation left) for each perturbation location (pelvis, middle and upper trunk). For the perturbations at the middle trunk and at the pelvis the mean joint torques are all of a similar magnitude. For the perturbations at the upper trunk the mean joint torques are larger for stronger pushes in both datasets, but not in between the datasets. The mean joint torques are larger for dataset A compared to dataset B. This could be because the subject from dataset A is taller and therefore, a push applied at the upper body has a higher influence on the motion.

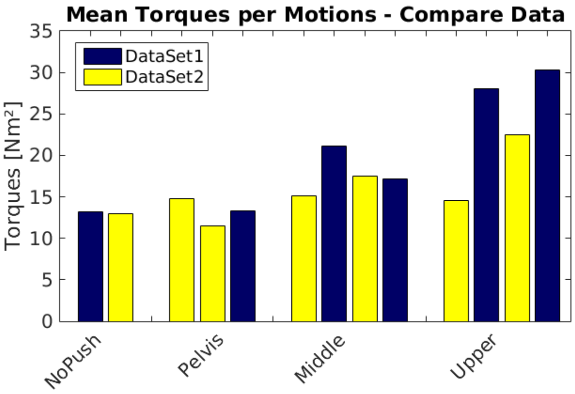

Figure 5.4: Comparison of the mean joint torques for the motions from the two datasets.

Second, we regard the mean joint torques over joints for the different kinds of perturbations calculated for the data from both datasets. To simplify the notation, in the following, we will only write torques meaning the mean joint torques.

First, the motions are grouped by the position of the point at the spine where the push is applied: 25 unperturbed motions, three pushes at the pelvis, four at the middle and four at the upper trunk, see Figure 5.5. The unperturbed motions result in the lowest torques for most of the joints. Only in both hip joints, the swing ankle and the lumbar the unperturbed motions do not result in the lowest joint torques. Nevertheless, in the hip joints and the lumbar, the lowest push points result in weakest torques and the highest push points in the largest torques. This also holds for all joints in the arms, body, and legs despite the ankle joints. While in the stance ankle the order is the opposite (largest torque for lowest push point, smallest torque for highest push point), in the swing ankle the perturbation at the middle trunk results in the largest torque and the perturbations at the upper trunk in the lowest torque.

Next, the motions are grouped by the strengths of the perturbations: 25 unperturbed motions, three pushes weaker than 150N, four between 150 and 200N and four more than 200N), see Figure 5.6. Again, the unperturbed motions result in the lowest torques for most joints. Only in both ankle joints, the unperturbed motions do not result in the lowest joint torques. While in the stance ankle the strongest pushes result in the lowest torques, and the middle pushes in the strongest torques, the middle pushes result in the lowest torques for the swing ankle and the weakest pushes in the strongest torques. The same holds for the swing knee. But here no significant difference in torques for the different strengths can be observed. Also for the lumbar and the neck joint the middle pushes result in the largest torques, but the weakest pushes result in the smallest torques. For all other joints stronger pushes result in larger joint torques. Therefore, the assumption “the stronger the perturbation and the higher the push point is located at the spine, the larger the torques in the joints” holds.

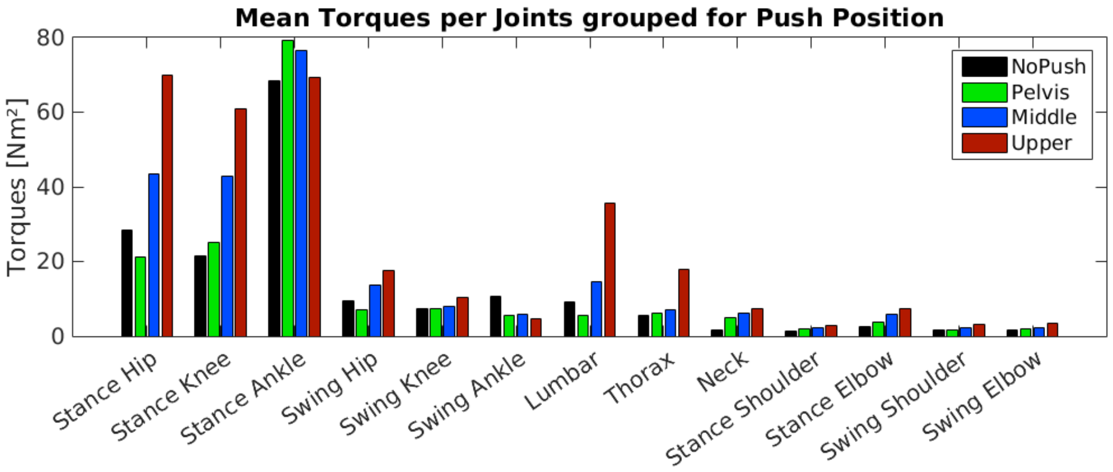

Figure 5.5: Comparison of the mean joint torques per joint for the different perturbations described by different colors (dark blue: unperturbed, light blue: pelvis, green: middle, yellow: upper).

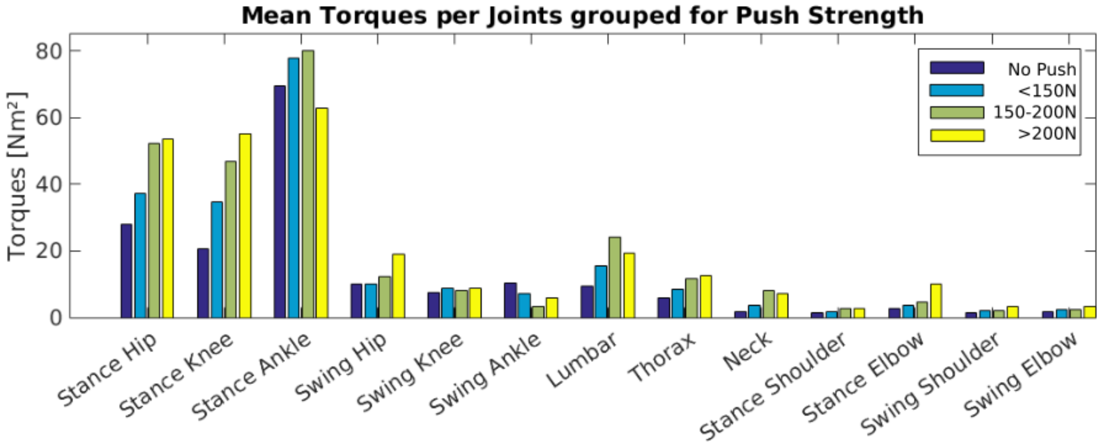

Figure 5.6: Comparison of the mean joint torques per joint for the different push strengths described by different colors (dark blue: unperturbed, light blue: weak pushes up to 150 N, green: pushes between 150 and 200 N, yellow: strong pushes more than 200 N).

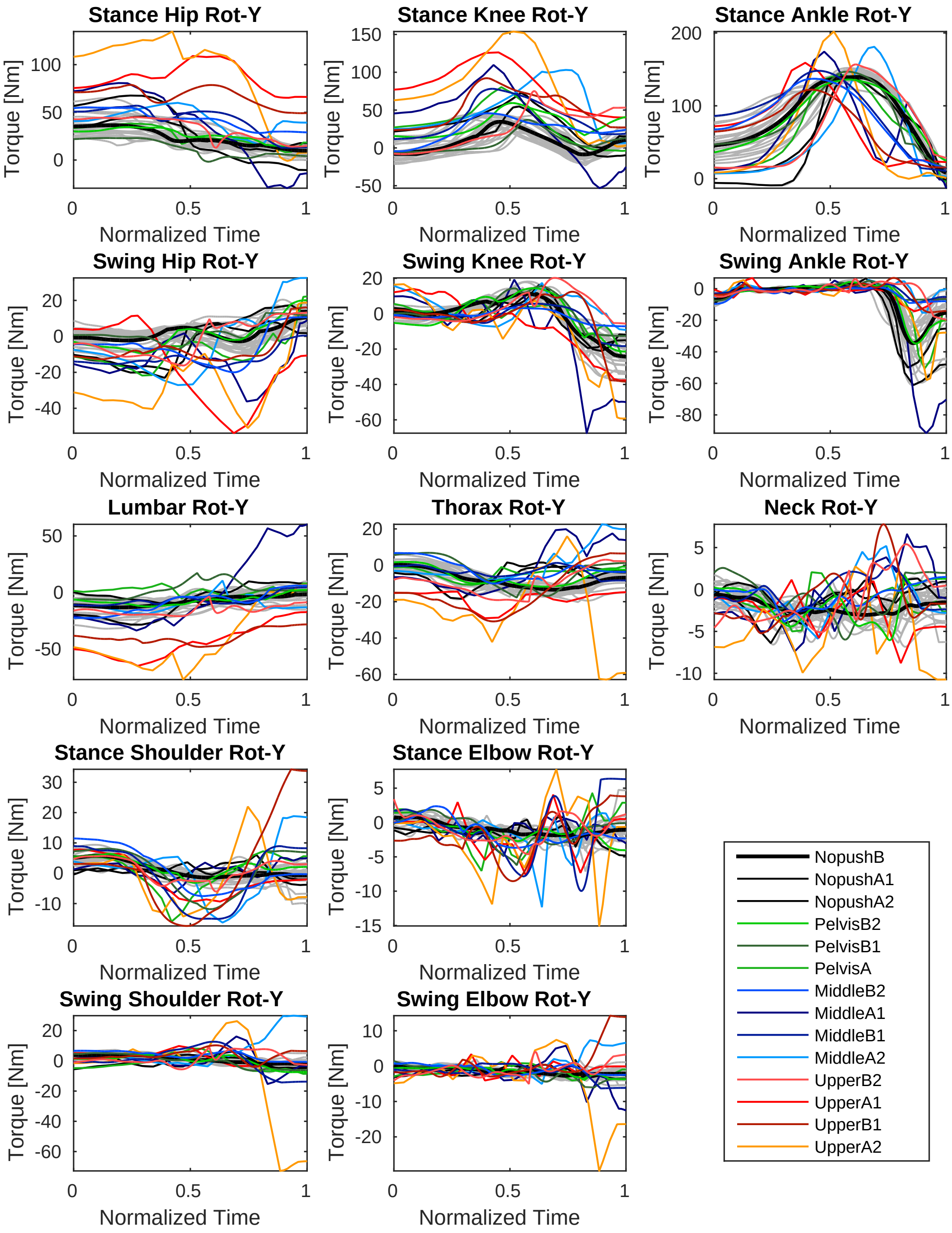

Figure 5.7: Internal torques in the joints of the model for motions from dataset A and B calculated by joint torque derivatives as control. The different colors represent the different perturbed motions. The unperturbed motions are marked by gray lines and the thick black line indicates the average of all regarded normal motions.

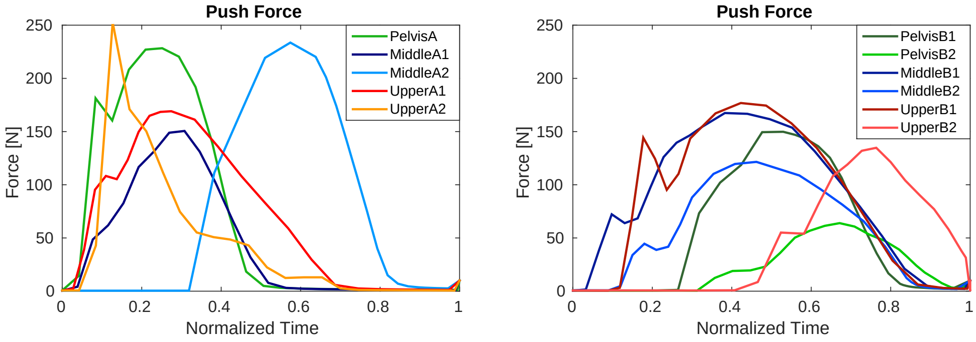

Figure 5.8: Strengths and profiles of the applied push forces, at different height of the spine for dataset A and B, normalized over end time (left: dataset A, right: dataset B).

Figure 5.8 shows the normalized push forces for dataset A (left) and dataset B (right). The normalization by the end time of the whole step enables to compare the data from the perturbed and unperturbed motions. Without a time normalization, it is possible to compare the end times of the different motions but not the specific trajectory properties for all joints.

Figure 5.7 shows the joint torques of the human model for dataset A and B with normalized time disregarding the time phases. The colored lines indicate the different perturbations, the gray lines the unperturbed motions. In most of the joints, the perturbed motions result in larger joint torques than the unperturbed motions. For the joints in the body as well as for the stance hip and knee and the swing hip, the joint torques are larger, the higher the point at the spine where the perturbation is applied. For all joints in the arms as well as for the stance ankle and the thorax, the joint torques for the two motions in the middle and upper trunk with the stronger perturbations (MiddleA2 and UpperA2) are largest. For the MiddleA2 and UpperB2 motions, the push starts later (and also the peak of the perturbation is later in time) than for the other motions, see Figure 5.8. For these motions also the joint torque increase in the stance knee and ankle, as well as the stance shoulder, occur later than for the other motions. Regarding the joint torques in the legs normalized for each phase time in Figure 5.10 this cannot be observed. Therefore it is important to take the different kinds of normalization into account.

In the previous plots, the motions are normalized by the end time. Figure 5.8 shows the forces for the perturbed motions of both datasets (left: dataset A, right: dataset B) normalized by the end time. In Figure 5.9 the forces for the two datasets are normalized for each gait phase. In the following plots, the motions are normalized by phase times. The phases are indicated by vertical lines. The analysis of these plots is split for the legs, the arms and the body joints including the neck. For some plots, the values are constant over a whole phase. Note, that for some motions this is due to very short phases (time = 0). In the plots, the perturbed steps are again indicated by solid colored lines. The average of the normal motions is plotted by a thick black line. The minimum and maximum of the unperturbed steps are plotted as a gray area. The colored lines in the bottom row indicate the start and the end time of the perturbation.

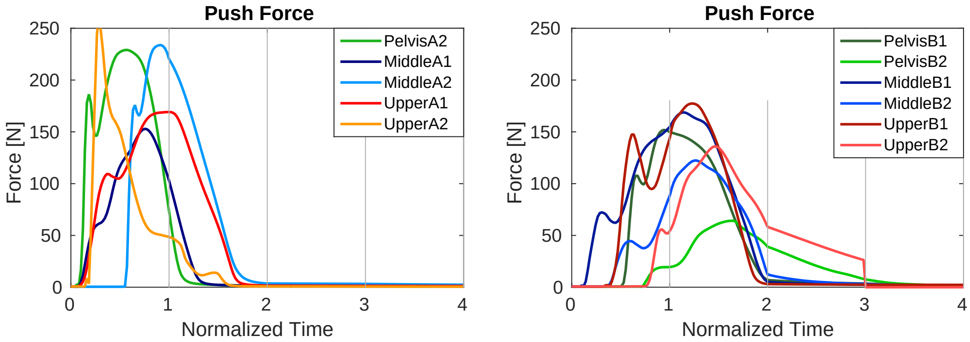

Figure 5.9: Strengths and profiles of the applied push forces, at different height of the spine for dataset A and B, normalized over time per phase (left: dataset A, right: dataset B).

Legs

The torques and joint angles of the legs during perturbed motions are taken into account, shown in Figure 5.10. The joint torques for the stance hip are higher during the first and second phase for the motions perturbed at the upper and middle trunk than for the unperturbed motions but of a similar shape. For the stance knee, these motions result in higher joint torques only during the second phase. For some motions perturbed at the upper trunk, the joint angles of the swing hip vary from the range of the unperturbed motions. The torques in the swing ankle are smaller for some push motions in the last two phases. Overall, comparing the joint angles of the perturbed motions and the unperturbed motions, there is not much difference.

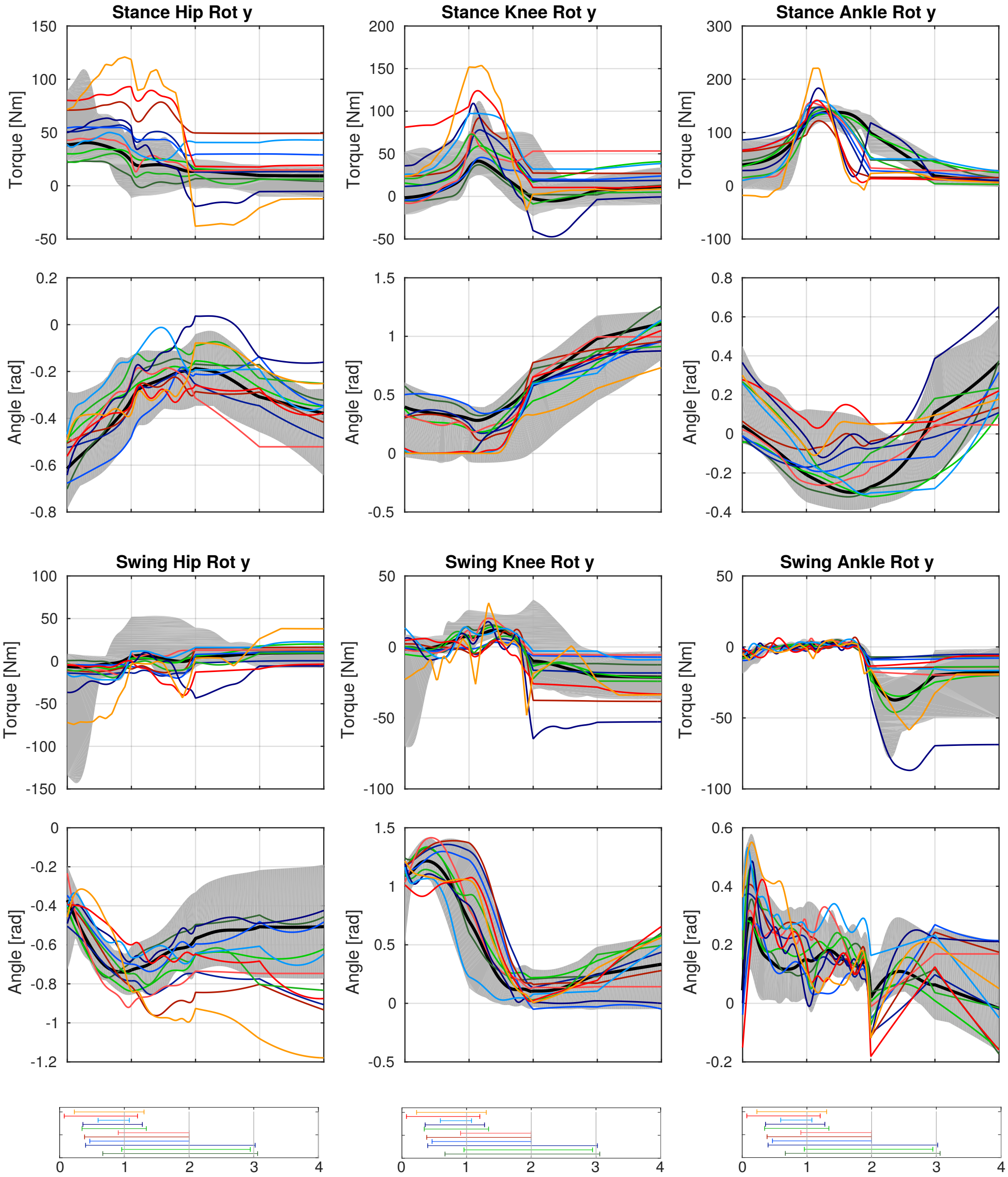

Figure 5.10: Averages of the joint torques and joint angles of the stance (upper) and swing (lower) legs for unperturbed steps (thick black line) and for perturbed steps (dashed lines) of the different push motions (colors). The colored lines in the bottom row indicate the start and end time of the perturbation.

Body

Here, the joint torques and joint angles of the body joints (neck, thorax and lumbar) are analyzed, see Figure 5.11. The lumbar and the thorax joint torques and joint angles are similar to the ones of the normal motions for most perturbed motions. The joint torques in the lumbar vary from the normal range for the upper body perturbations. A change in the neck joint angle can be observed when the push occurs for all motions from both datasets except for the motions perturbed at the pelvis. In Section 6.1 the reason for this observation is discussed.

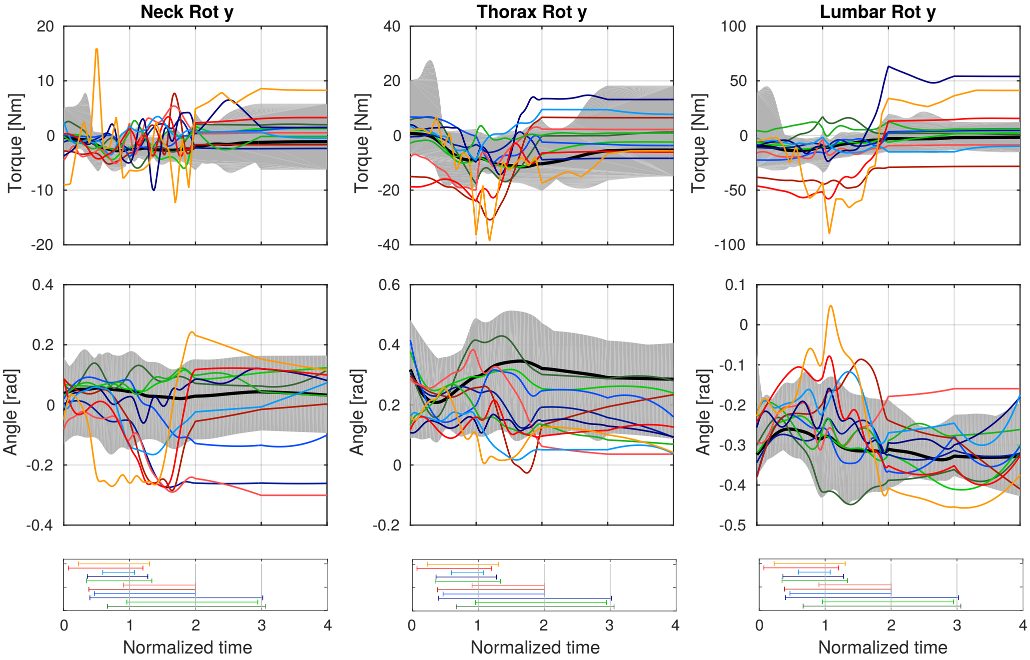

Figure 5.11: Averages of the joint torques and the joint angles of the body for unperturbed steps (thick black line) and for perturbed steps (dashed lines) of the different push motions (colors). The colored lines in the bottom row indicate the start and end time of the perturbation.

Arms

Next, the torques and joint angles of the arms shown in Figure 5.12 are analyzed, see. Stance and swing arm are named according to the stance and swing leg. For the stronger pushes in the upper and middle trunk, the joint angles of the stance shoulder differs a lot from the normal motions shortly after the perturbation start. Interestingly, this happens, the at the time, when the joint torques in this joint are at their minimum, see Section 1.3 for detailed analysis.

In the swing shoulder, all motions except the smaller push in the pelvis of dataset B (PelvisB1) show a significant difference to the normal range in the last three phases in the joint angle and also in the joint torques. For the unperturbed steps, the swing shoulder joint angle remains nearly zero for both datasets. Again the deviation appears in the second phase, but here it can not be seen clearly that the joint angle changes after the joint torques. In the swing elbow, the joint angles change before or without a significant change in the joint torques. Here the change in the joint angles could be caused by the change in the shoulder joint angles.

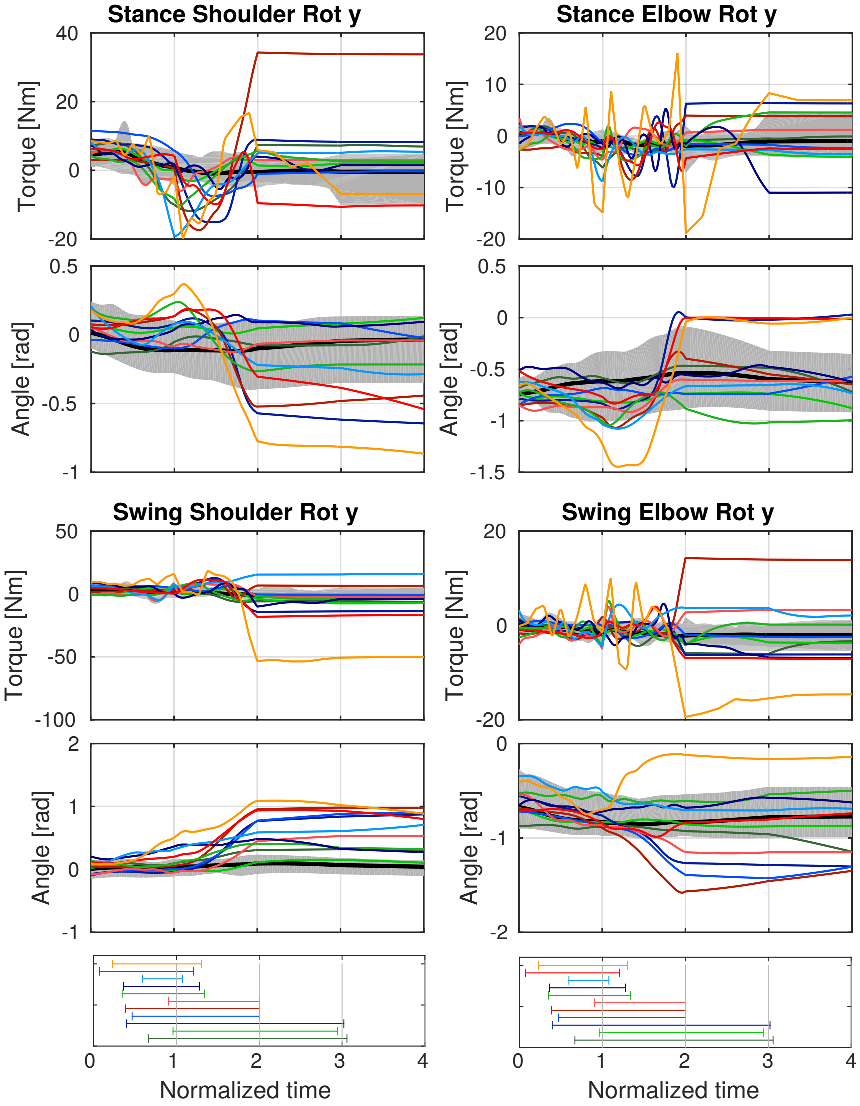

Figure 5.12: Averages of the joint torques and the joint angles of the arms for unperturbed steps (thick black line) and for perturbed steps (dashed lines) of the different push motions (colors). The colored triangles indicate the start of the perturbation. The colored lines in the bottom row indicate the start and end time of the perturbation.

5.2.3 Center of Mass

In this part, we concentrate on the analysis of the motion of the center of mass (CoM). Regarding the translation of the center of mass in the x-direction, the motion is faster for most of the perturbed motions compared to the unperturbed motions. The translations for the motions perturbed in the pelvis do not differ a lot from the normal motions. The translation in the z-direction is taller for most of the perturbed motions

5.2.4 Angular Momentum

In this section, we consider the angular momentum about the center of mass. Figure 5.13 (bottom plot) shows the angular momentum for the different perturbed motions. The angular momentum of most of the perturbed motions does not differ a lot from the unperturbed motions. Only the two motions perturbed at the upper body from dataset A differ significantly at the end of phase two from the range of unperturbed motions and the motions perturbed at the pelvis from dataset B differ in the last two phases.

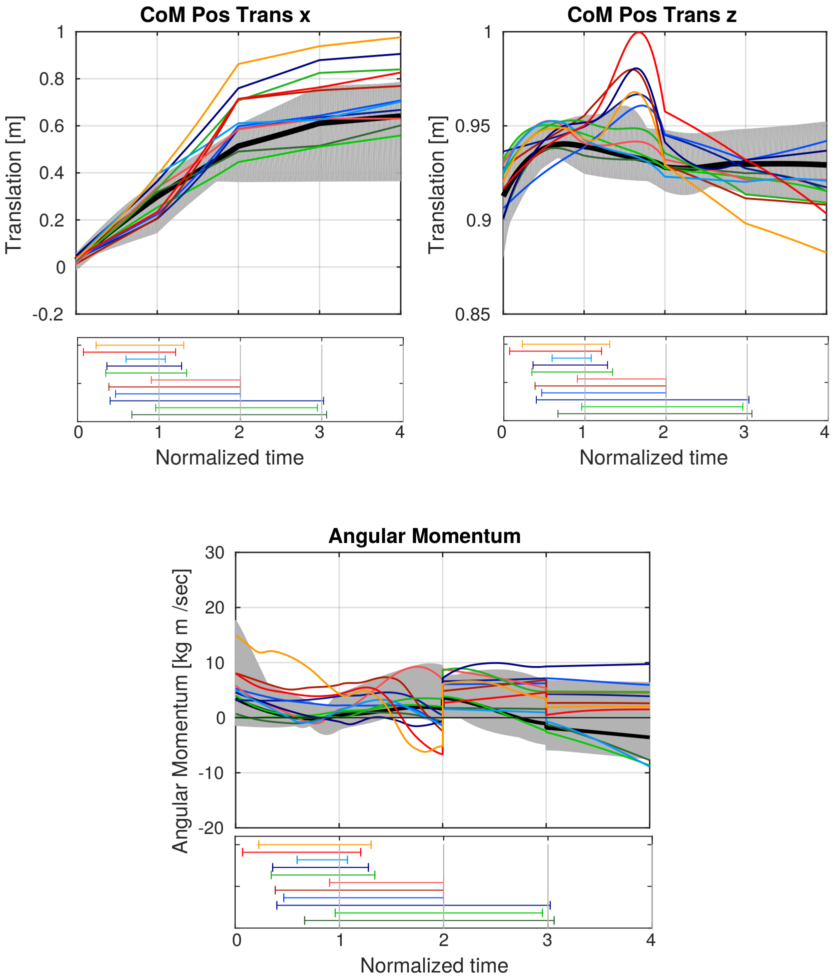

Figure 5.13: Average of the position of the center of mass (upper) and of the angular momentum (button) of unperturbed steps (thick black line and gray area) and of perturbed steps (solid lines) of eleven motions from datasets A and B. The different colors describe the different motions (green: Pelvis, blue: Middle trunk, red: Upper trunk). The colored lines in the bottom row indicate the start and end time of the perturbation.

5.2.5 Ground Reaction Force

Here, we analyze the ground reaction forces (GRF) for the perturbed motions and the unperturbed motions. Again the ground reaction forces for the perturbation occurring at the pelvis do not differ a lot from the unperturbed motions, see Figure 5.14 upper row. The general shape of the ground reaction force plots for the perturbed motions is the same as for the unperturbed motions mainly the phase timing differs.

5.2.6 Energy

Finally, we compare the kinetic and the potential energies for perturbed steps to steps without perturbation, see Figure 5.14 bottom row. For the perturbation at the middle and upper trunk, the potential energy differs a lot from the unperturbed motions during the second phase. For the perturbed motions, the kinetic energy rises, when the push occurs until the end of the second phase and remains at this level for the last two phases. The kinetic energy is higher, the higher the point at the spine is located where the perturbation is applied. The kinetic energy also increases for an increase of perturbation strength.

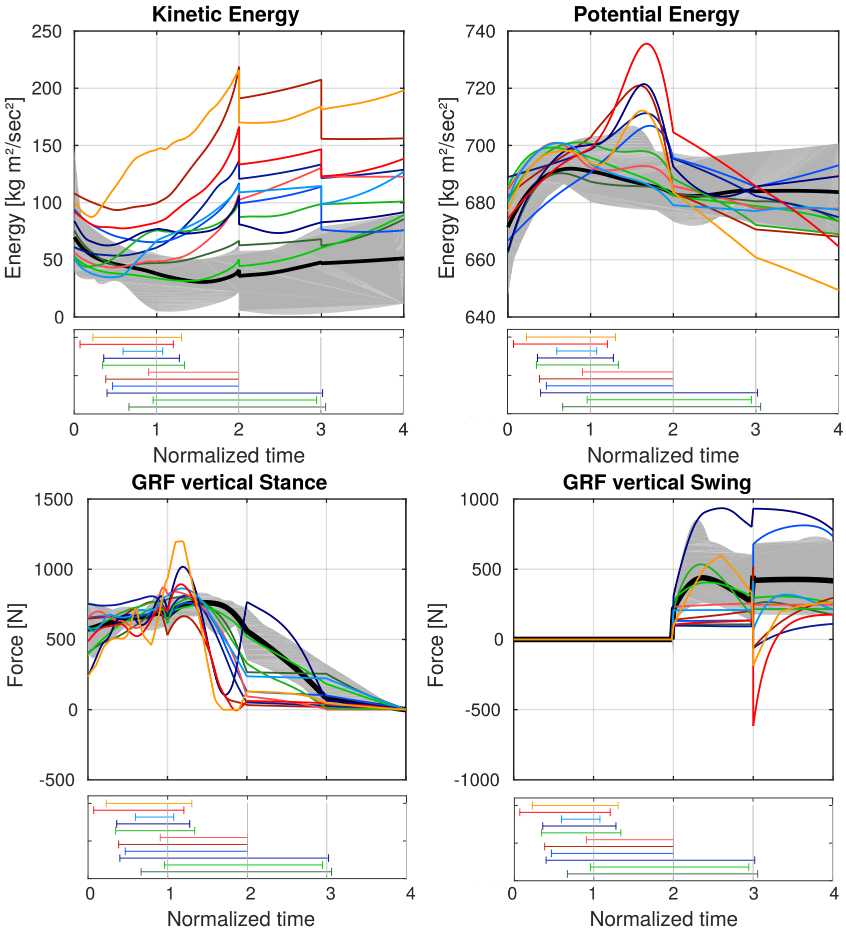

Figure 5.14: Average of the ground reaction force (upper row) of the stance leg (left) and the swing leg (right) as well as of the potential (bottom row, left) and the kinetic energy (bottom row, right) of unperturbed steps (thick black line and gray area) and of perturbed steps (solid lines) of eleven motions from dataset A and B. The different colors stand for the different motions (green: Pelvis, blue: Middle trunk, red: Upper trunk). The colored lines in the bottom row indicate the start and end time of the perturbation.

5.3 Summary

The observations in this chapter can be summarized as follows:

- The motions resulting from the reconstruction calculation represent the reference data well.
- For all joints but the ankle joints, the perturbations at the pelvis result in the lowest joint torques.
- Higher located perturbations result in larger joint torques.
- Stronger perturbations result in larger joint torques
- Angular momentum and ground reaction forces, as well as the center of mass of the perturbed motions, do not differ a lot from the unperturbed motions.
- Kinetic energy is larger the higher the push point is located at the spine.

Chapter 6

Sensing of Perturbation During Human Walking

To get a better understanding of the human push recovery motions, the sensing of the perturbation is essential. Also in the realization of push recovery motions for robots or prostheses, the sensing of the perturbation is a central problem. To be able to react to the perturbation, first, it has to be detected. The goal of this chapter is to determine how humans sense perturbations during walking motions to be able to mainly answer the following questions:

- Which of the human senses gives critical information to trigger a recovery motion?
- Which types of senses should be used in (bio-inspired) robots?

To this end, we compute hypothetical sensor data that might be used to detect a perturbation. The main outcomes from the previous Chapter 5 are further analyzed. In addition, the presented method is used to calculate additional relevant model data. Our results are generated using a simplified human model as described in Chapter 3.1 which allows us to analyze just the exact signals and outcome without taking the detailed internal process into account. We do not investigate the sensitivity of the exact reaction. Our analysis is based on the brought trajectories of the data, independent of the influence of the sensor properties to the quality of the signals. We can also neglect the influence of learning due to repeating a task because the trial set for each subject is limited. To be able to compare the perturbed and unperturbed walking motions, the trajectories are normalized in time for each phase. The necessity of this normalization is described in the previous Chapter 5. Only in the last part, we use not normalized trajectories for the analysis of the reaction times, meaning the time delay from sensory stimulus from the perturbation until an observable reaction motion.

6.1 Analysis of Sensory Influences

In Chapter 1 senses and reflexes relevant for balancing posture and the sensing of a perturbation during human walking motions are described. Probably the most relevant sensory systems in the scope of balancing posture are

- the somatosensory system - that detects the constellation of the joints towards each other (proprioception) and includes the sense of touch, which is capable of sensing the force at the push point,
- the vestibular system - that detects variation in balance,
- and vision - that is important to stabilize posture and remain in balance.

In our studies, pushes from the back during walking motions are analyzed. The perturbation cannot be seen or heard in advance. Therefore vision and the audible system are not relevant for predicting the perturbation. The subject was able to hear perturbation only at the point in time when the pushing device touches its surface. As our model exists only of rigid segments, the audible system cannot be displayed. Nevertheless, the touch and the applied force of the pushing device on the surface of the subject can be sensed by the somatosensory system. In our case, the model “knows” the applied force. As a mechanical reaction, joint angles might be different from the unperturbed motion. The ability of proprioception detects theses changes, indicating a perturbation. The somatosensory system is represented by the joint angles and joint torques already analyzed in the previous section. In this section, first, the changes of joint angles and joint torques in the legs, the arms, the neck, and the body will be analyzed. Second, it is analyzed, if a change in head orientation can be sensed to investigate the influence of vision and the vestibular system in the perturbation detection.

6.1.1 Somatosensory System

The somatosensory input can be represented by joint torques and joint angles in our model. In the previous Chapter 5, we already gave an overview of these data. Here, these observations and their influence on sensing a perturbation are presented in more detail.

Body

Here, the orientations of the three torso parts and the head are analyzed, plotted in Figure 6.1 (left: dataset A, right: dataset B). Regarding the right plots from dataset B, the following results are observed. For most of the motions, the head, the belly and the pelvis orientations for the perturbed motions differ from the normal motions, while the chest orientation differs only for the stronger pelvis perturbation. Regarding human robots, often the sensor of balance is located in the chest. The previous observation shows that with a balance sensor located in the chest, the perturbation would not be sensed for most cases. Placing additional balance sensors in the head, pelvis, and belly would give more accurate information about the perturbation of balance and allows for a faster and more specific reaction. Regarding now the results for dataset A (left plots), the orientations remain in the gray area for most of the motions except for the motions that are perturbed in the upper trunk for all torso parts as well as for the head. Therefore, the observation from dataset B cannot be proofed. It could now be argued why the observation holds for dataset B but not for dataset A. The following arguments could be the reason for this difference: First of all the subject from dataset A is much smaller than the subject from dataset B which could result in the difference in the joint torques. Second, the perturbations in dataset B remain for longer and are weaker than the ones in dataset A. This could also have an influence on the resulting joint torques. A larger set of perturbation has to be analyzed before generalizing this statement.

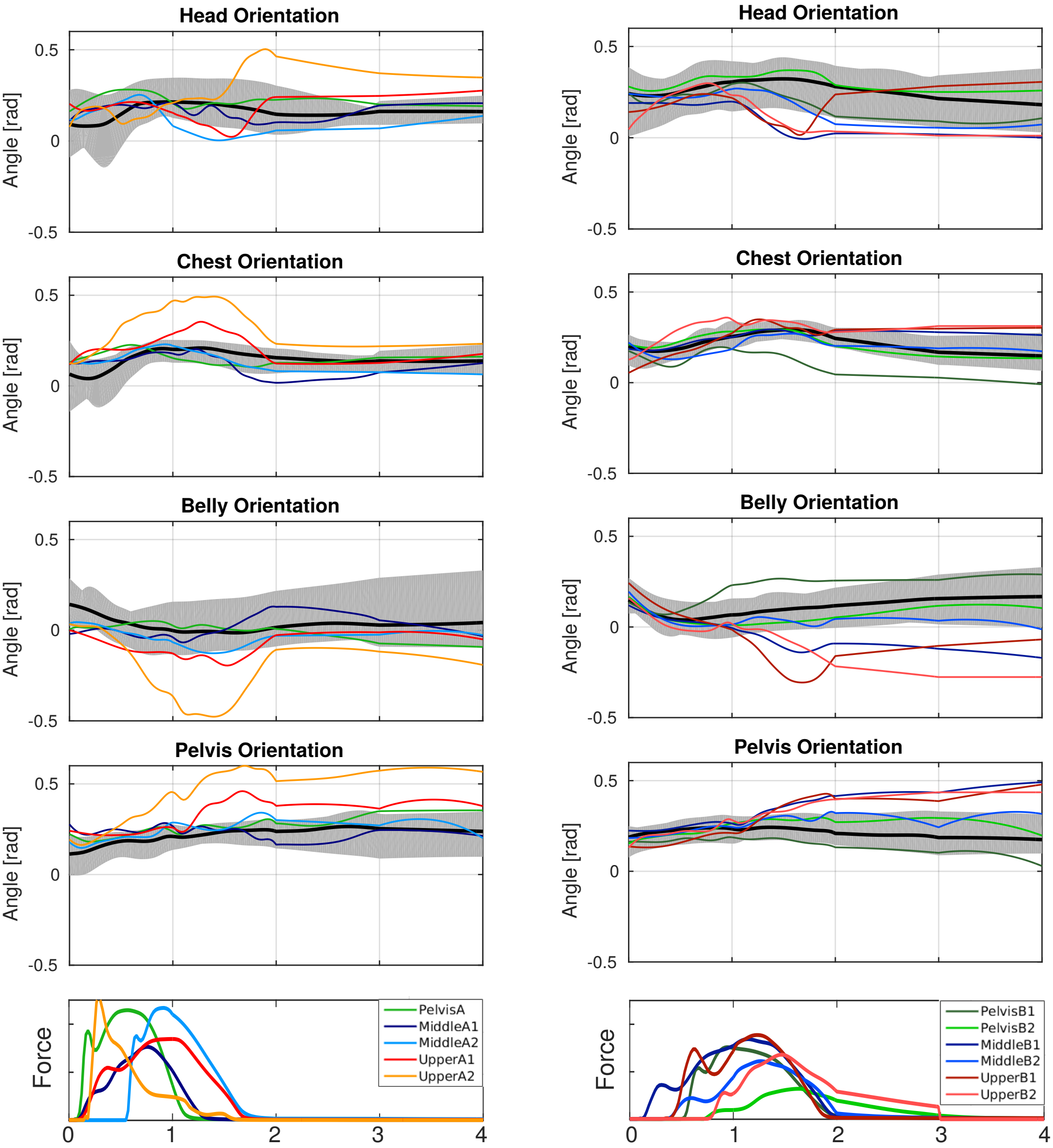

Figure 6.1: Average of the orientation angles of the body for unperturbed steps (thick black line) and for perturbed steps (solid colored lines) of the different push motions (left: dataset A, right: dataset B). The colored lines in the lowest row indicate the strength and the timing of the perturbation.

Arms

Figure 6.2 shows the joint angles and joint torques in the stance shoulder for dataset A and B. The joint torques in the stance shoulder start in the range of the unperturbed motions. When the push occurs, the joint torques of the stronger perturbed motions turn to negative values, get to the minimum in the second phase and return to positive values. Interestingly, the joint angles only vary from the range of the unperturbed steps starting from this turning point. The change of the joint torque to the other direction without a significant change in the joint angle is a reaction on the perturbation due to a passive holding moment or a reflex contraction as described in Section 1.4.

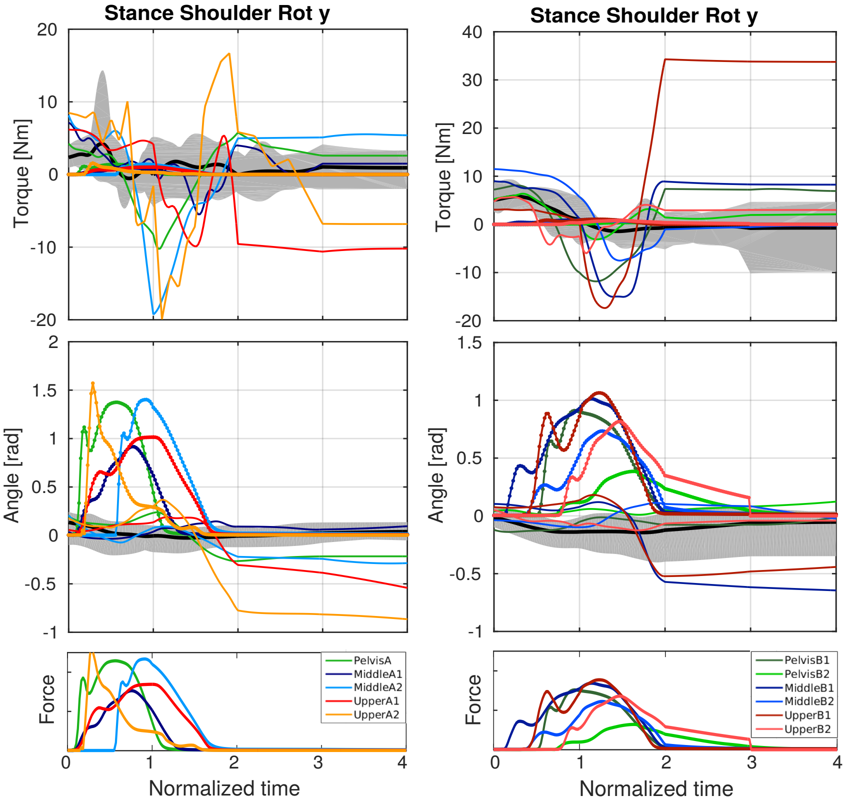

Figure 6.2: Joint torques and angles of the stance shoulder for unperturbed steps (thick black line) and for perturbed steps (solid colored lines) of the different push motions (left: dataset A, right: dataset B). The colored lines in the lowest row indicate the strength and the timing of the perturbation.

Neck

Figure 6.3 shows the joint torques and joint angles for dataset A (left) and dataset B (right). As already described in the previous chapter, the neck joint angle changes at the point in time when the push occurs for all but the motions perturbed at the pelvis. Again the tonic neck reflex can be of charge to maintain the balance, as the neck joints connect the body and the head. Therefore a change in the neck joint angle leads to a change in the muscle tension between the trunk and the limb which can be sensed by the mechanoreceptors. This can be seen in the change in joint torques in the upper row of Figure 6.3.

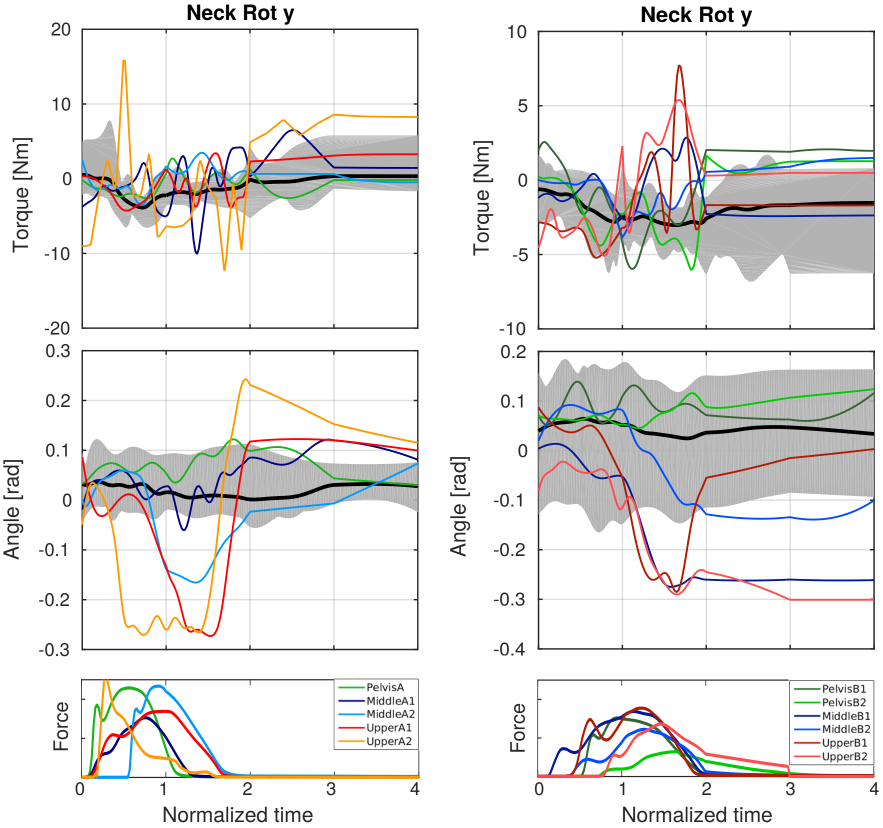

Figure 6.3: Joint torques and joint angles of the stance shoulder for normal steps (thick black line) and for perturbed steps (solid colored lines) of the different push motions (left: dataset A, right: dataset B). The colored lines in the lowest row indicate the strength and the timing of the perturbation.

6.1.2 Vision and Vestibular System

As described in Section 1.3.2, vision has a huge influence in the control of balance. Because our human model exists only of rigid segments, the motion of the eye cannot be implemented. In this scope, the influence of vision can be represented as the orientation of the head. Also, the vestibular system input can be represented by the orientation, the velocities, and the acceleration of the head. In this chapter, the influence of these variables on the ability to sense a perturbation is analyzed by comparing perturbed and unperturbed motions.

We regard the orientation and the transversal position as well as the velocities and the accelerations of the head, representing the influence of vision as well as the vestibular system, see Figures 6.4 and 6.5. No general rule holding for all motions can be observed. For the UpperA2 motion (orange line in Figure 6.4) a change in the transversal velocities in x and z-direction can be observed. Other motions

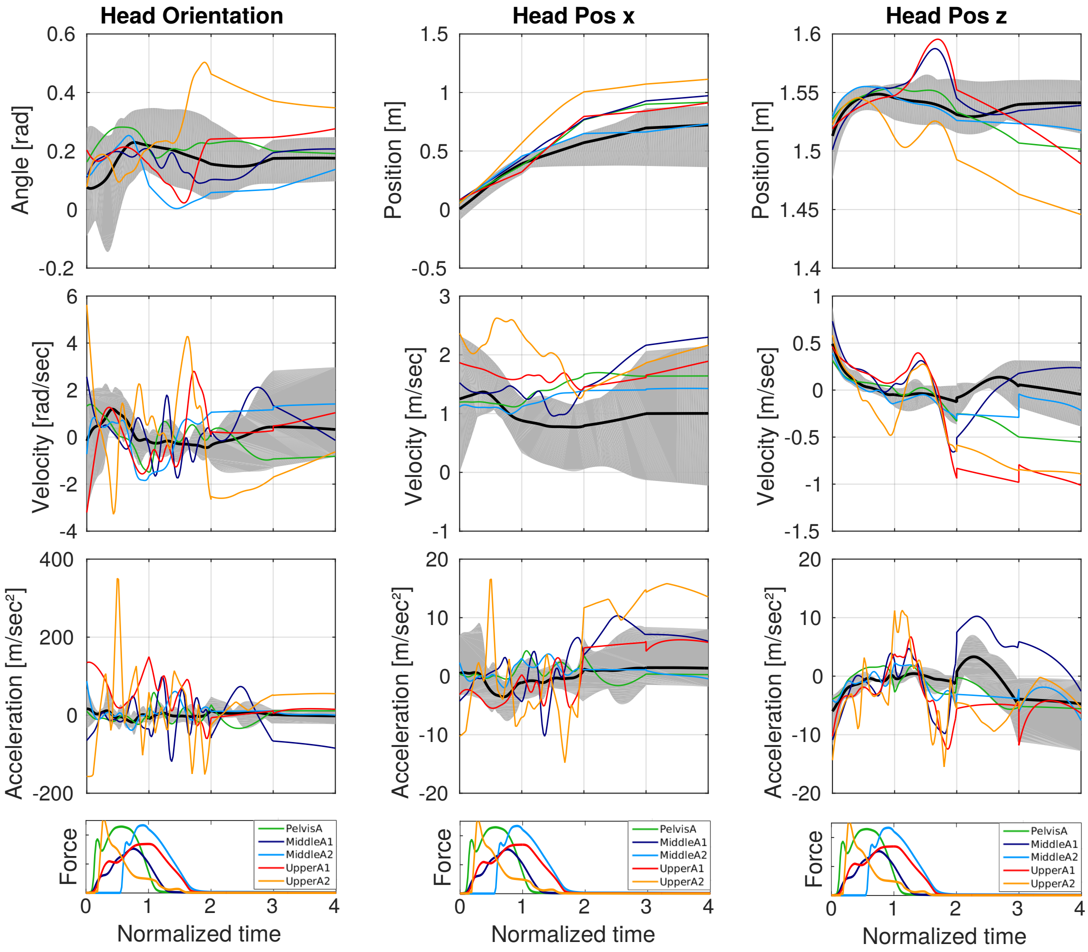

Figure 6.4: Orientation, position, velocities and acceleration of the head for unperturbed steps (thick black line) and for perturbed steps (solid colored lines) of the different push motions from dataset A. The colored lines in the lowest row indicate the strength and the timing of the perturbation.

differ later in time (MiddleA1, UpperA1, PelvisB1, MiddleB1, MiddleB2, UpperB1, UpperB2). This could be due to the peak shape of the UpperA2 motions, making the start of the perturbation very close to the maximal perturbation. A change in the head orientation can be observed at the point in time when the push occurs for the PelvisA, the MiddleA2, and all motions from dataset B, except for the PelvisB1 motion. This change can be sensed by the vestibular system and trigger a recovery motion. For the perturbations at the upper trunk, a change in the head orientation acceleration can be observed.

The change in the head orientation can be sensed by the otoliths of the labyrinth in the human ear leading to labyrinth reflexes, see Section 1.4. A time gap between the occurrence of the perturbation and the change in the orientation of the head can be observed for both datasets. This can either be due to the time delay of the sensory information process in the human and the inertia of the reaction or because the perturbation needs to apply a certain amount of energy until the human needs to react in a recovery motion.

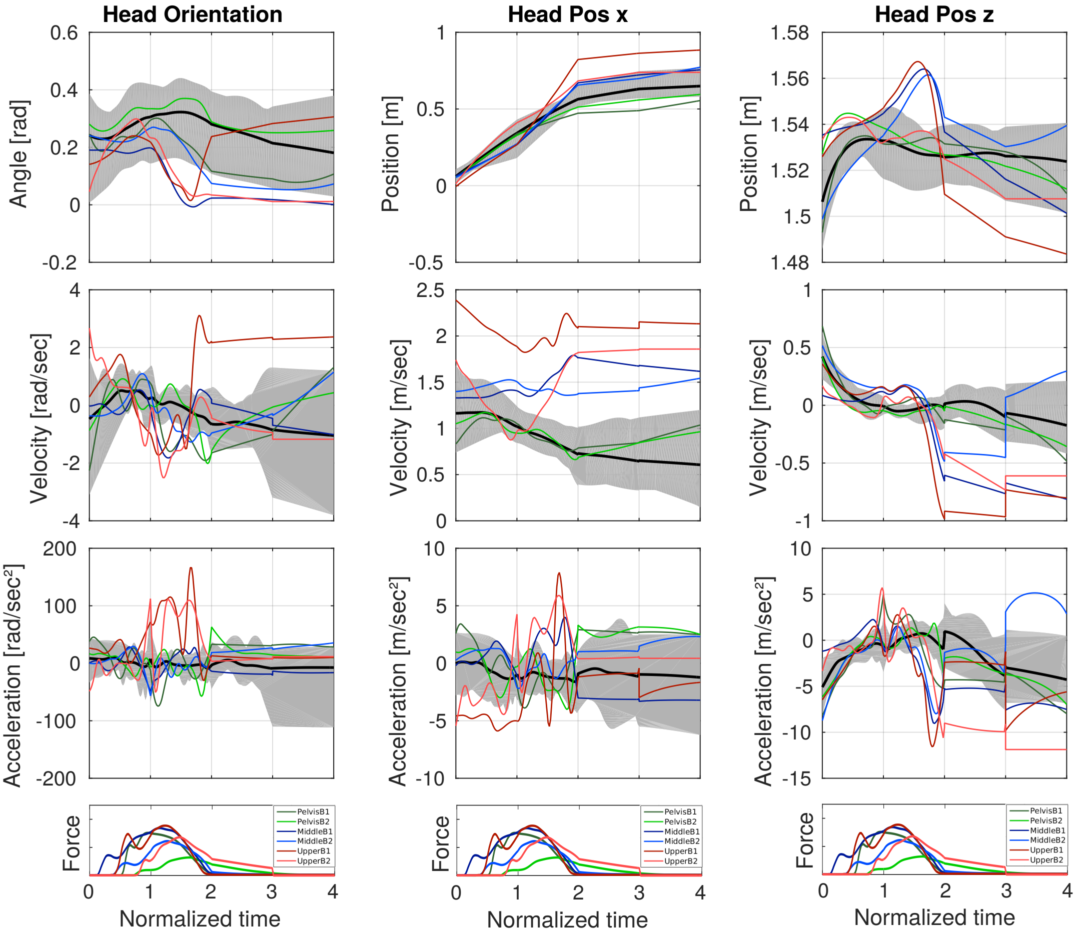

Figure 6.5: Orientation, position, velocities and acceleration of the head for unbperturbed steps (thick black line) and for perturbed steps (solid colored lines) of the different push motions from dataset B. The colored lines in the lowest row indicate the strength and the timing of the perturbation.

6.2 Analysis of the Reaction Time

In this section, we address the question on which sensory system is most relevant for sensing a perturbation based on the analysis of the reaction time. Knowing the reaction times of the specific sensory systems, the analysis of the reaction times in the perturbed walking motions can give a hint on which sensory system is involved in sensing the reaction. The exact time dependencies of the sensory and brain processing are described briefly in Chapter 1. Note, that with our approach only a first try of a better understanding of the process of the sensing of the perturbation can be given. A precise analysis of these time delays is not possible due to the strong dependency on the subjects, the tasks, and the sensory systems involved. Another reason why it is not easy to use the time delays as a hint on which sensory system is relevant for the detection of and reaction on a perturbation is that our model is not accurate enough. The time from the stimulus until reaching the brain is irrelevant in our scope because inner processes as the information from the stimulus until the reaction are modeled as a black box. Furthermore, the literature is not consistent concerning the specific times of the different sensory systems and the results are strongly dependent on the reaction task. For the reaction time of the sensory system, it is also relevant how many sensory systems are stimulated. In our case, we aim to determine the senses involved in the detection of perturbation during walking motions. The reaction time, in this case, describes the difference of the perturbation start and the point in time when the trajectory of the perturbed motions differs from the unperturbed motions. Here, we analyze the differences of the trajectories of the joint angles and joint torques in the swing and the stance shoulder.

To determine the reaction time, we regard not normalized plots of the joint angles. The analysis of the joint angles in the shoulders makes sense in this scope because there is not much motion in these angles for the unperturbed walking motions, see Figure 5.2, 5.3 and in the Appendix A3. Figure 6.6 shows the mean, maximal and minimal reaction times for the swing shoulder and the stance shoulder observed in the joint angles (upper row) and joint torques (bottom row). In the Appendix A3 a table including the exact reaction time values for the arm and head position is given. Note, that for two motions a negative reaction time is found. This could be because during the optimization the algorithm "knows" that a perturbation will occur. No further restriction other than the model dynamics is added to fix the motion to a normal gait until the point in time the perturbation is applied. This could influence the motions before the perturbation occurs. For most motions, this drawback can be neglected because the optimization leads to a good approximation of the reference data - in which the subjects did not know when, where and with how much strength the perturbation would be applied. Considering the reaction time until the change in the joint angle of the swing shoulder shown in Figure 6.6 upper left plot the values from dataset B suggest that the reaction time increases the further up the perturbation is applied. This also holds for the middle and upper trunk in dataset A but not for the one at the pelvis. In the stance shoulder, the reaction time increases for higher located perturbations for dataset A but at this joint, the reaction time decreases significantly for dataset B. In Section 1.3.4 reaction times from literature are summarized. The total mean reaction time of the joint angles over both datasets for the swing shoulder is 147 ms, which is longer than the mean reaction times of the other joints. Comparing this value to reaction times of simple tasks from literature, it is only a bit longer. A simple task is a task in which the subject only needs to press a button or catch a ruler without a choice of different possibilities. Recent research suggests that this time is 141 ms (auditory), 148 ms (visual) or 139 ms (touch) if only one sensory system is stimulated [82]. Investigating in more than one sensory system this time reduces. But, as mentioned, the times are not only strongly dependent on the number of sensory systems involved but also on the required task. The more complex, meaning the more possible reactions, the longer the reaction time. Comparing the simple reaction task of only pressing a button with a recovery motion from a perturbation, the latter is a lot more complex. Following the results from research, this would result in longer reaction times. The result of a quite short reaction time suggests that the human can process the information of a perturbation very effective. To be able to decide which senses are mainly involved in the detection of perturbation during human walking motions, our results are not sufficiently accurate.

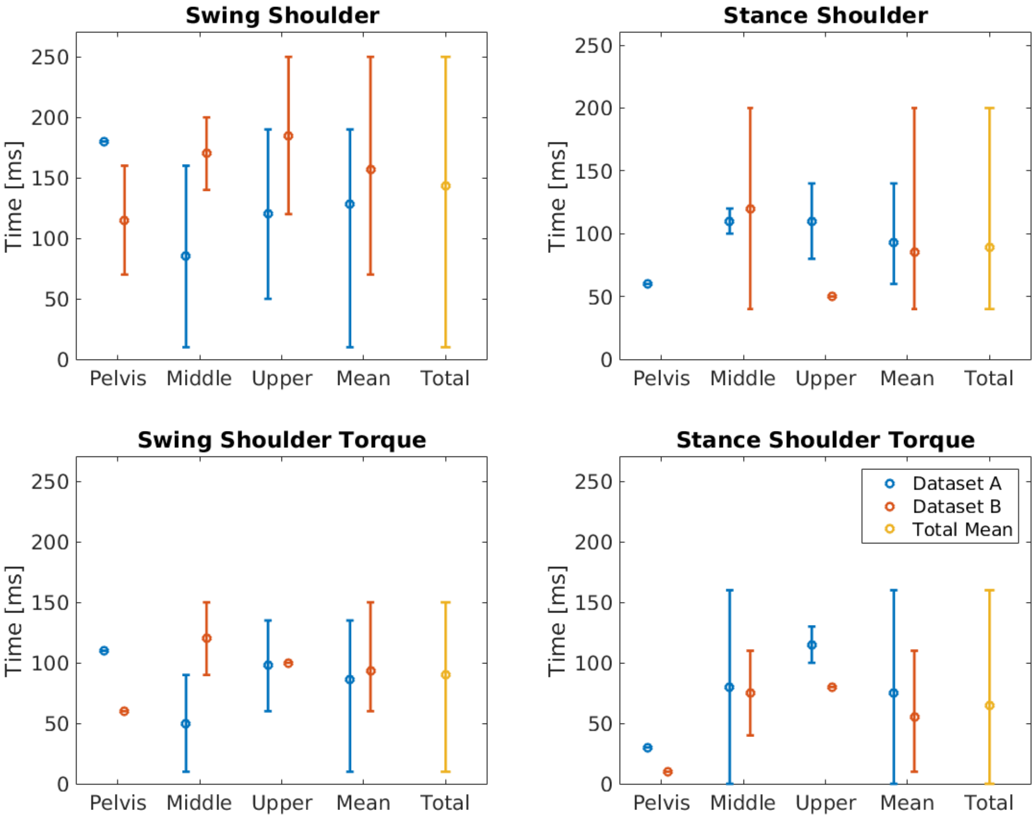

Figure 6.6: Minimal, maximal and mean reaction times of the swing shoulder for the two datasets.

Nevertheless, the reaction time for the different motions in the swing shoulder differs between 20 and 230 ms which is a huge variance and therefore does not give any hint on the sensory systems involved in the detection of the perturbation. The mean reaction time of the stance shoulder is 89 ms (min. 40, max. 200 ms) for the head position in x-direction 53 ms (min. 10, max. 180 ms) and in z-direction 118 ms (min. 50, max. 120 ms).

The reaction time until a change in the joint torque is shorter than the one of the joint angles regarded above, see bottom row of Figure 6.6. This shows that first the joint torques change and then the joint angles. Regarding the reaction times from joint torques, an increase if the reaction time the higher the push point is located can be observed for both datasets for the stance shoulder but not for the swing shoulder. Overall, no general dependency between the reaction times and the perturbation locations or push strengths can be found from the investigated data.

6.3 Conclusions

Comparing the reaction times from our calculation to the reaction times found in the literature shows that the reaction time to a perturbation during human walking is in the range of the reaction times to simple tasks using only one sensory system. This result suggests that the sensing of a perturbation during motion involves more than one sensory system because this task is more complex than a simple task but the processing time reduces if more than one sensory system is stimulated. This result indicates, that most probably, a combination of audible and tactile stimulation is in charge of first sensing a perturbation as regarded in this thesis.

Our investigations of the head orientation and position suggest, that for stronger perturbations at the upper body the vestibular and the visual system can sense the perturbation. A distinct difference between the orientation of the head in these perturbed motions and the unperturbed motions can be seen.

Nevertheless, our results indicate that mainly the somatosensory system is responsible for sensing perturbations during walking because a change in neck rotation can be observed before the change in head orientation. To apply these results to a robot, the robot needs to be able to sense the constellation of its joints all the time.

Moreover, our findings show that a sense of balance located at the chest does not detect all perturbations at the upper trunk during walking. In our data, only one perturbation in the pelvis leads to an orientation of the chest that differs from the range of unperturbed motions. The other perturbations can only be sensed in the other upper body parts, meaning the head, the upper and the middle trunk in our model.

Chapter 7

Synthesis of Human Push Recovery Motion During Walking

In this chapter perturbed human walking motions are generated using the methods introduced in the first Chapters of this thesis to be able to further analyze the influence of perturbations during human walking motions. First, the influence of the strength of the perturbation is analyzed based on a fixed objective function. Then the resulting motions from differing objective functions are compared to perturbed motions from reference data.

7.1 Analysis of the Influence of the Strength of the Perturbation

Regarding our set of reference data, the timing and the push strength vary from trial to trial. This makes it very difficult to analyze the influence of the strength of a perturbation alone. To this end, in this section, the timing and the location of the perturbation are constant. Only the push strength varies.

We are using the human model presented in Chapter 3 considering the types of pushes during periodic walking in which the aim is to maintain a motion close to the periodic one. We, therefore, formulate an objective function of an optimal control problem introduced in Chapter 4 that aims to minimize the gap to periodicity after one step of the motion. We add a second term that minimizes a weighted sum of joint torques squared resulting in a reduction of efforts over all joints which has proven to be a suitable criterion for many types of motions, [37, 38, 96, 161]. The push is added as a given function of time in the right-hand side of the dynamics. Initial conditions for the step, i.e. just before the onset of the push, are fixed to the conditions of the periodic motion at this very moment. The duration of phases, as well as the resulting step length (and all other positions and velocities), are free to be determined by the optimization. In this study, we do not investigate in reference data from a real human. To be able to analyze the influence of a perturbation, different push strengths are analyzed, while the timing and the position remain the same. We define the force as a polynomial of order four with a duration of 0.1 seconds and a maximal amplitude which varies between $150\,\mathrm{N}$ and $600\,\mathrm{N}$. These results are also presented in [159].

The approach presented in this chapter explicitly addresses large perturbations during periodic walking to go back to the gait cycle and not to stop to recover. It is the first optimization approach based on a whole-body model of human walking. While it may be too time-consuming to perform this type of computations on-line in the robotics context, the trajectories can easily be precomputed for different levels of pushes and executed according to the sense push signal, as we will discuss at the end of Section 7.1.2.

7.1.1 Optimal Control Problem Formulation

Formulating human motions as an optimal control problem as described in Section 4 includes two main parts. First, the dynamics of the multi-body model together with the gait cycle constraints, presented in Section 3, and second, a suitable objective function which defines the locally best solution on a manifold of feasible solutions, see Section 4.1, has to be defined. This is a beneficial way to solve the redundancy issue which is especially important in human walking and push recovery.

The dynamics of the multi-body model enter the OCP as a constraint in form of a differential equation; constraints for the gait cycle are implemented as nonlinear interior constraints in and as phase transition conditions and coupled conditions. The push function which specifies the duration, direction, contact point and intensity of the external force enters the right-hand side of the differential equation as an augmented control, which is the sum of internal and external forces (see Sec. 3.4).

In this motion synthesis study, we focus on the optimization of one single step. Since in the case of no perturbance, human gait is usually cyclic, in this case we formulate coupled constraints between $t = 0$ and $t = T$, such that the state $\boldsymbol{x}(T)$ at the end of the step is the mirrored constellation to the state at the beginning of the step at $t = 0$, more precise $\boldsymbol{x}(0) = \tilde{\boldsymbol{x}}(T)$. Note, that this includes all positions and joint angles (except the pelvis position in walking direction) and all corresponding velocities. In the following, we refer to this constraint as periodicity constraint as it enforces a symmetric, periodic gait. Note, that with this constraint the step length is already defined by the initial posture of the step. Hence, in the presence of an external force, this constraint has to be relaxed due to two reasons. First, to allow for a variable step length, and second to allow for a final state as a reaction to the push, which is not a mirrored constellation to the state at the beginning of the step, where no perturbance had been taken place so far. Because the optimal control problem models the behavior of a human who is pushed during walking, the goal of the recovery motion is, to be able to keep on walking afterward. Therefore, the periodicity constraint can not be neglected entirely and we look for recovery steps that are as periodic as possible, while still compensating the push. To this end we include a vector of slack variables $\boldsymbol{p}_{peri}$, substitute the periodicity constraint by the relaxed version

$$\boldsymbol{x}(0) = \boldsymbol{p}_{peri} + \tilde{\boldsymbol{x}}(T) \tag{7.1}$$

and include a minimization of a weighted sum of these slack variables in the objective function as Mayer term.

Note, that also the phase transition times $\boldsymbol{s} = (s_0, \ldots, s_{n_{ph}})$ are free variables, such that not only adjustment of step length p_{SL} but also of step duration T is taken into account for the computation of an optimal recovery motion.

Applied to the human model described in 3.1 we get an optimal control problem of the form from (4.1a)-(4.1f) with 32 state variables $\boldsymbol{x}$ consisting of the 16 joint angles $\boldsymbol{q}$ and 16 joint angle velocities $\dot{\boldsymbol{q}}$ and 13 control variables $\boldsymbol{u}$ consisting of the joint torques $\boldsymbol{\tau}$. The parameters $\boldsymbol{p}$ are described by the step length p_{SL} at the end of the step and 31 periodicity slack variables $\boldsymbol{p}_{peri}$ for the position and velocity gaps as described above.

For this motion synthesis study, we define an objective function consisting of two parts. Next to the minimization of the periodicity gap described above we define a further criterion which is a suitably weighted minimization of all squared joint torques divided by the resulting step length p_{SL}. It can be interpreted as a maximization of efficiency. The over-all objective function consists of a linear combination of these two terms, weighted in such a way that for a push of 0 N the optimal motion basically coincides with the version of the unperturbed case with a non-relaxed definition of the periodicity constraints

$$\Phi[\boldsymbol{x}, \boldsymbol{u}, \boldsymbol{p}, \boldsymbol{s}] = \min_{\boldsymbol{x}, \boldsymbol{u}, \boldsymbol{p}, \boldsymbol{s}} \boldsymbol{p}_{peri}^T \boldsymbol{W}_{\boldsymbol{p}} \boldsymbol{p}_{peri} \tag{7.2}$$

$$+ \min_{\boldsymbol{x}, \boldsymbol{u}, \boldsymbol{p}, \boldsymbol{s}} \frac{1}{p_{SL}} \sum_{j=1}^{n_{ph}} \int_{s_{j-1}}^{s_j} \boldsymbol{u}(t)^T \boldsymbol{W}_{\boldsymbol{u}} \boldsymbol{u}(t) dt. \tag{7.3}$$

7.1.2 Results

In this section we use the human model presented in Section 3.1 and the optimization environment described in Section 7.1.1 to compute push recovery motions for different push strengths during human walking applied to the back. There are three main goals of these computations.

- First, we are interested in the resulting full-body motions and differences of joint angles, angle velocities, and joint torques in comparison to the unperturbed case.
- Second, we are looking for measurable indicators, which might be good candidates to identify a push for humanoid robots.
- Third, we pay attention to relations between the strength of perturbation and characteristic quantities of the resulting recovery motion, such as step length or motion duration.

For the analysis of push recovery motions five different scenarios are considered: a quasi-periodic step without a push and four steps with a push described by a polynomial of order four, with a peak magnitudes of 150 N, 300 N, 450 N, and 600 N respectively, see Figure 7.1.

In this study only pushes from the back with a contact point at the pelvis are considered. The force in the y- and the z-direction is zero, such that the push occurs only in the sagittal plane. At time $t = 0$ s all four pushes have a non-zero value, increase to their maximal amplitude at $t = 0.25$ s and decrease to zero at $t = 0.1$ s with a continuously differentiable transition to the constant zero function. The calculation time for our implementation is in the order of minutes. Figure 7.2 shows the resulting motions for the different pushes.

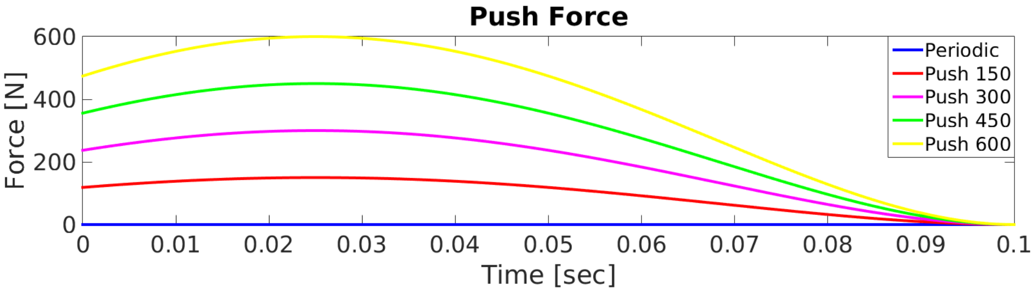

Figure 7.1: Investigated push force profiles in x-direction.

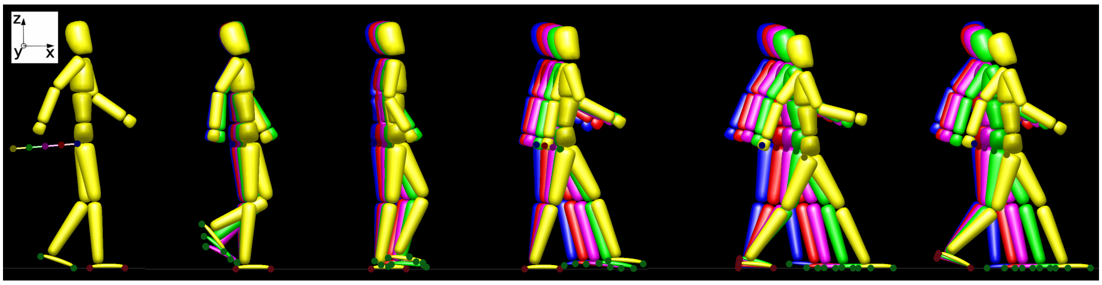

Figure 7.2: Motion of the sagittal human model for the five different push forces. The push strength increases from the back to the front: blue 0 N (periodic), red 150 N, magenta 300 N, green 450 N and yellow 600 N.

The main observations that can be made from the generated motions are the following:

- The step length increases when the maximum of pushing force increases, see also Figure 7.3 (left).
- The step becomes less periodic in the sense that the final state is less similar to the mirrored initial state, see also Figure 7.4.

It is reasonable that the hip and ankle joints show less periodicity than other joints, as they are responsible to allow for a longer step length. Similar observations are also made for the periodicity gap in the velocities. Interestingly, the step durance does not decrease monotonically as the peak force increases. For a very strong push of 600 N the step durance increases again, see also Figure 7.3 (right). This observation has to be studied in detail for more scenarios to investigate if there exists a systematical relation between the push strength, the step length and the step duration.

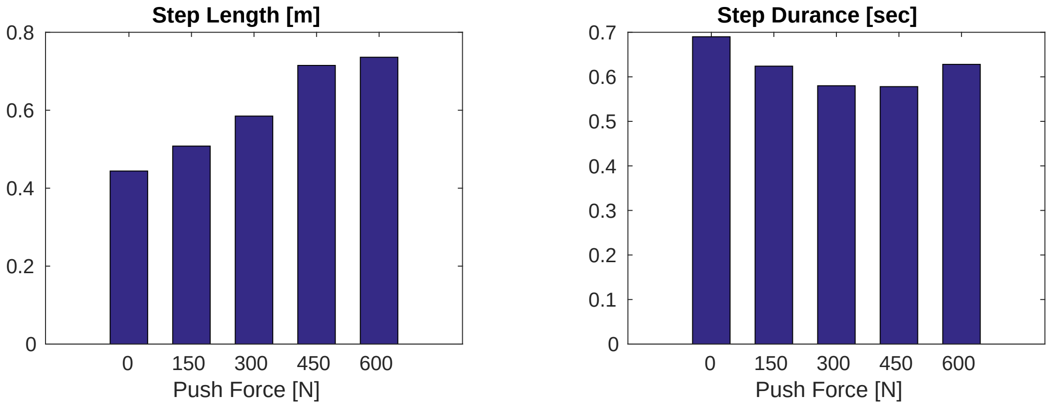

Figure 7.3: Step lengths (left) and step durances (right) of the motions resulting from the different force strengths.

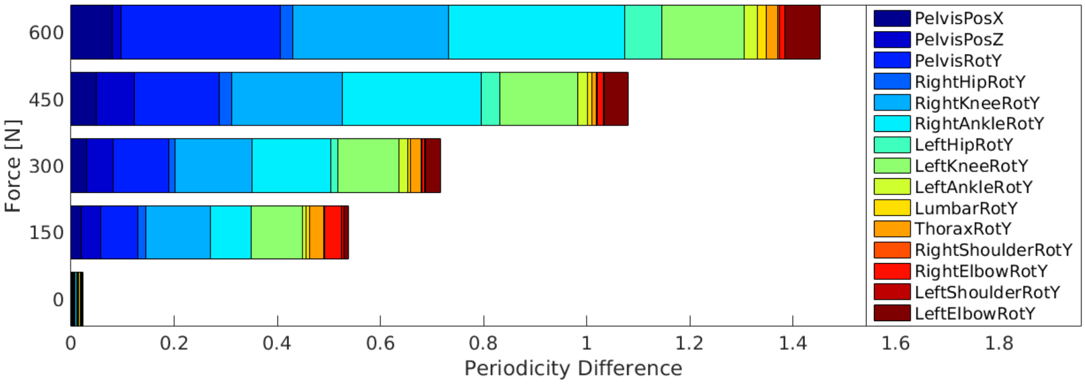

Figure 7.4: Minimized parameters of the relaxed periodic constraints for the position and orientation of the pelvis as well as the joint angles for the different push strengths.

Figure 7.5 shows the pelvis position and orientation as well as its velocities. The stronger the push is, the further the pelvis moves in the x-direction at the end of the step. Also, the velocity in the x-direction is higher the stronger the perturbance (see Figure 7.5, left). The z-position of the pelvis is lowered with an increase of the push. The velocity in this direction is also increased (see Figure 7.5, middle). The rotation around the y-axis does not show a high increase of the amplitude as well as the rotational velocity (see Figure 7.5, right). The same observation can be made for the other joint angles and joint angle velocities, see Figure 7.6 and 7.7. Only the right ankle shows a decrease in the joint angle but no significant higher absolute joint angle velocity for an increase of the perturbation. However, the joint torques are distinctly higher for stronger pushes. This observation does not only hold for the right ankle but also for the torques in most of the other joints.

These differences to normal gait can be interpreted as indicators for a sudden perturbance and could also be useful for humanoid robots. With the presented model it is possible to derive a relation between the currently performed limit cycle (parameterized by e.g. step length and average walking velocity), the type of push that occurs (parameterized by e.g. duration, direction, magnitude and contact point) and the optimal recovery motion (parameterized by e.g. step length and duration). Based on the relation between these parameters, an upper-level planer or look-up table can be derived to evaluate on-line the optimal step length and duration of a recovery step for the current state of the robot and the type of push. Furthermore, with the approach presented in this section and a dynamic robot model, full-body recovery motions can be computed off-line for a large variety of these parameters. As presented in [91], these motions can then be used as training data to learn movement primitives which are suitable to be evaluated in real-time for a given set of the above-mentioned parameters.

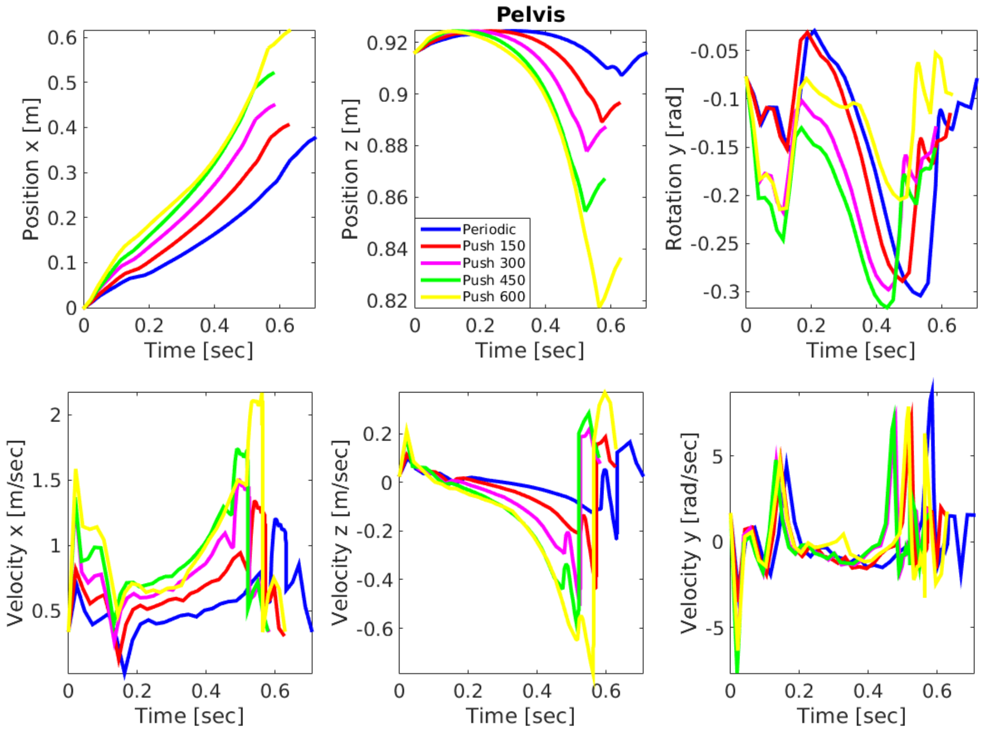

Figure 7.5: Subset of states for different push strengths. Upper line: the position and orientation of the pelvis, lower line: corresponding velocities.

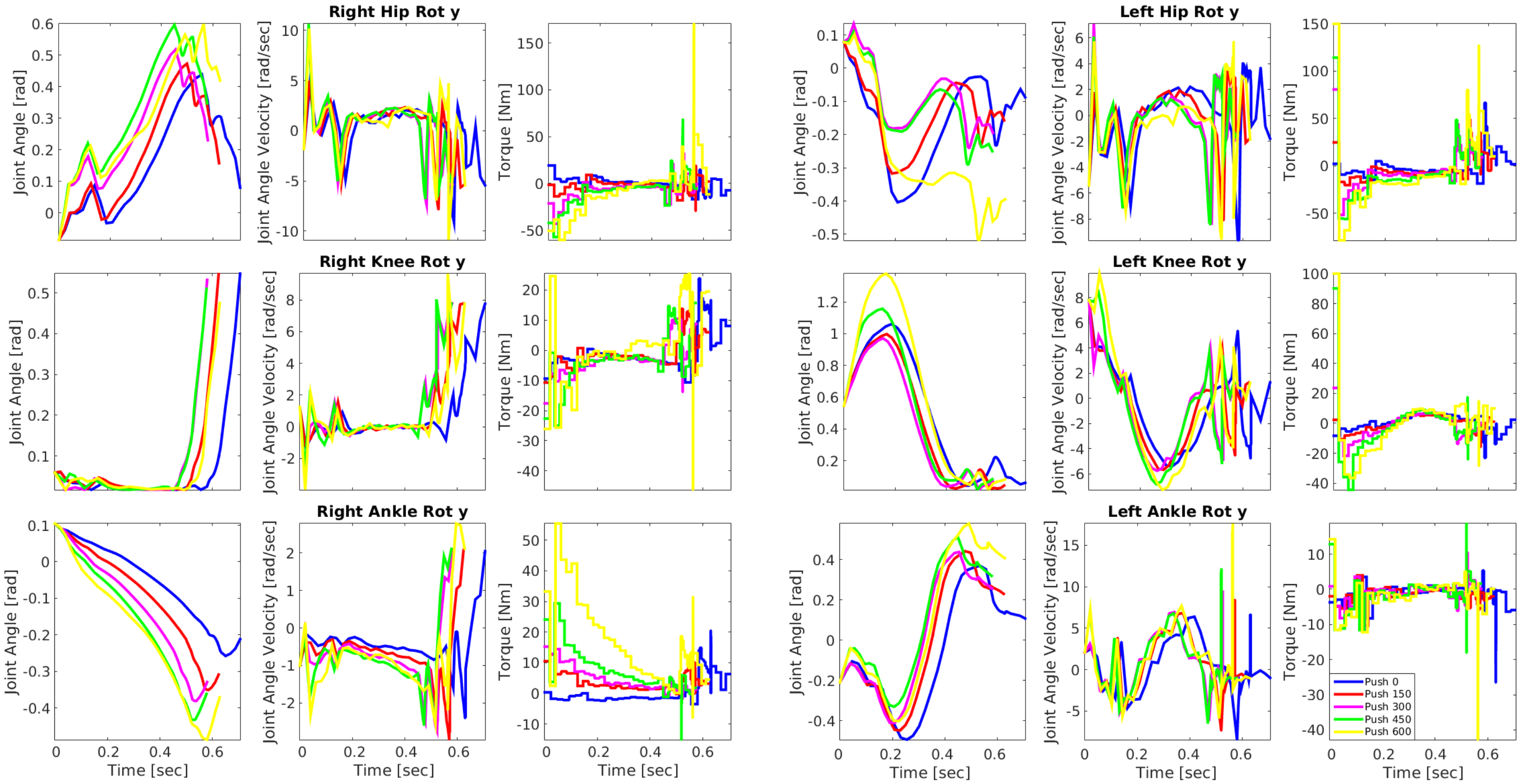

Figure 7.6: Joint angles, joint angle velocities and joint torques of the legs.

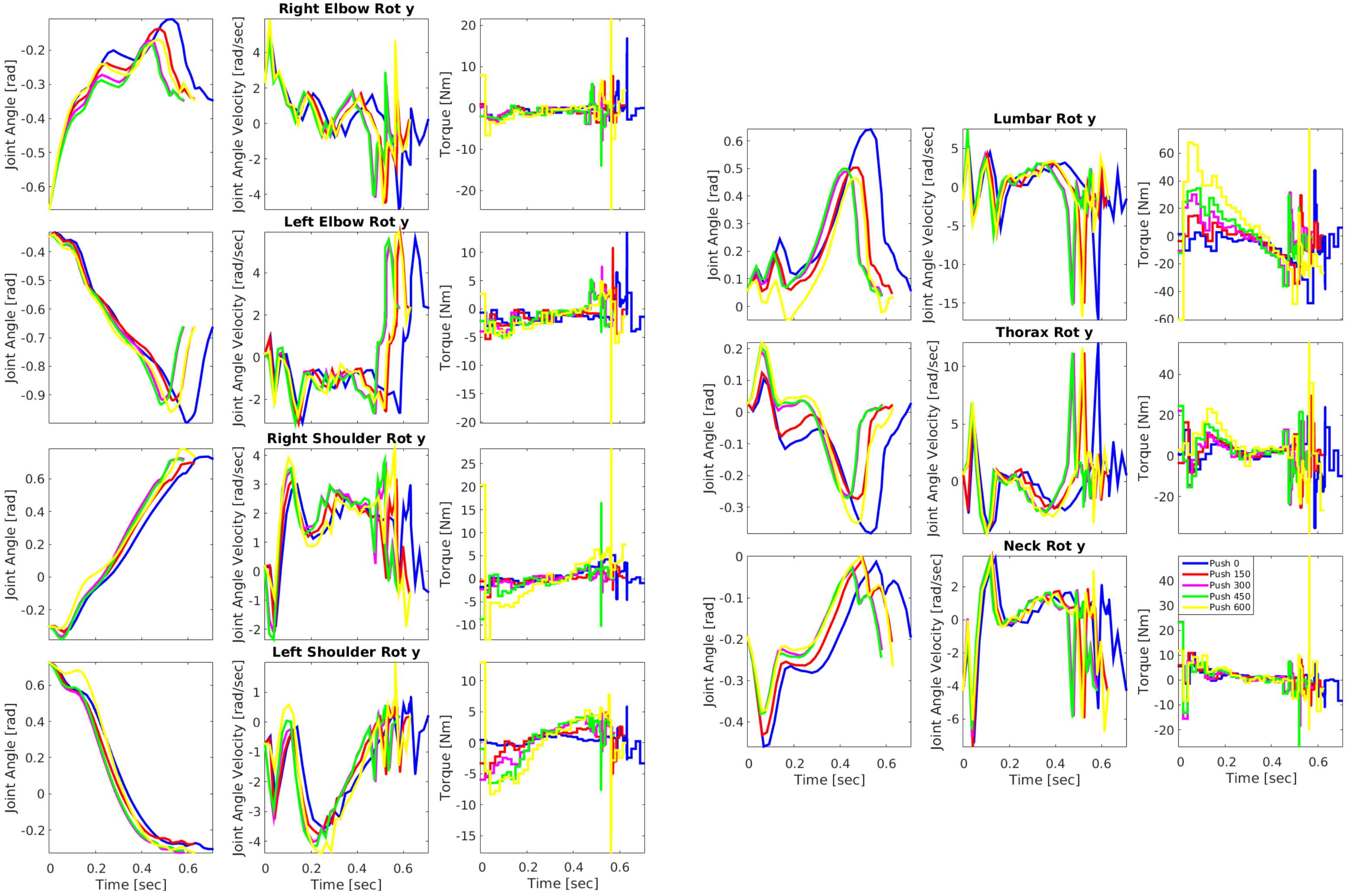

Figure 7.7: Joint angles, joint angle velocities and joint torques of the arms and the legs.

7.2 Similarity Analysis of Synthesized Perturbed Walking Motion to Reference Data

In this section we use a similar approach as in the previous Section to analyze the similarity of motions synthesized based on different objective functions and initial values to motions from reference data. Being based on a small set of scenarios neither the indicators nor the relations discussed in this section can be considered as a general rule. They are more a first sophisticated guess, where future research should go. Further research is necessary, if the derived indicators are valid for a wide range of motions and if they also take place in a robot, which does not actively react to the motion. As a first attempt, we investigated the synthesis of perturbed walking motions based on our reference data using a larger set of objective functions and perturbations than in the previous section.

7.2.1 Optimal Control Formulation

We use an optimal control problem as formulated in Section 4 with joint torque derivatives as controls as in Section 5. This results in 45 state variables, consisting of the joint angles, the joint angle velocities, and the active joint torques, and 13 control variables consisting of the active joint torques.

In the last section, we investigated only one objective function. Here, we analyze a broader set of objective functions. To be able to analyze the influence of the different joint torques, it would be interesting to regard the minimization derivatives of joint torques for an unsymmetric formulation. Optimally, each joint torque is considered independently, leading to 13 criteria:

$$\phi_i = \int_0^T \gamma_u^i \dot{u}_i^2 dt, \tag{7.4}$$

where γ_u^i defines an appropriate scaling of the torques for $i = 1,\ldots,13$. Apart from these objective functions, we also investigated in the following criteria:
a head stabilization

$$\phi_{14} = \int_0^T (\dot{q}_{neck} + \dot{q}_{thorax} + \dot{q}_{lumbar} + \dot{q}_{pelvis})^2 dt, \tag{7.5}$$

the maximization of step length

$$\phi_{15} = -p_{steplength}, \tag{7.6}$$

and the minimization of end time (maximization of step frequency)

$$\phi_{16} = T. \tag{7.7}$$

Unperturbed walking motions are nearly periodic. As described in Section 7.1.1, a perturbed walking motion is not periodic anymore. To this end, the following periodicity criteria similar to the one regarded in this chapter is included in our studies

$$\phi_{17} = \sum_{k=0}^{n_q+n_{\dot{q}}} \gamma_p^k p_{peri,k}^2, \tag{7.8}$$

where γ_p^k defines a scaling of the different periodicity parameters, that allows for a gap in the periodicity constraints resulting in unperiodic motions. We generated motions with these basal objective functions starting with initial values from the reference data. To be able to identify which motion is most human like, we define the following similarity measures:
the total similarity

$$d_{total} = \frac{1}{n_s}\sum_{k=0}^{n_s} d_{temp,k}(s_k,\tilde{s}_k) \tag{7.9}$$

$$+ \frac{1}{n_{\tilde{x}} n_{\tilde{t}}}\sum_{k=0}^{n_{\tilde{x}}} d_{post,k}(x_k,\tilde{x}_k), \tag{7.10}$$

consisting of the temporal similarity

$$d_{temp,k}(s_k,\tilde{s}_k) = |s_k - \tilde{s}_k|,\ k = 0,\ldots,n_s, \tag{7.11}$$

and of the postural similarity

$$d_{post,k}(x_k,\tilde{x}_k) = \frac{1}{n_{\tilde{t}}}\sum_{l=0}^{n_{\tilde{t}}-1} ||M(x_k(t_l)) - \tilde{x}_{k,l}||_2,\ k = 0,\ldots,n_{\tilde{x}}, \tag{7.12}$$

where M defines a function that transforms the state data to the format of the reference data. In our case, this is a projection of the state vector $\boldsymbol{x}$ to its position part $\boldsymbol{q}$ consisting of the joint angles and the position of the pelvis.

Note, that also in this formulation, the position is not fixed to the values of the reference data until the perturbation occurs. This means that the optimization algorithm can also change the position before the push occurs to prepare for the recovering of the perturbation. This is not possible for a human if he or she does not know that the perturbation will occur, which we assume in our setup.

7.2.2 Results

Figure 7.8 shows the mean total postural, temporal and total deviations of motions generated with the basal objective functions considered to reference data of unperturbed motions and motions perturbed at the pelvis, the middle and the upper trunk. Here, we consider motions from both datasets described in Section 2.4. For the unperturbed motions, the minimization of the derivative of the torque in the left knee leads to motions that are less human-like than all other objective functions. Human-like means in this case, that the similarity value is low. The bigger the similarity value the less human-like the motion. Note, that this does not hold for all unperturbed motions. Interestingly the minimization of the derivative of the torque of the left knee leads to quite human-like motions for the perturbations at the pelvis. Here, the minimization of time leads to the least human-like motions, followed by the minimization of the derivative of the right ankle torque. This observation also holds for the other push locations in the middle and the upper trunk. While the postural similarity does not differ a lot between the different objective functions, mainly the timing is not similar for these objective functions. For the perturbed motions, the maximization of the step length leads to a quite good fit of the step timing.

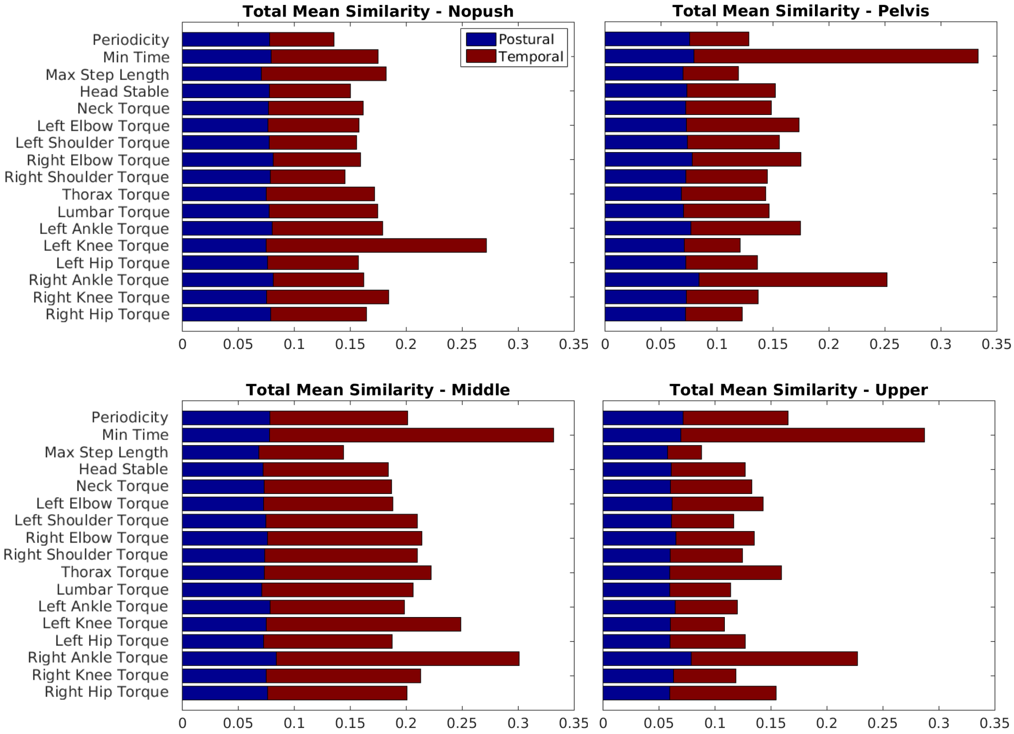

Figure 7.8: Total mean postural (blue) and temporal (red) similarities for the different push points and different basal objective functions.

Figure 7.9 shows the postural and temporal similarities for each joint and phase. While for the right body part, the minimization of the derivative of the right ankle torque leads to the least human-like motions, followed by the minimization of the derivative of the right elbow torque and the minimization of the time, in the left body part, the periodicity leads to least human-like motions followed by the minimization of the derivative of the right ankle torque. Here, the maximization of the step length also does not only lead to a good temporal similarity but also a good postural similarity on the left body part mainly caused by a good approximation of the left hip joint angle. This cannot be seen in the total joint torque because in the right hip the maximization of the step length leads to a bigger gap between generated motion and reference data.

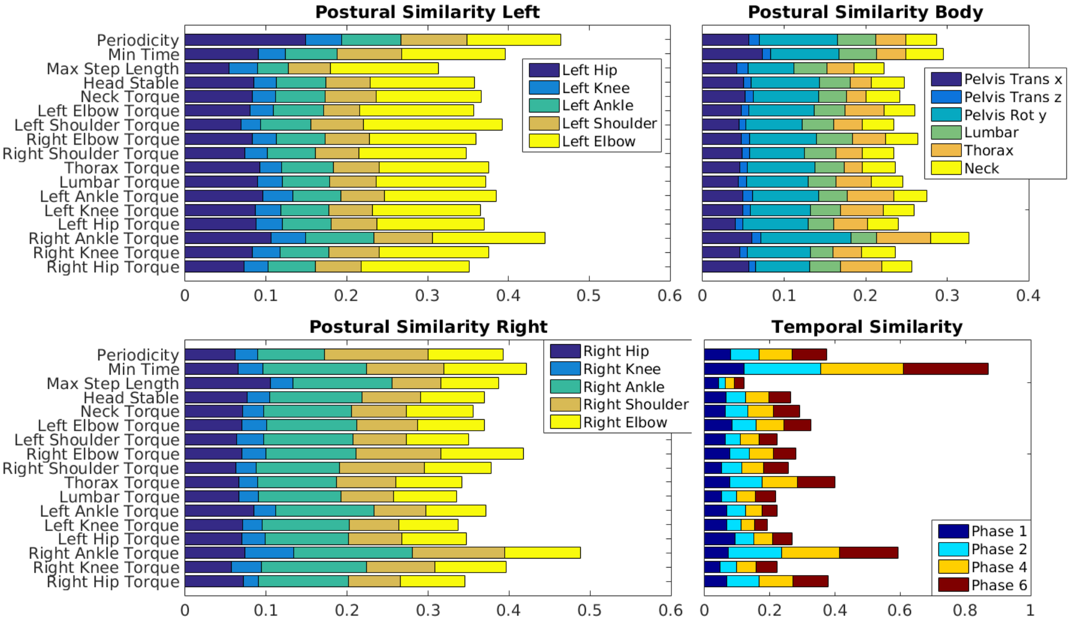

Figure 7.9: Postural and temporal similarities for the different basal objective functions for the motions perturbed at the upper trunk.

These results show that the resulting motions for the perturbed motions differ from the unperturbed motions for the same objective functions. Because the similarity between reference data and synthesized motions does not differ a lot between the different push locations for the regarded objective functions, the results indicate, that the use of inverse optimal control could lead to one general objective function for the regarded perturbations during gait. In our case the minimization of the derivative of the right ankle torque and the minimization of the end-time lead to motions less similar to the reference motion than the minimization of other joint torque derivatives.

7.3 Outlook: Inverse Optimal Control

In the previous section, the similarity of motions resulting from basal objective functions to reference data was analyzed. The overall goal is to determine an objective function that results in a human-like motion. To this end, the objective function can be formulated as a weighted linear combination of the basal objective function, e.g. the criteria regarded in the previous section. To identigy the most relevant criteria, meaning the weights of this linear combination, the presented optimal control problem can be included in an inverse optimal control problem [19, 117] (also called Bi-Level Optimal Control [7, 23]). This results in an objective function of the inner optimal control problem (which is exactly the problem presented in this chapter) as follows

$$\Phi[\boldsymbol{x}(t),\boldsymbol{u}(t),\boldsymbol{p},\boldsymbol{s},\boldsymbol{\omega}] = \sum_{k=0}^{n_\omega-1} \omega_k \phi_k(\boldsymbol{q},\dot{\boldsymbol{q}},\boldsymbol{u},\boldsymbol{s}). \tag{7.13}$$

The weights of this linear combination are determined including this OCP as constraints in a motion fitting problem (outer problem) which minimizes the distance of model variables to reference data from motion capture recordings like in the reconstruction approach in this thesis. The outer problem is defined by the following least-squares objective function which is similar to the total similarity measures we calculated above

$$\Psi(\boldsymbol{\omega}) = \frac{1}{n_{\tilde{x}} n_{\tilde{t}}} \sum_{k=0}^{n_{\tilde{x}}} \sigma_k \sum_{l=0}^{n_{\tilde{t}}-1} ||M(x_k^{(\omega)}(t_l)) - \tilde{x}_{k,l}||_2 \tag{7.14}$$

$$+ \frac{1}{n_s} \sum_{k=0}^{n_s} \sigma_{k+n_s} |s_k^{(\omega)} - \tilde{s}_k|. \tag{7.15}$$

In total, this results in a formulation as follows

$$\min_{\omega} \Psi(\omega) \text{ s.t. } \begin{cases} \min\limits_{(\boldsymbol{x},\boldsymbol{u},\boldsymbol{p},\boldsymbol{s})} \Phi[\boldsymbol{x}(t),\boldsymbol{u}(t),\boldsymbol{p},\boldsymbol{s},\boldsymbol{\omega}] \\ \text{s.t.} \begin{cases} \dot{\boldsymbol{x}}(t) = \boldsymbol{f}_i(t,\boldsymbol{x}(t),\boldsymbol{u}(t)), \text{ for } t \in \mathcal{I}_i, \\ \boldsymbol{x}(s_i^+) = \boldsymbol{x}(s_i^-) + c_i(s_i^-,\boldsymbol{x}(s_i^-)), \\ \boldsymbol{g}_i(t,\boldsymbol{x}(t),\boldsymbol{u}(t)) \geq \boldsymbol{0}, \text{ for } t \in \mathcal{I}_i, \\ \boldsymbol{r}_{eq}(\boldsymbol{x}(s_0),\ldots,\boldsymbol{x}(s_{n_{ph}}),\boldsymbol{p}) = \boldsymbol{0}, \\ \boldsymbol{r}_{ineq}(\boldsymbol{x}(s_0),\ldots,\boldsymbol{x}(s_{n_{ph}}),\boldsymbol{p}) \geq \boldsymbol{0}, \\ i = 1,\ldots,n_{ph}-1, \;\; s_0 = 0, \;\; s_{n_{ph}} = T, \end{cases} \\ \text{and } \sum\limits_{k=0}^{n_\omega-1} \omega_i = n_\omega. \end{cases} \tag{7.16}$$

Note, that the last equation is only needed for the solution algorithm COBYLA[1] from the open-source library NLOPT[2]. Using the solution algorithm BOBYQA [147] one of the weights of the objective function of the inner problem is fixed as a reference. Both algorithms are local, derivative-free and based on methods from Powell. Figure 7.10 visualizes this method.

---

[1] `http://maxima.sourceforge.net/docs/manual/en/maxima_43.html`

[2] `http://ab-initio.mit.edu/wiki/index.php/NLopt`

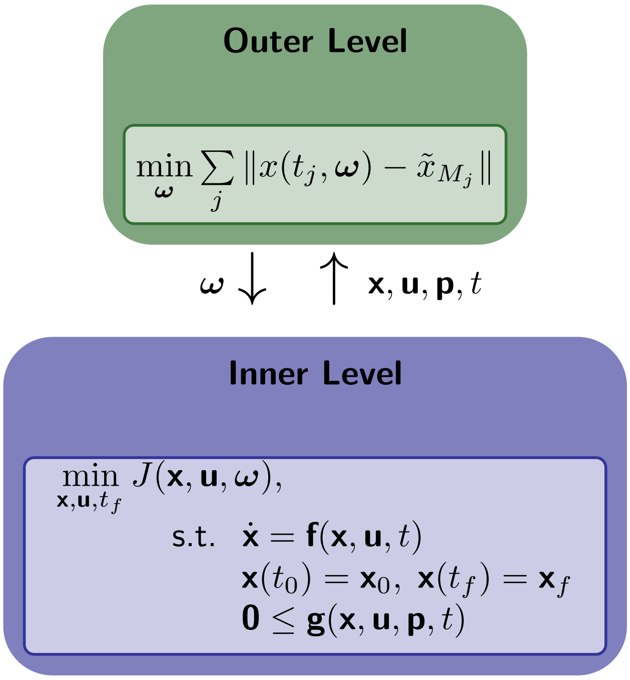

Figure 7.10: Overview of the BiLevel optimal control.

In [19] we investigated inverse optimal control for unperturbed human walking motions regarding the seven different objective functions. The first four are symmetrically grouped minimizations of joint torques: hips, body + neck, legs, and arms. The fifth is a head stabilization criterion followed by a maximization of step length and minimization of end time (maximization of step frequency). Calculating the weights of these objective functions for seven unperturbed walking motions using the inverse optimal control method, we could not identify different walking styles but find a close correlation between the weights of the different motions. These results motivate to further investigate in inverse optimal control formulations also for perturbed motions to also identify objective functions that result in perturbed human walking motions similar to data recorded from humans.

Chapter 8

Optimal Parameters for Compliant Joints During Push Recovery Motion

In Chapter 5 we have studied the torques of experimentally recorded perturbed human walking motions using a rigid multi-body system model, driven by internal joint torque derivatives. As the human body is controlled by muscles that have parallel elastic elements and there is another compliant tissue acting in the joints, this model might not fully capture what happens in the human. The work presented in this chapter enhances the pure human model by taking passive torques into account that act in parallel to the active torques. In the new model, additional spring-damper elements are added in all joints to the active torques, while in the upper body we maintain control by the active joint torques only. The study of human push recovery motions with this compliant model is presented in [95]. Parallel spring-damper elements have previously been introduced in [119] for a simple compass gait walker, in this case optimizing stability. They have also been used later, e.g. in [96] or [161], to optimize active joint torques. The kinematic motion of this model is fitted to motion capture data of a healthy person. Walking motions including pushes from the back are analyzed. Using optimal control the optimal spring design to support the perturbed walking motions is determined. The resulting active and passive joint torques and compliant parameters are analyzed. In this chapter, first, the compliant human model and the optimal control problem formulation for the motion reconstruction, then the numerical results are presented.

8.1 Compliant Human Model

The human model presented in Section 3.1 is controlled by the torques in the joints. This model is very simple and might not be able to fully capture what happens in the human, as the human body is controlled by muscles. A model controlled directly only by the internal joint torques is not able to model the parallel elastic elements and other compliant tissue acting in the joints. To be able to represent the human motion more naturally, a compliant human model which considers passive torques that act in parallel to the active torques, produced by active muscle contraction, is regarded.

Considering the application in robotics, using suitable spring-damper elements in parallel to the robot's actuators, the recovery actions of robots could be much more powerful. Spring-damper elements can produce additional torques that - if parameters are carefully chosen - can support the active torques and allow for higher total torques. Passive elements can help to reduce the average of active torques and to remove torque peaks. The resulting total torques may either be larger than what the actuators alone would be capable to produce or they are produced saving a significant amount of energy compared to the fully active case.

The influence of the stiffness of the joints on human stability abilities has been analyzed as an essential question to better understand human motions in [119]. Winter investigates how the central neural system controls and maintains an upright standing posture using a stiffness model based on the idea that muscles act as springs, [191]. An extensive analysis of the effect of joint stiffness on standing stability is presented in [34]. Fitzpatrick includes perturbation in his studies on stiffness in the ankle joints during standing, [45].

Except for the control in the lower body the compliant model used in our studies is the same as the human model presented in Section 3.1, see Figure 8.1. The model is controlled by the torques in the joints that summarize the influence of all related muscle forces. In the lower body, a spring-damper system is added to each joint to simulate the compliance and damping effects of the tissue, while in the upper body the control by the active joint torques only is maintained.

To model the compliance in the lower body, the total torques acting on each joint in the lower body are computed as a sum of the active and the passive torques

$$\tau_{\text{total}} = \tau_{\text{active}} + \tau_{\text{spring}} + \tau_{\text{damping}} = \tau_{\text{active}} + [-\kappa(q - q_0)] + [-d\dot{q}], \tag{8.1}$$

where κ is the spring constant, q_0 the spring rest position and d the damping constant. These values are assumed to be constant over the gait cycle but differ for each joint in the lower body (right hip, right knee, right ankle, left hip, left knee, left ankle). it is also possible to only include springs or damping elements in only parts of the lower body, see e.g. in the exoskeleton studies in Section 9.3. In the following τ_{active} is also referred to as τ_a. In the upper body, there are no spring-damper elements, such that $\tau_{\text{total}} = \tau_{\text{active}}$.

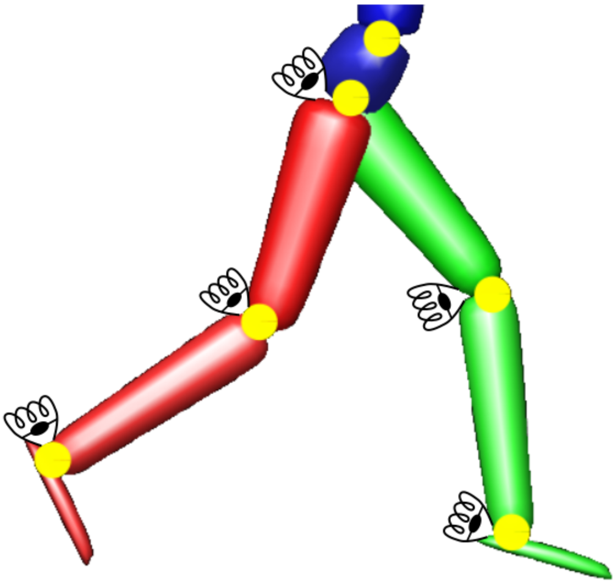

Figure 8.1: The joints and the indication of spring-damper systems at the lower body.

8.2 Optimal Control Problem Formulation

In this section, the human model is used including spring-damper elements in the lower body to mimic the compliant and damping effects of soft tissue in the joints as described in detail in Section 8.1. To analyze the torques in the joints and the according spring and damping parameters, we set up an optimal control problem as presented in Section 4.1.

In this case the system states are defined by $\boldsymbol{x} = (\boldsymbol{q},\dot{\boldsymbol{q}},\boldsymbol{\tau}_a)$ consisting of 16 joint angles $\boldsymbol{q}$, 16 joint angle velocities $\dot{\boldsymbol{q}}$ and 13 active joint torques $\boldsymbol{\tau}_a$. The control is defined by the derivative of the 13 active joint torques: $\boldsymbol{u} = \dot{\boldsymbol{\tau}_a}$. The system parameters $\boldsymbol{p}$ consist of the spring-damper parameters: the spring constant $\boldsymbol{\kappa}$, the spring rest position $\boldsymbol{q_0}$ and the damping constants $\boldsymbol{d}$ of the six lower body joints (hips, knees, and ankles). As for the other motion reconstruction formulations in this thesis, the phase times are fixed.

The objective function is described by

$$\sum_{i=1}^{n_{ph}} \int_{t_i}^{t_{i+1}} \omega_1 \alpha_{1_i} \|\tilde{\boldsymbol{q}}(t) - \boldsymbol{q}(t)\|_2^2 + \omega_2 \alpha_{2_i} \|\boldsymbol{\tau}_a\|_2^2. \tag{8.2}$$

The principal objective function minimizes the distance of the joint angles of the model $\boldsymbol{q}$ to the joint angles form reference data $\tilde{\boldsymbol{q}}$. The second part of the objective function minimizes the active part of the joint torques $\boldsymbol{\tau}_a$ to avoid that active and passive torques counteract. The parts of the objective function are weighted by the respective factors $\omega_i, i = 1,2$ which are chosen such that the first term is dominant.

8.3 Numerical Results

This section is dedicated to present the resulting torques and the corresponding optimal spring and damping parameters for different perturbed walking motions using the methods described in Sections 3 and 4. The main outcome is:

- The resulting model motions show a very good fit to the respective reference motions.
- The spring-damper systems in the lower body support the push recovery motions well.
- The parameters for the optimal spring-damper system vary between joints and motions.

We use the motions from dataset A presented in Section 2.4. Of the unperturbed motions, only the first two are taken into account. To simplify the notation *NoPushA1* is referred to as *NoPush1*, *NoPushA2* as *Nopush2*, *PelvisA* as *Pelvis*, etc. To be able to estimate how good the reference data are represented by the model approximation, the root mean squared error (RMS) of the model fit to the recorded data is calculated, split into a translational and a rotational error, see Table 8.1. The translational error is in the order of $2-3\,\mathrm{cm}$ cm, the rotational error of about $0.08\,\mathrm{rad}$ which can be considered as a very good fit.

Table 8.1: RMS errors of the motion reconstruction for the different considered motions.

RMS	**NoPush1**	**NoPush2**	**Pelvis**	**Middle1**	**Middle2**	**Upper1**	**Upper2**
Translation [m]	0.0136	0.0303	0.0000	0.0140	0.0141	0.0223	0.0200
Rotation [rad]	0.0515	0.837	0.0612	0.0632	0.0728	0.0648	0.0852

The optimal passive parameters for the spring-damper system in the lower body of the two-dimensional human model obtained from optimization differ not only between the joints but also between the regarded push recovery motions, see Table 8.2. The table shows the parameters of the spring-damper system as described in Section 3.1. The spring-damper system consists of three parameters: the damping parameter d, the spring parameter k and the spring rest position q_0. In this set of computations, the damping parameters in the hips are predefined to be zero; this is not a result of the computations. Other predefined choices are possible. Since the results are different in all cases studied, no general rules can be extracted except for the fact that the springs chosen for the stance leg are in general more powerful than the ones for the swing leg. A push seems to result in a stiffening of the stance leg while the swing leg is performing a fast swing forward.

Table 8.2: Optimal parameters of the spring-damper system in the lower body for the different motions.

	Motion	**Right Hip**	**Right Knee**	**Right Ankle**	**Left Hip**	**Left Knee**	**Left Ankle**
Damping	**NoPush1**	0	1.2617	0	0	0.8485	0.0340
	NoPush2	0	0	40	0	9.3087	24.5631
	Pelvis	0	7.4158	0.2788	0	0.2054	2.6485
	Middle1	0	3.9953	3.0880	0	1.4429	0.0474
	Middle2	0	1.4943	2.5114	0	0.4455	6.7618
	Upper1	0	1.8783	9.9746	0	1.5280	4.5959
	Upper2	0	1.6925	0.8268	0	0.4976	0.7795
RestPosition	**NoPush1**	0.3890	0.5580	1.0914	-0.6548	2.8659	-0.4816
	NoPush2	0.0407	0.7758	-1.6196	-0.0136	-1.5000	-1.8726
	Pelvis	0.6715	2.8920	0.8239	-3.4000	1.7477	-1.1638
	Middle1	0.3017	0.9100	1.2381	-3.4000	0.0919	-2.0000
	Middle2	-0.0797	1.2819	0.8493	0.4053	1.4626	-1.9638
	Upper1	0.2488	1.0199	1.1275	-0.5963	0.8170	-0.0024
	Upper2	1.3215	4.0000	1.1169	2.6000	4.0000	-0.6365
Spring	**NoPush1**	44.6747	130.6309	98.5722	10.9334	1.4903	0.5368
	NoPush2	79.8886	45.3160	0	14.3046	7.1295	8.9816
	Pelvis	14.4837	16.2579	117.9589	1.5480	3.9411	2.0012
	Middle1	54.4637	75.6381	88.8963	1.5235	0	0.4452
	Middle2	20.6783	30.4898	105.7615	6.9194	9.8413	0.6210
	Upper1	94.0943	76.9136	76.2269	26.4361	12.4060	32.3095
	Upper2	28.9122	16.6638	86.5982	0.4121	1.5633	1.7684

In general, the spring-damper systems support the joints very well, see Figure 8.2. The figure shows the average percentage of the active and the passive part of the total torque calculated by

$$P_{\text{active}} = \frac{\int_0^T |\tau_{active}(t)|dt}{\int_0^T |\tau_{total}(t)|dt} \approx \frac{\sum_{i=1}^n |\tau_{active}(t_i)|\Delta t_i}{\sum_{i=1}^n |\tau_{total}(t_i)|\Delta t_i} \tag{8.3}$$

and

$$P_{\text{passive k, d}} = \frac{\int_0^T |\tau_{passive\,k,d}(t)|dt}{\int_0^T |\tau_{total}(t)|dt} \approx \frac{\sum_{i=1}^n |\tau_{passive\,k,d}(t_i)|\Delta t_i}{\sum_{i=1}^n |\tau_{total}(t_i)|\Delta t_i} \tag{8.4}$$

with τ_{total} according to Equation (8.1), $\tau_{passive\,k,d} = \tau_{\text{spring}} + \tau_{\text{damping}}$ and $\Delta t_i = t_i - t_{i-1}$, which uses a discrete evaluation of the respective torques at n points along the motion. In all the joints and for all motions the active torque percentage is smaller than one (i.e. smaller than 100%) which means that the active torque is smaller than the total required torque. It is very small in most cases, meaning that the largest part is contributed by the passive elements. We, therefore, can conclude that the spring-damper system supports the motion in all cases. The sum of passive and active torque percentages is larger than one in most cases which means that it is not possible to find linear spring-dampers that support the motion at each instant in time, but that sometimes counteraction is necessary - though it is kept minimal due to the chosen objective function.

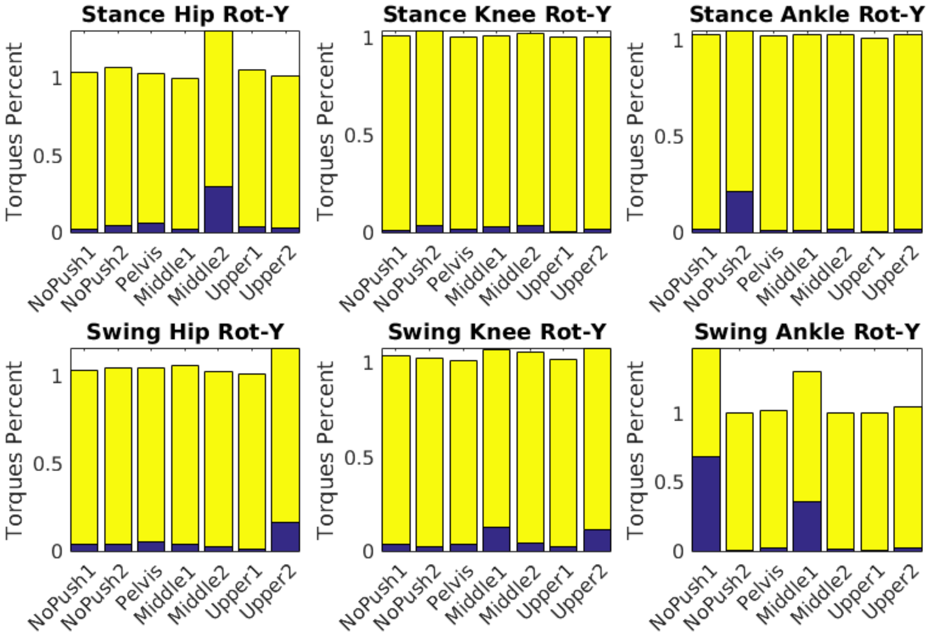

Figure 8.2: Percentage of the active (blue) and passive (yellow) part of the joint torques.

The support of the spring-damper system can also be observed regarding Figure 8.3-8.9. The figures show the different parts of the total torque (solid line): the damping torque (dotted line), the spring torque (dashed-dotted line) and the active torque (dashed line) during the whole step for the different push recovery motions. In all the plots the integral over the absolute values of the active torque is much smaller than the one of the total torques (which would have to be generated by the actuator alone if no passive elements were present), because of the contributions of the spring and damper torques.

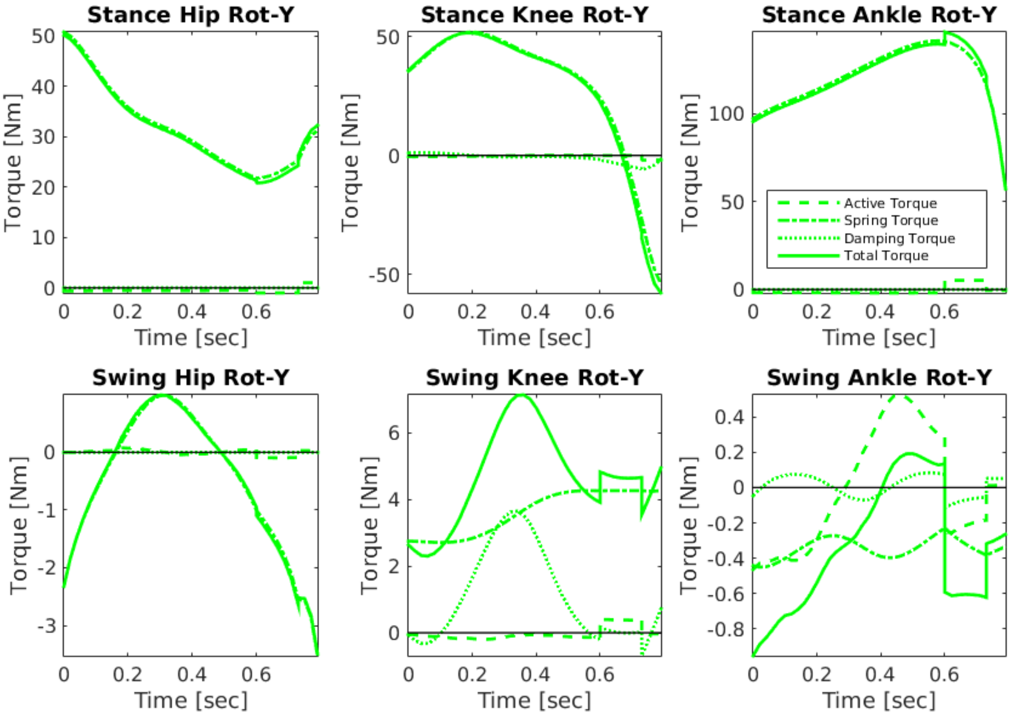

Figure 8.3: Different torque types for push case “NoPush1” : Damping (dots), spring (dotted dashed), active (dashed) and total (solid) torques.

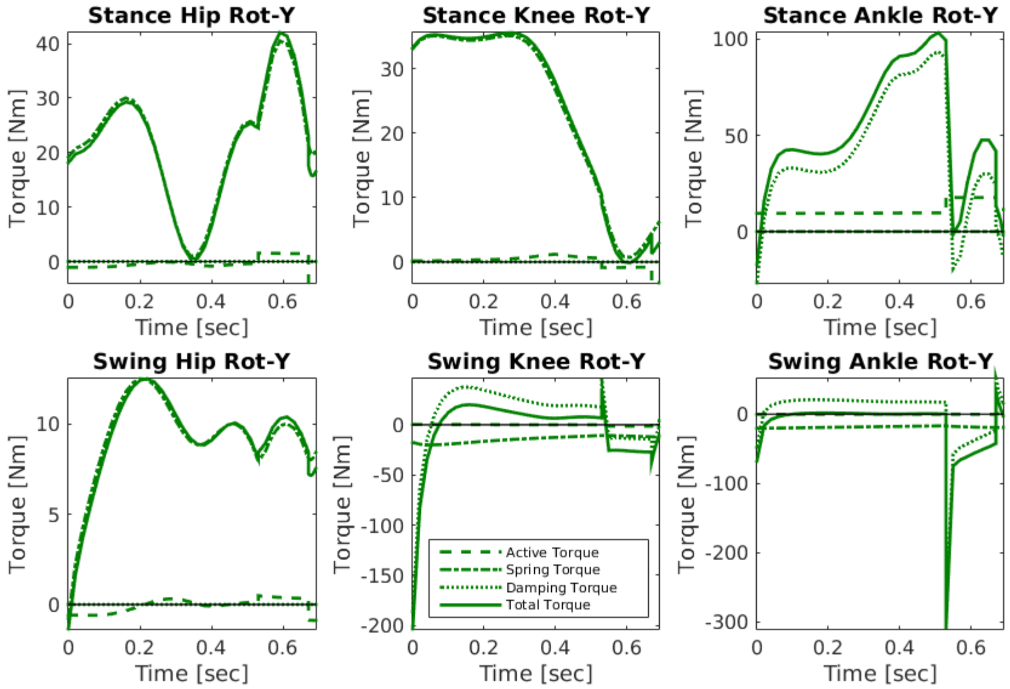

Figure 8.4: Different torque types for push case “NoPush2” : Damping (dots), spring (dotted dashed), active (dashed) and total (solid) torques.

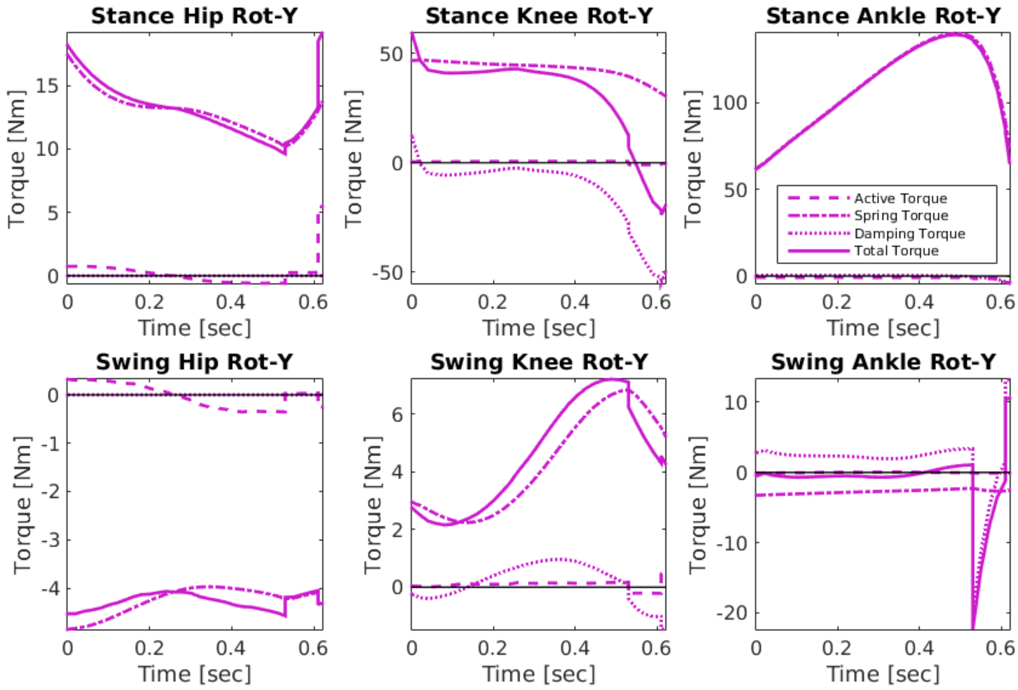

Figure 8.5: Different torque types for push case “Pelvis” : Damping (dots), spring (dotted dashed), active (dashed) and total (solid) torques.

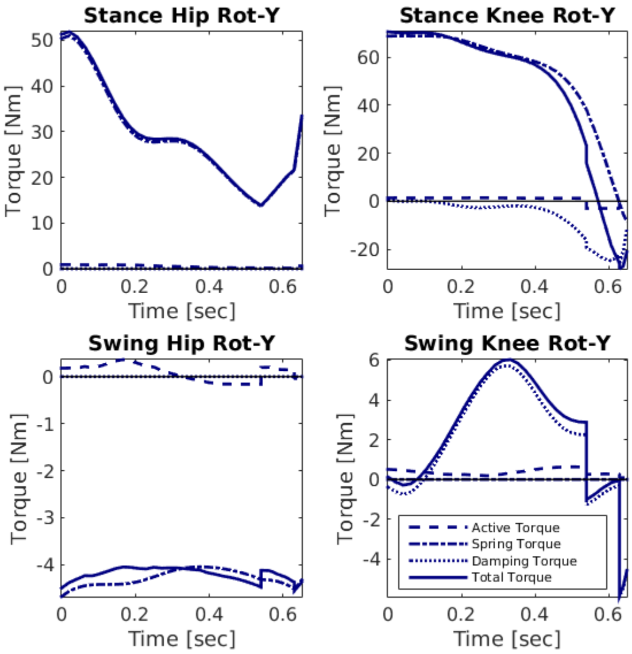

Figure 8.6: Different torque types for push case “Middle1” : Damping (dots), spring (dotted dashed), active (dashed) and total (solid) torques.

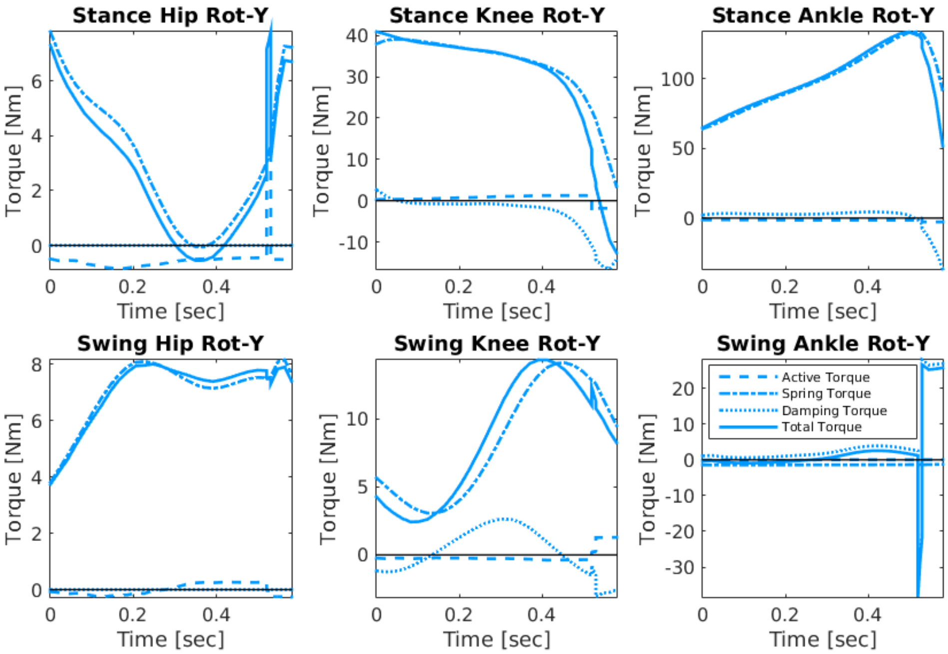

Figure 8.7: Different torque types for push case “Middle2” : Damping (dots), spring (dotted dashed), active (dashed) and total (solid) torques.

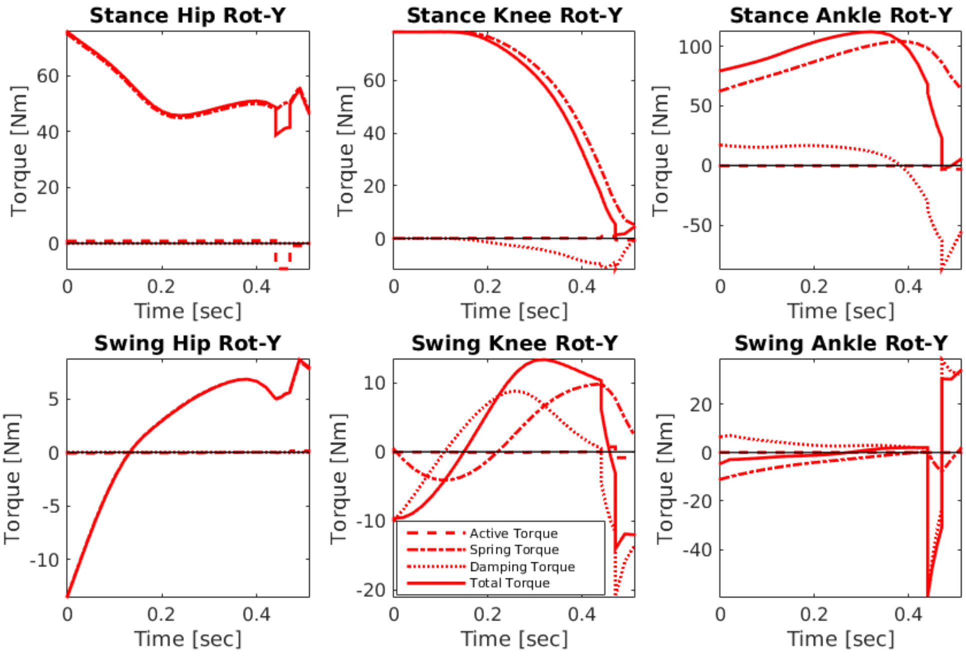

Figure 8.8: Different torque types for push case "Upper1" : Damping (dots), spring (dotted dashed), active (dashed) and total (solid) torques.

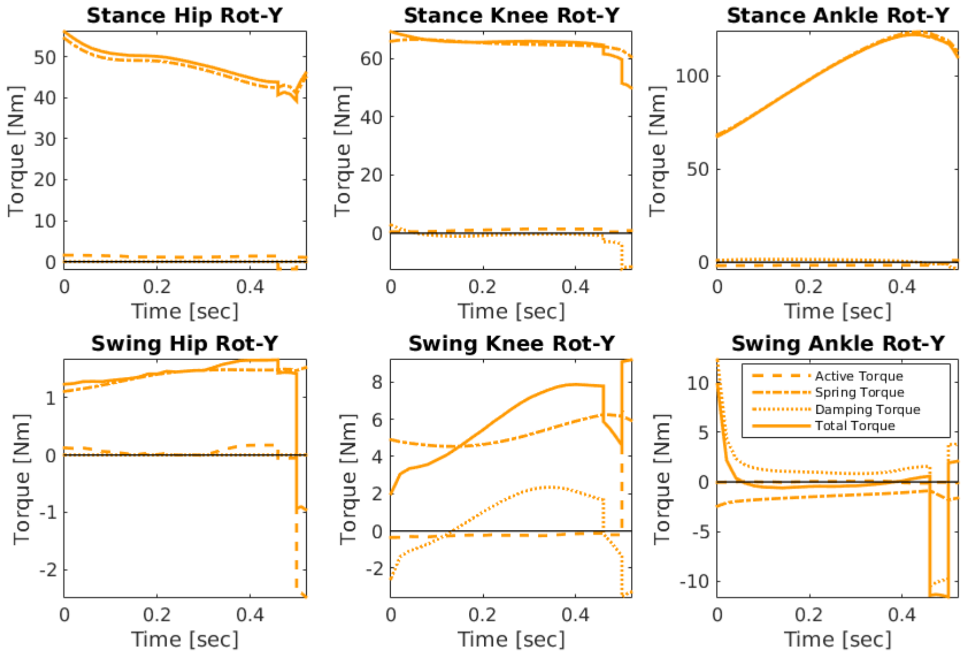

Figure 8.9: Different torque types for push case "Upper2" : Damping (dots), spring (dotted dashed), active (dashed) and total (solid) torques.

Chapter 9

Human Push Recovery Steps with Exoskeletons

Most people take it for granted to be able to move independently in their daily environment. Being forced to sit in a wheelchair, because the ability to walk has been lost, represents a severe cut in self-directed life. Exoskeletons provide a very promising future approach to help people, who still have both legs, but are not able to move them, to walk freely in their environment again and also to talk to people on eye level. Exoskeletons are robotic devices that are attached to the human body to support the motion by inducing external forces. They exist for different parts of the body to support different types of motions; for the described walking motion support obviously, exoskeletons for the lower limbs are most interesting.

Exoskeletons that provide full support for walking motions for daily life are still subject of current research. One difficulty in designing such devices is to estimate how strong the actuators of the exoskeleton have to be to fully drive the motion of the combined human-exoskeleton system during highly dynamic motions. It is important to consider that the exoskeletons must not only be able to support nominal motion situations such as walking in different terrains, but they also must be able to support recovery motions from large perturbations that may always occur.

In [32] the history of exoskeletons is summarized and the state-of-the-art development of lower limb exoskeletons and active orthoses is discussed. A design overview of the hardware, actuation, sensory and control systems for a large set of devices described in the literature is given. Herr provides in [59] a classification of exoskeletons into series exoskeletons and those parallel to the human limb, providing examples for each category. He also points out the challenges in the design of the different types of exoskeletons and gives future directions.

In [180] and [186] the advantages and feasibility of using compliant actuators in exoskeletons and the resulting need for smaller batteries are analyzed. Walsh et al. substitute the actuators in an exoskeleton by spring and damper elements to improve load-carrying for strong healthy subjects during slow walking, see [185]. However, this approach is not generalizable to provide full walking support for pathological gait with no actuation of the human. Also in [16] the requirement that must be fulfilled by compliant actuators is given. Rigid actuators usually consume more energy and may not be appropriate for human-machine interactions as requested for the use in exoskeletons. Apart from this advantage, compliant actuators improve the joint control by efficiently absorbing perturbations due to spasticity and spasmodic movements.

The approach of using inverse dynamics to estimate the joint torques during motions wearing exoskeletons is common in literature. However, most of the studies use immensely simplified models in which only the human, not the exoskeleton is modeled [72] or only the exoskeleton, but not the human is modeled, see [196, 121]. Often the joint torques of the exoskeleton are measured in experiments by torque sensors included in the exoskeleton, e.g. [72]. Hwang made investigations to evaluate the joint torques in the lower limb (hip and knee joint) during gait using torque sensors of an exoskeleton robot [72]. In [110] the joint torque in the human knee during level-ground walking is compared to torques in a knee prosthesis. Some researchers put a dummy human (which has the mass distribution of a human) into the exoskeleton to measure the joint torques necessary to move the human who does not move at all by himself, see [164]. A disadvantage of this approach is, that only motions of existing exoskeletons can be analyzed. With the simulation-based approach presented in this thesis, it is possible to even compute the joint torques needed for an exoskeleton that has not yet been built using the preliminary mass distribution. Based on the results, design suggestions can be made. Having developed and built a new exoskeleton based on the results of our approach, the method described above can then be used for validation purposes.

In the presented studies, combined human-exoskeleton models, based on the exoskeleton data from [92] are presented. The models can recover from large perturbations in the sagittal plane are presented. The inertia terms and masses of a human dynamics model are augmented by the terms representing the exoskeleton which is assumed to be fixed to the respective human segments. The combined human-exoskeleton model assumes that the joints of the exoskeleton are perfectly aligned at all times. Two exoskeleton configurations that differ mostly in weight are considered (Study 1). Additionally, a new compliant lower-limb exoskeleton model is studied (Study 2). In addition to the simulation of walking motions, our models allow for external impacts to simulate perturbations. In this work we consider pushes to the back of different strengths applied at different heights along the spine. Figure 9.1 shows an example of recovery motion from a push applied at the upper trunk. There is one picture for each start of the phases described in Section 3.3 and one during the phase and one for the end position of the motion. The kinematics (joint angles) of the combined human-exoskeleton models and the human model are fitted to reference data from motion capture experiments (see the white model in Figure 9.1) to determine and compare the joint torques as in [158]. The main contribution of these studies is the analysis of torques in the lower body during push recovery walking motions in rigid and compliant combined human-exoskeleton models. They are presented in [160] and [94]. The results can be used to improve the design of exoskeletons.

In the following Section 9.1, the human and the rigid and the compliant combined human-exoskeleton models are described. After a detailed analysis of the internal joint torques of the human model and the combined human-exoskeleton models for different motions with and without perturbation in a first study (see Section 9.2), the compliance parameters of the compliant combined human-exoskeleton model are analyzed in a second study (see Section 9.3).

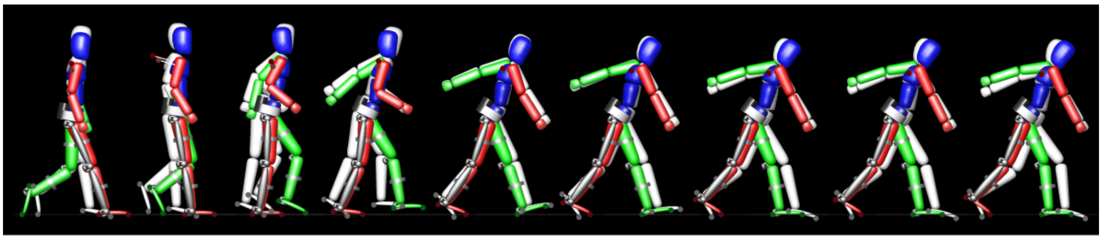

Figure 9.1: A picture series of a push recovery motion. The colored figures with the exoskeleton show the reconstructed motion of the compliant combined human-exoskeleton model, the white figure the reference data. There is one picture for each start of the phases described in Section 3.3 and one during the phase and one for the end position of the motion.

9.1 Exoskeleton Models

In this section the models used in the two studies presented in this chapter are described in detail. First two human-exoskeleton models driven by joint torques are introduced. How to include compliant actuators into these combined human-exoskeleton models is explained in the second part of this section.

9.1.1 Human-Exoskeleton Model

The combined human-exoskeleton models are shown in Figure 9.2. They are described by the same dynamical equations as the human model used for the motion reconstruction and motion synthesis studies in Chapter 5 and 7. The upper body joint torques are still generated only by human muscle torques but in the lower limb a combination of muscle torques and the forces provided by the exoskeleton lead to the total torque to execute a movement. To simulate the exoskeleton the masses and inertia terms of the original human segments are adjusted such that the segments in the new body context behave similar to the segments of the combined human-exoskeleton presented in [92], see Table 9.1. The data in the table are given as the percentage of the total human mass and height. To include them in the model, they are multiplied by the human body mass of $m = 75\,\mathrm{kg}$ for the human model, and by the sum of the human and the exoskeleton for the combined human-exoskeleton models:

- Human-exoskeleton HExo1: $83.333\,\mathrm{kg} = m * (1 + \frac{1}{9})$,
- Human-exoskeleton HExo2: $100\,\mathrm{kg} = m * (1 + \frac{1}{3})$.

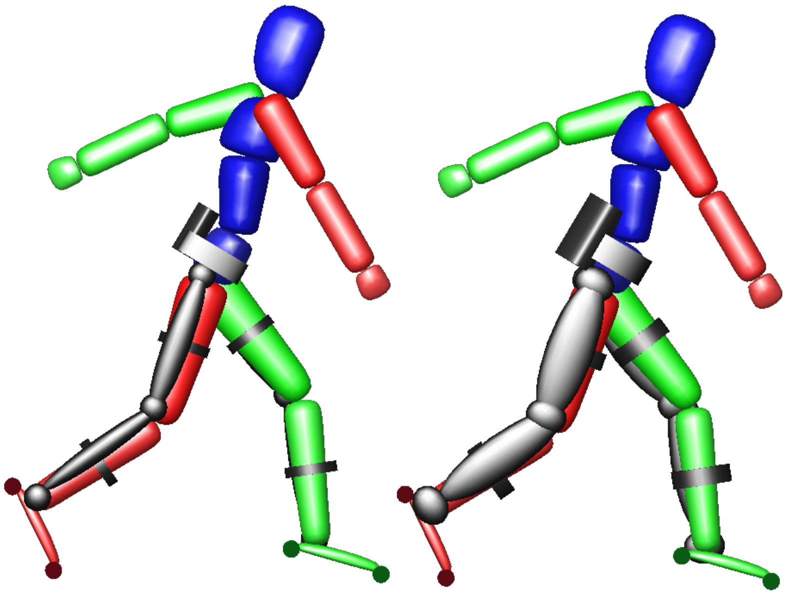

Figure 9.2: Left: the rigid combined human-exoskeleton model 1 (lighter exoskeleton), right: the rigid combined human-exoskeleton model 2 (heavier exoskeleton).

In the presented work, the motion data for the human and the exoskeletons are taken from measurements of the pushed person during motion capture experiments and [92]. The values of exoskeleton segments are combined to groups and added to the values of the thigh, shank, and foot of the human model using the following formulas

- for the masses $m_c = m_h + m_e$,
- for the center of mass $C_c = \frac{1}{m_c}(C_h m_h + C_e m_e)$,
- for the inertia term $I_c = I_h + m_h d_h^2 + I_e + m_e d_e^2$,
  where d_e defines the distance from the CoM of the exoskeleton segment to the corresponding CoM of combined human-exoskeleton segment C_c, d_h the according distance for the human.

Variables with the index c refer to the combined model, with h to the human model and e to the exoskeleton. The gyration terms are calculated by

$$g = \frac{1}{l}\sqrt{\frac{I}{m}}, \tag{9.1}$$

where l is the segment length.

Table 9.1: Parameters of the human model and the two combined human-exoskeleton models. The masses and segment lengths are given relative as the percentage of the total body mass and height. The center of mass is given relative to the respective segment length.

Segment	CoM Human			CoM HExo1			CoM HExo2		
	C_x	C_y	C_z	C_x	C_y	C_z	C_x	C_y	C_z
Lower Trunk	0.	0.	0.6115	0.	0.	0.6027	0.	0.	0.5859
Middle Trunk	0.	0.	0.4502	0.	0.	0.4502	0.	0.	0.4502
Upper Trunk	0.	0.	0.2999	0.	0.	0.2999	0.	0.	0.2999
Thigh	0.	0.	-0.3918	0.0203	0.0037	-0.3853	0.0469	0.0085	-0.3769
Shank	0.	0.	-0.4392	0.0502	0.0061	-0.4111	0.0880	0.0107	-0.3900
Foot	0.1576	0.	-0.6168	0.1338	0.	-0.5340	0.1129	0.	-0.4615
Upper Arm	0.	0.	-0.7461	0.	0.	-0.5772	0.	0.	-0.5772
Lower Arm	0.	0.	-0.4107	0.	0.	-0.4574	0.	0.	-0.4574
Hand	0.	0.	-0.7900	0.	0.	-0.7900	0.	0.	-0.7900
Head	0.	0.	0.5002	0.	0.	0.5002	0.	0.	0.5002

	Gyration Human			Gyration HExo1			Gyration HExo2		
	g_x	g_y	g_z	g_x	g_y	g_z	g_x	g_y	g_z
Lower Trunk	0.	0.	0.6115	0.	0.	0.6027	0.	0.	0.5859
Middle Trunk	0.	0.	0.4502	0.	0.	0.4502	0.	0.	0.4502
Upper Trunk	0.	0.	0.2999	0.	0.	0.2999	0.	0.	0.2999
Thigh	0.	0.	-0.3918	0.0203	0.0037	-0.3853	0.0469	0.0085	-0.3769
Shank	0.	0.	-0.4392	0.0502	0.0061	-0.4111	0.0880	0.0107	-0.3900
Foot	0.1576	0.	-0.6168	0.1338	0.	-0.5340	0.1129	0.	-0.4615
Upper Arm	0.	0.	-0.7461	0.	0.	-0.5772	0.	0.	-0.5772
Lower Arm	0.	0.	-0.4107	0.	0.	-0.4574	0.	0.	-0.4574
Hand	0.	0.	-0.7900	0.	0.	-0.7900	0.	0.	-0.7900
Head	0.	0.	0.5002	0.	0.	0.5002	0.	0.	0.5002

	Length all Models	Mass Human	Mass HExo1	Mass HExo2
	$[l]$	$[m]$	$[m]$	$[m]$
Lower Trunk	0.0837	0.1117	0.102	0.0874
Middle Trunk	0.1238	0.1633	0.1467	0.1225
Upper Trunk	0.098	0.1596	0.1436	0.1197
Thigh	0.2425	0.1416	0.1499	0.1624
Shank	0.2529	0.0433	0.0605	0.0863
Foot	0.0200	0.0137	0.0176	0.0235
Upper Arm	0.1618	0.0271	0.0244	0.0203
Lower Arm	0.1545	0.0162	0.0146	0.0122
Hand	0.0495	0.0061	0.0055	0.0046
Head	0.1395	0.0694	0.0625	0.0521

The human and the combined human-exoskeleton models do not differ in the body height of 1.8 m. Also, the segment lengths are the same in all models considered. If the data of a specific human and exoskeleton is available, the data for the combined model can be calculated using these formulae. As the presented data are scaled to the body mass and height, they can be used for a person of any weight combined with an exoskeleton weighting $\frac{1}{9}$ or $\frac{1}{3}$ of the human body weight.

9.1.2 Compliant Human-Exoskeleton Model

Based on the rigid combined human-exoskeleton model (HExo1) from the previous Section 9.1.1 and the compliant model from Section 8.1 spring-damper systems are included in all exoskeleton joints in the lower body to model the compliance of the exoskeleton

$$\begin{array}{cccccc} \tilde{\boldsymbol{\tau}} & = \tilde{\boldsymbol{\tau}}_{\boldsymbol{a}} & + \underbrace{[-\kappa(\boldsymbol{q}-\boldsymbol{q}_0)]} & + \underbrace{[-d\dot{\boldsymbol{q}}]} \\ = \tilde{\boldsymbol{\tau}}_{\text{total}} & = \tilde{\boldsymbol{\tau}}_{\text{active}} + & \tilde{\boldsymbol{\tau}}_{\text{spring}} & + \tilde{\boldsymbol{\tau}}_{\text{damping}}, \end{array} \tag{9.2}$$

where κ is the spring constant, q_0 the spring rest position and d the damping constant. This results in the new model HExoCompl shown in Figure 9.3. During the gait cycle, the values are set constant, but they differ for each of the exoskeleton joints in the ankles, the knees, and the hips. In the hip and in the knee, only springs are included. Only in the ankle joint, the damping parameter is not zero. Indifference to the work presented in Chapter 8, the values are set to the same constant for each leg. The reason is that while in Chapter 8 the spring-damper component was supposed to describe the compliance effect of the human muscles which can be assumed to be adjustable, here the spring-damper element describes a mechanical component of the exoskeleton which must be assumed to be constant and symmetric, since recovery motions should be equally possible with both legs. This results in the same spring-damper system in the left as in the right leg. This is important to include it into an exoskeleton if it is not possible to switch between different spring-damper configurations according to the different gait phases. Nowadays, there exist spring-dampers that allow for a change of parameters during a motion. Note, that for the human and the rigid combined human-exoskeleton models the total torque is equal to the active torque: $\tilde{\boldsymbol{\tau}} = \tilde{\boldsymbol{\tau}}_a$.

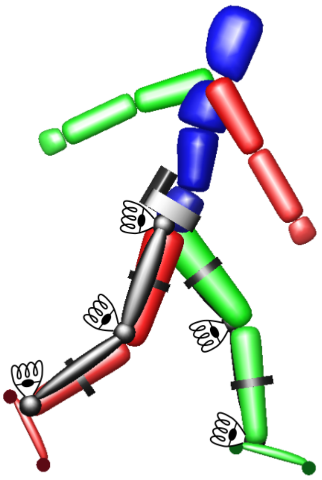

Figure 9.3: The compliant combined human-exoskeleton model HExoCompl.

9.2 Exoskeleton Parameter and Torque Analysis

In a first study the torques needed for perturbed human gait for the two combined human-exoskeleton models are analyzed.

9.2.1 Optimal Control Problem Formulation

To fit the combined human-exoskeleton models to reference data from experiments we define the following objective function for the optimal control problem presented in Section 4.1

$$\min_{\boldsymbol{x},\boldsymbol{u}} \sum_{j=1}^{n_{ph}} \int_{t_{j-1}}^{t_j} \omega_1 \sum_{k=0}^{n_q} \alpha_{1_k} (q_k(t) - \tilde{q}_k(t))^2 + \sum_{i=0}^{n_u} \omega_2 \alpha_{2_i} (\phi_i(t))^2. \tag{9.3}$$

The objective function (9.3) is formulated to determine the derivatives of the actuated joint torque trajectories $\dot{\tilde{\boldsymbol{\tau}}}_{\boldsymbol{a}}(t)$ that lead to joint angles $\boldsymbol{q}(t)$ that are as close as possible to the joint angles from reference data $\tilde{\boldsymbol{q}}$ while fulfilling several constraints. In addition we add the further criterion, which is a suitably minimization of all squared active actuated joint torque derivatives as regularization term for this study:

$$\phi(t) = \boldsymbol{u}(t) = \dot{\tilde{\boldsymbol{\tau}}}_{\boldsymbol{a}}(t), \tag{9.4}$$

scaled by the constants α_{m_n}, $n \in k,i$, $m = 1,2$. The parts of the objective function are weighted by constants ω_m, $m = 1,2$.

The states of the OCP are defined by the vector $\boldsymbol{x} = (\boldsymbol{q},\dot{\boldsymbol{q}},\tilde{\boldsymbol{\tau}}_{\boldsymbol{a}})^T$, consisting of the 16 joint angles $\boldsymbol{q}$, the according joint angle velocities $\dot{\boldsymbol{q}}$ and the 13 active actuated joint torques $\tilde{\boldsymbol{\tau}}_{\boldsymbol{a}}$, resulting in 45 state variables in total. The controls $\boldsymbol{u}$ of the OCP in this chapter are described by the time derivatives of the 13 active actuated joint torques $\dot{\tilde{\boldsymbol{\tau}}}_{\boldsymbol{a}}$ to smoothen the active actuated joint torques $\tilde{\boldsymbol{\tau}}_{\boldsymbol{a}}$. As in the other motion reconstruction cases for the human model, we do not have any parameters in the optimization. The phase times are fixed.

9.2.2 Results

In this section the torques during a set of different perturbed walking motions for the human model described in Section 3.1 are compared to the ones for the rigid combined human-exoskeleton models described in Section 9.1.1. The motions regarded in this study are those from dataset A described in Section 2.4. (Only two representative unperturbed motions are chosen: NoPushA1 and NoPushA2.) Again to simplify the notation *NoPushA1* is referred to as *NoPush1*, *NoPushA2* as *Nopush2*, *PelvisA* as *Pelvis*, etc. In the plots, they are distinguished by colors (no push (green), push at the pelvis (purple), push at the middle trunk (blue), push at the upper trunk (red/orange)). The models are distinguished by line styles: human model (solid lines), HExo1 (dashed lines) and HExo2 (dotted lines).

The main outcomes are:

- The human model, as well as the rigid combined human-exoskeleton models, can mimic the high dynamical push recovery motions very well.
- The heavier the exoskeleton, the higher the flexion torques in the lower limb joints.
- The flexion torques in the stance hip and knee, as well as the extension torques in the body (lumbar and thorax), are the larger, the higher the push point at the body.

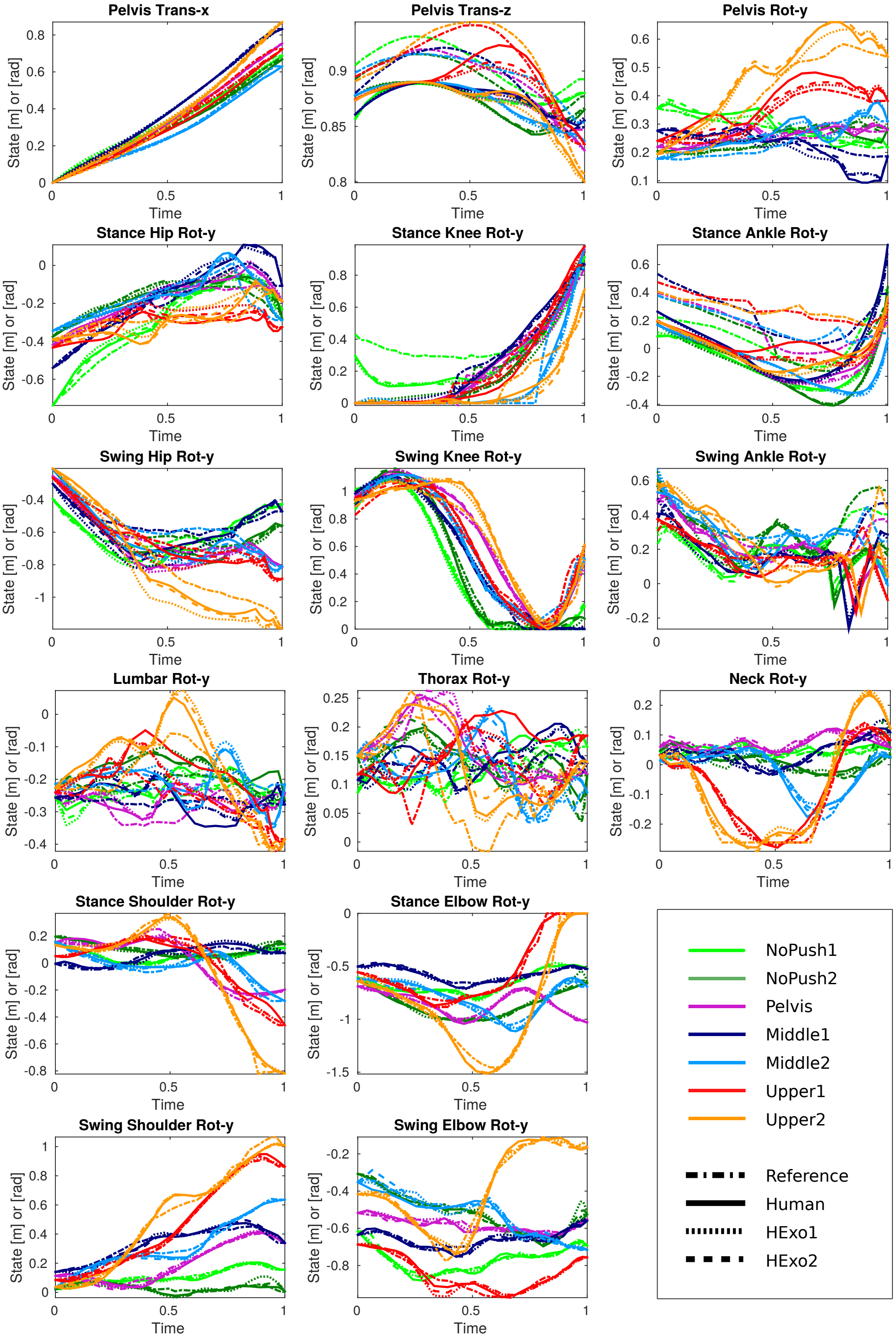

Figure 9.4: Position variables (joint angles, orientation about y-axis and translation in x- and z-direction of pelvis) for the different trials (green: no push, purple: pelvis, blue: middle trunk, red/orange: upper trunk) for the reference data (dashed-dotted lines), the human model (solid lines) and the two rigid combined human-exoskeleton models (dashed lines: HExo1, dotted lines: HExo2).

Before analyzing the torques of the human and the rigid combined human-exoskeleton models the joint angles of the models are compared to the reference data. Figure 9.4 shows the similarity of the joint angles and the transitions of the pelvis between the resulting motions of the regarded models and the reference data. The stance elbow/shoulder describes for the arm corresponding to the stance leg. The same holds for the swing arm segments. Compared to the other joints, a higher deviation in the ankle joints and the pelvis-height position can be observed. This is since our model assumes firm contact of the feet with the ground which is not necessarily the case for our reference data. Another reason for this observation is that our model has a stiff flat foot, while a real human can bend the foot and role over the ground more smoothly. The RMS errors of all joints are in the small range of 1 cm and 0.5° for the human model and the rigid combined human-exoskeleton models. Therefore, we are satisfied that our models give good approximations of the human movement.

Now, the resulting torques for the human and the two rigid combined human-exoskeleton models are analyzed. First, the differences between the torques of the human and the combined human-exoskeleton models are presented in detail, then the torques of the perturbed and unperturbed motions are compared.

The mean torques per motion are

$$\tau_{\text{mean}} = \frac{1}{t_{n_{ph}}} \sum_{j=1}^{n_{qa}} \sum_{i=1}^{N} |\tau_j(t_i)| \, (t_i - t_{i-1}), \tag{9.5}$$

where N is the overall number of shooting nodes from the optimization, $t_{n_{ph}}$ the duration of the motion and n_{q_a} the number of actuated joints.

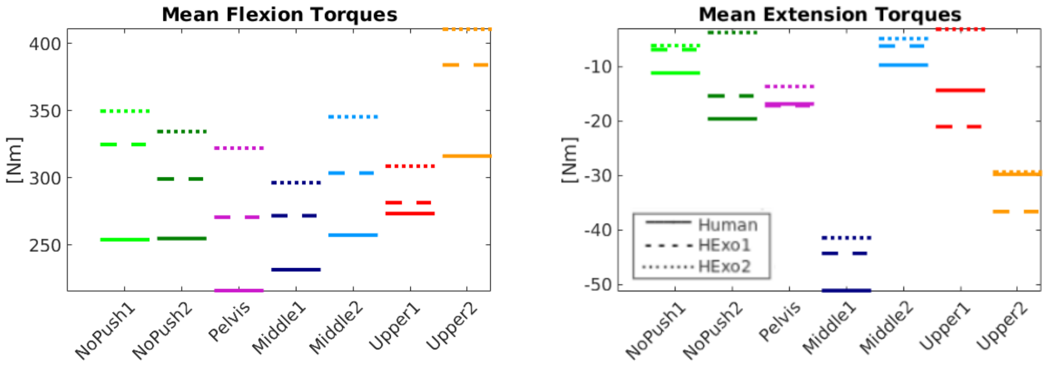

Figure 9.5: The mean flexion (left) and extension torques (right) over the lower limb joints for the different motions (green: no push, purple: pelvis, blue: middle trunk, red/orange: upper trunk). The different model configurations are differenced by different line styles (solid lines: human model, dashed lines: HExo1, dotted lines: HExo2).

The mean flexion (left) and extension (right) torques in the lower limb and upper body for the different models and motions are plotted in Figures 9.5 and 9.6. First, the differences between the joint torques of the different models are compared. Then, we investigate in the comparison of the extension and flexion torques for the different push locations.

For all motions, the flexion joint torques in the lower limb are higher the heavier the exoskeleton (9.5, left). The flexion torques for the human model are the smallest. For all motions, the flexion torques for the heavier exoskeleton are larger than for the lighter exoskeleton. The extension torques are signigicantly smaller than the flexion torques (9.5, right). In the lower limb, the extension torques for the human model are larger than for the combined human-exoskeleton models for some motions. Furthermore, the heavier human-exoskeleton model does not always result in the largest joint torques compared to the lighter one.

Regarding the upper body, the flexion, as well as the extension torques, do not differ a lot, see Figure 9.6. For most motions, the torques for the human model are larger than those for the combined human-exoskeleton models. The flexion torques in the upper body are much smaller than in the lower body. The extension torques in the upper body are of a similar magnitude as those in the lower body.

Considering the mean extension torques (see Figure 9.6) the minimal extension torques for the upper body pushes is significantly smaller than for the rest of the motions. However regarding the mean flexion torques (see Figure 9.5) an increase of the mean torques for the motions with a perturbation in comparison to the motions without a perturbation cannot be observed.

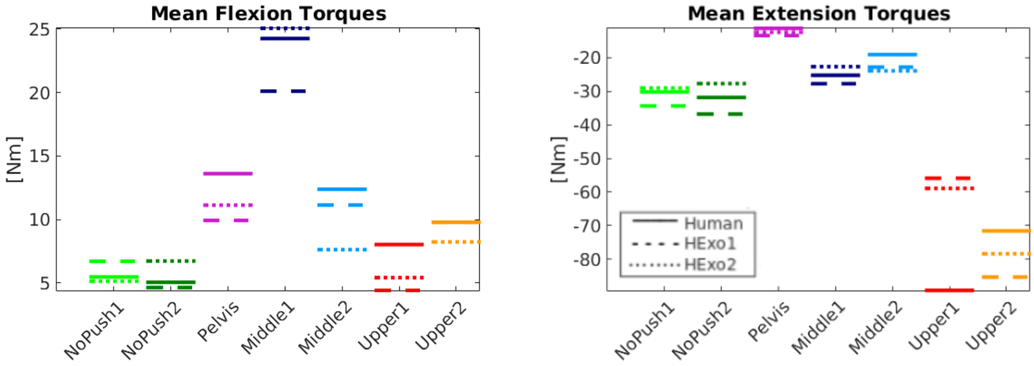

Figure 9.6: The mean flexion (left) and extension torques (right) over the upper body joints for the different motions (green: no push, purple: pelvis, blue: middle trunk, red/orange: upper trunk). The different model configurations are differenced by different line styles (solid lines: human model, dashed lines: HExo1, dotted lines: HExo2).

Therefore in Figure 9.7 the maximal torques of all flexion joint torques and the minimal torques of all extension joint torques of the motions are plotted for the different joints. Also, the maximal and the minimal torques needed for the unperturbed motions are marked by thick green horizontal lines. This is either equal to the NoPush1 or the NoPush2 line. For the stance hip and knee, the maximal flexion torques are larger the higher the push point is located at the body. The same holds for the minimal extension torque in the lumbar and in the thorax. In the stance leg and in the swing leg, the torques for the unperturbed motions are higher than for the perturbed motions for nearly all motions. In the arms, the maximal flexion torques of the unperturbed motions are half of the magnitude of the maximal flexion torques regarding the perturbed motions. For nearly all motions, the minimal extension torques for the unperturbed motions is smaller than for the perturbed motions in the arms and in the neck.

Regarding the swing hip, the stance hip and the stance knee, the torques needed for the perturbed motions are distinctly higher than the ones needed for the motions without a perturbation. For one of the pushes at the upper body (Upper2, orange) the required torques are more than twice as high than for unperturbed motions for one of the exoskeletons (HExo1, dashed line). This can also be observed for the swing hip. The increase of maximal joint torque needed for perturbed motions has to be considered in the design of an exoskeleton that can recover from a push by increasing the power of those joints significantly.

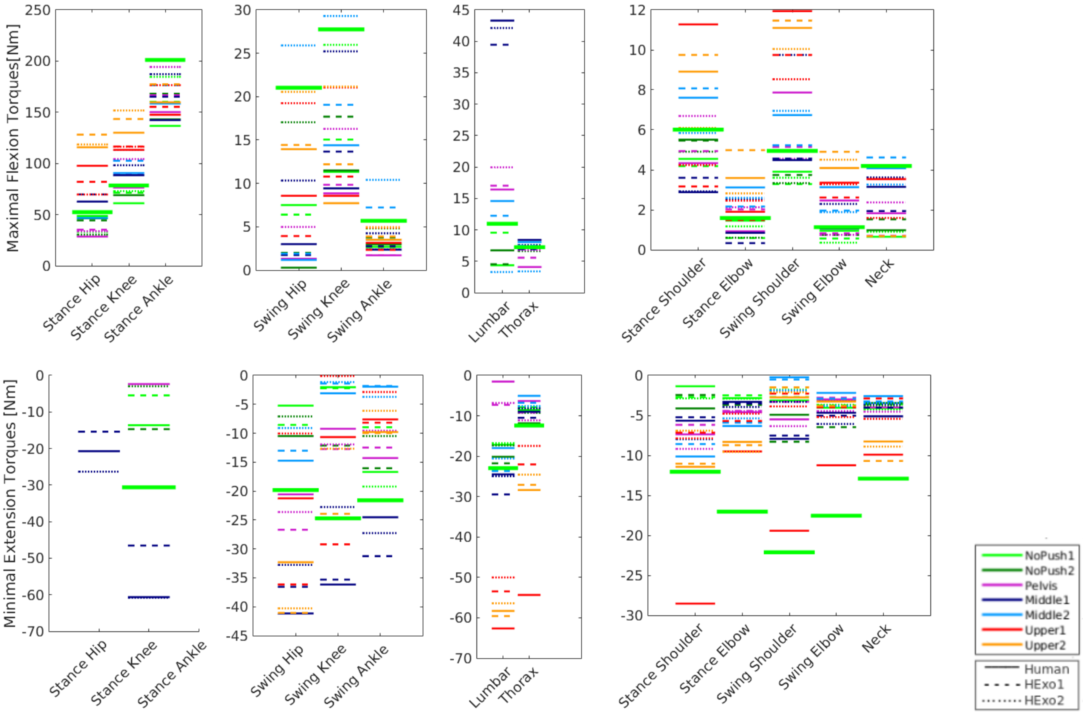

Figure 9.7: The maximal flexion joint torques (left) and minimal extension joint torques (right) of the motions (green: no push, purple: pelvis, blue: middle trunk, red/orange: upper trunk) for the different joints. The different model configurations are differenced by different line styles: solid lines: human model, dashed lines: HExo1, dotted lines: HExo2. The horizontal thick green line defines the maximal joint torque needed for the unperturbed motions.

Except for one push at the middle trunk 'Middle1', the motions without pushes result in higher swing ankle torques at the point in time of swing leg heel touchdown, see Figure 9.8, last subplot. This is because the push might also support the step motion as it is applied in the forward direction of the motions according to the point in time when it is applied. For the motion with a high peak push at the upper trunk (Upper2, orange) the torques in the stance hip, as well as in the swing hip, are distinctly higher than for the other motions, see Figure 9.8, the first column. This is due to the peak shape of this perturbation. In the upper body, a reasonable tendency of increasing torques for increasing push strength can be observed and the torques are the bigger the higher the push point is located at the body. This makes sense because for these motions, there is more movement in the upper body and the motions are much faster (the end time of these motions is about half a second, while the other perturbed motions take about 0.6 sec and the unperturbed motions 0.7 sec).

Figure 9.8 underlines the observations from Figure 9.5. For all motions, the joint torques for the combined human-exoskeleton models are larger than for the human model. A significant increase in the flexion joint torques can be observed if an exoskeleton is included in the model. Regarding the extension torques, the opposite can be observed: The heavier the exoskeleton, the lower the extension torque. This increase of flexion joint torques/decrease of extension torques is due to the additional mass of the exoskeletons that the combined models have to carry.

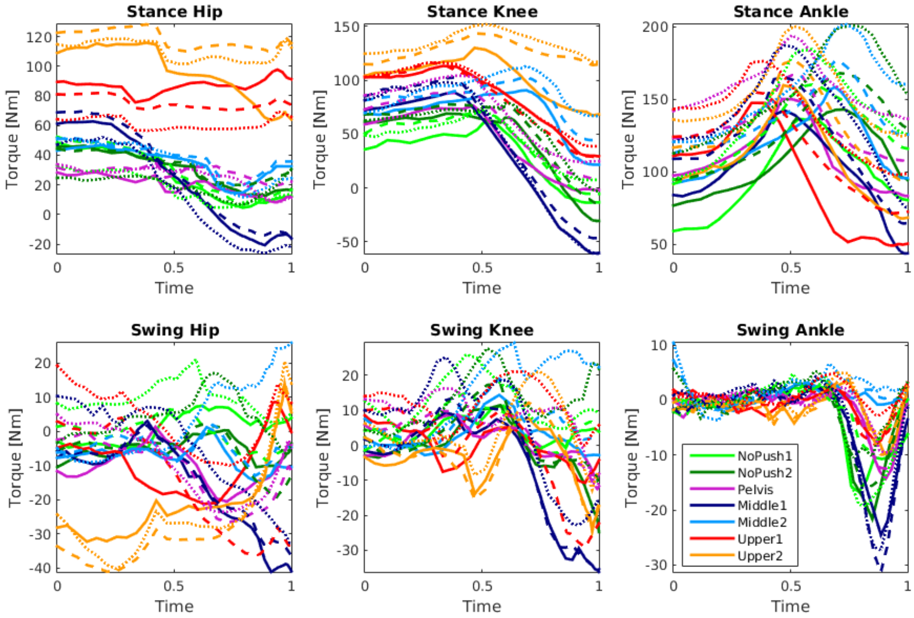

Figure 9.8: The torques in the lower limb joints for the different trials (green: no push, purple: pelvis, blue: middle trunk, red/orange: upper trunk) for the human model (solid line) and the two combined human-exoskeleton models (dashed lines: HExo1, dotted lines: HExo2).

9.3 Compliant Exoskeleton Parameter and Torque Analysis

In a second study the torques needed for human gait for the two combined human-exoskeleton models including compliant actuators are analyzed.

9.3.1 Optimal Control Problem Formulation

The optimal control problem for the compliance study is basically the same as for the previous study, see Section 9.2.1, except for the objective function. Again the difference of the resulting motion to reference data is minimized, but this time we define as the second term in 9.3 a suitable minimization of all squared active actuated joint torques

$$\phi(t) = \tilde{\boldsymbol{\tau}}_{\boldsymbol{a}}(t), \tag{9.6}$$

scaled by the constants $\alpha_{m_n}, n \in k{,}i, m = 1{,}2$.

Different from the combined human-exoskeleton model, we have compliance parameters in the case of the compliant models. As described in 9.1.2, we define spring-damper elements in the hips, knees, and ankles of the model. In this study, only in the ankles, damper elements are included. The hips and knees are represented as pure spring-elements. The model is assumed to be symmetric. Therefore the spring and damping parameters are chosen the same for the left (swing) and the right (stance) leg. The spring is defined by the spring parameter and the rest length of the spring. For the damping, we only have the damping parameter. In our case, this results in seven parameters for the optimization.

9.3.2 Results

In this section, the resulting active and passive torques using a spring-damper system additionally to the joint torques in the lower limb exoskeleton are analyzed and compared to the torques of the rigid combined human-exoskeleton models. The main outcome is:

- The compliant combined human-exoskeleton models can mimic the high dynamical push recovery motions very well.
- Spring-damper systems in the exoskeleton can reduce the required active torques for the motions considered.

As in the previous study without compliance, seven motions from dataset A, see Section 2.4, are taken into account. Again to simplify the notation *NoPushA1* is referred to as *NoPush1*, *NoPushA2* as *Nopush2*, *PelvisA* as *Pelvis*, etc. As for the human and the rigid combined human-exoskeleton models, the joint angles and transitions for the pelvis differ in a range of 1 cm or 0.5° and therefore the model data represent the reference data well.

Now the resulting torques for the compliant combined human-exoskeleton model are analyzed. In Table 9.2 the optimized parameters for the spring-damper system for the different motions are shown. Analyzing these parameters, it becomes clear that the spring parameters, the spring rest positions as well as the damping parameters for the ankle differ quite a lot between the different motions. Figure 9.9 shows the torques in the lower limbs of the compliant combined human-exoskeleton model (HExo-Compl) for the different regarded trials. These two plots are representative of the motions considered. The torques are defined as follows: damping (diamonds), spring (squares), active (circles) and total torque (dashed-dotted line). The curves show that the spring-damper systems in the exoskeleton can support the motions well. Even though the active and spring torques are counteracting from time to time - see for example Figure 9.9 (top) swing knee - the absolute value of the active torque is smaller than the total torque. The active torque leads to variations, e.g. small changes in the total torque, while the spring torque holds a more or less constant level. For most of the motions ('NoPush2', 'Pelvis', 'Middle2', 'Upper1', 'Upper2') damping has some influence. Damping helps to stabilize the touch-down of the swing heel ('NoPush2', 'Pelvis', 'Middle2' and 'Upper1'). For the Pelvis and Upper1 motion, the damping produces high torques in the stance ankle. The active torque in both ankle joints is comparatively small for all motions.

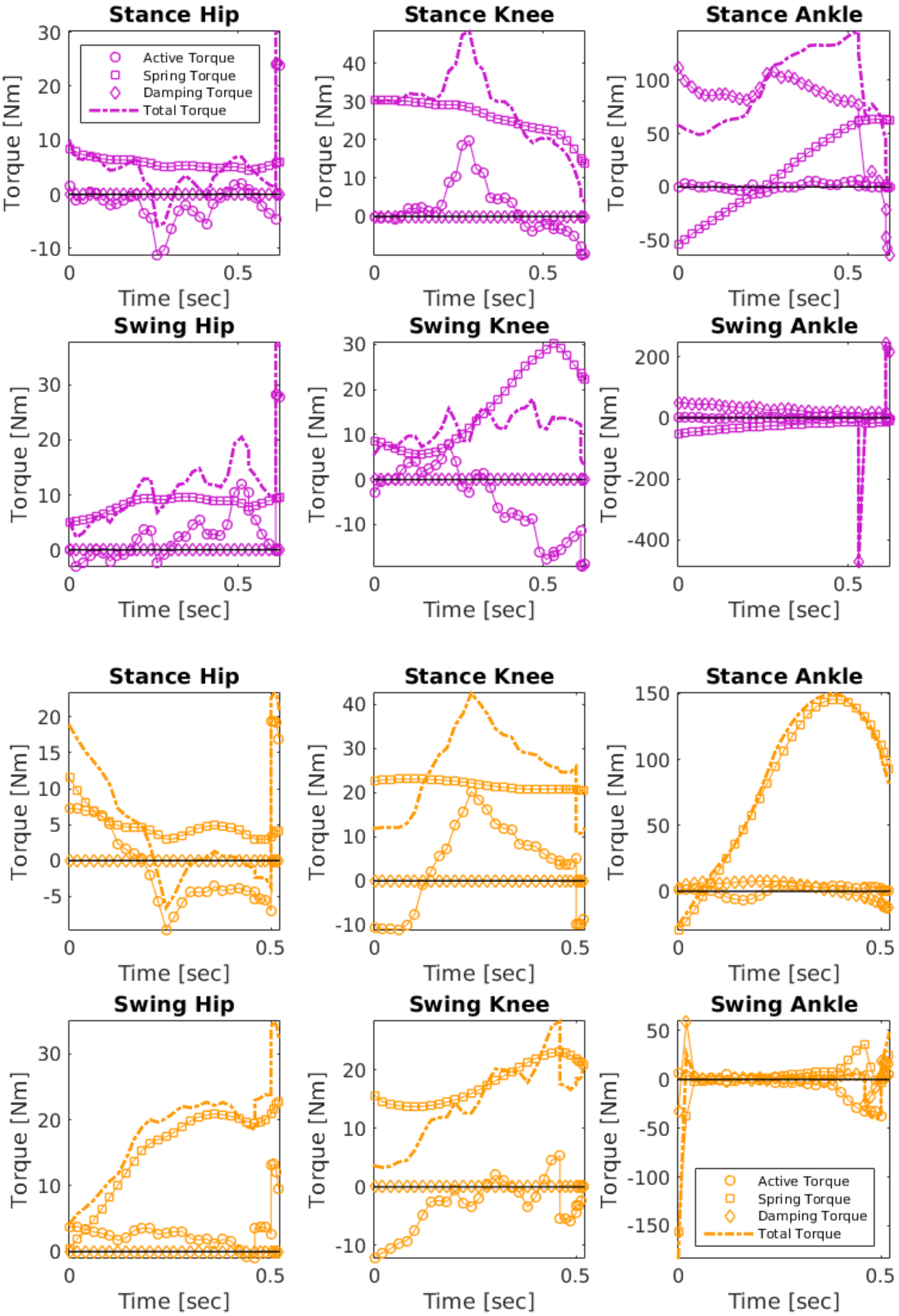

Figure 9.9: Different torque types for push case 'Pelvis' (top) and 'Upper2' (bottom): damping (diamonds), spring (squares), active (circles) and total (dashed-dotted) torques of the compliant combined human-exoskeleton model (HExoCompl).

Table 9.2: Optimal parameters of the spring-damper system in the lower body for the different motions.

	Joint	**NoPush1**	**NoPush2**	**Pelvis**	**Middle1**	**Middle2**	**Upper1**	**Upper2**
Damping	**Ankle**	2.1262	23.1758	60.0000	0.0000	9.3917	54.6864	3.3634
RestPosition	**Hip**	0.8849	0.0234	0.4222	-0.3317	1.3550	-0.0519	-0.0987
	Knee	1.8795	2.5035	1.4851	3.4000	1.0123	1.2541	2.9017
	Ankle	0.1941	0.1152	0.0262	0.1887	0.3428	0.1388	0.2328
Spring	**Hip**	7.3890	16.8759	7.9998	51.9691	4.5259	51.7537	22.9214
	Knee	8.3278	5.2565	20.4640	4.0532	25.3204	32.5317	7.9504
	Ankle	285.3533	217.5699	144.4288	334.1590	118.4477	68.3199	266.7282

Comparable to the previous Chapter 8, we investigate the active and passive parts of the joint torques. Figure 9.10 shows the active and passive parts of the torques during the different perturbed and unperturbed motions for the compliant combined human-exoskeleton model. They are expressed in percent of the total joint torque required:

$$P_{\text{active}} = \frac{\int_0^T |\tau_{active}(t)|dt}{\int_0^T |\tau_{total}(t)|dt} \approx \frac{\sum_{i=1}^n |\tau_{active}(t_i)|\Delta t_i}{\sum_{i=1}^n |\tau_{total}(t_i)|\Delta t_i}, \tag{9.7}$$

$$P_{\text{passivek,d}} = \frac{\int_0^T |\tau_{passivek,d}(t)|dt}{\int_0^T |\tau_{total}(t)|dt} \approx \frac{\sum_{i=1}^n |\tau_{passivek,d}(t_i)|\Delta t_i}{\sum_{i=1}^n |\tau_{total}(t_i)|\Delta t_i}, \tag{9.8}$$

$$\begin{aligned} \text{with } & \tau_{total}(t_i) = \tau_{active}(t_i) + \tau_{spring}(t_i) + \tau_{damping}(t_i), \\ & \tau_{passivek,d}(t_i) = \tau_{spring}(t_i) + \tau_{damping}(t_i) \text{ and } \Delta t_i = t_i - t_{i-1}. \end{aligned}$$

As the results show, the required active torques could be significantly reduced concerning the rigid case which is reflected by the fact that all blue bars are (much) smaller than one. It can also be seen that the blue and the yellow bars add up to more than one. This shows that even the optimally chosen spring-damper elements are momentarily working against each other in some cases, which is caused by the simple structure of the spring-damper element. However, what counts is the relative height of the blue bars, which supports the initial claim that with appropriately chosen spring-damper elements the active torque can be reduced significantly, i.e. energy can be saved, or higher total torques can be generated. Note, that for the application in the real exoskeleton the swing and stance leg has to be detected and the parameters resulting from our study can be applied accordingly.

Table 9.3 shows the mean active joint torques of the human and the rigid combined human-exoskeleton model HExo1, as well as of the compliant combined human-exoskeleton model HExoCompl for the different motions. Compared to the joint torques needed in the human and the rigid combined human-exoskeleton model, the active joint torques needed for the compliant model are reduced significantly - especially for the stance leg. The torques of the swing leg are already comparatively low for all motions. This observation leads to the statement that it is reasonable to include spring-damper systems in exoskeletons to reduce torques in the joints. This conclusion is consistent with the result of Figure 9.10 and shows the advantage of the approach to include spring-damper systems in exoskeletons to support push recovery motions during walking. However, including spring-damper systems in real exoskeletons, we do not know which of the motions considered will be performed. Therefore it would be necessary to calculate the torques of a representative dataset for all the motions considered in this work. Based on these results parameters for universal spring-damper systems of lower-limb exoskeletons to optimally support push recovery walking motions can be found averaging the results of all motions or even better optimizing all motions in parallel.

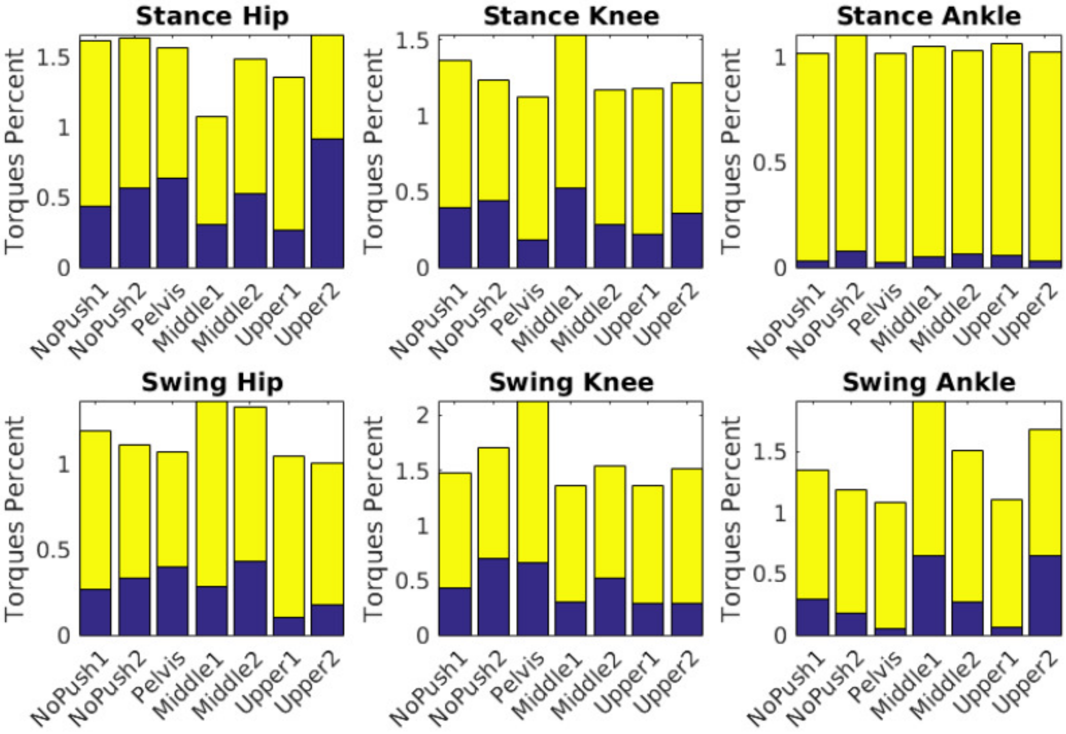

Figure 9.10: Comparison of the active (blue) and the passive (yellow) part of the joint torques during the different motions for the combined human exoskeleton model with spring-damper systems in the exoskeleton.

Table 9.3: Mean of the torques per joints needed for the human and the combined human-exoskeleton model with and without compliance. For the compliance model the active torques are regarded.

Model	**Joint**	**NoPush1**	**NoPush2**	**Pelvis**	**Middle1**	**Middle2**	**Upper1**	**Upper2**
Human	**Stance Hip**	41.6504	41.4903	24.1277	42.7445	40.1511	86.7392	98.6755
	Stance Knee	55.1408	68.5657	55.5505	73.5310	79.5295	85.5983	104.7686
	Stance Ankle	148.6679	144.4313	133.0200	129.0980	133.3102	97.3969	110.7032
	Swing Hip	6.5924	7.3922	12.5883	18.8163	8.6125	11.3241	23.6904
	Swing Knee	6.9178	6.6949	4.6745	12.9775	4.1919	4.9151	5.9522
	Swing Ankle	6.2350	5.8753	2.9624	5.5764	1.2659	1.7970	2.2557
HExo1	**Stance Hip**	46.9744	44.4715	34.3786	45.1499	44.2368	75.4515	119.7683
	Stance Knee	70.6615	77.4057	72.2516	80.9211	93.9898	84.0157	128.8392
	Stance Ankle	196.4403	171.9755	158.4421	152.1776	155.9935	116.3304	132.3490
	Swing Hip	5.4198	7.7140	13.7702	16.4776	5.8363	15.2722	30.4608
	Swing Knee	8.6719	7.4225	6.5299	14.6436	7.5719	9.6268	7.0609
	Swing Ankle	3.5910	5.5982	2.5285	6.7468	2.1728	1.8729	2.3247
HExo Compl	**Stance Hip**	5.2248	3.4340	3.7362	4.5497	4.6628	4.9145	5.5564
	Stance Knee	8.1216	8.0440	5.7859	8.3251	7.9544	7.1017	9.7060
	Stance Ankle	4.9678	5.6324	2.4067	5.0485	4.5915	4.8022	3.1026
	Swing Hip	4.9254	5.3865	4.3893	4.0329	5.1117	3.0572	3.0589
	Swing Knee	7.3280	9.5299	7.8397	4.2517	8.3814	5.6223	4.2740
	Swing Ankle	4.1590	4.2866	1.7853	4.0889	5.1388	2.1669	7.1878

Chapter 10

Summary and Future Work

In this thesis we approach the study of human push recovery motions combining methods from optimal control theory with rigid multi-body dynamics modeling leading to contributions in the following areas.

Database of Human Push Recovery Motions

As part of this thesis motion capture data of perturbed and unperturbed motions are recorded and collected in a database. Human walking is perturbed by pushes at differing heights at the spine with differing strength and timing. In this work, we also present an intense analysis of the different motions. The main observation is that the duration of the step decreases for perturbed motions compared to unperturbed ones.

Human Model for Push Recovery Motions

Human push recovery motions are very complex tasks that require good coordination between the body segments. We present a dynamic multi-body model with rigid segments that can cope with large perturbations during walking motions resulting in a highly redundant and underactuated system. The perturbation is modeled as an external force that is described by a continuous function of time.

Synthesis of Human Push Recovery Motions

To be able to analyze the underlying indicators that result in human-like motions, we present a motion synthesis approach. To this end, we formulate a multiple-stage optimal control problem that considers the dynamics of the model as constraints over the whole time. Due to the redundancy and highly nonlinearity of the considered motions, the problem is discretized according to a direct multiple shooting method. Analyzing the results for different push strengths shows that stronger perturbation results not only in a larger step length (less periodic motions) but also in an increase of the internal joint torques. The analysis of the influence of basal objective functions leads to a difference in the similarity between the perturbed and the unperturbed motions. The location of the perturbation does not influence the similarity result of the basal objective functions.

Reconstruction of Human Push Recovery Motions

An optimization-based simulation approach to obtain indicators form the recorded perturbed walking motions that are not easy or not measurable from real humans is presented. We set up a multiple-stage optimal control problem that considers the dynamics of the motions over the whole time horizon and fits the model to the motion in a least-squares sense. The motion resulting from the motion reconstruction of the data from our database leads to a good approximation of this reference data. With a set up as presented in this work, it is possible to gather data, that is hard to get from a real human, as the center of mass or the internal joint torques, as well as data, that is impossible to calculate with a kinematic model, as the calculation of ground reaction forces. The intensive analysis of the internal joint torques of perturbed and unperturbed motions proves the hypothesis: "The higher the push point at the spine and the stronger the perturbation, the larger the joint torques."

Analysis of Indicators for Sensing a Perturbation

The motion reconstruction approach is used to analyze various parameters that could help the human to sense the perturbation. A variation in the torso torques and also in the torso joints shortly after the point in time when the push occurs can be observed. Especially the neck joint differs from the range of unperturbed motions. This leads to the assumption that the somatosensory system can sense the perturbation and postural reflexes help to recover from the perturbation. The change in head orientation indicates that the vestibular system can sense the perturbation. Another result is that the chest is not a good position to place a balance sensor, because this point at the body does not differ for all perturbed motions from the unperturbed ones. Analyzing the reaction times shows that the human processes the sensory information from the perturbation very fast.

Analysis of Compliant Actuators during Human Push Recovery Motions

An optimization-based simulation approach to obtain the parameters of spring-damper systems that support the joints of a sagittal human model during perturbed walking motions in an optimal way is presented. The motions resulting from the motion reconstruction of the recorded motions give a very good approximation of these reference data. The parameters of the spring-damper system that support the motion optimally depend on the regarded motions and differ between the joints. The spring-damper systems support the human push recovery motions well. Humans can adjust their stiffness to the particular push experienced.

Joint Torques and Compliant Actuators in Combined Human-Exoskeleton Models during Human Push Recovery Motions

We have applied an innovative method to determine the torques needed in lower-limb exoskeletons to recover from perturbations during human walking. Combined human-exoskeleton models are set up, which simulate the dynamics of a human wearing an exoskeleton. As expected, the required torques increase for a heavier exoskeletons. A significant increase of the joint torques in relation to the push strength can be observed for the stance hip and knee, as well as for the swing hip. Setting up compliant combined human-exoskeleton models, it can be shown, that spring-damper systems lead to a significant reduction of the active torques needed for the regarded motions.

Outlook

The results of this work support the analysis of human push recovery motions. For future investigations it would be reasonable to deepen the presented approaches to the following extends.

Extension of the Database

In our studies, we investigate data for two young adults. To be able to generalize the results of this work, it is reasonable to investigate for more push recovery motions of more subjects. It would be valuable to have data from elderly people as well as typical adults to be able to compare the results for different age groups.

Extention of the Human Model

Due to the use of a two-dimensional model, only a limited set of perturbations during human walking motions can be taken into account in the presented approach. To this end, it would also be reasonable to extend the model to allow for more than one step. Also the extention of the model to three dimensions and multiple steps would allow for a more general set of perturbations and recovery motions. To allow for a better representation of the human senses, it would be reasonable to investigate in a more detailed human model.

Investigation in Muscle Models

In this work, we investigate in the analysis of how to choose the best spring-damping elements to support human motions best. In our studies, the spring and damping parameters could be independently chosen. In real a muscle this is not the case: the stiffness and damping of a muscle vary linearly with the force it develops at least for small stretches. Given this restriction, it is presently not clear precisely how the stiffness and damping properties affect human balance recovery. To this end, it is valuable to use muscle models instead of the spring-damper system and to deepen the spring-damper studies including variable stiffness elements instead of the constant ones regarded in the scope of this work.

Inverse Optimal Control of Human Push Recovery Motions

As described more precisely in Section 7.3, it would be valuable to investigate in the inverse optimal control formulation to be able to identify optimality criteria that underly a human motion as in [18, 19]. To this end, the optimal control problem from the motion generation formulation can be included in an inverse optimal control problem. As an objective function, a weighted linear combination of optimality criteria (basis functions) is formulated. To determine the weights of the objective function, and therefore the most relevant criteria, in the outer problem the distance from reference data to the model data is minimized. To be able to apply these methods, it is important to make sure that the investigated model can represent the motions that are to be analyzed. In this work, we present a rigid multi-body dynamic human model that can cope with heavy perturbation during walking which can be included in an inverse optimal control analysis to determine the weights of the objective function leading to human-like motions. To be able to identify rules how humans manage to recover from perturbation, we can apply these rules to models of humanoid robots or exoskeletons that might have some motion restriction compared to a human. Based on the identified rules recovery motions for these models can be computed and then be executed by the robot.

Appendix

A1 Subjects Segment Lengths

Table A1: Segment lengths subject for dataset A and B.

Segment	Definition	Length A [mm]	Length B [mm]
Forearm	elbow axis / ulnar styloid	290	260
Upper arm	glenhumeral axis / elbow axis	278	250
Shank	femoral condyles / medial malleolus	445	380
Thigh	greater trochanter / femoral condyles	462	400
Head & Neck	C7-T1 & first rip / ear canal	195	160
Shoulder	sternoclaviar joint / glenhumeral axis	220	175
Thorax	C7-T1 / T12-L1 & diaphragm	258	285
Abdomen	T12-L1 / L4-L5	142	130
Thorax & Abdomen	C7-T1 / L4-L5	407	400
Trunk	greater trochanter / glen humeral joint	495	400

A2 Perturbation and Recovery Motion Properties

Table A2: Timing of step and push for the motions in dataset A.

Motion	Step Duration [sec]	Phase0 [sec]	Phase1 [sec]	Phase3 [sec]	Phase5 [sec]	Push Start [sec]	Push End [sec]
NoPushA1	0.79	0.39	0.21	0.17	0.02		
NoPushA2	0.69	0.36	0.18	0.13	0.02		
NoPushA3	0.76	0.36	0.20	0.13	0.07		
NoPushA4	0.72	0.21	0.35	0.15	0.01		
Min NoPushA	0.69	0.21	0.18	0.13	0.01		
Max NoPushA	0.79	0.39	0.35	0.17	0.07		
Av. NoPushA	0.73	0.27	0.29	0.15	0.03		
PelvisA	0.62	0.26	0.27	0.08	0.01	0.09	0.35
MiddleA1	0.65	0.25	0.29	0.09	0.02	0.09	0.39
MiddleA2	0.58	0.37	0.15	0.01	0.05	0.22	0.48
UpperA1	0.51	0.14	0.30	0.03	0.04	0.01	0.35
UpperA2	0.52	0.22	0.24	0.04	0.02	0.05	0.32
Min PushA	0.51	0.14	0.15	0.01	0.01	0.01	0.32
Max PushA	0.65	0.37	0.30	0.09	0.05	0.22	0.48
Av. PushA	0.58	0.25	0.25	0.05	0.03	0.10	0.38

Table A3: Push force and step lengths before and after the step for the motions in dataset A.

Motion	Max Push Force [N]	Force Integral [N sec]	Step Length (SL) [m]	Previous SL [m]	SL Difference [m]
NoPushA1			0.561	0.624	0.063
NoPushA2			0.655	0.671	0.015
NoPushA3			0.558	0.574	0.016
NoPushA4			0.646	0.696	0.050
Min NoPushA			0.558	0.574	0.015
Max NoPushA			0.655	0.696	0.063
Av. NoPushA			0.620	0.655	0.043
PelvisA	227	44	0.635	0.415	0.220
MiddleA1	143	28	0.655	0.496	0.159
MiddleA2	223	47	0.405	0.390	0.015
UpperA1	169	34	0.481	0.419	0.062
UpperA2	247	24	0.847	0.443	0.404
Min PushA	143	24	0.405	0.390	0.015
Max PushA	247	47	0.847	0.496	0.404
Av. PushA	202	36	0.605	0.433	0.172

Table A4: Timing of step and push for the motions in dataset B.

Motion	**Step Duration** [sec]	**Phase0** [sec]	**Phase** [sec]	**Phase3** [sec]	**Phase5** [sec]	**Push Start** [sec]	**Push End** [sec]
NoPushB1	0.68	0.33	0.16	0.11	0.08		
NoPushB2	0.68	0.33	0.19	0.12	0.04		
NoPushB3	0.67	0.34	0.13	0.11	0.09		
NoPushB4	0.58	0.29	0.17	0.11	0.01		
NoPushB5	0.60	0.24	0.25	0.10	0.01		
NoPushB6	0.61	0.25	0.23	0.11	0.02		
NoPushB7	0.62	0.15	0.37	0.08	0.02		
NoPushB8	0.60	0.23	0.27	0.07	0.03		
NoPushB9	0.60	0.24	0.24	0.09	0.03		
NoPushB10	0.63	0.28	0.24	0.11	0.00		
NoPushB11	0.62	0.22	0.28	0.08	0.04		
NoPushB12	0.63	0.15	0.36	0.08	0.04		
NoPushB13	0.63	0.32	0.21	0.07	0.03		
NoPushB14	0.64	0.22	0.30	0.08	0.04		
NoPushB15	0.63	0.20	0.32	0.10	0.01		
NoPushB16	0.65	0.24	0.29	0.11	0.01		
NoPushB17	0.62	0.21	0.30	0.10	0.01		
NoPushB18	0.59	0.23	0.26	0.08	0.02		
NoPushB19	0.71	0.42	0.09	0.12	0.08		
NoPushB20	0.63	0.35	0.11	0.11	0.06		
NoPushB21	0.63	0.18	0.33	0.09	0.03		
NoPushB22	0.65	0.12	0.38	0.09	0.06		
NoPushB23	0.62	0.32	0.18	0.09	0.03		
Max NoPushB	0.71	0.42	0.38	0.12	0.09		
Min NoPushB	0.58	0.12	0.09	0.07	0.00		
Av. NoPushB	0.63	0.26	0.25	0.10	0.03		
PelvisB1	0.51	0.27	0.15	0.02	0.07	0.18	0.48
PelvisB2	0.56	0.25	0.21	0.06	0.04	0.24	0.56
MiddleB1	0.46	0.15	0.26	0.03	0.02	0.06	0.45
MiddleB2	0.50	0.15	0.27	0.03	0.05	0.07	0.45
UpperB1	0.44	0.13	0.28	0.02	0.01	0.05	0.43
UpperB2	0.55	0.32	0.20	0.03	0.00	0.29	0.55
Max PushB	0.56	0.32	0.28	0.06	0.07		
Min PushB	0.44	0.13	0.15	0.02	0.00		
Av. PushB	0.50	0.21	0.23	0.03	0.03		

Table A5: Push force and step lengths before and after the step for the motions in dataset B.

Motion	**Max Push Force** [N]	**Force Integral** [N sec]	**Step Length (SL)** [m]	**Previous SL** [m]	**SL Difference** [m]
NoPushB1			0.53	0.42	0.11
NoPushB2			0.49	0.49	−0.00
NoPushB3			0.49	0.52	−0.03
NoPushB4			0.60	0.59	0.01
NoPushB5			0.55	0.55	0.00
NoPushB6			0.53	0.55	−0.02
NoPushB7			0.64	0.61	0.03
NoPushB8			0.61	0.64	−0.03
NoPushB9			0.55	0.54	0.01
NoPushB10			0.57	0.58	−0.01
NoPushB11			0.57	0.59	−0.02
NoPushB12			0.58	0.57	0.01
NoPushB13			0.59	0.64	−0.05
NoPushB14			0.54	0.61	−0.07
NoPushB15			0.57	0.57	−0.00
NoPushB16			0.53	0.57	−0.04
NoPushB17			0.60	0.60	0.00
NoPushB18			0.59	0.66	−0.07
NoPushB19			0.42	0.48	−0.06
NoPushB20			0.52	0.47	0.05
NoPushB21			0.51	0.52	−0.01
NoPushB22			0.51	0.49	0.02
NoPushB23			0.54	0.58	−0.04
Max NoPushB			0.64	0.66	0.11
Min NoPushB			0.42	0.42	0.00
Av. NoPushB			0.60	0.61	−0.04
PelvisB1	149.84	29	0.50	0.55	−0.05
PelvisB2	63.94	13	0.52	0.49	0.03
MiddleB1	167.25	41	0.64	0.49	0.15
MiddleB2	121.24	29	0.64	0.58	0.06
UpperB1	178.06	38	0.79	0.59	0.20
UpperB2	134.79	25	0.60	0.58	0.02
Max PushB	178.06	41	0.79	0.59	0.20
Min PushB	63.94	13	0.50	0.49	0.02
Av. PushB	135.85	29	0.61	0.55	0.09

A3 Reaction Time

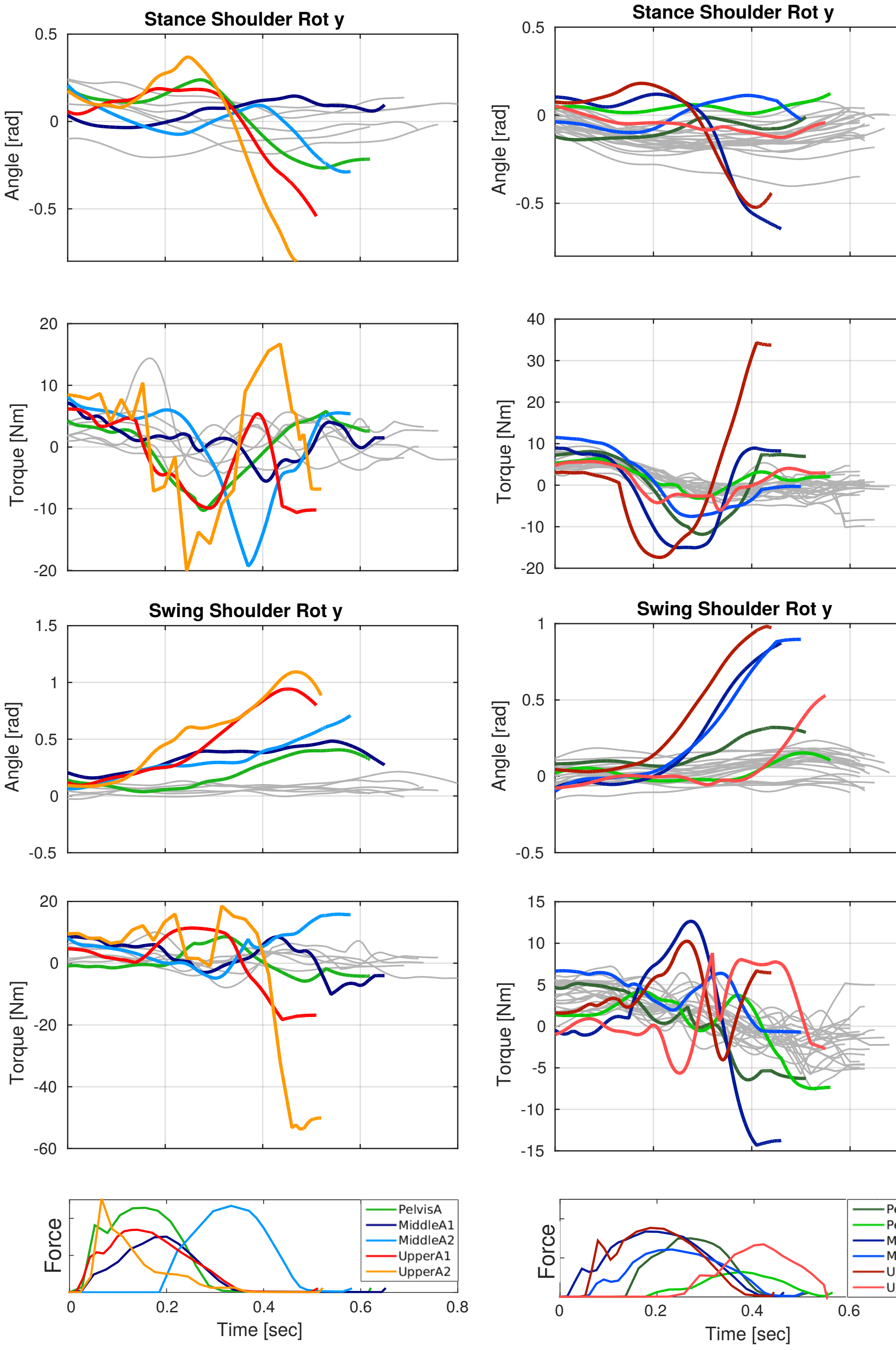

Figure A1: The joint angles of the arms for unperturbed steps (gray lines) and for perturbed steps (solid colored lines) of the different push motions (left: dataset A, right: dataset B). The colored lines in the lowest subplot indicate the strength and the timing of the perturbation.

Table A6: Reaction times of the motions from dataset A and B for the stance and swing shoulder as well as the head position. No value means that no deviation between perturbed and unperturbed motions can be observed.

Motion	**Swing Shoulder Anlge**	**Stance Shoulder Anlge**	**Swing Shoulder Torque**	**Stance Shoulder Torque**
PelvisA	180	60	110	30
MiddleA1	10		90	160
MiddleA2	160	120	10	0
UpperA1	190	80	135	130
UpperA2	50	140	60	100
Min Dataset A	10	60	10	0
Max Dataset A	190	140	135	160
Mean Pelvis A	180	60	110	30
Mean Middle A	85	110	50	80
Mean Upper A	120	110	98	115
Mean Dataset A	128	93	86	75
PelvisB1	70		−30	−50
PelvisB2	160		60	10
MiddleB1	140	40	90	40
MiddleB2	200	200	150	110
UpperB1	120	50	100	80
UpperB2	250		−40	−80
Min Dataset B	120	40	60	10
Max Dataset B	250	200	150	110
Mean Pelvis B	115		60	10
Mean Middle B	170	120	120	75
Mean Upper B	185	50	100	80
Mean Dataset B	157	85	93	55
Total Mean	143	89	90	65

A4 Exoskeleton with Compliant Controls

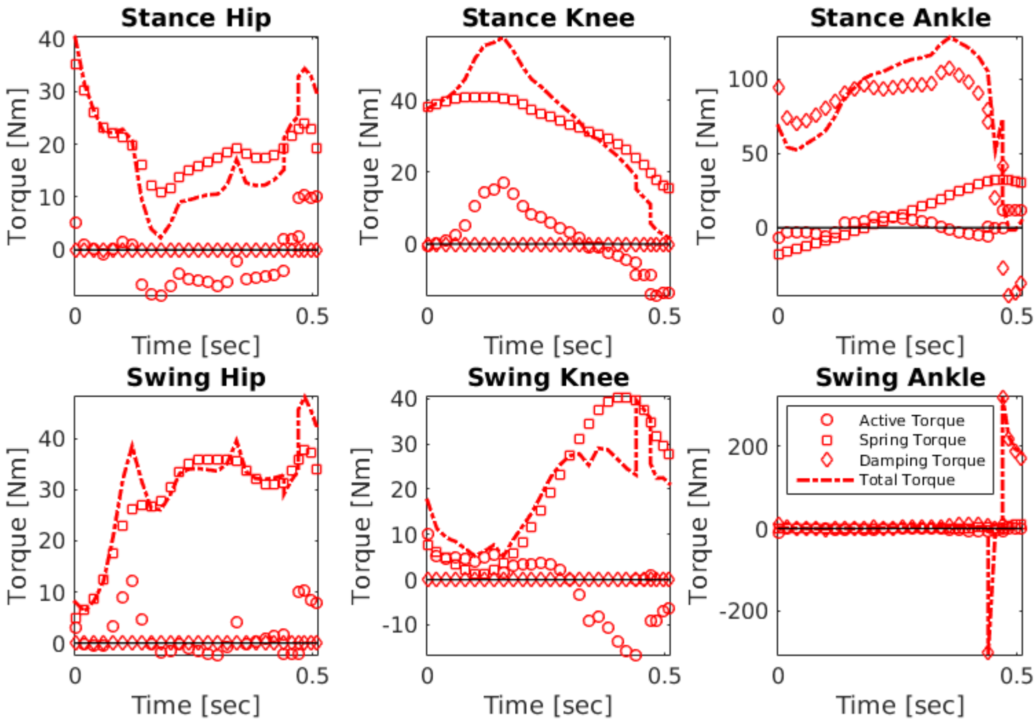

Figure A2: Different torque types for push case 'Upper1' : damping (diamonds), spring (squares), active (circles) and total (dashed-dotted) torques of the compliant combined human-exoskeleton model (HExoCompl).

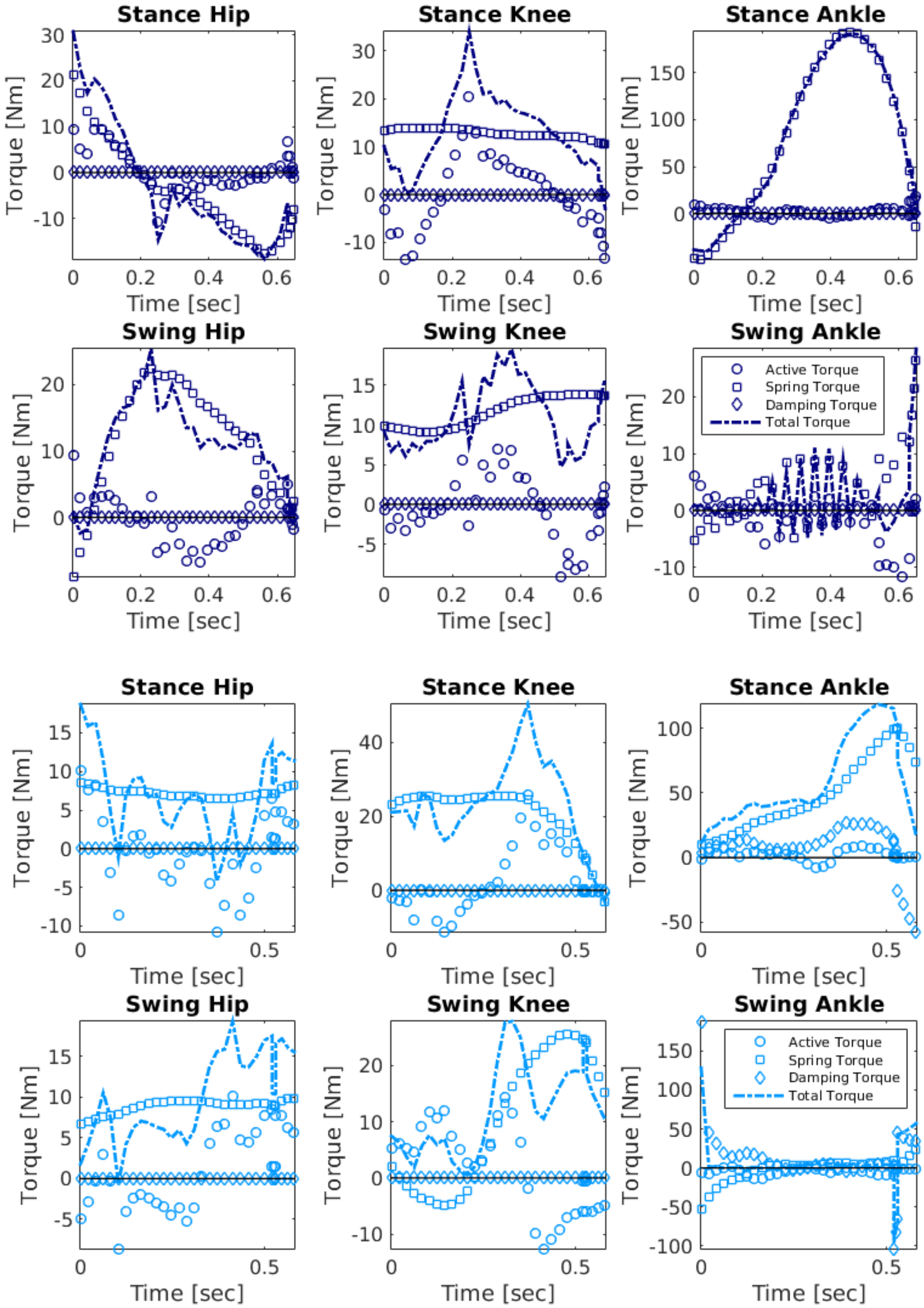

Figure A3: Different torque types for push case 'Middle1' (top) and 'Middle2' (bottom): damping (diamonds), spring (squares), active (circles) and total (dashed-dotted) torques of the compliant combined human-exoskeleton model (HExoCompl).

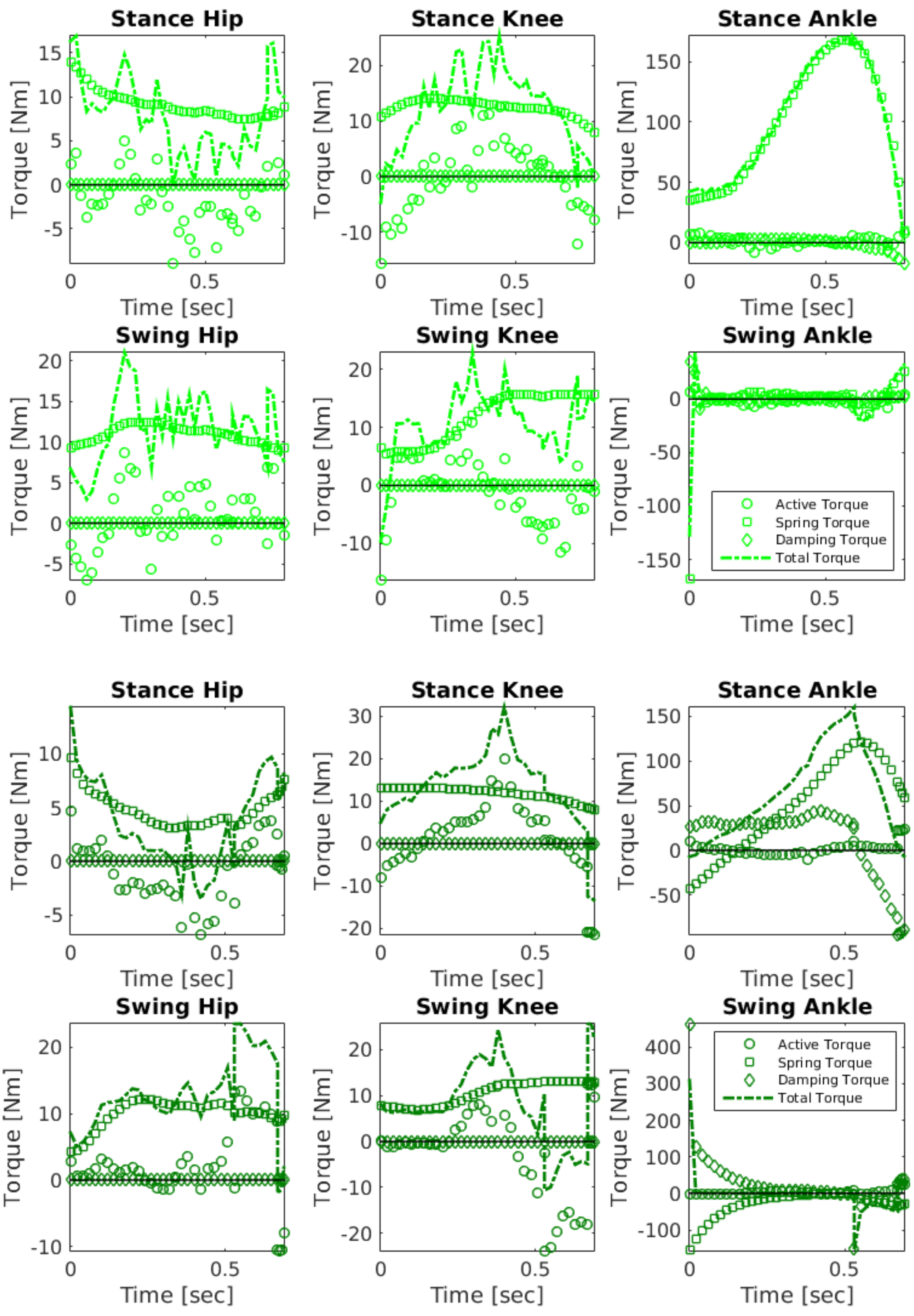

Figure A4: Different torque types for push case 'NoPush1' (top) and 'NoPush2' (bottom): damping (diamonds), spring (squares), active (circles) and total (dashed-dotted) torques of the compliant combined human-exoskeleton model (HExoCompl).

Bibliography

[1] Basic postural reflexes. *Acta Oto-Laryngologica*, 53(sup161):11–14, 1961. 17

[2] *WHO Global Report on Falls Prevention in Older Age*. World Health Organization, 2007. 1

[3] A. H. Adiwahono. *Push recovery through walking phase modification for bipedal locomotion*. PhD thesis, National University of Singapore, 2011. 8

[4] Z. Aftab, T. Robert, and P. Wieber. Ankle, hip and stepping strategies for humanoid balance recovery with a single model predictive control scheme. In *2012 12th IEEE-RAS International Conference on Humanoid Robots (Humanoids 2012)*, pages 159–164, Nov 2012. 9

[5] Z. Ahsan, T. K. Uchida, A. Subudhi, and C. P. Vyasarayani. Stability of Human Balance With Reflex Delays Using Galerkin Approximations. *Journal of Computational and Nonlinear Dynamics*, 11(4), 12 2015. 041009. 1, 11

[6] Claude Alain, Stephen R. Arnott, Stephanie Hevenor, Simon Graham, and Cheryl L. Grady. “what” and “where” in the human auditory system. *Proceedings of the National Academy of Sciences*, 98(21):12301–12306, 2001. 16

[7] S. Albrecht, M. Leibold, and M. Ulbrich. A bilevel optimization approach to obtain optimal cost functions for human arm movements. *Numerical Algebra, Control and Optimization*, 2, 2012. 82

[8] R. M. Alexander. The gaits of bipedal and quadrupedal animals. *The International Journal of Robotics Research*, 3(2):49–59, 1984. 3

[9] K. Amano, N. Goda, S. Nishida, Y. Ejima, T. Takeda, and Y. Ohtani. Estimation of the timing of human visual perception from magnetoencephalography. *Journal of Neuroscience*, 26(15):3981–3991, 2006. 16

[10] L. Assländer and Robert J. Peterka. Sensory reweighting dynamics in human postural control. *Journal of Neurophysiology*, 111(9):1852–1864, May 2014. 14

[11] T. M. Assman. Humanoid push recovery stepping in experiments and simulations. Master’s thesis, Eindhoven University of Technology, 2012. 1, 7, 11

[12] H. G. Bock and K. J. Plitt. A multiple shooting algorithm for direct solution of optimal control problems*. *IFAC Proceedings Volumes*, 17(2):1603 – 1608, 1984. 9th IFAC World Congress: A Bridge Between Control Science and Technology, Budapest, Hungary, 2-6 July 1984. 2, 37, 39, 40

[13] T. C. Britton, B. L. Day, P. Brown, J. C. Rothwell, P. D. Thompson, and C. D. Marsden. Postural electromyographic responses in the arm and leg following galvanic vestibular stimulation in man. *Experimental Brain Research*, 94(1):143–151, May 1993. 15, 17

[14] S. Carver, T. Kiemel, and J.. Jeka. Modeling the dynamics of sensory reweighting. *Biological Cybernetics*, 95(2):123–134, Aug 2006. 14

[15] M. Cenciarini and R. J. Peterka. Stimulus-dependent changes in the vestibular contribution to human postural control. *Journal of Neurophysiology*, 95(5):2733–2750, 2006. PMID: 16467429. 14

[16] M. Cestari, D. Sanz-Merodio, J. C. Arevalo, and E. Garcia. An adjustable compliant joint for lower limb exoskeletons. In *IEEE/ASME Transactions on Mechatronics*, volume 20, 2015. 95

[17] A. H.S. Chan and A. W.Y. Ng. Finger response times to visual, auditory and tactile modality stimuli. In *Lecture Notes in Engineering and Computer Science*, volume 2196, pages 1449–1454. Newswood Limited, 2012. 15, 16

[18] D. Clever and K. Mombaur. On the relevance of common humanoid gait generation strategies in human locomotion - an inverse optimal control approach. In H.G. Bock, X.P.and Rannacher Hoang, and J. R., Schlöder, editors, *Modeling, Simulation and Optimization of Complex Processes - HPSC 2015*, page 12 pages. Springer, 2015. 113

[19] D. Clever, R. M. Schemschat, M. L. Felis, and K. Mombaur. Inverse optimal control based identification of optimality criteria in whole-body human walking on level ground. In *2016 6th IEEE International Conference on Biomedical Robotics and Biomechatronics (BioRob)*, pages 1192–1199, June 2016. 82, 83, 113

[20] L. A. Cohen. Role of eye and neck propioceptive mechanisms in body orientation and motor coordination. *Journal of Neurophysiology*, 24(1):1–11, 1961. PMID: 13694396. 13

[21] L. Colasanto, N. G. Tsagarakis, and D. G. Caldwell. A compact model for the compliant humanoid robot coman. In *2012 4th IEEE RAS EMBS International Conference on Biomedical Robotics and Biomechatronics (BioRob)*, pages 688–694, June 2012. 10

[22] S. H. Collins, M. B. Wiggin, and G. S. Sawicki. Reducing the energy cost of human walking using an unpowered exoskeleton. *Nature*, 522(7555):212–215, 2015. 1

[23] B. Colson, P. Marcotte, and G. Savard. An overview of bilevel optimization. *Annals of Operations Research*, 153(1):235–256, April 2007. 82

[24] S. Dafarra, F. Romano, and F. Nori. Synthesis of a predictive push-recovery controller: Simulation results on the icub humanoid robot. 05 2017. 9

[25] C. J. Dakin, J. T. Inglis, and J.-S. Blouin. Short and medium latency muscle responses evoked by electrical vestibular stimulation are a composite of all stimulus frequencies. *Experimental Brain Research*, 209(3):345–354, Mar 2011. 17

[26] C. J. Dakin, G. M. Lee Son, J. T. Inglis, and J.-S. Blouin. Frequency response of human vestibular reflexes characterized by stochastic stimuli. *The Journal of Physiology*, 583(3):1117–1127, 2007. 17

[27] D. Denny-Brown and Charles Scott Sherrington. On the nature of postural reflexes. *Proceedings of the Royal Society of London. Series B, Containing Papers of a Biological Character*, 104(730):252–301, 1929. 17

[28] J. Dichgans, R. Held, L. R. Young, and T. Brandt. Moving visual scenes influence the apparent direction of gravity. *Science*, 178(4066):1217–1219, 1972. 14

[29] M. Diehl, H. G. Bock, H. Diedam, and P.-B. Wieber. Fast Direct Multiple Shooting Algorithms for Optimal Robot Control. In *Fast Motions in Biomechanics and Robotics*, Heidelberg, Germany, 2005. 37, 40

[30] H.C. Diener, J. Dichgans, B. Guschlbauer, and H. Mau. The significance of proprioception on postural stabilization as assessed by ischemia. *Brain Research*, 296(1):103 – 109, 1984. 13

[31] V. Dietz, T.J. Feuerstein, and W. Berger. Significance of dopamine receptor antagonists in human postural control. *Neuroscience Letters*, 117(1):81 – 86, 1990. 13

[32] A. M. Dollar and H. Herr. Lower extremity exoskeletons and active orthoses: Callenges and state-of-the-art. In *IEEE Transactions on Robotics*, volume 24, pages 144–158, February 2008. 95

[33] B. B. Edin. Quantitative analysis of static strain sensitivity in human mechanoreceptors from hairy skin. *Journal of Neurophysiology*, 67(5):1105–1113, 1992. PMID: 1597700. 13

[34] W. T. Edwards. Effect of joint stiffness on standing stability. *Gait and Posture*, 25:432–439, 2007. 86

[35] J. Englsberger, C. Ott, M. A. Roa, A. Albu-Schäffer, and G. Hirzinger. Bipedal walking control based on capture point dynamics. In *2011 IEEE/RSJ International Conference on Intelligent Robots and Systems*, pages 4420–4427, Sep. 2011. 9

[36] G. S. Faber, C. C. Chang, I. Kingma, and J. T. Dennerlein. A novel wearable measurement system for ambulatory assessment of joint loading in the occupational setting. `https://www.xsens.com/customer-cases/indoa-novel-wearable-measurement-system-ambulatory-assessment-joint-loading-occupational-setting/`. Accessed: 2019-06-14. 21

[37] M. Felis and K. Mombaur. Modeling and optimization of human walking. In K. Mombaur and K. Berns, editors, *Modeling, Simulation and Optimization of Bipedal Walking*, volume 18 of *Cognitive Systems Monographs*, pages 31–42. Springer Berlin Heidelberg, 2013. 71

[38] M. L. Felis. *Modeling Emotional Aspects in Human Locomotion*. PhD thesis, Heidelberg University, 2015. 71

[39] M. L. Felis. Meshup - visualization tool for multibody systems based on skeletal animation, 2016. Accessed: 29 February 2016. 23

[40] M. L. Felis. Rbdl: An efficient rigid-body dynamics library using recursive algorithms. *Autonomous Robots*, pages 1–17, 2016. 2, 30, 31, 39

[41] M. L. Felis, K. Mombaur, and A. Berthoz. Mathematical modeling of emotional body language during human walking. In H. G. Bock, X. P. Hoang, R. Rannacher, and J. P. Schlöder, editors, *Modeling, Simulation and Optimization of Complex Processes - HPSC 2012*, pages 25–35. Springer International Publishing, 2014. 30

[42] R. Ferber, L. R. Osternig, M. H. Woollacott, N. J. Wasielewski, and J.-H. Lee. Reactive balance adjustments to unexpected perturbations during human walking. *Gait & Posture*, 16(3):238 – 248, 2002. 1, 8

[43] R. Fitzpatrick, D. Burke, and S. C. Gandevia. Task-dependent reflex responses and movement illusions evoked by galvanic vestibular stimulation in standing humans. *The Journal of Physiology*, 478(2):363–372, 1994. 17

[44] R. C. Fitzpatrick and B. L. Day. Probing the human vestibular system with galvanic stimulation. *Journal of Applied Physiology*, 96(6):2301–2316, 2004. PMID: 15133017. 17

[45] R. C. Fitzpatrick, J. L. Taylor, and D. I. McCloskey. Ankle stiffness of standing humans in response to imperceptible perturbation: reflex and task-dependent components. *Journal of Physiology*, 454:533–547, 1992. 86

[46] P. A. Forbes, B.L. Luu, E. A. Van der Loos, H. F. M.and Croft, J. T. Inglis, and J.-S. Blouin. Transformation of vestibular signals for the control of standing in humans. *Journal of Neuroscience*, 36(45):11510–11520, 2016. 17

[47] N. Forss, R. Hari, R. Salmelin, A. Ahonen, M. Hämäläinen, M. Kajola, J. Knuutila, and J. Simola. Activation of the human posterior parietal cortex by median nerve stimulation. *Experimental Brain Research*, 99(2):309–315, May 1994. 15, 17

[48] C. Geiger and C. Kanzow. *Numerische Verfahren zur Lösung unrestringierter Optimierungsaufgaben*. 1999. 37, 42

[49] T. Ghuntla, H. Mehta, P. Gokhale, and C. Shah. A comparison and importance of auditory and visual reaction time in basketball players. *Saudi Journal of Sports Medicine*, 14(1):35–38, 2014. 15

[50] P. E. Gill, W. Murray, and M. Wright. Practical optimization. *Academic Press*, 1997. 37, 42

[51] Philip Gill, Walter Murray, and Michael Saunders. User's guide for qpopt 1.0: A fortran package for quadratic programming. 05 1997. 44

[52] S. Goddard Blythe. *The Significance of Primitive and Postural Reflexes*, pages 29–63. 03 2017. 17

[53] A. Goswami, S. Yun, U. Nagarajan, S. Lee, K. Yin, and Shivaram Kalyanakrishnan. Direction-changing fall control of humanoid robots: theory and experiments. *Autonomous Robots*, 36(3):199–223, Mar 2014. 8

[54] J. D. Greenspan. Influence of velocity and direction of surface-parallel cutaneous stimuli on responses of mechanoreceptors in feline hairy skin. *Journal of Neurophysiology*, 68(3):876–889, 1992. PMID: 1432054. 13

[55] M. Günther, S. Grimmer, T. Siebert, and R. Blickhan. All leg joints contribute to quiet human stance: A mechanical analysis. *Journal of Biomechanics*, 42(16):2739 – 2746, 2009. 1, 11

[56] F. J. Haran and E. A. Keshner. Sensory reweighting as a method of balance training for labyrinthine loss. *Journal of Neurologic Physical Therapy*, 32(4):186—-191, Dec 2008. 14

[57] D. Hecht and M. Reiner. Sensory dominance in combinations of audio, visual and haptic stimuli. *Experimental Brain Research*, 193(2):307–314, Feb 2009. 15

[58] D. Hecht, M. Reiner, and A. Karni. Multisensory enhancement: gains in choice and in simple response times. *Experimental Brain Research*, 189(2):133, May 2008. 15

[59] H. Herr. Exoskeletons and orthoses: Classification, design challenges and future directions. *Journal of NeuroEngineering and Rehabilitation*, 6(21), June 2009. 95

[60] H. Herr and M. Popovic. Angular momentum in human walking. *Journal of Experimental Biology*, 211(4):467–481, 2008. 10

[61] A. L. Hof, S. M. Vermerris, and W. A. Gjaltema. Balance responses to lateral perturbations in human treadmill walking. *Journal of Experimental Biology*, 213(15):2655–2664, 2010. 1, 8

[62] C. Hoffmann, C. Kirches, A. Potschka, S. Sager, L. Wirsching, and M. Diehl. *MUSCOD User Manual*. 2011. 37

[63] A. G. Hofmann. *Robust Execution of Bipedal Walking Tasks From Biomechanical Principles*. PhD thesis, Massachusetts Institute of Technology, 2006. 1

[64] F. B. Horak. Clinical Measurement of Postural Control in Adults. *Physical Therapy*, 67(12):1881–1885, 12 1987. 1, 7, 9, 11

[65] F. B. Horak. Postural orientation and equilibrium: what do we need to know about neural control of balance to prevent falls? In *Age and Ageing*, volume 35-S2, page ii7–ii11, 2006. 7, 8, 12

[66] F. B. Horak and J. M. Macpherson. *Handbook of Physiology - A critical, comprehensive presentation of physiological knowledge and concepts, Chapter 7: Postural orientation and equilibrium.* Oxford University Press, 1996. 11, 13, 14

[67] G.A. Horstmann and V. Dietz. The contribution of vestibular input to the stabilization of human posture: A new experimental approach. *Neuroscience Letters*, 95(1):179 – 184, 1988. 13

[68] M. Hoshiyama, R. Kakigi, S. Koyama, S. Watanabe, and M. Shimojo. Activity in posterior parietal cortex following somatosensory stimulation in man: Magnetoencephalographic study using spatio-temporal source analysis. *Brain Topography*, 10(1):23–30, Sep 1997. 17

[69] E. T. Hsiao and S. N. Robinovitch. Biomechanical influences on balance recovery by stepping. *Journal of Biomechanics 32*, pages 1099–1106, 1999. 1, 7, 11

[70] E. T. Hsiao and S. N. Robinovitch. The effect of step length on young and elderly women's ability to recover balance. *Journal of Biomechanics 22*, pages 547–580, 2007. 8

[71] Y. Hu. *The role of compliance in humans an humanoid robots locomotion*. PhD thesis, Heidelberg University, 2017. 10

[72] B. Hwang and D. Jeon. A method to accurately estimate the muscular torques of human wearing exoskeletons by torque sensors. *Sensors*, pages 8337–8357, 2015. 8, 96

[73] K. Inui, X. Wang, Y. Tamura, Y. Kaneoke, and R. Kakigi. Serial Processing in the Human Somatosensory System. *Cerebral Cortex*, 14(8):851–857, 08 2004. 15, 17

[74] A. Jain, R. Bansal, A. Kumar, and K. Singh. A comparative study of visual and auditory reaction times on the basis of gender and physical activity levels of medical first year students. *International Journal of Applied and Basic Medical Research*, 5:122, 05 2015. 15, 16

[75] B. Jalgha, D. Asmar, and I. Elhajj. A hybrid ankle/hip preemptive falling scheme for humanoid robots. In *2011 IEEE International Conference on Robotics and Automation*, pages 1256–1262, May 2011. 9

[76] S. Jatsun, S. Savin, and A. Yatsun. Comparative analysis of global optimization-based controller tuning methods for an exoskeleton performing push recovery. In *2016 20th International Conference on System Theory, Control and Computing (ICSTCC)*, pages 107–112, Oct 2016. 10

[77] S. Jatsun, S. Savin, and A. Yatsun. Motion control algorithm for exoskeleton push recovery in the frontal plane. In Aleksandar Rodić and Theodor Borangiu, editors, *Advances in Robot Design and Intelligent Control*, pages 474–481, Cham, 2017. Springer International Publishing. 10

[78] R. Kabbaligere, B.-C. Lee, and C. S. Layne. Balancing sensory inputs: Sensory reweighting of ankle proprioception and vision during a bipedal posture task. *Gait & Posture*, 52:244 – 250, 2017. 14

[79] S. Kajita, F. Kanehiro, K. Kaneko, K. Fujiwara, K. Harada, K. Yokoi, and H. Hirukawa. Biped walking pattern generation by using preview control of zero-moment point. In *2003 IEEE International Conference on Robotics and Automation (Cat. No.03CH37422)*, volume 2, pages 1620–1626 vol.2, Sep. 2003. 9

[80] S. Kajita, F. Kanehiro, K. Kaneko, K. Yokoi, and H. Hirukawa. The 3d linear inverted pendulum mode: a simple modeling for a biped walking pattern generation. In *Proceedings 2001 IEEE/RSJ International Conference on Intelligent Robots and Systems. Expanding the Societal Role of Robotics in the the Next Millennium (Cat. No.01CH37180)*, volume 1, pages 239–246 vol.1, Oct 2001. 8

[81] E. R. Kandel, J. H. Schwartz, T. M. Jessel, S. A. Siegelbaum, and A. J. Hudspeth. *Principles of Neral Science*. McGraw-Hill Publishing, 2012. 11

[82] K. Kasozi, N. Elvis Mbiydzenyuy, S. Namubiru, A. Safiriyu, S. Sulaiman, A. Okpanachi, and H. Ninsiima. A study on visual, audio and tactile reaction time among medical students at kampala international university in uganda. *African Health Sciences*, 18:828, 08 2018. 15, 16, 68

[83] L. Kaul and T. Asfour. Human push-recovery: Strategy selection based on push intensity estimation. In *ISR - 47st International Symposium on Robotics*, 2016. 1, 7, 11

[84] P. Kaur, M. Paul, and J. Sandhu. Auditory and visual reaction time in athletes, healthy controls, and patients of type 1 diabetes mellitus: A comparative study. 2006. 15, 16

[85] C. T. Kelley. *Iterative Methods for Optimization*. 1999. 37

[86] Bryan J. Kemp. Reaction time of young and elderly subjects in relation to perceptual deprivation and signal-on versus signal-off conditions. 1973. 15, 16

[87] T. Kiemel, K. S. Oie, and J. J. Jeka. Multisensory fusion and the stochastic structure of postural sway. *Biological Cybernetics*, 87(4):262–277, Oct 2002. 14

[88] I.-S. Kim, Y.-J. Han, and Y.-D Hong. Stability control for dynamic walking of bipedal robot with real-time capture point trajectory optimization. *Journal of Intelligent & Robotic Systems*, Jan 2019. 9

[89] M. Kim and S. H. Collins. Once-per-step control of ankle-foot prosthesis push-off work reduces effort associated with balance during walking. *Journal of NeuroEngineering and Rehabilitation*, 12(43), 2015. 9

[90] T. J. Klein, John Jeka, Tim Kiemel, and M. Anthony Lewis. Navigating sensory conflict in dynamic environments using adaptive state estimation. *Biological Cybernetics*, 105(5):291–304, Dec 2011. 8

[91] K. H. Koch, D. Clever, K. Mombaur, and D. Endres. Learning movement primitives from optimal and dynamically feasible trajectories for humanoid walking. In *15th IEEE-RAS International Conference on Humanoid Robots (Humanoids)*, pages 866–873. IEEE, 2015. 75

[92] K. H. Koch and K. Mombaur. Exoopt - a framework for patient centered design optimization of lower limb exoskeletons. In *IEEE International Conference on Rehabilitation Robotics*, pages 113–118. IEEE, 2015. 96, 97, 98

[93] T. Koolen, T. de Boer, J. Rebula, A. Goswami, and J. Pratt. Capturability-based analysis and control of legged locomotion, part 1: Theory and application to three simple gait models. *The International Journal of Robotics Research*, 31(9):1094–1113, 2012. 9

[94] R. M. Kopitzsch, D. Clever, and K. Mombaur. Optimal spring-damper systems to support push recovery motions during walking of humans wearing lower-limb exoskeletons. *Journal of Advanced Robotics*, 31(22):1238–1252, 2017. 96

[95] R. M. Kopitzsch and K. Mombaur. *Using Spring-Damper Elements to Support Human-Like Push Recovery Motions*, pages 227–241. Springer International Publishing, Cham, 2018. 85

[96] J. Koschorreck and K. Mombaur. Optimization of somersaults and twists in platform diving. *Computer Methods in Biomechanics and Biomedical Engineering*, 12(2-1), 2009. 71, 85

[97] E. A. Kramarow, L. Chen, H. B. Hedegaard, and M. Warner. Deaths from unintentional injury among adults aged 65 and over: United states, 2000-2013. *NCHS data brief*, 199:199, 2015. 1, 8

[98] M. Krause, J. Englsberger, P.-B. Wieber, and C. Ott. Stabilization of the capture point dynamics for bipedal walking based on model predictive control. *IFAC Proceedings Volumes*, 45(22):165 – 171, 2012. 10th IFAC Symposium on Robot Control. 9

[99] J. R. Lackner and M. S. Levine. Changes in apparent body orientation and sensory localization induced by vibration of postural muscles: vibratory myesthetic illusions. *Aviation, space, and environmental medicine*, 50 4:346–54, 1979. 13

[100] D. Lee and J. Lishman. Visual proprioceptive control of stance. *Journal of Human Movement Studies*, 1:87–95, 06 1975. 14

[101] D. N. Lee and E. Aronson. Visual proprioceptive control of standing in human infants. *Perception & Psychophysics*, 15(3):529–532, May 1974. 14

[102] Y. Lee, K. Lee, S.-S. Kwon, J. Jeong, C. O'Sullivan, M. S. Park, and J. Lee. Push-recovery stability of biped locomotion. *ACM Trans. Graph.*, 34(6):180:1–180:9, October 2015. 7

[103] D. B. Leineweber, I. Bauer, H. G. Bock, and Schlöder J. P. An efficient multiple shooting based reduced SQP strategy for large-scale dynamic process optimization - Part I: theoretical aspects. pages 157 – 166. 2003. 37, 39

[104] F. Lestienne, J. F. Soechting, and A. Berthoz. Postural readjustments induced by linear motion of visual scenes. *Experimental Brain Research*, 28:363–384, 1977. 14

[105] S. Lim, S. N. Oh, and K. I. Kim. Balance control for biped walking robots using only zero-moment-point position signal. *Electronics Letters*, 48(1):19–20, January 2012. 9

[106] N. Maalouf, I. H. Elhajj, E. Shammas, and D. Asmar. Humanoidpushrecoveryusingsensoryreweighting. *RoboticsandAutonomousSystems*, 94:208–218, May 2017. 8

[107] C. D. MacKinnon and D. A. Winter. Control of whole body balance in the frontal plane during human walking. *Journal of Biomechanics*, 26(6):633 – 644, 1993. 9

[108] A. Mahboobin, P. J. Loughlin, M. S. Radfern, S. O. Anderson, C. G. Atkeson, and K. Hodgins, J. Sensory adaptation in human balance control: Lessons for biomimeticrobotic bipeds. *Neral Neworks*, 21:621–627, 2008. 8, 14

[109] A. Mahboobin, P. J. Loughlin, M. S. Redfern, and P. J. Sparto. Sensory re-weighting in human postural control during moving-scene perturbations. *Experimental Brain Research*, 167(2):260–267, Nov 2005. 14

[110] E. C. Martinez-Villalpando and H. Herr. Agonist-antagonist active knee prosthesis: A preliminary study in level-ground walking. *Journal of Rehabilitation Research and Development*, pages 361–374, 2009. 96

[111] P. B. C. Matthews. Where does sherrington's "muscular sense" originate? muscles, joints, corollary discharges? *Annual Review of Neuroscience*, 5(1):189–218, 1982. PMID: 6462096. 13

[112] C. Maurer, T. Mergner, and R.J. Peterka. Multisensory control of human upright stance. *Experimental Brain Research*, 171(2):231, Nov 2005. 14

[113] K. H. Mauritz and V. Dietz. Characteristics of postural instability induced by ischemic blocking of leg afferents. *Experimental Brain Research*, 38(1):117–119, Jan 1980. 13

[114] Patricia M. McAndrew, Jason M. Wilken, and Jonathan B. Dingwell. Dynamic stability of human walking in visually and mechanically destabilizing environments. *Journal of Biomechanics*, 44(4):644 – 649, 2011. 1, 8

[115] T. Mergner. A neurological view on reactive human stance control. *Annual Reviews in Control*, 34(2):177 – 198, 2010. 14

[116] Outdoor Falls Among Middle-Aged and Older Adults: A Neglected Public Health Problem. Li, w. and keegan, t. h. m. and sternfeld, b. and sidney, s. and quesenberry, c. p. and kelsey, j. l. *American Journal of Public Health*, 96(7):1192–1200, 2006. 1, 8

[117] K. Mombaur, A. Truong, and J.-P. Laumond. From human to humanoid locomotion—an inverse optimal control approach. *Autonomous Robots*, 28(3):369–383, December 2009. 82

[118] K. D. Mombaur, R. W. Longman, H. G. Bock, and J. P. Schlöder. Open-loop stable running. *Robotica*, 23(01):21 – 33, January 2005. 8

[119] K. D. Mombaur, R. W. Longman, J. P. Schlöder, and H. G. Bock. Optimizing spring-damper design in human-like walking that is asymptotically stable without feedback. In *Proceedings of International Conference on High Performance Scientific Computing 2006*, Lecture Notes in Scientific Computing, Hanoi, Vietnam, 2008. Springer. 85, 86

[120] M. Morisawa, S. Kajita, F. Kanehiro, K. Kaneko, K. Miura, and K. Yokoi. Balance control based on capture point error compensation for biped walking on uneven terrain. In *2012 12th IEEE-RAS International Conference on Humanoid Robots (Humanoids 2012)*, pages 734–740, Nov 2012. 9

[121] M. Mungiole, H. P. Crowell, and A. C. Boynton. Exoskeleton power and torque requirements based on human biomechanics. In *Army Research Lab*, 2002. 96

[122] M. Nardini and D. Cowie. *The development of multisensory balance, locomotion, orientation and navigation*. 09 2012. 12

[123] L. M. Nashner, C. L. Shupert, F. B. Horak, and F. O. Black. Chapter 33 organization of posture controls: an analysis of sensory and mechanical constraints. In J.H.J. Allum and M. Hulliger, editors, *Afferent Control of Posture and Locomotion*, volume 80 of *Progress in Brain Research*, pages 411 – 418. Elsevier, 1989. 13

[124] L. M. Nashner and P. Wolfson. Influence of head position and proprioceptive cues on short latency postural reflexes evoked by galvanic stimulation of the human labyrinth. *Brain Research*, 67(2):255 – 268, 1974. 17

[125] J. G. Nelson. The effect of water immersion and body position upon perception of the gravitational vertical. *Aerospace Medicine*, 39(8):806–811, 1967. 13

[126] D. Nenchev and A. Nishio. Ankle and hip strategies for balance recovery of a biped subjected to an impact. *Robotica*, 26:643–653, 09 2008. 9

[127] J. Nocedal and S. J. Wright. *Numerical Optimization*, volume 43 of *Springer Series in Operations Research*. Springer, 1999. 37, 42

[128] C.A. Oatis. *Kinesiology: The Mechanics and Pathomechanics of Human Movement*. Lippincott Williams & Wilkins, 2004. 10

[129] K. Oie, S. Carver, T. Kiemel, J. Barela, and J. Jeka. 5.24 the dynamics of sensory reweighting: A temporal symmetry. *Gait & Posture*, 21:29, 2005. 14

[130] A. S. C. Oliveira, L. Gizzi, U. G. Kersting, and D. Farina. Modular organization of balance control following perturbations during walking. *Journal of Neurophysiology*, pages 1895–906, 2012. 8

[131] R. A. Ozdemir, A. Pourmoghaddam, and W. H. Paloski. Sensorimotor posture control in the blind: Superior ankle proprioceptive acuity does not compensate for vision loss. *Gait & Posture*, 38(4):603 – 608, 2013. 12

[132] M. T. G. Pain and A. Hibbs. Sprint starts and the minimum auditory reaction time. *Journal of Sports Sciences*, 25(1):79–86, 2007. PMID: 17127583. 15, 16

[133] H. Panic, A. S. Panic, P. DiZio, and J. R. Lackner. Direction of balance and perception of the upright are perceptually dissociable. *Journal of Neurophysiology*, 113(10):3600–3609, 2015. PMID: 25761954. 13

[134] J. H. Park and K. D. Kim. Biped robot walking using gravity-compensated inverted pendulum mode and computed torque control. In *Proceedings. 1998 IEEE International Conference on Robotics and Automation (Cat. No.98CH36146)*, volume 4, pages 3528–3533 vol.4, May 1998. 8

[135] S. Park, F. Horak, and A. Kuo. Postural feedback responses scale with biomechanical constraints in human standing. *Experimental brain research. Experimentelle Hirnforschung. Expérimentation cérébrale*, 154:417–27, 03 2004. 9

[136] J. H. Pasma, T. A. Boonstra, S. F. Campfens, A. C. Schouten, and H. Van der Kooij. Sensory reweighting of proprioceptive information of the left and right leg during human balance control. *Journal of Neurophysiology*, 108(4):1138–1148, 2012. PMID: 22623486. 14

[137] S. Patil and S. Phatale. Auditory and visual reaction time - a tool for early detection of neuropathy in diabetics. *International Journal of Health Sciences and Research*, 5(4):141–146, 2015. 15

[138] W. Paulus, A. M. Straube, and T. Brandt. Visual stabilization of posture. physiological stimulus characteristics and clinical aspects. *Brain : a journal of neurology*, 107 (Pt 4):1143–63, 1984. 14

[139] R. J. Peterka. Sensorimotor integration in human postural control. *Journal of Neurophysiology*, 88(3):1097–1118, 2002. PMID: 12205132. 10, 12

[140] R. J. Peterka and M. S. Benolken. Role of somatosensory and vestibular cues in attenuating visually induced human postural sway. *Experimental Brain Research*, 105(1):101–110, Jul 1995. 13

[141] R. J. Peterka and P. J. Loughlin. Dynamic regulation of sensorimotor integration in human postural control. *Journal of Neurophysiology*, 91(1):410–423, 2004. PMID: 13679407. 14

[142] V. Pettorossi and M. Schieppati. Neck proprioception shapes body orientation and perception of motion. *Frontiers in human neuroscience*, 8:895, 11 2014. 13

[143] M. Pijnappels, M. F. Bobbert, and J. H. van Dieën. Push-off reactions in recovery after tripping discriminate young subjects, older non-fallers and older fallers. *Gait & Posture*, 21(4):388 – 394, 2005. 9

[144] B. Pleger and A. Villringer. The human somatosensory system: From perception to decision making. *Progress in Neurobiology*, 103:76 – 97, 2013. Conversion of Sensory Signals into Perceptions, Memories and Decisions. 17

[145] M. Potter, B. Wyble, C. Hagmann, and E. McCourt. Detecting meaning in rsvp at 13 ms per picture. *Attention, perception & psychophysics*, 76, 12 2013. 16

[146] M. J. D Powell. The convergence of variable metric mmethod for nonlinearly constrained optimization calculations. pages 27–63, 1978. 43

[147] M. J. D. Powell. The BOBYQA algorithm for bound constrained optimization without derivatives. 2009. 82

[148] J. Pratt and R. Tedrake. Velocity-based stability margins for fast bipedal walking. In *Fast Motions in Robotics and Biomechanics - Optimization and Feedback Control*, Lecture Notes in Control and Information Science. Springer, 2006. 8, 9

[149] R. Proctor and D. Schneider. Hick's law for choice reaction time: A review. *The Quarterly Journal of Experimental Psychology*, 71:1–56, 04 2017. 15

[150] A. Rao. A survey of numerical methods for optimal control. *Advances in the Astronautical Sciences*, 135, 01 2010. 37, 40

[151] K. Rayner. Eye movements in reading and information processing: 20 years of research. *Psychological Bulletin*, pages 372–422, 1998. 16

[152] K. Rayner, T. Smith, G. Malcolm, and J. Henderson. Eye movements and visual encoding during scene perception. *Psychological science*, 20:6–10, 12 2008. 16

[153] J. Rebula, F. Canas, J. Pratt, and A. Goswami. Learning capture points for humanoid push recovery. In *2007 7th IEEE-RAS International Conference on Humanoid Robots*, pages 65–72, Nov 2007. 9

[154] S. N. Robinovitch, F. Feldman, Y. Yang, R. Schonnop, P. M. Leung, T. Sarraf, J. Sims-Gould, and M. Loughin. Video capture of the circumstances of falls in elderly people residing in long-term care: an observational study. *The Lancet*, 381(9860):47 – 54, 2013. 1

[155] J.-P. Roll, J.-P. Vedel, and R. Roll. Chapter 10 eye, head and skeletal muscle spindle feedback in the elaboration of body references**this paper is based on presentations given at two different meetings on posture and locomotion held in marseilles (june 1988) and in rheinfelden (september 1988). In J.H.J. Allum and M. Hulliger, editors, *Afferent Control of Posture and Locomotion*, volume 80 of *Progress in Brain Research*, pages 113 – 123. Elsevier, 1989. 13

[156] G. Roth. *Fühlen, Denken, Handeln - Wie das Gehirn unser Verhalten steuert.* Suhrkamp Verlag, 2003. 15

[157] B. S. Roudsari, B. E. Ebel, P. S. Corso, N.-A. M. Molinari, and T. D. Koepsell. The acute medical care costs of fall-related injuries among the u.s. older adults. *Injury*, 36(11):1316 – 1322, 2005. 1

[158] R. M. Schemschat, D. Clever, M. L. Felis, E. Chiovetto, M. Giese, and K. Mombaur. Joint torque analysis of push recovery motions during human walking. In *2016 6th IEEE International Conference on Biomedical Robotics and Biomechatronics (BioRob)*, pages 133–139, June 2016. 45, 96

[159] R. M. Schemschat, D. Clever, M. L. Felis, and K. Mombaur. Optimal push recovery for periodic walking motions. *IFAC-PapersOnLine*, 49(14):93 – 98, 2016. 6th IFAC Workshop on Periodic Control Systems PSYCO 2016. 71

[160] R. M. Schemschat, D. Clever, and K. Mombaur. Optimization based analysis of push recovery during walking motions to support the design of lower-limb exoskeletons. In *2016 IEEE International Conference on Simulation, Modeling, and Programming for Autonomous Robots (SIMPAR)*, pages 224–231, Dec 2016. 96

[161] G. Schultz and K. Mombaur. Modeling and optimal control of human-like running. *IEEE/ASME Transactions on Mechatronics*, 15(5):783 – 792, October 2010. 8, 71, 85

[162] G. Schweigart, S. Heimbrand, T. Mergner, and W. Becker. Perception of horizontal head and trunk rotation: modification of neck input following loss of vestibular function. *Experimental Brain Research*, 95(3):533–546, Aug 1993. 13

[163] V. B. Semwal and G. C. Nandi. Study of humanoid push recovery based on experiments. *CoRR*, abs/1405.4450, 2014. 8

[164] N. Shaari, I. Md Isa, and T. Jun. Torque analysis of the lower limb exoskeleton robot design. *ARPN Journal of Engineering and Applied Sciences*, pages 9140–9149, 2015. 96

[165] M. Shafiee-Ashtiani, A. Yousefi-Koma, and M. Shariat-Panahi. Robust bipedal locomotion control based on model predictive control and divergent component of motion. In *2017 IEEE International Conference on Robotics and Automation (ICRA)*, pages 3505–3510, May 2017. 9

[166] M. Shafiee-Ashtiani, A. Yousefi-Koma, M. Shariat-Panahi, and M. Khadiv. Push recovery of a humanoid robot based on model predictive control and capture point. In *2016 4th International Conference on Robotics and Mechatronics (ICROM)*, pages 433–438, Oct 2016. 10

[167] Jose Shelton and Gideon Praveen Kumar. Comparison between auditory and visual simple reaction times. *Neurosci Med*, 1(1):30–32, 2010. 15, 16

[168] A. Shumway-Cook and M. H. Woollacott. The growth of stability. *Journal of Motor Behavior*, 17(2):131–147, 1985. PMID: 15140688. 14

[169] E. Spyrakos-Papastavridis, G. A. Medrano-Cerda, N. G. Tsagarakis, J. S. Dai, and D. G. Caldwell. A push recovery strategy for a passively compliant humanoid robot using decentralized lqr controllers. In *2013 IEEE International Conference on Mechatronics (ICM)*, pages 464–470, Feb 2013. 10

[170] M. A. Srinivasan and R. H. LaMotte. Tactile discrimination of shape: responses of slowly and rapidly adapting mechanoreceptive afferents to a step indented into the monkey fingerpad. *Journal of Neuroscience*, 7(6):1682–1697, 1987. 13

[171] B. Stephens. Humanoid push recovery. In *2007 7th IEEE-RAS International Conference on Humanoid Robots*, pages 589–595, Nov 2007. 8, 9

[172] B. Stephens. *Push recovery control for force-controlled humanoid robots*. PhD thesis, The Robotics Institute Carnegie Mellon University, 2011. 10

[173] B. J. Stephens and C. G. Atkeson. Push recovery by stepping for humanoid robots with force controlled joints. In *2010 10th IEEE-RAS International Conference on Humanoid Robots*, pages 52–59, Dec 2010. 8

[174] K. A. Tahboub. Biologically-inspired humanoid postural control. *Journal of Physiology-Paris*, 103(3–5):195–210, 2009. 8, 13

[175] J. L. Taylor and D. I. McCloskey. Proprioception in the neck. *Experimental Brain Research*, 70(2):351–360, Apr 1988. 13

[176] O. Terlemez, S. Ulbrich, C. Mandery, M. Do, N. Vahrenkamp, and T. Asfour. Master motor map (mmm) - a framework and toolkit for capturing, representing, and reproducing human motion on humanoid robots. volume 2015, pages 0–0, 11 2014. 2, 23

[177] P. D. Thompson, J. G. Colebatch, P. Brown, J. C. Rothwell, B. L. Day, J. A. Obeso, and C. D. Marsden. Voluntary stimulus-sensitive jerks and jumps mimicking myoclonus or pathological startle syndromes. *Movement Disorders*, 7(3):257–262, 1992. 15, 16

[178] K.-Y. Tu and W.-C. Lee. Analysis and study of human joint torque and motion energy during walking on various grounds. In Prahlad Vadakkepat, Jong-Hwan Kim, Norbert Jesse, Abdullah Al Mamun, Tan Kok Kiong, Jacky Baltes, John Anderson, Igor Verner, and David Ahlgren, editors, *Trends in Intelligent Robotics*, pages 73–81, Berlin, Heidelberg, 2010. Springer Berlin Heidelberg. 8

[179] H. van der Kooij, R. Jacobs, B. Koopman, and F. van der Helm. An adaptive model of sensory integration in a dynamic environment applied to human stance control. *Biological Cybernetics*, 84(2):103–115, Jan 2001. 14

[180] H. van der Kooij, J.F. Veneman, and R. Ekkelenkamp. Compliant actuation of exoskeletons. In *Mobile Robots, Towards New Applications*, 2006. 95

[181] C. L. Vaughan. Are joint torques the holy grail of human gait analysis? *Human Movement Science*, 15(3):423 – 443, 1996. 8

[182] M. Vlutters, E. van Asseldonk, and H. Kooij. Reduced center of pressure modulation elicits foot placement adjustments, but no additional trunk motion during anteroposterior-perturbed walking. *Journal of Biomechanics*, 68, 12 2017. 9

[183] M. Vukobratović and B. Borovac. Zero-moment point - thirty five years of its life. *International Journal of Humanoid Robotics*, 01(01):157–173, 2004. 9

[184] L. M. Wagner, J. C. Dionne, J. R. Zive, and P. A. Rochon. Fall risk care processes in nursing home facilities. *Journal of the American Medical Directors Association*, 12(6):426 – 430, 2011. 1, 8

[185] C. J. Walsh, K. Endo, and H. Herr. A quasi-passive leg exoskeleton for load-carrying augmentation. *International Journal of Humanoid Robotics*, 4(3), 2007. 95

[186] S. Wang, W. van Dijk, and H. van der Kooij. Spring uses in exoskeleton actuation design. In *IEEE International Conference on Rehabilitation Robots*, 2011. 95

[187] Y. Wang, R. Xiong, Q. Zhu, and J. Chu. Compliance control for standing maintenance of humanoid robots under unknown external disturbances. In *2014 IEEE International Conference on Robotics and Automation (ICRA)*, pages 2297–2304, May 2014. 10

[188] D. A. Wardle. The time delay in human vision. *The Physics Teacher*, 36(7):442–444, 1998. 16

[189] Meagan J. Warnica, Tyler B. Weaver, Stephen D. Prentice, and Andrew C. Laing. The influence of ankle muscle activation on postural sway during quiet stance. *Gait & Posture*, 39(4):1115 – 1121, 2014. 1, 11

[190] D. A. Winter. Human balance and posture control during standing and walking. *Gait & Posture*, 3(4):193 – 214, 1995. 8, 9

[191] D. A. Winter, A. E. Patla, F. Prince, M. Ishac, and K. Gielo-Perczak. Stiffness control of balance in quiet standing. *Journal of Neurophysiology*, 80:1211–1221, 1998. 86

[192] A. Wit and A. Czaplicki. Inverse dynamics and artificial neural network applications in gait analysis of the disabled subjects. In *Human Movement*, pages 93–102, 2008. 8

[193] M. Wu, L. Ji, D. Jin, and Y. Pai. Minimal step length necessary for recovery of forward balance loss with a single step. *Journal of Biomechanics 40*, pages 1559–66, 2007. 1, 7, 11

[194] S.-J. Yi, B.-T. Byoung-Tak Zhang, Hong D., and D. D. Lee. Online learning of a full body push recovery controller for omnidirectional walking. *11th IEEE-RAS International Conference on Humanoid Robots*, 2011. 9

[195] S. Yun and A. Goswami. Momentum-based reactive stepping controller on level and non-level ground for humanoid robot push recovery. In *2011 IEEE/RSJ International Conference on Intelligent Robots and Systems*, pages 3943–3950, Sep. 2011. 10

[196] A. Zoss and H. Kazerooni. Design of an electrically actuated lower extremity exoskeleton. *Advanced Robotics*, 20:967–988, 2006. 96